FUNDAMENTAL STUDIES OF WATER OXIDATION AT MODEL HEMATITE ELECTRODES PREPARED BY ATOMIC LAYER DEPOSITION

By

Benjamin M. Klahr

A DISSERTATION

Submitted to
Michigan State University
in partial fulfillment of the requirements
for the degree of

Chemistry – Doctor of Philosophy

2013

ABSTRACT

FUNDAMENTAL STUDIES OF WATER
OXIDATION AT MODEL HEMATITE ELECTRODES
PREPARED BY ATOMIC LAYER DEPOSITION

By

Benjamin M. Klahr

An increasing global demand for energy, combined with an awareness of anthropogenic climate change, has recently fueled the search for abundant, carbon neutral energy sources. The sun offers an enormous amount of energy that is practically inexhaustible and well distributed across Earth. Thus, it is an ideal source for meeting our future energy needs in a carbon neutral fashion. This work focuses on using hematite and sunlight to oxidize water, which is the rate limiting step of splitting water into the energy dense fuel, hydrogen, and the byproduct, oxygen. Hematite is abundant, absorbs a large fraction of the solar spectrum and has an appropriately placed valence band for water oxidation. However, the often cited poor bulk properties, and slow charge transfer kinetics require large applied potentials to oxidize water. Atomic layer deposition (ALD) was utilized to deposit uniform thin films of hematite on transparent conductive substrates as model electrodes to better understand the nature of the limitations in the bulk and at the surface. Comparison of the oxidation of water to the oxidation of fast redox shuttles allowed for the separation of bulk and surface processes. A combination of electrochemical impedance spectroscopy, photoelectrochemical and electrochemical measurements were employed to determine the cause of the large required applied potential. It was found that photogenerated holes initially oxidize the electrode surface under water oxidation conditions, which is attributed to the first step in water oxidation. A critical number of these surface intermediates need to be

generated in order for subsequent hole-transfer steps to proceed. At low applied potentials, these intermediates are subject to recombination from the large concentration of electrons in the conduction band due to low band bending. At higher applied potentials, high band bending eliminates surface recombination and the charge collection efficiency of the electrolyte reaches unity. A water oxidation mechanism is proposed to interpret these results. In addition, fundamental studies of hematite electrodes coated with the phosphate mediated cobalt oxide catalyst were performed. The catalyst was found to reduce the surface recombination mentioned above. However, oxidized cobalt oxide was still subject to electron recombination at low applied potentials. This recombination was reduced with the use of an alumina blocking layer, which resulted in a modified hematite electrode capable of oxidizing water with a near unity charge collection efficiency at low applied potentials.

ACKNOWLEDGEMENTS

I would like to thank my advisor, Professor Tom Hamann, for his patience, wisdom and guidance throughout my PhD. Tom has provided abundant support and opportunities, for which I am extremely grateful. Perhaps most importantly, Tom's critical insight and integrity has provided a great model which has influenced how I approach scientific research. In addition, Tom was able to secure funding which allowed me to perform the research presented herein. Specifically, I would like to thank Michigan State University, the donors of the American Chemical Society Petroleum Research Fund (#51099-DNI10) and the National Science Foundation (CHE-1150378) for funding Tom who could in turn fund me.

I would like to thank my colleagues Alex Martinson and Shannon Riha from Argonne National Lab as well as Sixto Gimenez, Francisco Fabregat-Santiago and Juan Bisquert from Universitat Jaume I. The fruitful collaborations I have had with these highly capable people have helped shape me into the scientist I am today. I would also like to thank my lab-mates for contributing to a fun and productive working environment. Specifically, I am grateful for the fruitful discussions with Jesse Ondersma and collaborations with Kelley Young and Omid Zandi.

Finally, I would like to thank my friends, family, parents and brothers for their endless support. I cannot count the ways these people have contributed to my ongoing personal and professional development. Specifically, I would like to thank my wife and best friend, Ashlea Klahr. As part of the goal to contribute equally to our partnership, this dissertation represents an attempt to keep up with her.

TABLE OF CONTENTS

LIST OF TABLES

LIST OF FIGURES

Chapter 1:

Introduction

1.1 Motivation

The total average worldwide primary power demand was approximately 15 TW in 2010 (corresponding to the use of 484 x 10^{18} J).[1] Due to the world's increasing population and industrialization, the total primary power demand is expected to increase to 23 TW by the year 2035.[1] Approximately 70 % of the supplied power is, and is expected to continue to be, derived from the combustion of fossil fuels.[1] This combustion is the primary component of huge levels of carbon dioxide emissions of approximately 30 billion metric tons a year, which is expected to increase to 40 billion metric tons by 2030.[1-3] It is now widely accepted that that the release of carbon dioxide from this combustion is a major contributor to global climate change.[3] There are many negative environmental consequences associated with climate change, including increasing droughts, increasing population experiencing water stress, widespread coral mortality, decreases in crop productivity, and a rise in sea-level.[2,4] In addition to environmental hazards, the reliance on imported fossil fuels can lead to political and economic instability. Therefore, it is imperative to develop easily distributable, carbon-neutral sources of energy in order to minimize these consequences.[2,4]

1.2 Approach

Of all of the carbon-neutral power options that currently exist (solar, wind, biofuels, hydro, geothermal), solar is the only one that can realistically be implemented on a large enough scale to supply the world's energy demands.[5-7] The sun illuminates the earth with ~120,000 TW of power, where utilizing ~0.01% of it has the potential of satisfying the world's energy demands in a carbon neutral fashion.[6] Solar energy is well-distributed across the most populous areas of

the globe, which provides the resource accessible where it is needed most. This makes solar energy an ideal method of powering the planet.

Efficient solar energy conversion has been around for decades through the use of crystalline-silicon photovoltaics. However, these devices require highly pure materials which increase the manufacturing costs. This results in a high price of \$0.35 $(kW\text{-}hr)^{-1}$ which is not competitive with the cost of energy derived from fossil fuels of 0.02 to 0.05 $(kW\text{-}hr)^{-1}$.[5,6,8] The high cost of electricity production from solar conversion continues to thwart wide spread use of this technology. In addition, solar energy is diurnal and intermittent, while our energy demands are not. Thus, if the vast solar energy resource is ever to be used to supply a significant fraction of the world's ever-increasing energy demand, cheap and efficient methods of energy collection and storage need to be developed.

Analogous to photosynthesis, storing solar energy in chemical bonds (i.e. solar fuels) would be an ideal method. This is preferable for certain applications (e.g. transportation) compared to storing electricity in batteries which are still expensive and have limited capacities. A particularly attractive example of this approach is using solar energy to split water into H_2 and O_2, where the H_2 could subsequently be used in a fuel cell or other energy conversion scheme. This process can be described by the simplified equations:

$$4H^+ + 4e^- \rightarrow 2H_2 \qquad (1\text{-}1)$$

$$2H_2O \rightarrow O_2 + 4H^+ + 4e^- \qquad (1\text{-}2)$$

Forty years ago, the breakthrough report by Fujishima and Honda demonstrated the feasibility of this approach with phtoelectrochemical (PEC) water splitting on TiO_2 photoelectrodes.[9]

Unfortunately, TiO_2 has a large band gap of 3.2 eV and absorbs only UV light making it impractical for economic water splitting. Since then, there has been significant effort to develop efficient, unassisted water splitting systems. In order to achieve this, a given material must satisfy a number of requirements including strong visible light absorption, efficient charge carrier separation and transport, facile interfacial charge-transfer kinetics, appropriate positions of the conduction and valence band energy levels with respect to required reaction potentials and good stability in contact with aqueous solutions.[10] While such systems were heavily investigated several decades ago, no material so far has fulfilled all the required conditions.[11,12]

Realistically, it is expected to be very challenging to synthesize or discover a material that is capable of absorbing a sufficient fraction of the solar spectrum, as well as providing enough driving force for both reactions (1-1) and (1-2). An alternative approach would be to design a system that contains two absorbers, one absorbing long wavelengths, and one absorbing shorter wavelengths. In addition to being capable of absorbing a greater percentage of the solar spectrum, this has the benefit of being able to separately tune the potential of holes capable of oxidizing water (which come from the conduction band of the semiconductor on the left in Figure 1-1), and the potential of electrons capable of reducing protons (which come from the valence band of the semiconductor on the right in Figure 1-1).[13] Also, this design takes into account the requisite practical consideration of being able to separate the evolved H_2 and O_2.

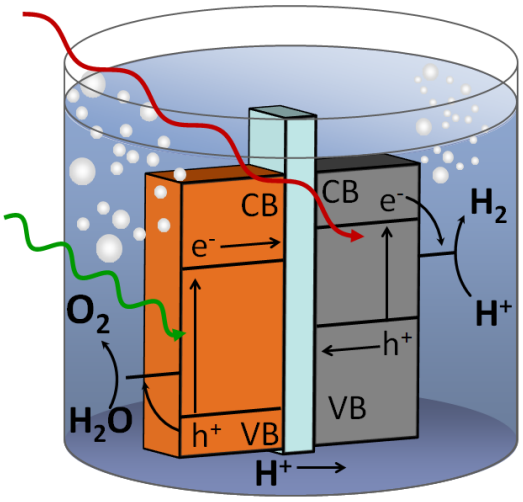

Figure 1-1. Relative energy diagram of a photolectrochecmial cell employing an oxygen evolving (orange) and a hydrogen evolving (gray) semiconductor in tandem. For interpretation of the references to color in this and all other figures, the reader is referred to the electronic version of this dissertation.

Hematite (α-Fe_2O_3) is one promising candidate for the water oxidation half reaction (semiconductor on the left of Figure 1-1) of PEC water splitting due to its adequate absorption of visible light up to 590 nm through its ~2.1 eV band gap, and its valence band energy which, through the absorption of light, generates energetic holes capable of oxidizing water.[14-20] Importantly, for practical reasons, hematite is nontoxic, abundant and extremely stable under caustic conditions.[17,21] This would ensure the economic viability for long term, large scale applications. Attempts to utilize hematite electrodes for solar energy conversion, however, have resulted in very modest energy conversion efficiencies.[22,23] The combination of a low minority charge carrier mobility and short lifetimes, results in a very short charge collection length of

between 2 and 20 nm.[13,15] The minority charge mobility mechanism is best described by small polaron hopping, thus the short charge collection length is inherent to the chemical structure of hematite.[24,25] This short charge collection length is especially problematic since the light absorption depth can be up to 375nm for 550 nm light. Figure 1-2 shows the value $3/\alpha$, which according to Beer's law is the thickness required to absorb 95% of the light at that wavelength.

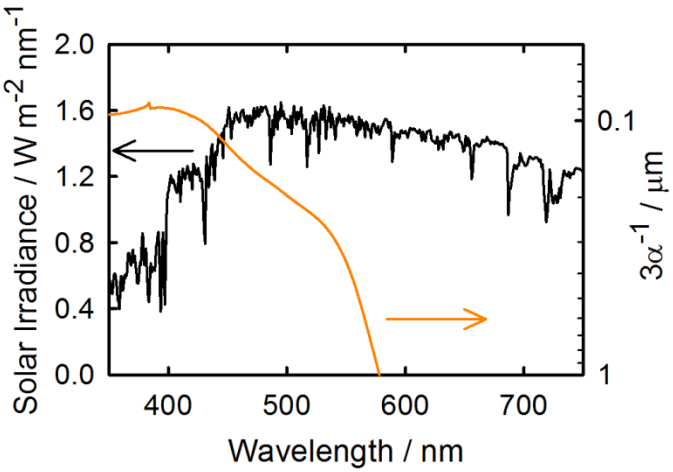

Figure 1-2. AM 1.5 Solar Irradiance (black line) and the thickness required for hematite to absorb 95% of the light, $3/\alpha$ (orange line).

An early attempt to overcome this short collection length was performed by Itoh and Bockris who stacked thin film hematite-substrate layers which effectively absorbed more light while collecting a higher fraction of minority carriers as more charge carriers were generated within a short distance of the semiconductor-electrolyte interface.[26,27] Subsequently, many techniques including colloidal solution deposition, reactive ballistic deposition, electrochemical anodization, spray pyrolysis, and chemical vapor deposition have been used to create new nanostructures of hematite in attempts to maximize light absorption while minimizing the length

minority carriers must travel before being collected.[14,19,28-35] Despite these attempts, the best electrodes only produce current densities on the order of five times lower than the possible 12.5 mA cm^{-2} of a semiconductor with a 2.1 eV band gap.[36] In addition, a large applied potential is required to achieve this currents, which has thus far been attributed to slow water oxidation kinetics at the surface of hematite.[13,37]

1.3 Objectives

It is the purpose of this dissertation to deeply understand the limitations of hematite in the bulk, and the nature of the limited charge transfer at the surface. Recently, such attempts to study these limitations were performed with nanostructured electrodes. While these have the benefit of generating a significant amount of charge near the surface and are able to achieve relatively high photocurrent densities, identifying the precise structure-function relationship is difficult utilizing such a variety of nanostructured electrode morphologies. In addition many nanostructured electrodes are difficult to reproduce and often have inconsistent real surface areas. In this work we use atomic layer deposition (ALD) to deposit hematite electrodes in order to investigate the nature of both bulk and charge transfer limitations of water oxidation. ALD allows the reproducible deposition of pinhole-free, conformal films with a controllable thickness at angstrom resolution.[38-40] Importantly, the self-limiting gas phase mechanism of ALD is an ideal technique for depositing thin films on high aspect ratio scaffolds which are deposited identically to the thin films used herein.[14] Thus, the lessons learned on the model thin films can be directly applied to nanostructured electrodes prepared by ALD. The thin, planar films used herein provide an ideal electrode for fundamental studies as they avoid the complexity and irregularities of most nanostructured surfaces.

REFERENCES

REFERENCES

1. **** *Energy Information Administration: www.eia.doe.gov*.

2. Pachauri, R. K. a. R., A. *IPCC 2007: Climate Change 2007: Synthesis Report. Contribution of Working Groups I, II, and III to the Fourth Assessment Report to the Intergovernmental Panel on Climate Change*, 2008.

3. Moomow, W.; Yamba, F.; Kamimoto, M.; Maurice, L.; Nyboer, J.; Urama, K.; Weir, T. In *IPCC Special Report on Renewable Energy Sources and Climate change Mitigation*; Edenhofer, O., Pichs-Madruga, R., Sokona, Y., Seyboth, K., Matschoss, P., Kadner, S., Zwickel, T., Eickemeier, P., Hansen, G., Schlömer, S., von Stechow, C., Eds.; Cambridge University Press: United Kingdom and New York, NY, USA, 2011.

4. Kerr, R. A. *Science*, **2007**, *318*, 1230-1231.

5. Lewis, N. S. *MRS Bull.* **2007**, *32*, 808-820.

6. Crabtree, G. W.; Lewis, N. S. *Phys. Today* **2007**, *60*, 37-42.

7. Lewis, N. S.; Nocera, D. G. *PNAS*, **2006**, *103*, 15729-15735.

8. Green, M. A.; Emery, K.; Hishikawa, Y.; Warta, W. *Prog. Photovoltaics*, **2009**, *17*, 85-94.

9. Fujishima, A.; Honda, K. *Nature*, **1972**, *238*, 37-38.

10. Walter, M. G.; Warren, E. L.; McKone, J. R.; Boettcher, S. W.; Mi, Q. X.; Santori, E. A.; Lewis, N. S. *Chem Rev.* **2010**, *110*, 6446-6473.

11. Bolts, J.; Wrighton, M. *J. Phys. Chem.* **1976**, *80*, 2641-2645.

12. Butler, M. A.; Ginley, D. S. *J. Mat. Sci.* **1980**, *15*, 1-19.

13. Dareedwards, M. P.; Goodenough, J. B.; Hamnett, A.; Trevellick, P. R. *J. Chem. Soc., Faraday Trans. 1 F* **1983**, *79*, 2027-2041.

14. Lin, Y. J.; Zhou, S.; Sheehan, S. W.; Wang, D. W. *J. Am. Chem. Soc.* **2011**, *133*, 2398-2401.

15. Kennedy, J. H.; Frese, K. W. *J. Electrochem. Soc.* **1978**, *125*, 709-714.

16. Marusak, L. A.; Messier, R.; White, W. B. *J. Phys. Chem. Solids*, **1980**, *41*, 981-984.

17. Hardee, K. L.; Bard, A. J. *J. Electrochem. Soc.* **1977**, *124*, 215-224.

18. Hamann, T. W. *Dalton Trans.* **2012**, *41*, 7830-7834.

19. Duret, A.; Gratzel, M. *J. Phys. Chem. B* **2005**, *109*, 17184-17191.

20. Bindaar, G.; Dareedwards, M. P.; Goodenough, J. B.; Hamnett, A. *J. Chem. Soc. - Far. Trans.* **1983**, *79*, 1199-1213.

21. Finklea, H. O. *Semiconductor Electrodes*; Elsevier: Amsterdam, 1988.

22. Lindgren, T.; Wang, H. L.; Beermann, N.; Vayssieres, L.; Hagfeldt, A.; Lindquist, S. E. *Sol. Energy Mater. Sol. Cells,* **2002**, *71*, 231-243.

23. Sivula, K.; Le Formal, F.; Grätzel, M. *ChemSusChem*, **2011**, *4*, 417-417.

24. Goodenough, J. B. *Prog. Solid State Chem.* **1971**, *5*, 145-399.

25. Kerisit, S.; Rosso, K. M. *J. Chem. Phys.* **2007**, *127*, 124706-124710.

26. Itoh, K.; Bockris, J. O. *J. Appl. Phys.* **1984**, *56*, 874-876.

27. Itoh, K.; Bockris, J. O. *J. Electrochem. Soc.* **1984**, *131*, 1266-1271.

28. Bjorksten, U.; Moser, J.; Gratzel, M. *Chem. Mat.* **1994**, *6*, 858-863.

29. Hahn, N. T.; Ye, H. C.; Flaherty, D. W.; Bard, A. J.; Mullins, C. B. *ACS Nano* **2010**, *4*, 1977-1986.

30. Mohapatra, S. K.; John, S. E.; Banerjee, S.; Misra, M. *Chem. Mater.* **2009**, *21*, 3048-3055.

31. Sivula, K.; Zboril, R.; Le Formal, F.; Robert, R.; Weidenkaff, A.; Tucek, J.; Frydrych, J.; Gratzel, M. *J. Am. Chem. Soc.* **2010**, *132*, 7436-7444.

32. Cherepy, N. J.; Liston, D. B.; Lovejoy, J. A.; Deng, H. M.; Zhang, J. Z. *J. Phys. Chem. B,* **1998**, *102*, 770-776.

33. Cesar, I.; Sivula, K.; Kay, A.; Zboril, R.; Graetzel, M. *J. Phys. Chem. C,* **2009**, *113*, 772-782.

34. Kay, A.; Cesar, I.; Gratzel, M. *J. Am. Chem. Soc.* **2006**, *128,* 15714-15721.

35. Beermann, N.; Vayssieres, L.; Lindquist, S. E.; Hagfeldt, A. *J. Electrochem. Soc.* **2000**, *147*, 2456-2461.

36. Tilley, S. D.; Cornuz, M.; Sivula, K.; Grätzel, M. *Angew. Chem. Int. Ed.* **2010**, *49*, 6405-6408.

37. Upul Wijayantha, K. G.; Saremi-Yarahmadi, S.; Peter, L. M. *Phys. Chem. Chem. Phys.* **2011**, *13*, 5264-5270.

38. George, S. M. *Chem. Rev.* **2010**, *110*, 111-131.

39. Hamann, T. W.; Martinson, A. B. F.; Elam, J. W.; Pellin, M. J.; Hupp, J. T. *Adv. Mater.* **2008**, *20*, 1560–1564.

40. Hamann, T. W.; Martinson, A. B. F.; Elam, J. W.; Pellin, M. J.; Hupp, J. T. *J. Phys. Chem. C* **2008**, *112*, 10303-10307.

Chapter 2:

Thickness Dependence of Thin Film Hematite Deposited by Atomic Layer Deposition

Adapted with permission from:

Photoelectrochemical Investigation of Ultrathin Film Iron Oxide Solar Cells Prepared by Atomic Layer Deposition, Benjamin M. Klahr, Alex B.F. Martinson, and Thomas W. Hamann, *Langmuir*, **2011**, *27*, (1), 461-468.

2.1 Abstract

Atomic layer deposition was used to grow conformal thin films of hematite with controlled thickness on transparent conductive oxide substrates. The hematite films were incorporated as photoelectrodes in regenerative photoelectrochemical cells employing an aqueous $[Fe(CN)_6]^{3-/4-}$ electrolyte. Steady state current density vs. applied potential measurements under monochromatic and simulated solar illumination were used to probe the photoelectrochemical properties of the hematite electrodes as a function of film thickness. Combining the photoelectrochemical results with careful optical measurements allowed us to determine an optimal thickness for a hematite electrode of ~20 nm. Mott-Schottky analysis of differential capacitance measurements indicated a depletion region of ~17 nm. Thus, only charge carriers generated in the depletion region were found to contribute to the photocurrent.

2.2 Introduction

The water oxidation efficiency of hematite electrodes suffers due to a large amount of recombination within the bulk. This is often attributed to the very low minority collection lengths of between 2 and 20 nm.[1,2] The studies often cited, have calculated these values by fitting experimental photoelectrochemical measurements of water oxidation to the Gartner equation. This derivation is made under the assumption that all minority carriers generated within the depletion layer are able to reach the surface. While this may be the case of many semiconductor electrodes, the uniquely low minority carrier lifetime of hematite prevents this from being true (see below and chapter 4).[3-5] This indirect method for calculating the minority collection length therefore presents a significant opportunity for error.

Another way of measuring these lengths is to synthesize thin films that have a thickness on the order of the charge collection length. In addition, thin films should serve as excellent model system to determine the feasibility of overcoming the poor bulk properties of hematite by controlling the dimensions. To this end spray pyrolysis was used to prepare thin films of hematite for water oxidation photocatalysis.[6,7] While spray pyrolysis is a convenient method for preparing thin films, the films are not especially uniform, the thickness is difficult to control, and the reproducibility is questionable. Other techniques, including chemical vapor deposition, electrodeposition, sputtering, and more recently reactive ballistic deposition, have also been used to prepare films of hematite, however they all suffer from similar lack of precise dimensional control and uniformity.[8-13] Further, since water is generally the redox species, the overall performance may depend on the water oxidation step, not strictly the hematite electrode, which can complicate interpretation of the bulk parameters.

In this work we use atomic layer deposition, ALD, to deposit conformal thin films of iron oxide to investigate the photoelectrochemical properties as a function of film thickness. ALD is a self-limiting process which deposits at most a single atomic layer at a time by alternating pulses of a metal precursor and an oxidizer.[14] Hematite has been deposited previously via ALD employing ferrocene and oxygen as the metal precursor and the oxidizer, respectively, however recent work performed by Martinson *et. al.* has demonstrated high growth rates at low deposition temperatures can be achieved by employing ozone as the oxidizer.[15-19] Ferrocene and ozone were therefore selected as the precursors for the ALD of iron oxide in this work. The unique self-limiting property of ALD results in uniform films with highly controllable thicknesses.[20,21] Importantly, since ALD is not a line-of-sight technique, it can be used to make vertically oriented 'thin films' which are prepared in an identical fashion to the model thin films.[22] Thus lessons learned with our model system thin films can be directly applied to nanostructured architectures with precisely controlled dimensions fabricated via ALD.[16]

2.3 Experimental

2.3.1 Atomic Layer Deposition

Atomic layer deposition was performed using a Savannah 100 instrument (Cambridge Nanotech Inc.). Thin films of iron oxide were deposited on fluorine doped tin oxide (FTO) coated glass (Hartford Glass, 12 Ω cm^{-2}) by ALD using ferrocene and O_3 as precursors. Cleaned FTO substrates were treated with 0.1 M HCl, rinsed with isopropanol and blown dry with nitrogen prior to deposition. Ferrocene (Aldrich) was purified by sublimation by heating to 70°C on a hotplate prior to use. The O_3 was made by a Yanco Industries ozone generator (10

wt% in 62 sccm ultra high purity O_2). The nitrogen carrier gas was kept at 5 sccm. The ferrocene precursor cylinder was heated to 70°C, however the vapor pressure was still low and not detectable by our pressure gauge. The substrate chamber was maintained at 200°C. Exposure times of 20 and 60 seconds were used for ferrocene and O_3, respectively, with an 8 second nitrogen purge time between pulses. After deposition, iron oxide electrodes were heated to 500 °C at a rate of 17 °C / min., sintered at 500 °C for 30 minutes and allowed to cool to room temperature over 2 hours. Sintering was found to increase the stability of the electrodes. The ALD of iron oxide was found to be very sensitive to the substrate surface (e.g. growth rate and uniformity), therefore all measurements presented herein were performed on films deposited on nominally identical FTO substrates. Three series of electrodes were made by varying cycles from 100 up to 1,200 cycles. All values reported are the average of the data sets acquired with the three series of electrodes with errors bars representing the standard deviation.

Films were characterized by X-ray diffraction, XRD, using Cu Kα radiation (Rigaku D-max operating at 45 KV and 100 mA) and Raman spectroscopy. Small angle XRD was performed using a Bruker D2 Phaser. Raman spectra were recorded using a 100 mW argon ion laser (Melles Griot CW) at 514.5 nm, an Olympus BH-2 microscope assembly, and a Spex 1250 spectrograph with a 600 grooves/mm holographic grating. The detector was a Symphony 2000 x 800 charge-coupled device (Horiba Jobin-Yvon). Morphology and thickness of the films were determined by field emission scanning electron microscopy using a Hitachi S-4700 FESEM. Absorbance and reflectance measurements were made using a Perkin Elmer Lambda 35 UV-Vis spectrometer with a Labsphere integrating sphere.

2.3.2 Absorbance Calculation

The absorbance spectra of the films were measured by illuminating from the substrate-electrode (SE) interface such that the incident light had to be corrected for passing through and being reflected by the substrate as illustrated in Figure 2-1.

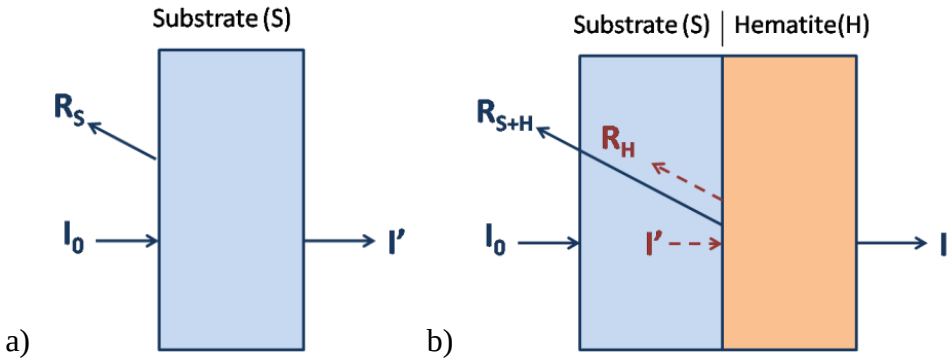

Figure 2-1. Diagram indicating the light reflectance and transmittance of (a) the FTO substrate (S) and (b) the substrate plus hematite film (H). All parameters are a function of wavelength and are described in the text. Parameters in blue are directly measurable and terms in red are calculated.

The Napierian absorbance of the hematite thin films, A_H, at a given wavelength, λ, is given by the equation:

$$A_H(\lambda) = -\ln\left(\frac{I(\lambda)}{I'(\lambda)\left(1-R_H(\lambda)\right)}\right) \tag{2-1}$$

where $I(\lambda)$ is the intensity of light that is transmitted through the substrate and hematite film, $I'(\lambda)$ is the intensity of light that is transmitted through the substrate, and $R_H(\lambda)$ is the reflectance of the substrate/hematite interface (Figure 2-1b). The measured transmittance of the substrate, $T_S(\lambda)$, is given by

$$T_S(\lambda) = \frac{I'(\lambda)}{I_0(\lambda)} \tag{2-2}$$

where $I_0(\lambda)$ is the incident light intensity (Figure 2-1a). The measured transmittance of the substrate and hematite film, $T_{S+H}(\lambda)$, is given by

$$T_{S+H}(\lambda) = \frac{I(\lambda)}{I_0(\lambda)} \tag{2-3}$$

(Figure 2-1b). The ratio of the measured transmittances is therefore:

$$\frac{T_{S+H}(\lambda)}{T_S(\lambda)} = \frac{I(\lambda)}{I'(\lambda)} \tag{2-4}$$

Substituting equation (2-4) into equation (2-1) yields:

$$A_H = -\ln\left(\frac{T_{S+H}(\lambda)/T_S(\lambda)}{(1-R_H(\lambda))}\right) \tag{2-5}$$

The value of $R_H(\lambda)$ that is needed is the fraction of light incident on the substrate/hematite interface, $I'(\lambda)$, that is reflected. The measured reflectance of the substrate/hematite interface is given by the difference of the measured reflectance of the substrate and the measured reflectance of the substrate and hematite: $R_{S+H}(\lambda) - R_S(\lambda)$. This expression, however, does not take into account the light that is absorbed by the substrate. The reflectance in terms of $I'(\lambda)$ is therefore obtained by dividing the measured reflectance ($R_{S+H}(\lambda) - R_S(\lambda)$) by the transmitted light, $T_S(\lambda)$ incident on the interface. The light reflected by the substrate/hematite interface actually passes through the substrate twice (once to the interface, then again to the detector), therefore the reflected light needs to be divided by T_S again. The corrected expression for $R_H(\lambda)$ is then given by:

$$R_H(\lambda) = \frac{\left(R_{S+H}(\lambda) - R_S(\lambda)\right)}{\left(T_S(\lambda)\right)^2} \tag{2-6}$$

Substituting equation (2-6) into (2-5) yields the final equation for the absorbance of the hematite film, fully corrected for reflectance and absorbance of the substrate where all parameters are measureable, which is employed herein:

$$A_H = -\ln\left(\frac{T_{S+H}(\lambda)/T_S(\lambda)}{\left(1-\frac{\left(R_{S+H}(\lambda)-R_S(\lambda)\right)}{T_S(\lambda)^2}\right)}\right) \tag{2-7}$$

A similar equation was presented by Beerman et. al. to find the absorbance of nanorod hematite on a FTO substrate.[23]

2.2.3 Photoelectrochemical Measurements

Iron oxide electrodes were masked with a 60 μm Surlyn film (Solaronix) to prevent scratching of the very thin films. Surlyn films were first adhered to the surface at 85°C and then melted to the electrode at 115°C. Electrodes were clamped to a custom made glass electrochemical cell. The solution was referenced to a homemade Ag/AgCl electrode which was frequently compared to a Radiometer Analytical saturated calomel electrode (SCE). High surface area platinum mesh was used as a counter electrode. All experiments shown used an aqueous electrolyte containing 200 mM KCl, 20 mM $K_3Fe(CN)_6$ (Sigma-Aldrich), and 200 mM $K_4Fe(CN)_6 \cdot 3H_2O$ (Mallinckrodt Baker) which were purified via re-crystallization. Aqueous solutions were maintained at pH 12 (KOH). Sandwich cells were made by applying light pressure to 120 μm Surlyn film sandwiched between a hematite electrode and a cleaned FTO counter. Electrochemical impedance measurements were made using an Eco Chemie Autolab

potentiostat coupled with Nova electrochemical software using a 10 mV amplitude perturbation and sweeping frequencies from 10 to 10^5 Hz. Capacitance data were fit using ZView software (Scribner Associates). Photoelectrochemical measurements were made with a Gamry Instruments Reference 600 potentiostat. The light source was a Xe arc lamp interfaced with a Horiba Jobin Yvon MicroHR monochromator. An AM 1.5 solar filter and neutral density filters were used to simulate sunlight at 100 mW/cm^2.

2.4 Results and Discussion

2.4.1 Thin Film Characterization

While growing samples for this study, additional thick-film samples were grown concurrently in our ALD reactor, in order to facilitate characterization. The powder XRD spectrum for an annealed thick film (consisting of approximately 3,700 ALD cycles and estimated to be ~200 nm by SEM) of iron oxide deposited on an FTO substrate is displayed in Figure 2-2a. The XRD spectrum is dominated by peaks due to the underlying FTO substrate. There are additional well-defined peaks present, however, which can be assigned to hematite (α-Fe_2O_3). Peaks were assigned using the International Union of Crystallography (IUCr) database, in agreement with films using different deposition methods including spin coating and spray pyrolysis.[24,25] XRD spectra obtained from thinner films had very low signal which could not be interpreted unambiguously. Low angle XRD was also performed on films 10-60 nm and no peaks could be seen down to 1 degree.

Raman spectroscopy is often used to analyze the structure of iron oxides due to the very different spectra of the common forms: hematite (α-Fe_2O_3), maghemite (γ-Fe_2O_3) and magnetite (Fe_3O_4). Figure 2-2b shows a Raman spectrum gathered from the same thick film (~200 nm) of

iron oxide deposited on FTO as the XRD measurements. All peaks correspond with Raman scattering from the crystal structure of α-Fe_2O_3 previously reported except for the peaks at 660 and 1320 cm^{-1}.[26] Although magnetite has a very strong characteristic peak at 660 cm^{-1} no other signals of magnetite were found in the XRD spectrum. This peak has been attributed to disorder in the crystal lattice and the breaking of symmetry upon crystallization.[27] The peak at1320 cm^{-1} has been found to be related to the peak at 660 cm^{-1}as an overtone peak. Both peaks at 660 and 1320 cm^{-1} are expected to be Raman inactive in perfect crystals.[28] A hump can also be seen around 1100 cm^{-1} which is likely due to background scattering from the FTO. The large scattering of the substrate thwarted attempts to measure thinner films (≤ 60 nm) on FTO with Raman spectroscopy; no distinguishable peaks were evident, even when integrating the signal for up to 6 hours. The combination of XRD and Raman data show that the only observable crystallographic phase in the iron oxide deposited with ALD using ferrocene and ozone is α-Fe_2O_3 (hematite).

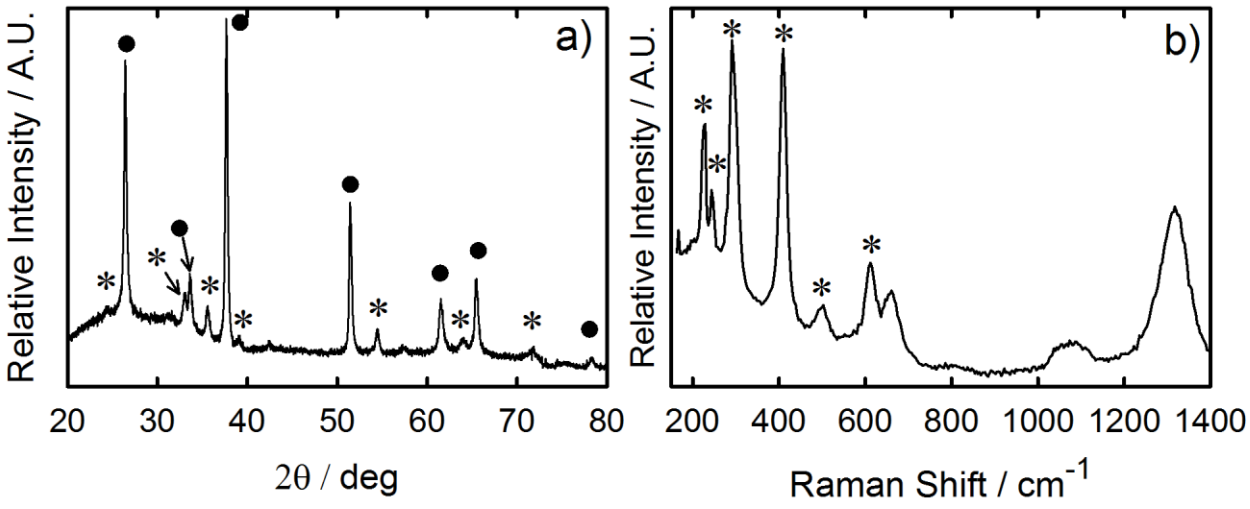

Figure 2-2. (a) X-ray diffraction pattern and (b) Micro Raman spectrum of iron oxide film prepared by ALD on FTO. Peaks are labeled for α-Fe_2O_3(*) and the SnO_2 substrate (•).

Figure 2-3a shows the absorbance spectra, which have been corrected for reflectance and the FTO substrate absorbance, of hematite films grown with an increasing number of ALD cycles. The absorption onset at around 560 nm for all samples is consistent with a 2.1-2.2 eV bandgap of hematite reported in many other studies.[29-33] Figure 2-3b shows the absorbance at a single wavelength (410 nm) as a function of ALD cycles from 100 to 1,200 cycles. The data represent the averaged value from measurements of three independently prepared series of thin film hematite electrodes with error bars representing the standard deviation. Ideal ALD behavior predicts that thickness should increase linearly with cycles, however the absorbance increases linearly with ALD cycles only over the first 500 cycles. A recent report suggested that strain could produce increased absorption coefficients, α, in thin (~25 nm) hematite films.[24] In that work, the reflectance of the films was not accounted for which can be significant as shown in Figure 2-3b. In addition, the thickness was determined by SEM, which is not a particularly accurate method. Therefore we regard conclusions about strain induced changes in α with skepticism. A recent investigation of the ALD mechanism of hematite using ferrocene and ozone as precursors indicated that the thinnest (6.7 nm) films had slightly higher α compared to films 12 nm; films thicker than 12 nm had essentially constant α.[19] We note that a different substrate was employed in that work (quartz) which can have a significant effect on the very thinnest films. The growth rate, however, was reported to be linear. In any case, the initial linear increase in absorbance with ALD cycles is either due to linear growth with an approximately constant α, or coincidentally offsetting growth-rates and α. We apply Ockham's razor and assume the former:

approximately linear growth for films grown with up to 500 ALD cycles and constant α. Using an absorption coefficient of 2.2×10^5 cm^{-1} at 410 nm (this value is in agreement with several other reports and is used to calculate thickness for other films throughout this paper[8,19,29]), the growth rate is calculated to be approximately 0.62 Å per cycle by analyzing the slope of the best fit line for the first 500 cycles in Figure 2-3c.[29] After 500 ALD cycles, the growth rate decreases and becomes slightly non-linear. A detailed analysis of the ALD mechanism of hematite using ferrocene and ozone as precursors is presented elsewhere.[19] From here on, the electrode thicknesses will be referenced in terms of nanometers instead of ALD cycles, taken from the data presented in Figure 2-3c. The thicknesses given represent average thicknesses resulting from a given number of ALD cycles from at least three independently prepared samples. For example, 3 electrodes made in separate batches using 300 ALD cycles have thicknesses of 20 ± 2.2 nm, which are all referred to as 20 nm electrodes for the sake of ease of discussion.

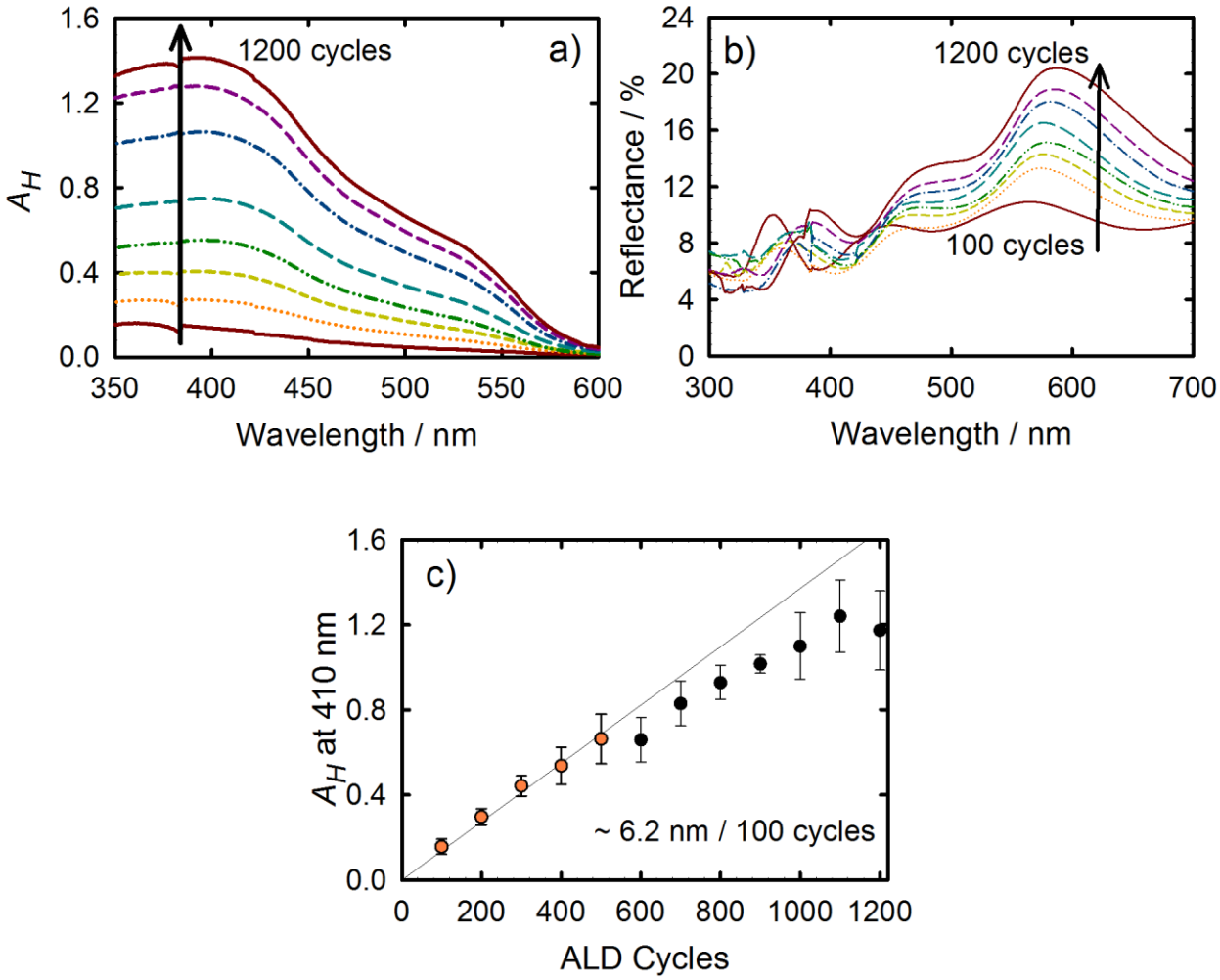

Figure 2-3. (a) Calculated absorbance spectra and (b) measured reflectance spectra of hematite thin films prepared with 100, 200, 300, 500, 700, 900, 1000, 1200 ALD cycles. (c) Relationship of the absorbance at 410 nm with ALD cycles. The line of best fit only represents the first 5 data points (orange circles).

SEM images can be seen in Figure 2-4. Figures 2-4a, 2-4b and 2-4c are top down views of a blank FTO substrate, a 22 nm film and a 50 nm film respectively. The texture of the blank FTO is maintained with a 22 nm film deposited on top of it suggesting deposition is uniform and conformal as expected. However, the 50 nm films show the formation of spherical particles

suggesting that at some point, the ALD process of hematite changes. This change in morphology with thicker films is consistent with the deviation from linear growth shown in Figure 2-3c. The cross section image of a 1,200 cycle electrode, shown in Figure 2-4d, indicates that the thickness is approximately 50 nm. The thickness, d = 50 nm, is in excellent agreement with the absorbance of this electrode, A_H = 1.1, and the absorption coefficient, α = 2.2 × 10^5 cm^{-1} at 410 nm, according to Beer's Law ($A_H = \alpha d$).

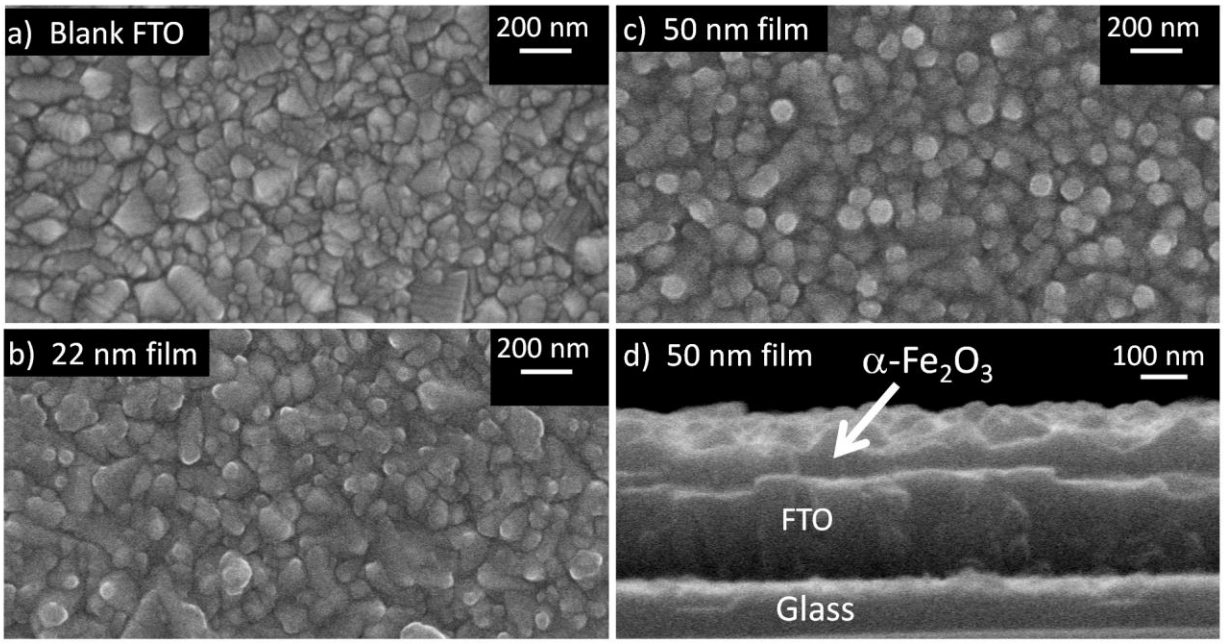

Figure 2-4. Top down SEM images of (a) blank FTO (b) 22 nm film (c) 50 nm film. (d) A cross section SEM image of a 50 nm film.

2.4.2 Photoelectrochemical Measurements

Steady state current density, *J*, vs. applied potential, *E*, measurements were performed on three series' of thin film hematite electrodes ranging from 7 to 56 nm in contact with an aqueous ferricyanide/ferrocyanide electrolyte.[34,35] Figure 2-5a shows representative *J-E* curves measured

in the dark and in response to simulated AM 1.5 illumination (100 mW cm^{-2}). Figure 2-5b shows the average short circuit current densities, J_{SC}, as a function of thickness. The J_{SC} values were taken at the Nernstian potential, E_S, of the ferricyanide/ferrocyanide electrolyte (190 mV vs. SCE) since this potential best approximates the short circuit current density of a 2-electrode cell. Initially, for the ~3 thinnest electrodes, J_{SC} increases linearly with thickness. The increased photocurrent is partially due to the thicker electrodes absorbing more photons. The J_{SC} increases faster than can be accounted for just by an increase in light absorption however; the 20 nm electrodes absorb approximately twice as many photons as the 7 nm electrodes, but has over four times the photocurrent. In other words, the absorbed photon to current efficiency, APCE, appears to increase for these electrodes. The photocurrent is essentially constant for electrodes thicker than 20 nm, despite the fact that these electrodes absorb an increasing fraction of incident light, indicating the APCE decreases for these electrodes.

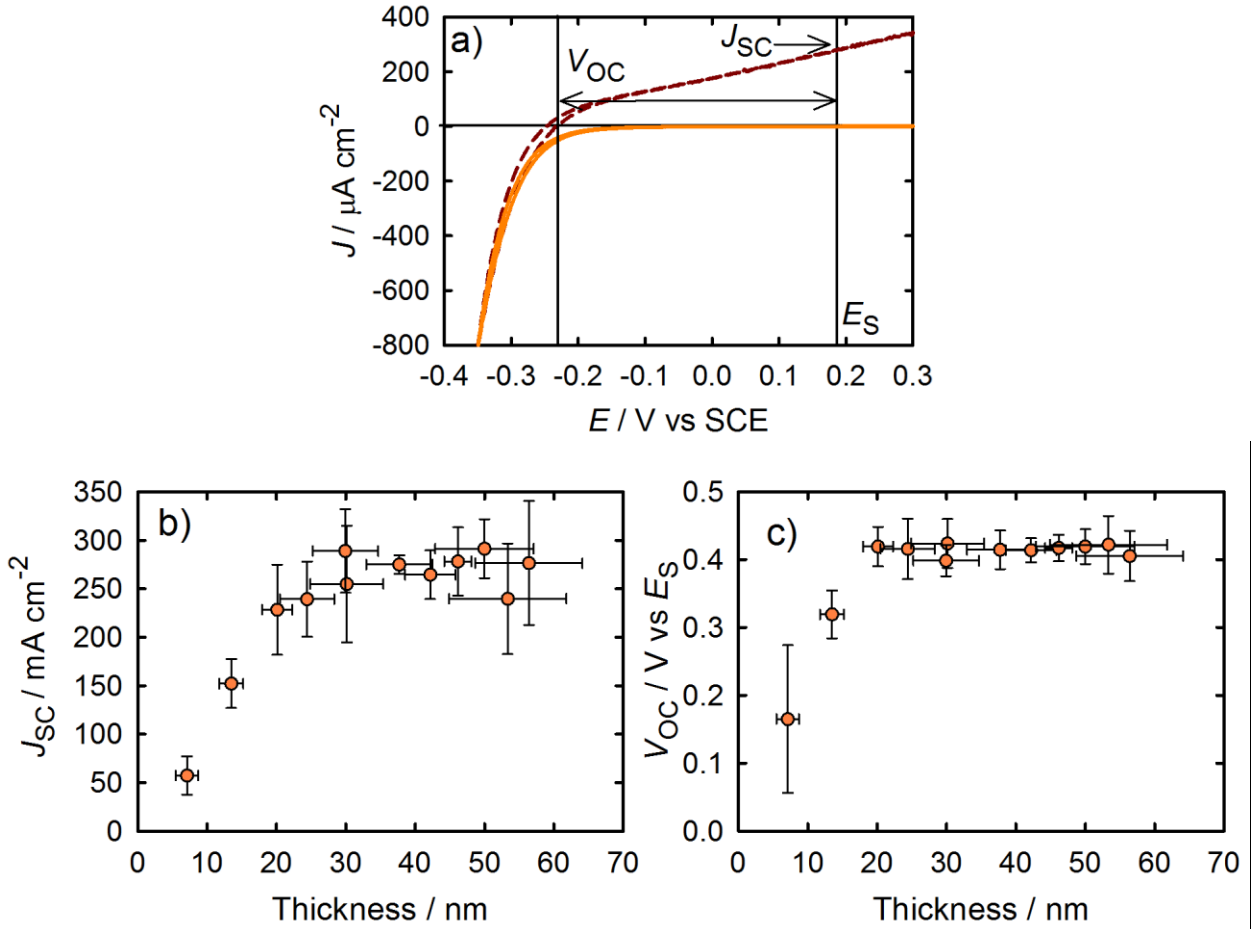

Figure 2-5. (a) Current density *vs.* applied potential curves measured in the dark (solid orange line) and under simulated AM 1.5 illumination (dashed red line) for a 20 nm thick electrode. (b) Photocurrent density and (c) open circuit voltage extracted from *J* vs. *E* curves *vs.* film thickness.

The APCE is calculated by the equation: $APCE(\lambda) = \frac{IPCE(\lambda)}{Absorptance(\lambda)}$, where IPCE($\lambda$) is the incident photon-to-current efficiency at a given wavelength and the absorptance is the percentage of incident photons absorbed by the hematite at that wavelength. Therefore, IPCE measurements were performed for all of the α-Fe_2O_3 electrodes. IPCE measurements were also

measured at E_S. Figure 2-6a shows a representative IPCE spectrum for a 20 nm electrode (additional IPCE spectra are provided in the supporting information). The dominant trends of the IPCE spectra are consistent with the J_{SC} results, as expected since the photocurrent under white light is just the sum of photocurrent response from monochromatic light. The reflectance of hematite varies with respect to number of ALD cycles/thickness (see Figure 2-3b), which is therefore convoluted in the trends of photocurrent and IPCE response to increasing film thickness. In order to correct for any reflectance dependence, the absorptance was calculated by $Absorptance = 1 - e^{-A_H}$ where A_H is calculated in equation (2-7). Figure 2-6a shows the spectrum of the percentage of incident photons that are absorbed by the 20 nm hematite film overlaid with the IPCE spectrum. The APCE's were then calculated by dividing the IPCE spectra by the percentage of photons absorbed at each wavelength (spectra shown in appendix 2). Figure 2-6b shows the APCE at different wavelengths as a function of thickness. The overall trend shows an increase in APCE with thickness for electrodes up to 20 nm thick, consistent with the large initial increase in J_{SC}. The APCE's decrease for all thicker electrodes as expected for a constant J_{SC} and increasing light absorption.

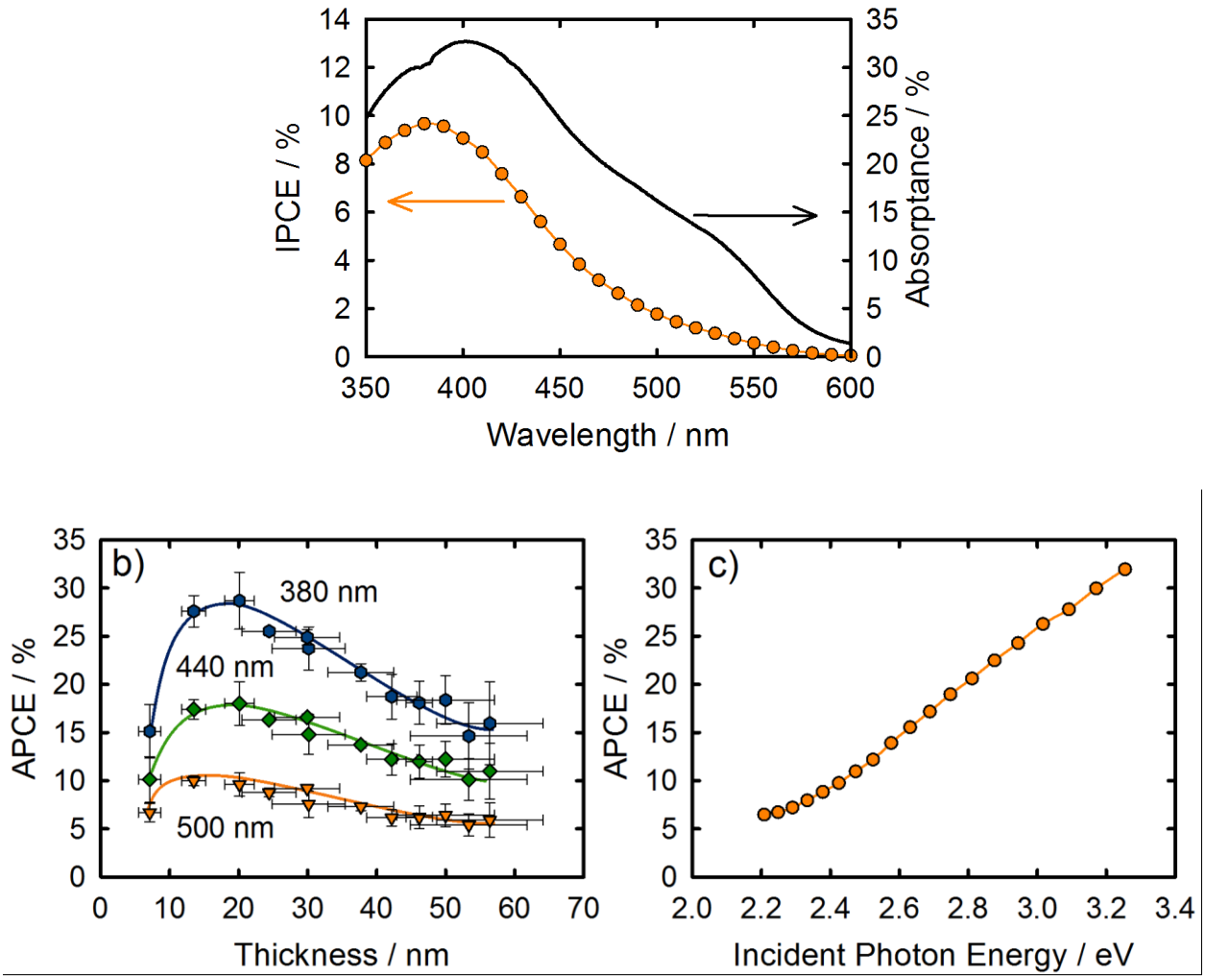

Figure 2-6. (a) The IPCE (orange circles) and absorptance spectra (solid black line) for a 20 nm thick α-Fe_2O_3 film (b) The trend in APCE at several wavelengths for increasing α-Fe_2O_3 film thickness. The lines drawn are only to guide the viewer's eye and do not represent a fit. (c) The APCE plotted as a function of the incident photon energy for a 20 nm electrode.

The trends in the APCE with thickness can be understood in terms of drift (charge carriers moving in response to an electric field) competing with recombination (which is reflected in the lifetime, τ) described by the hole drift length, L_p^{drift}:[36]

$$L_p^{drift} = \mu E \tau \tag{2-8}$$

where μ is the hole mobility (0.2 $cm^2\ V^{-1}\ s^{-1}$)[37] and E is the electrostatic field. The field is a result of the depletion region which develops from the equilibration of the semiconductor Fermi level (E_F) with the solution potential (E_S).[38] The maximum field (E_{max}) which exists at the electrode / electrolyte interface is given by

$$E_{\max} = \frac{qN_D}{\kappa\varepsilon_0} W \tag{2-9}$$

where N_D is the dopant density, W is width of the depletion layer, κ is the dielectric constant of the semiconductor (32 for hematite) and ε_0 is the permittivity of a vacuum (8.854×10^{-12} C V^{-1} m^{-1}).[38-40] The depletion width depends on the voltage drop across the semiconductor depletion region, V_{sc}, according to:[38]

$$W = \sqrt{\frac{2\kappa\varepsilon_0 V_{sc}}{qN_D}} \tag{2-10}$$

The dopant density and voltage drop were determined through differential capacitance, C, vs. applied potential measurements. We note that Mott-Schottky analysis is only valid for planer surfaces (or when the surface roughness is either much larger or much smaller than the depletion width) not dominated by surface state capacitance (which would result in a frequency dependence); the films measured herein fulfill these criteria. The capacitances were determined by fitting the remarkably ideal impedance data (displayed in Figure 2-7a) to a simple Rs(C-Rp) equivalent circuit over a frequency range spanning five orders of magnitude. The resultant capacitance values, shown in Figure 2-7b, were fit to the Mott-Schottky equation:

$$\left(\frac{A_S}{C}\right)^2 = \frac{2}{q\kappa\varepsilon_0 N_D}\left(E - E_{FB} - \frac{kT}{q}\right) \qquad (2\text{-}11)$$

where A_s is the surface area of the electrode. The roughness factor of FTO has been estimated to be 1.5 when correcting the Mott Schottky calculations for the real surface area.[41,42] The slope produced a dopant density of 7.14×10^{18} cm^{-3} and the intercept produced a flat-band potential (E_{FB}) of -0.40 vs. SCE.[43] Since only high purity ferrocene and ozone were introduced to the ALD chamber, we speculate that the dopants must be a residual carbon impurity or oxygen vacancies in the lattice. Accounting for the dependence of the flat band potential with dopant density, our experimental determination of E_{FB} is in good agreement with literature values.[2,44,45] If the entire potential drops across the semiconductor (such that $V_{sc} = V_{bi} = E_{FB} - E_s = 0.59$ V), the depletion width would be ~17 nm thick.

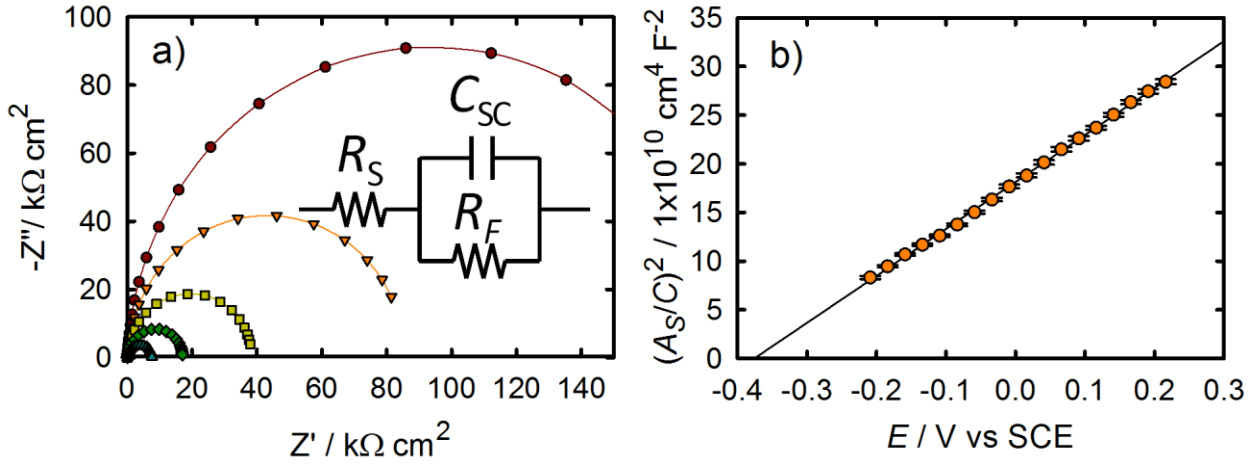

Figure 2-7. (a) Impedance spectra of a hematite electrode prepared with 1,200 ALD cycles for applied potentials of -0.034 (red circles), -0.059 (orange downward pointing triangles), -0.084 (yellow squares), -0.109 (green diamonds), -0.134 (teal upward pointing triangles) V vs SCE. Capacitances were determined by fitting data to a simple Rs(C-Rp) circuit shown in inset. (b) Mott-Schottky plot with the errors of those fits represented in the error bars shown (generally smaller than the symbols).

The thickness of the optimal electrodes is ~20 nm, which is approximately equal to the length of the maximum depletion region. The increasing electric field that develops for electrodes from 7 to 20 nm would result in an increased L_p^{drift}, which can account for the increase in APCE for these electrodes. It has also been hypothesized that a "dead layer" exists as a result of the substrate-hematite junction which renders very thin films inactive.[46] This has been at least partially overcome more recently by adding various metal oxide under-layers and through doping of the hematite.[46-48] However, it is still unclear how these modifications fix this dead layer, thus we continue our discussion of the results in terms of an increasing L_p^{drift}.

Electrodes thicker than ~20 nm are larger than the depletion region and no additional photocurrent is produced. These data are consistent with the explanation that only a fraction of the holes that are produced within the depletion region are collected, and holes generated in the bulk do not contribute to the photocurrent.

The L_p^{drift} can be estimated using literature values for the minority carrier lifetimes. The lifetime of holes in both thin film and single crystal hematite was found to be 4.2 ps by ultrafast transient absorption and reflectance measurements.[3] The E_{max} determined from equations 2-9 and 2-10, with V_{SC} = 0.59 V, produces a hole drift length of 5.8 nm. The electric field varies as a function of distance in the space charge region.[38] Since the charge carrier concentrations are spatially dependent, the lifetime should also be a function of position in the space charge region.[49] Thus, the calculated drift length of 5.8 nm should be considered a maximum value. Nevertheless, a drift length of 5.8 nm is in reasonable agreement with our results, where we found electrodes with an optimal film thickness of ~20 nm to have APCEs of 10 – 30 %.

In the analysis presented above, we assumed that the photoelectrochemical properties are constant for all of the material layers deposited, and only the thickness of the hematite was changing. In order to test this hypothesis, the APCE response due only to the last 20 nm deposited (corresponding roughly to the depletion region) was calculated for all electrodes. The calculation consisted of multiplying the APCEs by the percentage of incident photons absorbed only in the 20 nm adjacent to the solution. The percentages of photons absorbed only in the depletion region were calculated by subtracting the percentage of photons absorbed in the rest of the film from unity as if it was an optical filter. Aside from the very thin electrodes, the APCEs

of the depletion region were found to be essentially constant for all electrodes (Figure 2-8). This is consistent with our assumption that material properties, when thicker than the depletion region, are essentially invariant with thickness, and that only charge carriers absorbed near the electrolyte interface contribute to the photocurrent.

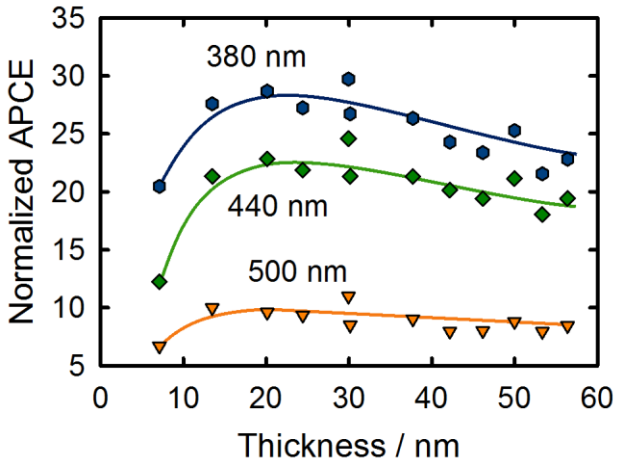

Figure 2-8. APCEs for several wavelengths normalized for the light absorbed only in the ~20 nm adjacent to the electrode / electrolyte interface as a function of thickness. Lines are drawn only to guide the viewer's eye and do not represent a fit.

In addition to the APCE dependence on electrode thickness, there is a striking dependence of APCE with wavelength of incident light (Figure 2-6c). The wavelength dependence is inversely related to the absorption profile; a slightly larger fraction of higher energy photons will be absorbed farther away from the electrolyte interface than lower energy photons since illumination is through the back substrate. This trend continues even as electrodes are made thicker and fewer low energy photons are absorbed in the depletion region. APCEs were also measured on sandwich cells from both the substrate-electrode (SE) and the electrolyte-electrode (EE) interfaces. After correcting for the absorption of the counter electrode and

electrolyte, the APCEs show the same wavelength dependence (Figure 2-9). Thus we discount differences in light penetration depths as a significant contributing factor. The trend in APCE with thickness for all wavelengths appear to be the same – i.e. all wavelengths have a maximum value for electrodes 20 nm thick – which indicates they are all limited by drift. We therefore suggest that the wavelength (energy) dependence of the APCE is a consequence of hot charge carriers (generated with higher energy photons) having higher mobilities and/or longer lifetimes (slower recombination) which produce longer drift lengths. The relaxation of hot carriers is generally on the femtosecond time regime, which could increase lifetimes by a similar amount, however there is no evidence the lifetime would increase linearly with photon energy.[3] Lacking direct evidence, we speculate that higher energy holes have linearly increasingly higher mobilities enabling a higher fraction to reach the interface and be collected. A more detailed understanding of this phenomenon is currently under investigation.

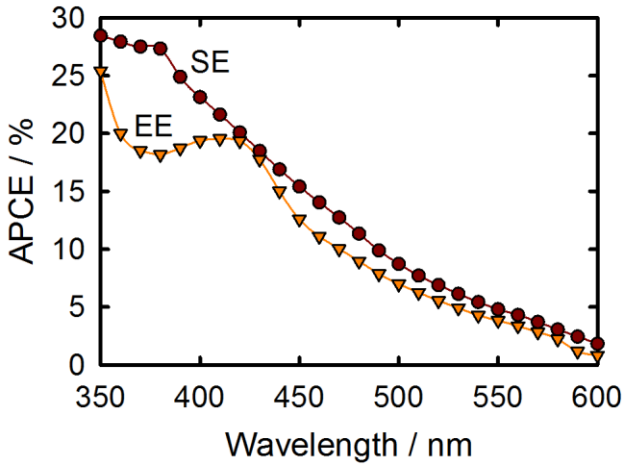

Figure 2-9. APCEs calculated when shining light from the substrate-electrode interface (SE) and the electrolyte-electrode interface (EE). EE APCE values were corrected for light absorption of the FTO counter electrode and electrolyte.

The open circuit voltage, V_{oc}, (seen in figure 2-5c) was measured as the difference between the potential at which no current density flows relative to E_s. The V_{oc} also increases sharply with thickness until 20 nm then remains essentially constant. The increasing V_{oc} with thickness can be explained by the diode equation:

$$V_{OC} = \frac{\gamma kT}{q} \ln \frac{J_{SC}}{J_0} \tag{2-12}$$

where γ is the diode quality factor, k is the Boltzmann constant, T is temperature, q is the charge of an electron, and J_0 is the recombination current density.[49] The increasing photocurrent accounts for only a minor fraction of the ~250 mV increase in V_{oc} from samples ~20 nm thick, compared to samples ~7 nm thick. Therefore, J_0, which consists of the sum of all recombination including surface state recombination, J_{ss}, bulk recombination, J_{br}, depletion region recombination, J_{dr}, and electron transfer from the semiconductor to the electrolyte, J_{et}, shown in Figure 2-10, must decrease over the first ~20 nm.

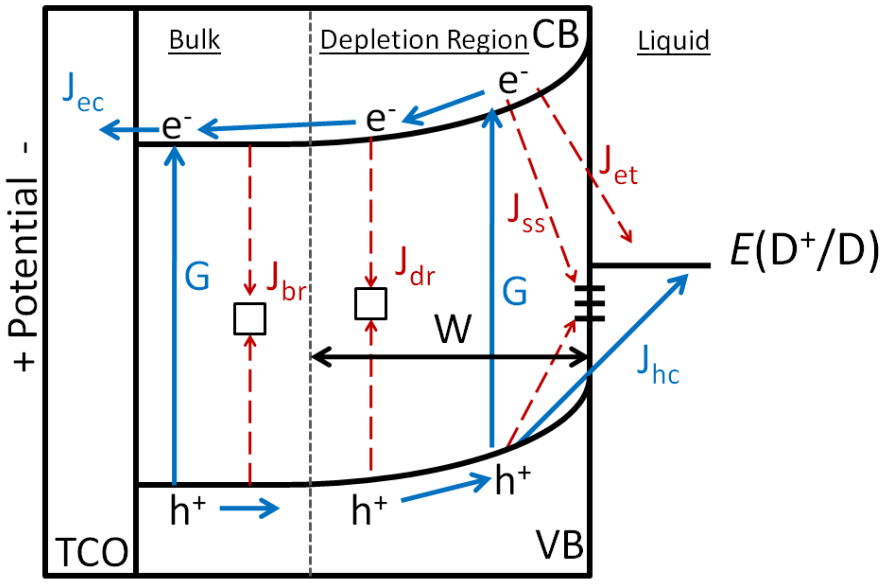

Figure 2-10. Qualitative energy diagram showing the favorable pathways of minority carriers being generated (G) and being collected as current (J_{photo}) as well as the unfavorable recombination pathways including bulk recombination (J_{br}) depletion region recombination (J_{dr}) surface state recombination (J_{ss}) and electron transfer (J_{et}).

The development of the space charge region can also explain the large initial increase in V_{OC} for electrodes from 7 to 20 nm thick. As the electrode thickness increases, the ratio of surface area to bulk decreases, and a field develops to drive electrons from the surface and holes towards it. We therefore attribute the trend of decreasing J_0 (increasing V_{OC}) with thickness to decreasing recombination at the surface: J_{ss} and/or J_{et}. As discussed in chapter 6, J_{ss} is shown to be insignificant when a fast redox shuttle is used to collect holes. On the other hand, an increasing thickness for films smaller than the depletion region would increase the electric field within the semiconductor for an a given applied potential since very thin films would be

completely depleted. This would cause lower amounts of band bending, and a higher concentration of electrons at the surface and a higher J_{et}. The constant voltage of electrodes ≥ 20 nm is thus attributed to a fully developed electric field and a constant J_{et}.

The measurements reported herein were performed very carefully; however a note should be made regarding possible error involved with the analysis presented above due to uncertainties in literature constants. Absorption coefficients reported in the literature range from 1.3×10^5 to 2.5×10^5 cm^{-1} at 410 nm.[1,29,40,50] Thus our use of 2.2×10^5 cm^{-1} at 410 nm, albeit consistent with our SEM measurements, may result in a slight error in film thickness and growth rate.[29] A bigger issue is the uncertainty in the dielectric constant. Literature values for the dielectric constant of hematite range from 12-120.[39,40,51-53] Again, we used a moderate (and what we believe to be most relevant) reported value of 32.[40] A larger dielectric constant would produce a smaller dopant density, larger depletion region, smaller electric field, and shortened drift length. Our results taken together, however, are very consistent with the model of an optimal electrode thickness that is slightly smaller than the maximum depletion width, and a drift length that is shorter than the depletion width.

2.5 Conclusions

Use of atomic layer deposition allowed for precise structure-function relationships to be made for thin film hematite electrodes in regenerative photoelectrochemical cells. We found that there is an optimal film thickness of 20 ± 2.2 nm which balances the development of an electrostatic field with having a short collection distance. Use of films thicker than ~20 nm may have comparable photovoltaic parameters (J_{SC} and V_{OC}), but come at a cost of wasted material

and absorbed photons. The maximum APCE values are unfortunately still rather low, in agreement with the calculated drift length being shorter than the film thickness. Low APCEs result from recombination being kinetically competitive with charge extraction. Our data, especially the wavelength dependence of the APCEs, is consistent with bulk recombination being the dominant recombination mechanism which limits the overall performance of hematite electrodes. The thinnest films have an unexpectedly low APCE and V_{OC} which is attributed to the fact that they are thinner than the depletion region, which results in under-devolved electric field, causing a large electron recombination from the conduction band to solution. Bulk region recombination follows Shockley-Reed-Hall formalism where the hole lifetime is inversely proportional to the trap state density.[49] Thus, either increasing the hole mobility or minimization of mid-bandgap traps is necessary in order to improve performance. Use of intentional dopants such as titanium and silicon have been shown to result in improved IPCEs, attributed to increasing electrical conductivity, passivation of grain boundaries, or morphological modification.[8,54] Alternatively, optimization of the ALD process (temperature, precursors, etc.) could result in more pristine films that exhibit longer lifetimes. Achieving the near unity APCEs required for efficient energy conversion is a very challenging task; however the potential benefits are great enough to warrant further study. We believe the systematic approach employed here, and by others, can eventually achieve this goal.[8]

2.6 Acknowledgements

T.W.H. would like to thank MSU for providing a generous start-up package in support of this work. A.B.F.M. acknowledges the support of the Energy Frontier Research center (DE-SC0001059) at the Argonne-Northwestern Solar Energy Research (ANSER) Center.

APPENDIX

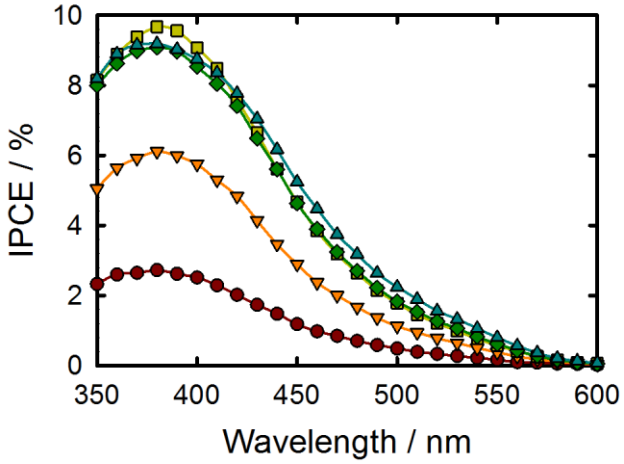

Figure A2-1 IPCE spectra for hematite electrodes prepared by 100 (red circles), 200 (orange downward facing triangles), 300 (yellow squares), 800 (teal upward facing triangles), and 1200 ALD cycles (green diamonds).

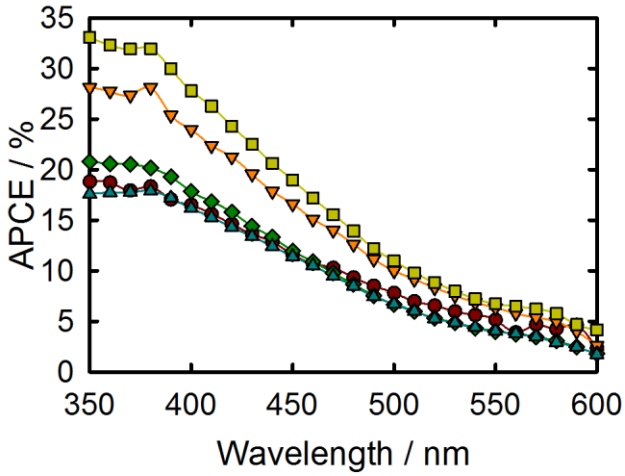

Figure A2-2. (a) APCE spectra for hematite electrodes prepared by 100 (red circles), 200 (orange downward facing triangles), 300 (yellow squares), 800 (teal upward facing triangles), and 1200 ALD cycles (green diamonds).

REFERENCES

REFERENCES

1. Kennedy, J. H.; Frese, K. W. *J. Electrochem. Soc.* **1978**, *125*, 6.

2. Dareedwards, M. P.; Goodenough, J. B.; Hamnett, A.; Trevellick, P. R. *J. Chem. Soc., Faraday Trans. 1 F*, **1983**, *79*, 2027-2041.

3. Joly, A. G.; Williams, J. R.; Chambers, S. A.; Xiong, G.; Hess, W. P.; Laman, D. M. *J. Appl. Phys.* **2006**, *99*, 6.

4. Gartner, W. W. *Phys. Rev.* **1959**, *116*, 84-87.

5. Wilson, R. H. *J. Appl. Phys.* **1977**, *48*, 4292-4297.

6. Cesar, I.; Sivula, K.; Kay, A.; Zboril, R.; Graetzel, M. *J. Phys. Chem. C*, **2009**, *113*, 772-782.

7. Le Formal, F.; Gratzel, M.; Sivula, K. *Adv. Funct. Mater.* **2010**, *20*, 1099-1107.

8. Glasscock, J. A.; Barnes, P. R. F.; Plumb, I. C.; Savvides, N. *J. Phys. Chem. C*, **2007**, *111*, 16477-16488.

9. Spray, R. L.; Choi, K. S. *Chem. Mat.* **2009**, *21*, 3701-3709.

10. Fu, Y. Y.; Wang, R. M.; Xu, J.; Chen, J.; Yan, Y.; Narlikar, A.; Zhang, H. *Chem. Phys. Lett.* **2003**, *379*, 373-379.

11. Prakasam, H. E.; Varghese, O. K.; Paulose, M.; Mor, G. K.; Grimes, C. A. *Nanotechnology*, **2006**, *17*, 4285-4291.

12. Sartoretti, C. J.; Alexander, B. D.; Solarska, R.; Rutkowska, W. A.; Augustynski, J.; Cerny, R. *J. Phys. Chem. B*, **2005**, *109*, 13685-13692.

13. Hahn, N. T.; Ye, H. C.; Flaherty, D. W.; Bard, A. J.; Mullins, C. B. *ACS Nano*, **2010**, *4*, 1977-1986.

14. Ritala, M.; Leskela, M. In *Handbook of Thin Film Materials*; Nalwa, H. S., Ed.; Academic Press: San Diego, 2001; Vol. 1, p 103.

15. Scheffe, J. R.; Frances, A.; King, D. M.; Liang, X. H.; Branch, B. A.; Cavanagh, A. S.; George, S. M.; Weimer, A. W. *Thin Solid Films*, **2009**, *517*, 1874-1879.

16. Rooth, M.; Johansson, A.; Kukli, K.; Aarik, J.; Boman, M.; Harsta, A. *Chem. Vap. Deposition*, **2008**, *14*, 67-70.

17. Lie, M.; Fjellvag, H.; Kjekshus, A. *Thin Solid Films*, **2005**, *488*, 74-81.

18. Bachmann, J.; Jing, J.; Knez, M.; Barth, S.; Shen, H.; Mathur, S.; Gosele, U.; Nielsch, K. *J. Am. Chem. Soc.* **2007**, *129*, 9554-9555.

19. Martinson, A. B. F.; DeVries, M. J.; Libera, J. A.; Christensen, S. T.; Hupp, J. T.; Pellin, M. J.; Elam, J. W. *J. Phys. Chem. C* **2011**, *115*, 4333-4339.

20. Hamann, T. W.; Martinson, A. B. F.; Elam, J. W.; Pellin, M. J.; Hupp, J. T. *J. Phys. Chem. C*, **2008**, *112*, 10303-10307.

21. Hamann, T. W.; Martinson, A. B. F.; Elam, J. W.; Pellin, M. J.; Hupp, J. T. *Adv. Mater.* **2008**, *20*, 1560–1564.

22. Martinson, A. B. F.; Elam, J. W.; Liu, J.; Pellin, M. J.; Marks, T. J.; Hupp, J. T. *Nano Lett.* **2008**, *8*, 2862-2866.

23. Beermann, N.; Vayssieres, L.; Lindquist, S. E.; Hagfeldt, A. *J. Electrochem. Soc.* **2000**, *147*, 2456-2461.

24. Souza, F. L.; Lopes, K. P.; Longo, E.; Leite, E. R. *Phys. Chem. Chem. Phys.* **2009**, *11*, 1215-1219.

25. Duret, A.; Gratzel, M. *J. Phys. Chem. B* **2005**, *109*, 7.

26. deFaria, D. L. A.; Silva, S. V.; deOliveira, M. T. *J. Raman Spectrosc.* **1997**, *28*, 873-878.

27. Bersani, D.; Lottici, P. P.; Montenero, A. *J. Raman Spectrosc.* **1999**, *30*, 355-360.

28. Leon, C. P.; Kador, L.; Zhang, M.; Muller, A. H. E. *J. Raman Spectrosc.* **2004**, *35*, 165-169.

29. Marusak, L. A.; Messier, R.; White, W. B. *J. Phys. Chem. Solids*, **1980**, *41*, 981-984.

30. Kung, H. H.; Jarrett, H. S.; Sleight, A. W.; Ferretti, A. *J. Appl. Phys.* **1977**, *48*, 2463-2469.

31. Gilbert, B.; Frandsen, C.; Maxey, E. R.; Sherman, D. M. *Phys. Rev. B*, **2009**, *79*.

32. Mohanty, S.; Ghose, J. *J. Phys. Chem. Solids*, **1992**, *53*, 81-91.

33. Tahir, A. A.; Wijayantha, K. G. U.; Saremi-Yarahmadi, S.; Mazhar, M.; McKee, V. *Chem. Mater.* **2009**, *21*, 3763-3772.

34. Finklea, H. O. *Semiconductor Electrodes*; Elsevier: Amsterdam, 1988.

35. Anderman, M.; Kennedy, J. H. *J. Electrochem. Soc.* **1984**, *131*, 1565-1570.

36. Mihailetchi, V. D.; Wildeman, J.; Blom, P. W. M. *Phys. Rev. Lett.* **2005**, *94*, 4.

37. Bosman, A. J.; Vandaal, H. J. *Adv. Phys.* **1970**, *19*, 1-&.

38. Tan, M. X.; Laibinis, P. E.; Nguyen, S. T.; Kesselman, J. M.; Stanton, C. E.; Lewis, N. S. *Prog. Inorg. Chem.* **1994**, *41*, 21-144.

39. *CRC Handbook of Chemistry and Physics*; 81 ed.; Lide, D. R., Ed.; CRC Press, 2001.

40. Glasscock, J. A.; Barnes, P. R. F.; Plumb, I. C.; Bendavid, A.; Martin, P. J. *Thin Solid Films,* **2008**, *516*, 1716-1724.

41. Cameron, P. J.; Peter, L. M. *J. Phys. Chem. B* **2003**, *107*, 14394-14400.

42. Fattori, A.; Peter, L. M.; McCall, K. L.; Robertson, N.; Marken, F. *J. Solid State Electrochem.* **2010**, *14*, 1929-1936.

43. ****, the errors of these calculated values propagated from fitting the capacitance data were insignificant.

44. Lindgren, T.; Wang, H. L.; Beermann, N.; Vayssieres, L.; Hagfeldt, A.; Lindquist, S. E. *Sol. Energy Mater. Sol. Cells*, **2002**, *71*, 231-243.

45. Kennedy, J. H.; Frese, K. W. *J. Electrochem. Soc.* **1978**, *125*, 723-726.

46. Hisatomi, T.; Brillet, J.; Cornuz, M.; Le Formal, F.; Tetreault, N.; Sivula, K.; Gratzel, M. *Faraday Discuss.* **2012**.

47. Zandi, O.; Klahr, B. M.; Hamann, T. W. *Energy Environ. Sci.* **2013**, *6*, 634-642.

48. Hisatomi, T.; Le Formal, F.; Cornuz, M.; Brillet, J.; Tetreault, N.; Sivula, K.; Gratzel, M. *Energy Environ. Sci.* **2011**.

49. Nelson, J. *The Physics of Solar Cells*; Imperial College Press: London, 2003.

50. Souza, F. L.; Lopes, K. P.; Longo, E.; Leite, E. R. *Phys. Chem. Chem. Phys.* **2009**, *11*, 1215-1219.

51. Papaioannou, J. C.; Patermarakis, G. S.; Karayianni, H. S. *J. Phys. Chem. Solids* **2005**, *66*, 839-844.

52. Kulkarni, S. S.; Lokhande, C. D. *Mater. Chem. Phys.* **2003**, *82*, 151-156.

53. Quinn, R. K.; Nasby, R. D.; Baughman, R. J. *Mater. Res. Bull.* **1976**, *11*, 1011-1017.

54. Kay, A.; Cesar, I.; Gratzel, M. *J. Am. Chem. Soc.* **2006**, *128*, 15714-15721.

Chapter 3:

Current and Voltage Limiting Processes in Thin Film Hematite Electrodes

Adapted with permission from:

Current and Voltage Limiting Processes in Thin Film Hematite Electrodes, Benjamin M. Klahr and Thomas W. Hamann, *Jounral of Physical Chemistry C*, **2011**, *115*, (16), 8393-8399.

3.1 Abstract

Atomic layer deposition was used to grow conformal thin films of hematite on transparent conductive oxide substrates and used as electrodes in regenerative photoelectrochemical cells (PECs). Systematic variations of the contacting electrolyte and redox shuttles were performed to determine the rate limiting processes of hematite PECs. Steady state current density vs. applied potential measurements were employed to show that when the fast, one electron redox shuttles are used, hole collection is not the rate limiting step; however, hole collection is the rate limiting step when hematite is employed for water oxidation. Electron transfer was found to be significant which limits the open circuit photovoltage. We further demonstrate that with variations of the pH and redox potentials of the contacting electrolyte, increases in both the photocurrent density and photovoltage can be achieved, which is attributed to increasing the built-in voltage.

3.2 Introduction

In the previous chapter, we used atomic layer deposition (ALD) to create a series of conformal hematite thin films, with thickness from ~5 – 60 nm, to determine structure-function relationships in regenerative PECs.[1] ALD is a unique technique, which is capable of producing very thin films which are conformal and pinhole free, such as those employed herein.[2,3] We found that a film thickness of 20 ± 2.2 nm maximizes the internal quantum yield. This optimal thickness balances the development of an electrostatic field with having a short collection distance. Even with ~20 nm thick films, however, the maximum APCE values are unfortunately significantly less than unity, which results in suboptimal photocurrents. In addition, the photovoltage was less than the maximal value. The photocurrent is a result of the generation of charge carriers by light absorption, G, separation of the charge carriers by the electrostatic field, and collection of the minority carriers (holes for a n-type semiconductor) by the contacting electrolyte, J_{hc}, shown in Figure 3-1. The photovoltage is limited by the primary recombination processes, including bulk recombination, J_{br}, depletion region recombination, J_{dr}, surface state recombination, J_{ss}, and electron transfer, J_{et}, shown in Figure 3-1 as red dashed arrows. While we were preparing this manuscript, Dotan et. al. reported using H_2O_2 as a fast hole collector to deconvolute the performance of the hematite films from the rate limiting process of water oxidation.[4] In this work we employ a similar strategy by using fast, one-electron outer-sphere redox shuttles. In addition, we perform systematic variations of the contacting electrolyte to elucidate the dominant recombination mechanism which limits the photovoltage of hematite electrodes in PECs. The resultant framework allows for interpretation of the pH dependence of

the photovoltaic performance. We also investigate a series of redox shuttles to demonstrate a new strategy to overcome the processes limiting the performance of hematite PECs. If hematite, or a similar material, will ever be used effectively for solar energy conversion, it is crucial to identify and overcome these bottlenecks. The work presented herein represents an important step in achieving that goal.

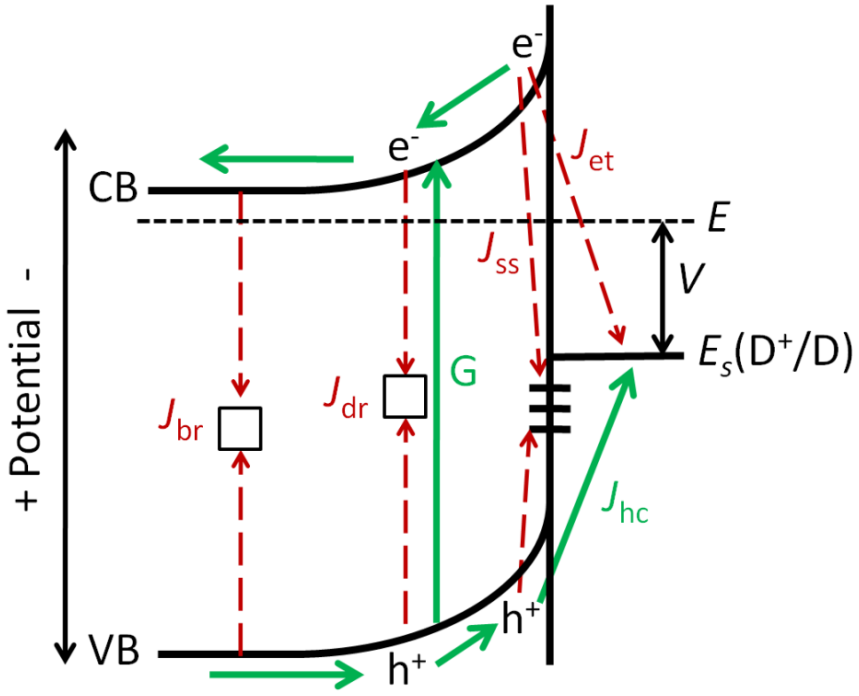

Figure 3-1. Qualitative energy diagram showing the favorable pathways (green solid arrows) of charge being generated by light absorption, *G*, driven to the electrolyte interface by the electric field in the depletion region (drift) and collected, J_{hc}, by a redox couple, D^+/D, in solution. Also shown are the deleterious recombination pathways (red dashed arrows) including bulk recombination, J_{br}, depletion region recombination, J_{dr}, surface state recombination, J_{ss}, and electron transfer, J_{et}.

3.3 Experimental

The synthesis and characterization of hematite films deposited by atomic layer deposition (ALD) was described in detail in Chapter 2.[1] The thin films were all deposited on fluorine-doped tin oxide (FTO) substrates. Multiple films approximately 30 nm thick were prepared and employed in the measurements described herein, since this thickness has previously produced the highest combination of photocurrent density and photovoltage, and thus overall efficiency. While the magnitude of results between various electrodes exhibited some variance, the trends were all consistent. For clarity of presentation, the results reported herein are for a single 33 nm thick electrode. Hematite electrodes were masked with a 60 μm Surlyn film (Solaronix) before being clamped to a custom made glass electrochemical cell to prevent scratching of the thin films. $K_3Fe(CN)_6$ (Sigma-Aldrich) and $K_4Fe(CN)_6 \cdot 3H_2O$ (Mallinckrodt Baker) were purified by recrystallization. K_4IrCl_6 and K_3IrCl_6 were purchased from Sigma-Aldrich and used as received. $K_5Mo(CN)_8 \cdot 2H_2O$ and $K_5W(CN)_8 \cdot 2H_2O$ were prepared by literature procedures.[5,6] Unless stated otherwise in the text, 200 mM of $K_4Fe(CN)_6 \cdot 3H_2O$ and 20 mM of $K_3Fe(CN)_6$ were used. For alternative redox shuttles, 100 mM of the reduced form and 10 mM of the oxidized form were used. Bulk electrolysis was employed to prepare the oxidized form of molybdenum and tungsten species until an amount of charge had been passed to produce a desired concentration. All electrolytes contained 200 mM KCl. Solutions were all maintained at pH 12 (KOH) unless otherwise noted. Otherwise, phosphate buffers were used to maintain solutions at approximately pH 7 and pH 8, and borate buffers were used to maintain solutions at approximately pH 9 and pH 10. Electrochemical measurements were referenced to a homemade Ag/AgCl electrode which was frequently compared to a Radiometer Analytical saturated calomel

electrode (SCE). High surface area platinum mesh was used as a counter electrode. Photoelectrochemical measurements were made with a Gamry Instruments Reference 600 potentiostat. The light source was a Xe arc lamp interfaced with a Horiba Jobin Yvon MicroHR monochromator. An AM 1.5 solar filter and neutral density filters were used to simulate sunlight at 100 mW/cm^2. All photoelectrochemical measurements were performed by shining light from the substrate-electrode (SE) interface.

3.4 Results and Discussion

3.4.1 [Donor] Dependence

Steady state current density, *J*, vs. applied potential, *E*, curves were measured for a 33 nm thin film hematite electrode in contact with an aqueous pH 12 $[Fe(CN)_6]^{3-/4-}$ electrolyte. A typical *J-E* curve measured under 100 mW cm^{-2} illumination can be seen in Figure 3-2a. Since the photocurrent density is not constant with potential, for purposes of comparison we define the photocurrent density, J_{photo}, at the formal potential, $E°$, of the contacting redox couple ($E°$ = 0.250 V vs. SCE for $[Fe(CN)_6]^{3-/4-}$). J_{photo} was also determined at a constant potential to isolate the performance of the hematite electrode from changes in the solution potential which varies with donor/acceptor ratio in accord with the Nernst equation. The open circuit voltage, V_{OC}, is defined as the difference between the applied potential which results in zero measured current and $E°$. The concentrations of the reduced form (electron donor) of the $[Fe(CN)_6]^{3-/4-}$ redox couple was varied from 1 mM to 400 mM while maintaining a constant concentration (20 mM) of the oxidized form (electron acceptor). Dark *J-E* curves were found to be invariant with respect to variations of donor concentration as expected. Figure 3-2b shows the J_{photo} extracted

from *J-E* curves taken in response to varying light intensities a function of donor concentration. It can be seen that J_{photo} initially increases with the concentration of donor, but quickly reaches a saturation current at relatively low concentrations (~20 mM). J_{photo} remained constant for donor concentrations 20 – 400 mM, shown in Figure 3-2c. Figure 3-2d shows results of current density transients, also measured at the formal potential, in response to 100 mW cm^{-2} illumination. For very low concentrations of donor (< 20 mM), there was an initial current spike which quickly decayed into a lower steady state value. This behavior is consistent with J_{photo} being limited by diffusion of the redox couple to the electrode surface.[7,8] For donor concentrations higher than 20 mM, the instantaneous current density remained constant at a value equal to the value of photocurrent density extracted from the *J-E* curves. As long as sufficient redox shuttle is present to support diffusion to the photoelectrode surface, the current density is independent of donor concentration. In addition, the measured V_{OC}'s were approximately constant with donor concentration as expected (see Appendix). The rate of hole collection at the hematite electrode surface should depend on the concentration of donor (hole collecting species). Since no increase in photovoltaic performance is observed with increasing donor concentration (i.e. increased rate of hole collection), we conclude that the interfacial hole collection kinetics are not the rate limiting process controlling the photovoltaic performance of hematite electrodes in contact with the $[Fe(CN)_6]^{3-/4-}$ electrolyte. This result is in agreement with conclusions reported by Dotan *et. al.* who employed H_2O_2 as a hole collector.[4]

J-E curves were also measured for each concentration of donor in response to different light intensities. Figure 3-2b shows that when the J_{photo} is not limited by diffusion (at high

donor concentrations), and J_{photo} increases proportionally with light intensity. A linear increase in J_{photo} with incident light intensity is observed for intensities from 1 – 400 mW cm^{-2} (see Appendix). The small deviations from linear behavior were determined to be due to wavelength variations of the neutral density filters employed to adjust the light intensity. Very linear behavior is seen with monochromatic light (see Appendix), however in this case, we are restricted to lower light intensities. The independence of J_{photo} with donor concentration coupled with the linear increase of J_{photo} with light intensity are consistent with J_{photo} only being limited by the charge collection length which limits the number of holes that reach the electrode interface, in agreement with our previous conclusions.[1]

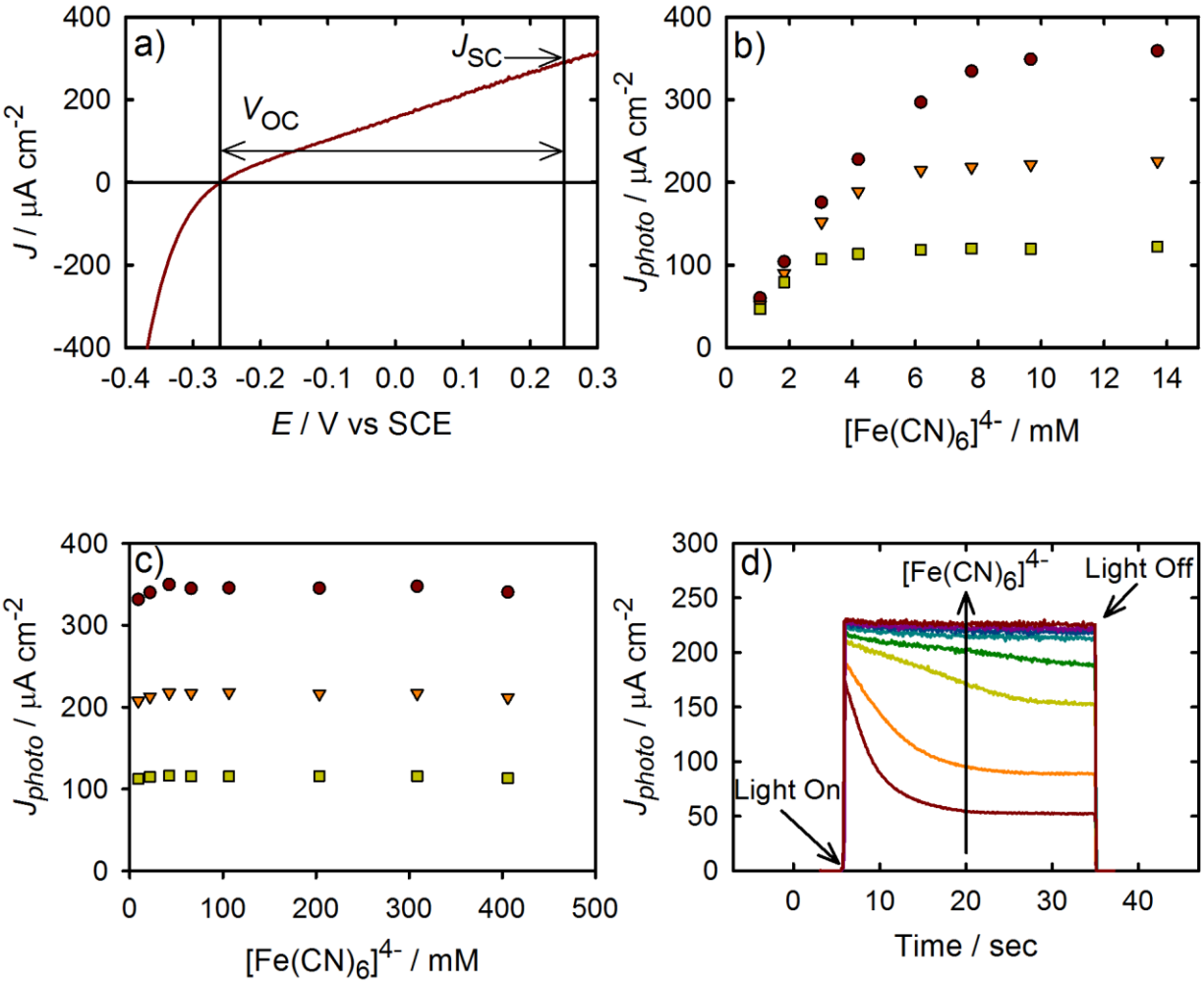

Figure 3-2: (a) A *J-E* curve for a 33 nm hematite film under 100 mW cm^{-2} illumination in contact with a pH 12 [Fe(CN)$_6$]$^{3-/4-}$ electrolyte containing 200 mM reduced and 20 oxidized species. (b - c) Plots of the photocurrent density measured as a function of donor concentration ([Fe(CN)$_6$]$^{4-}$) for light intensities of 50 mW cm^{-2} (yellow squares), 100 mW cm^{-2} (orange triangles) and 160 mW cm^{-2} (red circles). (d) Current transients measured in response to 100 mW cm^{-2} illumination for donor concentrations from 2 – 400 mM.

3.4.2[Acceptor] Dependence

J-E curves were also measured in contact with an aqueous pH 12 $[Fe(CN)_6]^{3-/4-}$ electrolyte with a constant concentration of the reduced form (donor) of the redox couple (200 mM) while varying the concentration of the oxidized form (acceptor) from 20 – 700 mM. Figure 3-3a shows a semi-logarithmic plot of the dark *J-E* curves for the varying concentrations. The dark current density, at a given potential, is proportional to the concentration of acceptor, indicating first order behavior. The only recombination mechanism that depends on acceptor concentration is back electron transfer, J_{et} (see Figure 3-1). Analysis of the slope of the dark ln(-*J)* vs. *E* curves, which is equal to $q/\gamma kT$, indicates that $\gamma = 2$, and thus recombination is not first order with respect to surface electron concentration.[9,10]

Under one sun illumination, the photocurrent density was found to be essentially independent of acceptor concentration. This behavior is expected since we demonstrated that the photocurrent density is limited by the rate of holes reaching the electrode interface to be collected, and acceptors in solution should therefore not contribute to the photocurrent generation processes (see Figure 3-1). A semi-logarithmic plot of V_{OC} as a function of acceptor concentration can be seen in figure 3-3b. The V_{OC} was found to decrease at a rate of 147 mV per 10-fold increase in [A] at pH 12. According to the diode equation[9]

$$V_{OC} = \frac{\gamma kT}{q} \ln\left(\frac{J_{SC}}{J_0}\right) \tag{3-1}$$

where *k* is the Boltzmann constant, *T* is temperature, J_{SC} is the short circuit photocurrent density, and J_0 is recombination exchange current density, the V_{OC} should vary linearly with the

logarithm of J_0. The 147 mV per decade slope indicates that γ ~2, in good agreement with the dark *J-E* measurements. Also shown is a plot of the applied potential required to produce a dark current density of 500 μA cm^{-2}. The V_{OC} changes with acceptor concentration in identical fashion (~147 mV per decade) as the dark current density predicts, demonstrating that superposition holds. In addition, since J_0 is the sum of all recombination current densities[9,10]

$$J_0 = J_{br} + J_{ss} + J_{dr} + J_{et} \tag{3-2}$$

the dependence of V_{OC} on [A] indicates that J_{et} is the dominant pathway such that $J_0 \approx J_{et}$. Thus, interfacial electron transfer is the recombination mechanism which limits the photovoltage. We note that this contradicts the conclusions of recent work using H_2O_2 as a hole scavenger.[4] In that work, however, the effects of recombination were inferred from measurements of the photocurrent density, which is not always affected by recombination.

Back electron transfer from conduction band electrons, including surface-state capture as an intermediate parallel pathway, to acceptors in solution can be described by the rate law:[11]

$$J_{et} = -qk_{et}[A]n_s + k_{sol}[A]N_{ss}f_{ss} \tag{3-3}$$

where *A* is the electron acceptor concentration in solution, n_s is the concentration of electrons in the conduction band, k_{et} is the electron-transfer rate constant from conduction band electrons, N_{ss} is the density of surface states, f_{ss} is the fraction of surface states that are filled with electrons, and k_{sol} is the electron-transfer rate constant from surface traps. This rate law would thus produce first order behavior with respect to [A], but not n_s, which is consistent with our

observation. We therefore tentatively conclude that surface-state mediated electron transfer is a contributing pathway of recombination, in addition to direct electron transfer from conduction band electrons. Work is ongoing in our laboratory to address the mechanistic details of this reaction.

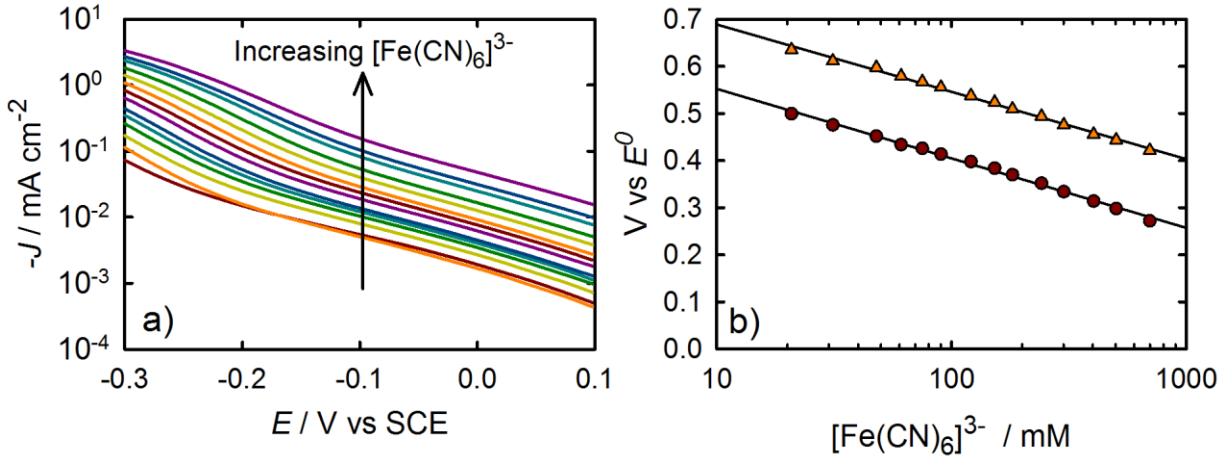

Figure 3-3: a) Semi-logarithmic plot of dark *J-E* curves of PECs as a function of acceptor concentration ($[Fe(CN)_6]^{3-}$), from 20 to 700 mM. b) Plot of V_{OC} (red circles) and the applied potential to achieve a given dark current density (orange triangles) as a function of acceptor concentration ($[Fe(CN)_6]^{3-}$).

3.4.3 pH Dependence

It has previously been shown that increasing the pH of the electrolyte improves the photovoltaic performance of hematite electrodes.[12,13] To the best of our knowledge, however, the cause of the improvement has not been established. In order to address this point, *J-E* curves were measured in aqueous electrolytes with the pH adjusted from 7 – 12, both with and without the $[Fe(CN)_6]^{4-/3-}$ redox shuttle. Dark *J-E* curves can be seen in figure 3-4a without the

$[Fe(CN)]_6^{4-/3-}$ redox shuttle. Anodic current is seen at very positive potentials attributed to the oxidation of water. The current onset potential shifts negatively by approximately ~63 mV per pH (sampled at 500 μA). The water oxidation potential should increase by -59 mV per pH in accord with the Nernst equation. Therefore, assuming the overpotential required to oxidize water with valence band holes is pH independent, the shift in the current onset potential is due to a concurrent -59 mV per pH shift in the valence band potential, E_{VB}/q. This is in excellent agreement with literature, where the E_{FB} of hematite has been shown to increase at the Nernstian rate of ~59 mV per pH for sintered polycrystalline,[14,15] and single crystal hematite.[16,17] *J-E* curves measured under 100 mW cm^{-2} illumination with no redox couple can be seen in figure 3-4b. Even at pH 12, significant photocurrent only exists at potentials more positive than 0.4 V vs SCE, in agreement with literature reports. Hematite is often employed as a water oxidation photocatalyst, and a majority of recent papers studying the photoelectrochemistry of hematite focused on water oxidation.[18-21] Water oxidation at hematite electrodes has been calculated to be a very slow process, however.[22] Since the photocurrent density is much lower at a given potential and pH compared with the results above when $[Fe(CN)_6]^{4-/3-}$ is employed as a redox couple, water oxidation appears to be the rate limiting step of the photocurrent density production. The measurements performed herein with the $[Fe(CN)_6]^{4-/3-}$ redox couple, however, are all performed at potentials negative of 0.3 V vs SCE, and thus are not significantly affected by the side reaction of water oxidation.

Figure 3-4c shows *J-E* curves measured under 100 mW cm^{-2} illumination for solution pH values from 7 – 12 in the presence of the $[Fe(CN)_6]^{4-/3-}$ redox shuttle. Clearly, the photocurrent density at more negative potentials increases with pH. Plots of the J_{photo} and V_{OC} extracted from *J-E* curves as a function of pH can be seen in figure 3-4d. Recently, we have suggested that the photocurrent of thin film hematite electrodes is controlled by the electric field that develops in the depletion region.[1] The width of the depletion region in turn depends on the voltage drop across the semiconductor, V_{SC}, (or the difference between the flat band potential, E_{FB}, and the solution potential, E_S where $V_{SC} = E_{FB} - E_S$).[23] Thus, the increasing J_{photo} with pH can be attributed to the larger depletion region that develops as the flat band potential shifts negatively. The V_{OC} increases by ~42 mV per pH, which is somewhat less than expected due to the ~59 mV per pH shift in the conduction band edge. This can be explained by the fact that although increasing pH raises the conduction band, it also increases the driving force, $-\Delta G^\circ$, for back electron transfer, which we showed above to be the voltage limiting recombination mechanism (see J_{et} in figure 3-1).[24,25] The increase in $-\Delta G^\circ$ should result in an increase in k_{et}, as well as k_{sol}, in equation (3-3), assuming normal region behavior.[24,25] Unfortunately, since first order behavior in n_s was not observed, and we were not able to quantify the product $N_{ss}f_{ss}$ in equation (3-3), we cannot calculate rate constants to verify this. Nevertheless, an increase in recombination rate constants due to an increasing $-\Delta G^\circ$ with pH can readily account for a ~12 mV decrease in V_{OC} per pH unit.

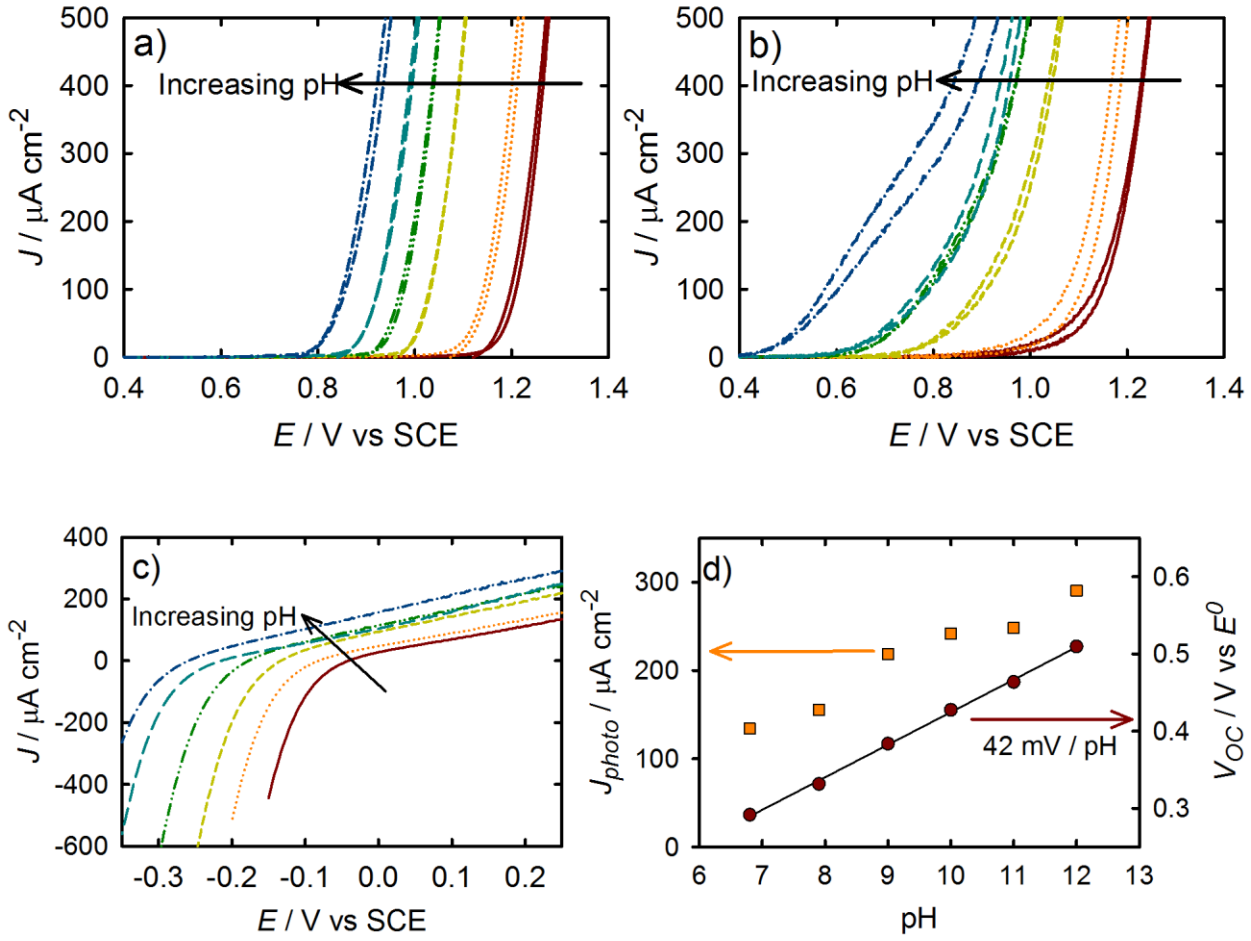

Figure 3-4: Plots of *J-E* curves in aqueous electrolytes, where current is attributed to H_2O oxidation, in pH 6.8 (red solid line), pH 8 (orange dotted line), pH 9 (yellow short dashed line), pH 10 (green dashed double dotted line), pH 11 (light blue long dashed line), pH 12 (dark blue dashed dotted line) in the (a) dark and (b) under 100 mW cm^{-2} illumination. c) *J-E* curves in aqueous electrolytes containing the $[Fe(CN)_6]^{3-/4-}$ redox couple at pH 6.8 (red solid line), pH 8 (orange dotted line), pH 9 (yellow short dashed line), pH 10 (green dashed double dotted line), pH 11 (light blue long dashed line), pH 12 (dark blue dashed dotted line) d) Plots of J_{photo} and V_{OC}, extracted from the *J-E* plots in (c), as a function of pH.

3.4.4 Redox Potential Dependence

The built-in voltage is the difference between the Fermi level in the semiconductor and the solution potential. The pH increases the voltage drop by increasing the Fermi level (flat band potential) of the semiconductor electrode. Decreasing the solution potential should likewise increase the voltage drop, and thus the photocurrent and photovoltage. To test this hypothesis, a homologous series of four different redox shuttles with formal potentials spanning 500 mV were prepared. The redox couples and their formal potentials are listed in Table 3-1. Each solution contained 100 mM of the electron donor species and 10 mM of the electron acceptor species in a pH 6.8 buffered 0.05M solution of KH_2PO_4/K_2HPO_4. Solutions were kept at a neutral pH to maximize solubility and stability for all the redox couples investigated. Concentrations were limited by the least soluble redox couple, $[IrCl_6]^{3-/4-}$. Plots of *J-E* curves measured in the dark, referenced to their respective $E°$, can be seen in figure 3-5a. The dark current density decreases in response to the solution potential being made more positive. Since superposition was shown to hold, this decrease in dark current density is expected to translate into an increase in V_{OC}. The light *J-E* curves for cells employing $[Fe(CN)_6]^{3-/4-}$ and $[IrCl_6]^{3-/4-}$ as redox shuttles are shown in figure 4b. In this configuration, the *J-E* curves correspond to a relative measure of the photovoltaic efficiency. The light curves for $[Mo(CN)_8]^{3-/4-}$ and $[W(CN)_8]^{3-/4-}$ are not shown because these couples are not very stable when exposed to light, however preliminary results were found to be consistent with the trends reported for the other couples.

The J_{photo} approximately triples when $[IrCl_6]^{3-/4-}$ is used compared with $[Fe(CN)_6]^{3-/4-}$, in addition to an increase in V_{OC} of ~330 mV. This value is less than the difference between the

490 mV solution potentials of the redox couples. Similar to the pH dependence studies above, the entire change in V_{SC} caused by a positive shift in $E°$ is not gained in the V_{OC}, most likely due to an increased driving force for electron transfer from the conduction band of the semiconductor to the solution. The effects of an increasing J_{et} (J_{sol}) can be seen in the dark *J-E* curves plotted against a fixed reference in supporting information. This plot shows that as V_{SC} is increased the dark current at a given potential vs a fixed reference also increases simply because the increased driving force as no other recombination pathways exist in the dark. Similarly to the pH dependence study, as the $E°$ becomes more positive and V_{SC} increases, the photocurrent and V_{OC} increase. Again, this is because an increasing V_{SC} results in a larger depletion region and a higher electric field, driving holes to the electrolyte interface to be collected.

Table 3-1. Formal Potentials of Outer-sphere Redox Shuttles Employed

Redox shuttle	$E°$ / V vs SCE
$Fe(CN)_6^{3-/4-}$	0.25
$Mo(CN)_8^{3-/4-}$	0.33
$W(CN)_8^{3-/4-}$	0.60
$IrCl_6^{3-/4-}$	0.74

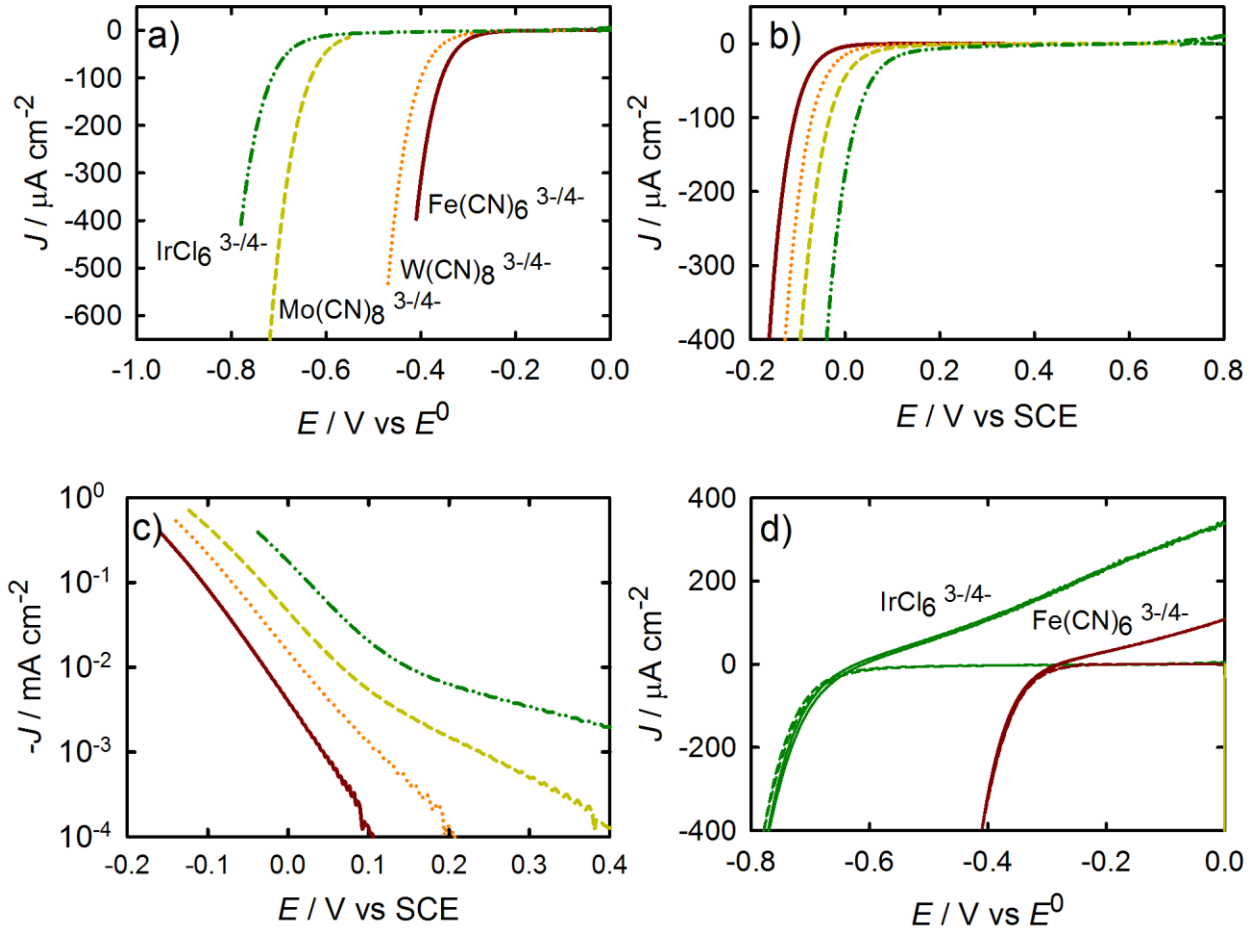

Figure 3-5. Dark *J-E* curves for a hematite electrode in contact with the redox couples $[Fe(CN)_6]^{3-/4-}$ (red solid line), $[W(CN)_8]^{3-/4-}$ (orange dotted line), $[Mo(CN)_8]^{3-/4-}$ (yellow dashed line) and $[IrCl_6]^{3-/4-}$ (green dash-dot-dash line) measured vs. (a) their respective solution potentials and (b) SCE. (c) Dark *J-E* where *J* is plotted on a log scale. (d) Two-electrode measurements of *J-V* curves for $[Fe(CN)_6]^{3-/4-}$ (red) and $[IrCl_6]^{3-/4-}$ (green) in the dark (dashed) and under AM 1.5 simulated light, 100 mW cm^{-2} (solid).

3.5 Conclusions

Through variations in the concentration of reduced species and incident light intensity, we have shown that photocurrent density of hematite electrodes is not limited by the rate of hole collection by the $[Fe(CN)_6]^{4-/3-}$ redox shuttle. Instead, the photocurrent is strictly dependant on the fraction of photogenerated holes that reach the semiconductor-electrolyte interface. We performed analogous measurements employing $[IrCl_6]^{3-/4-}$ as the redox shuttle and verified that hole collection is not the rate limiting step for this system either. The substantially lower photocurrent densities when an aqueous electrolyte was used without redox shuttle, however, indicate that the water oxidation step is rate limiting. This can be at least partially overcome through introducing water oxidation catalysts at the hematite surface.[26] Comparisons of water oxidation with use of redox shuttles such as $[Fe(CN)_6]^{4-/3-}$ should therefore provide a convenient framework for determining the effectiveness of a catalyst.

Electron transfer from the semiconductor to the redox couple was identified to be the dominant (i.e. V_{OC} limiting) recombination mechanism. As a consequence, it is not viable to obtain the entire possible increase in V_{OC} though increases in the pH, since this produces a concomitant increase in the driving force for back electron transfer. Nevertheless, an increase in pH does lead to an increase in V_{OC}. We further demonstrated that, analogous to increasing the pH, the V_{OC} can be increased through use of more positive redox shuttles. For example, use of $[IrCl_6]^{3-/4-}$ as the redox couple at pH 7 produced a V_{OC} of 0.61 V. To the best of our knowledge, this is the highest V_{OC} reported using a hematite electrode. If a higher pH could be

used in conjunction with such a redox shuttle with a positive potential, we expect even further significant improvements in V_{OC}, and thus efficiency, to be possible. Unfortunately, such positive redox shuttles are generally not stable in basic media. An alternative way to increase the V_{OC} would be through use of a barrier layer at the electrode surface to slow recombination. Such a strategy has been demonstrated on dye sensitized solar cells by employing thin alumina layers on the TiO_2 surface to curb the back electron transfer.[7,27-29] Recently, this strategy has been explored by the deposition of oxides such as alumina and silica on nanostructured hematite.[30,31]

To date, the highest efficiency regenerative PEC employing a hematite electrode was reported by Sanchez et. al. who combined a Ge-doped hematite electrode and a $[Fe(CN)_6]^{3-/4-}$ electrolyte at pH 9.1 to achieve an efficiency of 0.06%.[32] We estimate an potential efficiency of 0.04% by multiplying the current density measured at the solution potential (0.31 mA cm^{-2}), the open circuit potential relative to the solution potential (0.55 V) and the fill factor (0.24) and dividing by the incident power (100 mW cm^{-2}). While we acknowledge that this is not the true energy conversion efficiency, since our measurements were performed with a 3-electrode setup, this value represents a reasonable comparison of performance. Although our goal in this work was not to achieve maximum efficiency, the nearly record efficiency using a very thin film hematite electrode in contact with an $[IrCl_6]^{3-/4-}$ redox couple at a pH 6.8 is significant. These efficiencies, however, are still substantially below the ~15% maximum efficiency for a 2.2 eV bandgap material. In our case, since only very thin films were examined to minimize losses due

to bulk recombination, only a relatively small fraction of incident light is absorbed. Therefore, the most straightforward way to increase the overall efficiency is to increase the light absorption while maintaining a short charge carrier collection length. This strategy is currently being pursued by many research groups. We point out, however, that use of such nanostructued electrodes in contact with aqueous electrolytes make it very challenging to identify the bottlenecks preventing substantially higher efficiencies from being achieved. We believe that systematic investigations on controllable model systems, such as those presented here, will ultimately allow for the design of a system with superior efficiencies. Finally, one issue not addressed so far is the very poor fill factors (typically less than 0.3) which are generally observed with hematite electrodes. This problem is the subject of chapter 4.

3.6 Acknowledgments

TWH would like to thank Michigan State University for providing a generous start-up package in support of this work.

APPENDIX

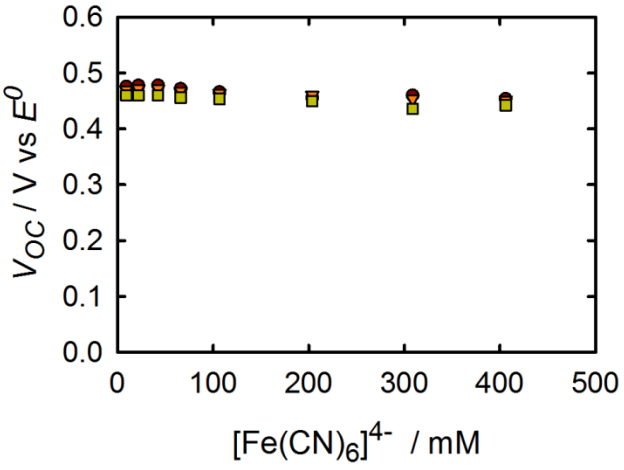

Figure A3-1: V_{OC} as function of $[Fe(CN)_6]^{4-}$ for under 50 mWcm^{-2} (yellow squares), 100 mW cm^{-2} (orange triangles), and 160 mW cm^{-2} (red circles) of white light.

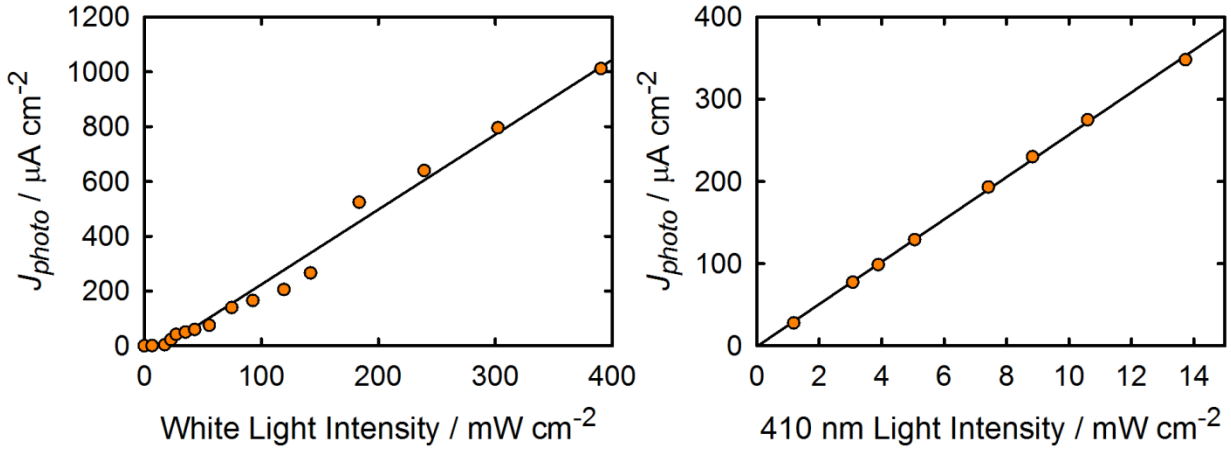

Figure A3-2: a) Plot of short-circuit photocurrent density vs. (a) white light intensity (b) monochromatic (410 nm) light intensity.

REFERENCES

REFERENCES

1. Klahr, B. M.; Martinson, A. B. F.; Hamann, T. W. *Langmuir*, **2011**, *27*, 461-468.

2. George, S. M. *Chem. Rev.* **2010**, *110*, 111-131.

3. Standridge, S. D.; Schatz, G. C.; Hupp, J. T. *J. Am. Chem. Soc.* **2009**, *131*, 8407-8409.

4. Dotan, H.; Sivula, K.; Gratzel, M.; Rothschild, A.; Warren, S. C. *Energy Environ. Sci.* **2011**, *4*, 958-964.

5. Leipoldt, J. G.; Bok, L. D. C.; Cilliers, P. J. *Z. Anorg. Alleg. Chem.* **1974**, *409*, 343-344.

6. Leipoldt, J. G.; Bok, L. D. C.; Cilliers, P. J. *Z. Anorg. Alleg. Chem.* **1974**, *407*, 350-352.

7. Klahr, B. M.; Hamann, T. W. *J. Phys. Chem. C*, **2009**, *113*, 14040-14045.

8. Nelson, J. J.; Amick, T. J.; Elliott, C. M. *J. Phys. Chem. C*, **2008**, *112*, 18255-18263.

9. Nelson, J. *The Physics of Solar Cells*; Imperial College Press: London, 2003.

10. Lewis, N. S.; Rosenbluth, M. L. In *Photocatalysis: Fundamentals and Applications*; Serpone, N., Pelizzetti, E., Eds.; John Wiley & Sons: New York, 1989.

11. Fajardo, A. M.; Lewis, N. S. *J. Phys. Chem. B*, **1997**, *101*, 11136-11151.

12. Kennedy, J. H.; Frese, K. W. *J. Electrochem. Soc.* **1978**, *125*, 709-714.

13. Beermann, N.; Vayssieres, L.; Lindquist, S. E.; Hagfeldt, A. *J. Electrochem. Soc.* **2000**, *147*, 2456-2461.

14. Launay, J. C.; Horowitz, G. *J. Cryst. Growth* **1982**, *57*, 118-124.

15. Anderman, M.; Kennedy, J. H. *J. Electrochem. Soc.* **1984**, *131*, 21-26.

16. McGregor, K. G.; Calvin, M.; Otvos, J. W. *J. Appl. Phys.* **1979**, *50*, 369-373.

17. Kennedy, J. H.; Frese, K. W. *J. Electrochem. Soc.* **1978**, *125*, 723-726.

18. Souza, F. L.; Lopes, K. P.; Longo, E.; Leite, E. R. *Phys. Chem. Chem. Phys.* **2009**, *11*, 1215-1219.

19. Sivula, K.; Zboril, R.; Le Formal, F.; Robert, R.; Weidenkaff, A.; Tucek, J.; Frydrych, J.; Gratzel, M. *J. Am. Chem. Soc.* **2010**, *132*, 7436-7444.

20. Tahir, A. A.; Wijayantha, K. G. U.; Saremi-Yarahmadi, S.; Mazhar, M.; McKee, V. *Chem. Mater.* **2009**, *21*, 3763-3772.

21. Cesar, I.; Sivula, K.; Kay, A.; Zboril, R.; Graetzel, M. *J. Phys. Chem. C*, **2009**, *113*, 772-782.

22. Dareedwards, M. P.; Goodenough, J. B.; Hamnett, A.; Trevellick, P. R. *J. Chem. Soc., Faraday Trans. 1 F*, **1983**, *79*, 2027-2041.

23. Tan, M. X.; Laibinis, P. E.; Nguyen, S. T.; Kesselman, J. M.; Stanton, C. E.; Lewis, N. S. *Prog. Inorg. Chem.* **1994**, *41*, 21-144.

24. Hamann, T. W.; Gstrein, F.; Brunschwig, B. S.; Lewis, N. S. *J. Am. Chem. Soc.* **2005**, *127*, 13949-13954.

25. Hamann, T. W.; Gstrein, F.; Brunschwig, B. S.; Lewis, N. S. *Chem. Phys.* **2006**, *326*, 15-23.

26. Tilley, S. D.; Cornuz, M.; Sivula, K.; Grätzel, M. *Angew. Chem. Int. Ed.* **2010**, *49*, 6405-6408.

27. Ondersma, J. W.; Hamann, T. W. *J. Phys. Chem. C*, **2010**, *114*, 638-645.

28. Hamann, T. W.; Farha, O. K.; Hupp, J. T. *J. Phys. Chem. C*, **2008**, *112*, 19756-19764.

29. DeVries, M. J.; Pellin, M. J.; Hupp, J. T. *Langmuir*, **2010**, *26*, 9082-9087.

30. Spray, R. L.; McDonald, K. J.; Choi, K.-S. *J. Phys. Chem. C* **2011**, *115*, 3497-3506.

31. Le Formal, F.; Tetreault, N.; Cornuz, M.; Moehl, T.; Gratzel, M.; Sivula, K. *Chem. Sci.* **2011**.

32. Sanchez, H. L.; Steinfink, H.; White, H. S. *J. Solid State Chem.* **1982**, *41*, 90-96.

Chapter 4:

Voltage Dependent Photocurrent of Thin Film Hematite Electrodes

Adapted with permission from:

Voltage dependent photocurrent of thin film hematite electrodes, Benjamin M. Klahr and Thomas W. Hamann, *Applied Physics Letters*, **2011**, 99, 063508.

4.1 Abstract

The current density (J) vs. applied voltage (V) curves of thin-film hematite electrodes under illumination exhibit non-ideal behavior. As a result very poor fill factors and photocurrent densities are generally observed. A simple model is presented to describe the photocurrent density behavior of hematite photoelectrodes, which assumes only drift collection of holes in a uniform electric field. Excellent agreement is found between the model and experimental results. Use of this model provides important insight into the limitations of hematite electrodes as well as strategies to achieve improved efficiency.

4.2 Introduction

The previous two chapters demonstrated that the use of outersphere redox shuttles or H_2O_2 as hole scavengers, can collect essentially all of the holes that reach the surface.[1,2] This has also been shown by Dotan *et. al.* with the use of H_2O_2.[3] The use of such hole scavengers is then able to de-convolute the rate limiting process of water oxidation at the surface from the other processes in the bulk of the hematite. We again employ this strategy of using a fast redox couple in order to elucidate the fundamental limitations of this material in the bulk.

The power conversion efficiency, η, of a regenerative photoelectrochemical cell, PEC, is given by the fraction of the maximum power output, $P_{\max}$, to the incident solar power, P_{in}. The maximum power output is the product of the photocurrent density and the voltage at the power point, usually expressed as

$$\eta = \frac{P_{\max}}{P_{in}} = \frac{J_{sc} \cdot V_{oc} \cdot ff}{P_{in}} \tag{4-1}$$

where J_{sc} is the photocurrent density at short-circuit, V_{oc} is the open-circuit photovoltage, and *ff* is the fill factor. Hematite-based PEC's suffer from concomitantly sub-optimal J_{sc}'s, V_{oc}'s and *ff* 's. Recent efforts have focused on developing nanostructures and introducing high levels of impurities (such as Si, Ti, Al, Ge, and Nb), primarily in order to improve J_{sc}.[4-9] These strategies have produced some promising results, however the overall power conversion efficiency is still very modest. We recently employed a series of straightforward systematic studies to determine several limitations on the performance of thin-film hematite in terms of both the photocurrent density and the photovoltage in regenerative PEC's.[1,2] While these lessons point to several

straightforward routes of increasing the photocurrent and photovoltage, the low fill factor, which has been typically less than 0.3, has not been addressed in detail. In this work we aim to explain cause of the poor fill factors which limit the power conversion efficiency of hematite electrodes. These results provide additional insights into the operational principles of hematite PEC's and further identifies the physical parameters which must be addressed if hematite, or analogous materials, will ever be used effectively.

4.3 Experimental

Hematite electrodes were deposited on fluorine doped tin oxide (FTO) coated glass substrates by atomic layer deposition, ALD, as described in chapter 2.[1] The results reported herein were from a single 33 nm hematite electrode, however additional nominally identical electrodes were also measured and produced nominally identical results. The electrolyte consisted of 200 mM of $K_4Fe(CN)_6 \cdot 3H_2O$, 20 mM of $K_3Fe(CN)_6$ and 200 mM KCl in a pH 12 aqueous solution (KOH).

4.4 Results and Discussion

Figure 4-1 shows typical plots of the current density, *J*, measured as a function of applied voltage, *V*, of a thin-film hematite electrode in the dark and under 100 mW cm^{-2} (AM 1.5) illumination. The dark *J-V* curve is highly rectifying, however the *J-V* curve under illumination is sloped. This non-ideal light *J-V* behavior results in a diminished fill factor, and thus energy conversion efficiency. We note that similar looking *J-V* curves have been reported elsewhere when fast hole collecting redox species are employed, including the highest reported power conversion efficiency of a regenerative, hematite photoelectochemical cell.[9] As a consequence, no fill factor greater than 0.31 has been reported.[9] This is in contrast to the

maximum fill factor of 0.8 that can be achieved with a V_{OC} of 0.5 V, according to the diode equation (below).

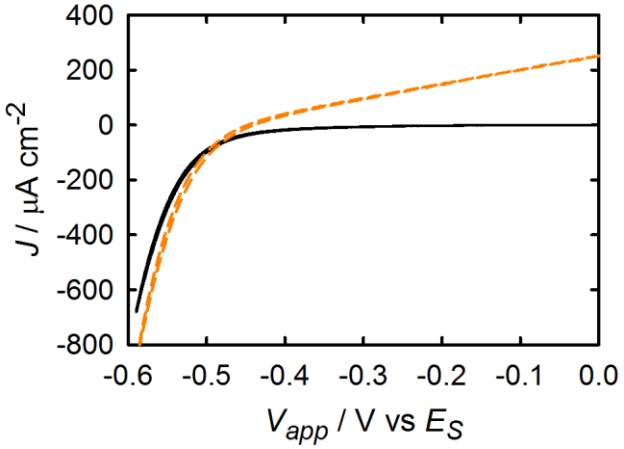

Figure 4-1. Current density vs. applied potential curves for PEC employing a 33 nm hematite electrode in conjunction with a pH 12 $[Fe(CN)_6]^{3-/4}$ electrolyte under 1 sun illumination (orange dashed line) and in the dark (solid black line).

In general a *J-V* curve can be described using the diode equation:

$$J = J_{photo} - \left[J_0 \left(exp\left(\frac{-q(V + IR_s)}{\gamma kT} \right) - 1 \right) - \left(\frac{V + IR_s}{R_{sh}} \right) \right] \quad (4\text{-}2)$$

where J_{photo} is the photocurrent density, J_0 is the exchange current density, k is the Boltzmann constant, and T is temperature, γ is the diode quality factor, R_s is a series resistance and R_{sh} is the shunt resistance.[10] In principle, γ, R_s, and/or R_{sh} can cause a sloped *J-V* curve and diminished fill factor as seen in figure 4-1. We have previously shown that the diode quality factor is approximately 2 for these thin-film hematite electrodes, which cannot account for the severe slope of the light *J-V* curves.[2] The series resistance of these films were measured by several

methods including electrochemical impedance spectroscopy (EIS), which produced R_S 110 Ω (figure 4-2a), and by plotting dV/dJ vs 1/J, which produced R_S 23 Ω (figure 4-2b).[11]

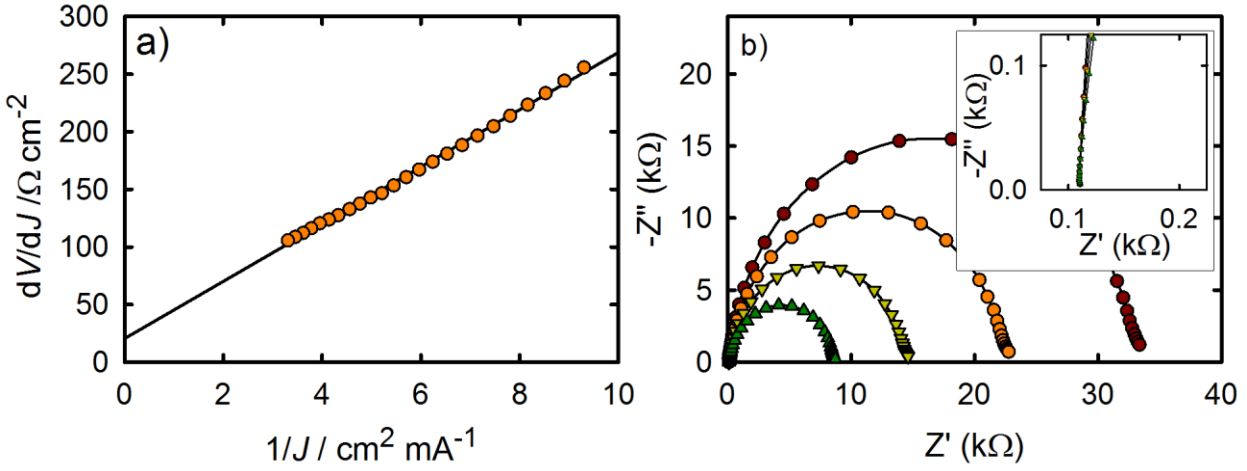

Figure 4-2. Series resistance of the hematite photoelectrochemical cell measured by plotting (a) dV/dJ vs 1/J, where the y-intercept is the series resistance (~23 Ω), and (b) Nyquist plots showing the intercept at Z' as the series resistance (~110 Ω) with a zoomed in view as the insert.

Because the voltage drop due to a resistance of ~100 Ω with the small currents produced is insignificant, the effects of series resistance on the light J-V curves is negligible. Another possible cause of the non-ideal light J-V curves is a low shunting resistance. Shunting – for example pinholes in the film allowing charge transfer from the FTO to the solution – would be especially problematic when fast, reversible redox couples are employed, such as $[Fe(CN)_6]^{3-/4-}$. ALD is a unique deposition technique, however, which is known to produce conformal pinhole free films, even when much thinner films than the 33 nm film measured here are deposited.[12,13] In addition, we note that if there were a low shunting resistance, it would be reflected in the dark

J-V curve as well as the light.[10] As mentioned above, however, the dark *J-V* curve is highly rectifying, which allows us to tentatively rule out shunting as the cause of the non-ideal light *J-V* curves. The Gartner model is often used to interpret voltage dependent photocurrent densities.[14,15] The Gartner model neglects recombination in the depletion region; however we have previously shown that depletion region recombination is significant in hematite electrodes.[2] In addition, the Gartner model was derived under reverse bias conditions which results in a $V^{1/2}$ dependence of J_{photo}, which cannot reasonably fit or explain our data.

We have recently suggested that the photocurrent of hematite electrodes is strictly limited by the drift length of holes, which in turn is dependent on the voltage drop across the electrode.[1,2] For example, we showed that increasing the pH and/or decreasing the solution potential, which increases the built in voltage, V_{bi}, results in a concomitant increase in the short circuit photocurrent density.[2] This situation is analogous to amorphous silicon p-i-n junction photovoltaic cells, PV's, whose performance is largely dominated by the voltage drop across the intrinsic region.[10] Amorphous silicon PV's can also suffer from sub-optimal fill factors arising from non-ideal light *J-V* curves. Hegedus has developed a model to describe such *J-V* curves of amorphous Si PV's, which we adopt here to explain the light *J-V* curves of hematite electrodes.[11] In this model, the dark *J-V* is described by the bracketed term in equation 4-1. This is in excellent agreement with the measured dark *J-V* behavior of hematite electrodes with $\gamma = 2$, $R_s = 0\ \Omega$, $R_{sh} = \infty$, and $J_0 = 3$ nA cm^{-2} (shown in figure 4-3).

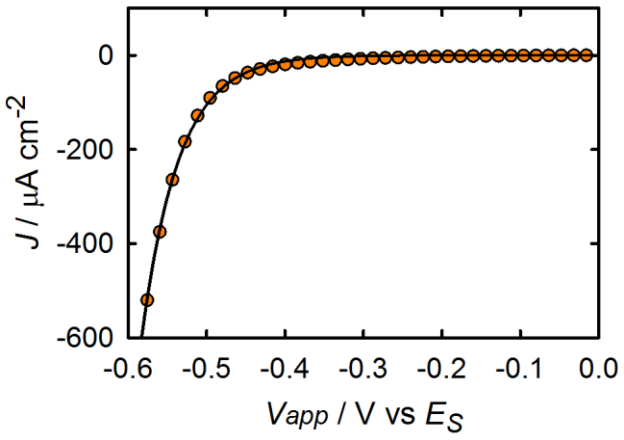

Figure 4-3. Experimental dark *J-V* curve (orange circles) fit to the diode equation (black line). Fitting yields $\gamma = 2$ and $J_0 = 3$ nA cm^{-2} assuming $R_s = 0$ Ω, and $R_{sh} = \infty$. Correcting for the ~100 Ω series resistance has a negligible effect.

The photocurrent density is described as the product of the optically saturated photocurrent density, given by the flux of photons that are absorbed by the material, J_{abs}, and the collection efficiency, $\eta(V)$, which is a function of voltage:

$$J_{photo}(V) = J_{abs} \cdot \eta(V) \tag{4-3}$$

The collection efficiency is described by the equation:

$$\eta(V) = \frac{\mu \tau V_{bi}}{D^2}\left[1 - \left(\frac{V}{V_{bi}}\right)\right] \tag{4-4}$$

where μ is the minority carrier mobility, τ is the minority carrier lifetime, and D is the electrode thickness. Note that equation (4-4) only includes the contribution of charge that is generated within an electric field. The original equation derived by Hegedus to describe amorphous silicon also included a term which accounted for the diffusion of charge through a concentration

gradient.[11] However, based on our results from chapter 2, we estimate that diffusion can be neglected. The result is an equation where linear photocurrent density vs. applied voltage curves are expected. The quantity $\mu\tau V_{bi} / D$ is the hole drift length, assuming a uniform field across the electrode, at no applied voltage. The collection efficiency is thus expected to increase with increasing hole lifetime and mobility, and decrease with an increasing electrode thickness. This is in agreement with our previously reported electrode thickness dependence of J_{photo}; a constant J_{photo} with increasing electrode thickness (thus increasing J_{abs}) was attributed to a concomitantly decreasing $\eta(V)$.[1] The collection efficiency is also linearly dependent on the applied voltage relative to the V_{bi}, going to zero when the applied voltage offsets the built-in voltage. An illustration of these two extreme conditions, when $V = 0$ and when $V = V_{bi}$ can be seen in Figure 4-4.

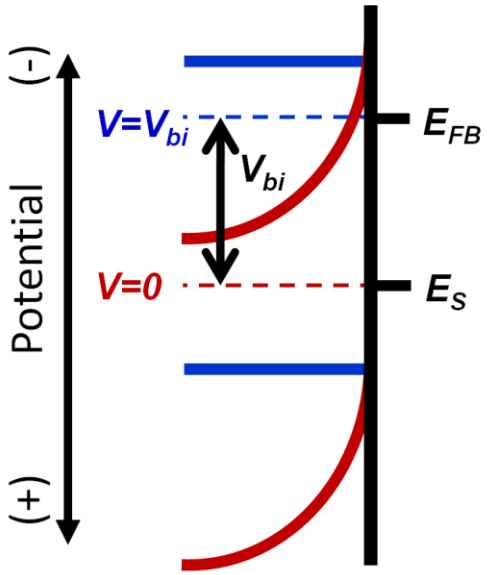

Figure 4-4. Qualitative energy diagram showing the conduction bands and valence bands when $V = 0$ (red lines) and when $V = V_{bi}$ (blue lines).

In order to test this model of the photocurrent density, $J_{photo}(V)$ was extracted by subtracting the experimental dark current density from the *J-V* curve under illumination (the black solid line from orange dashed line in figure 4-1). In addition, the incident light intensity was varied from 35 to 390 mW cm^{-2}, which is only expected to affect J_{abs}. The resultant plots of $J_{photo}(V)$ are shown in figure 4-5 for varying light intensities. In all cases, the plots of $J_{photo}(V)$ are linear over the entire voltage range measured, consistent with equations (4-3) and (4-4). The slope of the $J_{photo}(V)$ increases with increasing light intensity, as expected for increasing J_{abs}. We note that any shunting resistance would not be sensitive to incident light intensity, thus supporting our above claim that shunting does not significantly contribute to the poor fill factors observed. In addition, we found that J_{SC} increases linearly with increasing light intensity (see Appendix of Chapter 3).

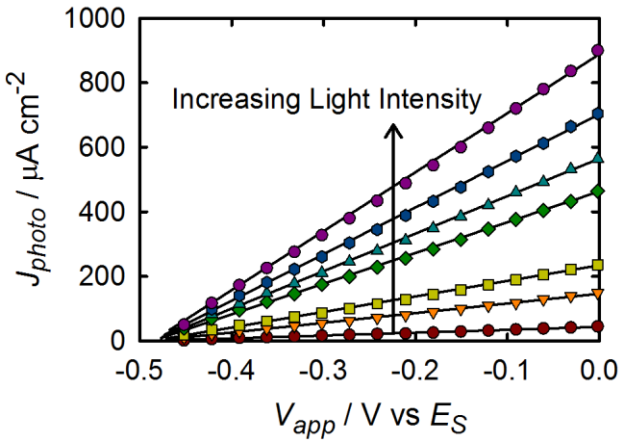

Figure 4-5. The experimental photocurrent for varying light intensity (colored shapes) and the linear fit (solid line) of equation (4-3) and (4-4).

A J_{abs} value was calculated at each light intensity by multiplying the absorbtance and the incident photon spectral flux. Using this method, J_{abs} values were calculated to be between 0.4 to 13 mA cm^{-2} for incident white light intensities ranging from 35 to 390 mW cm^{-2}. Figure 4-6a shows a very linear plot of J_{sc} vs. J_{abs}. The slope of this plot should be equal to the collection efficiency at $V = 0$, which is ~7%. This is in very close agreement with the collection efficiency of 8.8% calculated by integrating the absorbed photon to current efficiency shown in figure 4-6b. This small collection efficiency accounts for the modest current densities generally observed with hematite photoelectrodes. The product of $\mu\tau/D^2$ was determined by fitting the $J_{photo}(V)$ data to equations (4-3) and (4-4), with fixed calculated values of J_{abs}. The fit yielded a value of $\mu\tau/D^2 = 0.14\ V^{-1}$. Using literature values for μ (0.2 $cm^2\ V^{-1}\ s^{-1}$)[16] and τ (5 ps)[17] and our measured values for D (33 nm), the product of $\mu\tau/D^2$ is calculated to be 0.092 V^{-1}, in excellent agreement with the fitted value. We note that the lifetime of 5 ps was measured under high incident light intensities and therefore may underestimate the lifetime in response to the light intensities employed in our measurements since (at least in part) additional recombination mechanisms such as Auger recombination can diminish the lifetime under such high injection conditions. In addition, the V_{bi} can be determined by the intercept of the $J_{photo}(V)$ plots (when $J_{photo} = 0$), which was found to be 0.49 V. Ideally, the V_{bi} is the difference between the flat band potential, E_{FB}, and the solution potential, E_S; the calculated value for V_{bi} based on Mott Schottky analysis of nominally identical films is 0.59 V, also in reasonable agreement with the fit value produced here.[1]

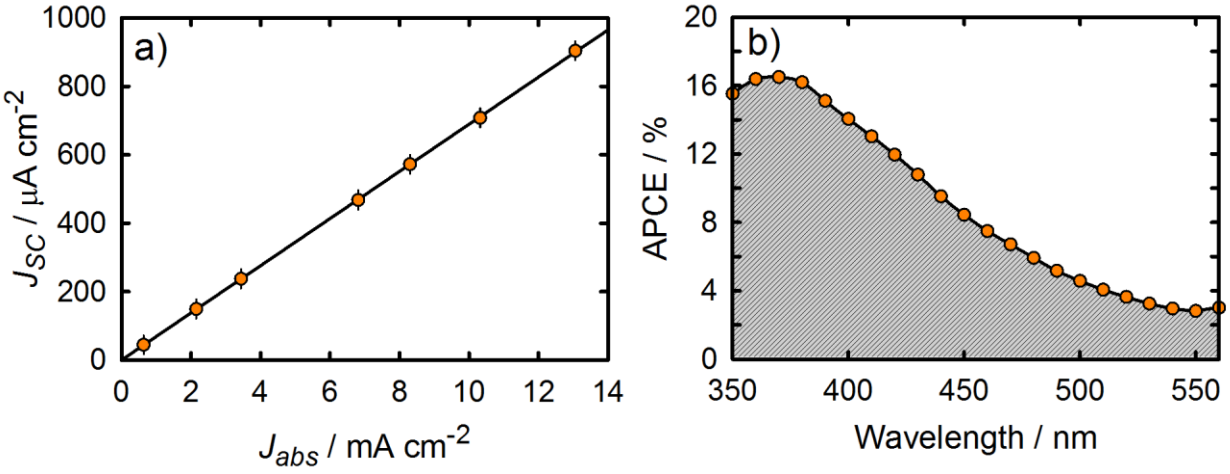

Figure 4-6. (a) Plot of J_{sc} vs. J_{abs}; the slope of this plot is equal to the collection efficiency at V = 0, which is ~7%. (b) The absorbed photon to current efficiency (APCE). Integrating between 350 and 560 nm gives a collection efficiency of 8.8%.

4.5 Conclusion

In conclusion, we were able to accurately describe the total photovoltaic behavior of hematite electrodes using a modified version of the diode equation, with a linearly dependent photocurrent on voltage. This analysis allowed us to identify a very short hole drift length as the cause of the generally observed poor fill factors, in addition to the sub-optimal photocurrent densities. An additional feature of the model presented is the ability to extract the product of $\mu\tau$ (assuming the electrode thickness is known) as well as V_{bi}, which we showed to be in good agreement with literature values, from simple *J*-*V* measurements. This model thus provides a useful framework to guide improvement of this enticing material.

4.6 Acknowledgements

TWH would like to thank Michigan State University for a generous start-up package in support of this work.

REFERENCES

REFERENCES

1. Klahr, B. M.; Martinson, A. B. F.; Hamann, T. W. *Langmuir*, **2011**, *27*, 461-468.

2. Klahr, B. M.; Hamann, T. W. *J. Phys. Chem. C*, **2011**, *115*, 8393-8399.

3. Dotan, H.; Sivula, K.; Gratzel, M.; Rothschild, A.; Warren, S. C. *Energy Environ. Sci.* **2011**, *4*, 958-964.

4. Cesar, I.; Sivula, K.; Kay, A.; Zboril, R.; Graetzel, M. *J. Phys. Chem. C,* **2009**, *113*, 772-782.

5. Glasscock, J. A.; Barnes, P. R. F.; Plumb, I. C.; Savvides, N. *J. Phys. Chem. C,* **2007**, *111*, 16477-16488.

6. Sartoretti, C. J.; Alexander, B. D.; Solarska, R.; Rutkowska, W. A.; Augustynski, J.; Cerny, R. *J. Phys. Chem. B,* **2005**, *109*, 13685-13692.

7. Kleiman-Shwarsctein, A.; Huda, M. N.; Walsh, A.; Yan, Y.; Stucky, G. D.; Hu, Y.-S.; Al-Jassim, M. M.; McFarland, E. W. *Chem. Mater.* **2009**, *22*, 510-517.

8. Sanchez, C.; Sieber, K. D.; Somorjai, G. A. *J. Electroanal. Chem.*, **1988**, *252*, 269-290.

9. Sanchez, H. L.; Steinfink, H.; White, H. S. *J. Solid State Chem.* **1982**, *41*, 90-96.

10. Nelson, J. *The Physics of Solar Cells*; Imperial College Press: London, 2003.

11. Hegedus, S. S. *Prog. Photovoltaics Res. Appl.* **1997**, *5*, 151-168.

12. Ritala, M.; Leskela, M. In *Handbook of Thin Film Materials*; Nalwa, H. S., Ed.; Academic Press: San Diego, 2001; Vol. 1, p 103.

13. George, S. M. *Chem. Rev.* **2010**, *110*, 111-131.

14. Gartner, W. W. *Phys. Rev.* **1959**, *116*, 84-87.

15. Reichman, J. *Appl. Phys. Lett.* **1980**, *36*, 574-577.

16. Bosman, A. J.; Vandaal, H. J. *Adv. Phys.* **1970**, *19*, 78.

17. Joly, A. G.; Williams, J. R.; Chambers, S. A.; Xiong, G.; Hess, W. P.; Laman, D. M. *J. Appl. Phys.* **2006**, *99*, 6.

Chapter 5:

Photoelectrochemical Impedance Spectroscopy of Hematite Electrodes: The Role of Surface States

Adapted with permission from:

Water Oxidation at Hematite Electrodes: The Role of Surface States, Benjamin M. Klahr, Sixto Gimenez, Francisco Fabregat-Santiago, Thomas W. Hamann, and Juan Bisquert. *Journal of the American Chemical Society*, **2012**, *134*, 4294-4302.

5.1 Abstract

Thin film hematite electrodes prepared by Atomic Layer Deposition were used to study the photoelectrochemical properties of this material under water splitting conditions. We employed impedance spectroscopy to analyze the general mechanism of water oxidation at different conditions of voltage, light intensity and electrolyte pH. A general physical model is proposed, which includes the existence of a surface state at the semiconductor/liquid interface where holes accumulate. The strong correlation between the charging of this state with the reduction in charge transfer resistance and the photocurrent onset provides new evidence that the accumulation of holes in surface states is responsible for water oxidation. The charging of this surface state under illumination is also related to the shift of the measured flat band potential.

5.2 Introduction

Thus far, the discussed experiments have focused on elucidating the limitations of bulk hematite by eliminating the rate limiting step of water oxidation at hematite electrodes through the use of a fast redox shuttle. Focus is now shifted to the reaction of interest - using photogenerated holes to oxidize water at the surface of hematite. Recently, a series of studies based on different characterization techniques have improved our understanding of the factors controlling the water splitting performance of hematite photoelectrodes.[1-4] These works have pointed out the crucial role of the accumulation of holes at the surface of hematite electrodes under visible light which is responsible for a highly anodic current onset potential. However, the nature of this accumulated charge, and the role it plays in the water oxidation mechanism is still under debate.

We employed phtoelectrochemical (PEC) impedance spectroscopy (IS) to determine the general mechanism of water oxidation. Our results are based on the analysis of surface state capacitance,[5-8] a concept developed in the 1980s, which provides evidence of the accumulation of holes in surface states at the semiconductor/electrolyte interface. We have found that the charge-transfer reaction to oxidize water occurs from these surface states rather than from holes from the valence band; the photocurrent onset appears only after holes start to accumulate in these surface sites.

5.2.2 Impedance Spectroscopy Background

Impedance Spectroscopy is a common tool used in electrochemistry for the analysis of electrical properties of materials and interfaces. A small amplitude AC potential perturbation, $\tilde{V}$, is applied around a constant bias potential. The resulting oscillating current, $\tilde{i}$, is measured from which an impedance can be calculated by $Z(\omega) = \frac{\tilde{V}}{\tilde{i}}$. In the presence of a

capacitor, Z includes a real (Z') and imaginary (Z") component which is represented as a single point for a single frequency on a plot of Z" vs. Z' (often termed "Nyquist plots"). The frequency of the AC signal is swept over the relevant range of AC frequencies, ω, (typically from MHz to mHz) to build the Nyquist plots such as those shown in figure 5-4. The spectroscopic scan can be resolved into a combination of resistances and capacitors in a given arrangement, called the equivalent circuit (EC). The EC is a useful tool for the interpretation of experimental results, provided that the different elements and their particular arrangement possess physical meaning. It is sometimes claimed that the interpretation of the results based on an EC is ambiguous, based on the fact that different equivalent representations of a given Z(ω) function are possible. While there is a variety of possible representations of a single physical-chemical model, it is also true that the EC allows for the conveyance of a great amount of information if a model is sufficiently simplified that the resulting fits contain only one solution, yet not oversimplified so that the EC parameters can be related to the relevant physical processes in a useful way. Thus, while IS is straightforward to measure, the main problem is the extraction of information contained in the data. It is important, therefore, to clarify the basis for a given approach to treat the experimental results, and we describe ours in the following.

The main purpose for employing IS in this case is to understand the characteristic plots of current density with respect to applied bias voltage under steady state conditions, *J-V*. Indeed, the *J-V* characteristics are used to derive the efficiency, considering the number of photons impinging on the semiconductor.[9] The total resistance, R_{tot}, of a point on a *J-V* curve can be calculated by the equation

$$R_{tot} = \left(A_S \frac{\partial J}{\partial V} \right)^{-1} \qquad (5\text{-}1)$$

where A_S is the surface area of the electrode. Similarly, the resistance can be measured with

IS, however R_{tot} is able to be split into components which is made possible by the frequency dependent impedance of a capacitor, $Z = (i\omega C)^{-1}$.

For a sufficiently thick and doped semiconductor material, there are three capacitances which are well established in the literature. First, there is the depletion layer capacitance, C_{sc}, which is described by the Mott-Schottky (MS) equation:

$$\left(\frac{A_S}{C_{sc}}\right)^2 = \frac{2}{q\kappa\varepsilon_0 N_D}\left(V - E_{fb} - \frac{k_B T}{q}\right) \tag{5-2}$$

where V is the applied voltage, E_{fb} is the flat band potential, N_D is the dopant density, k_B is Boltzmann's constant, T the absolute temperature, q is elementary charge, κ is the dielectric constant of the semiconductor (taken to be 32 for the hematite)[10] and ε_0 is the vacuum permittivity (8.854×10^{-12} C V^{-1} m^{-1}). In addition, there is the series connection of the Helmholtz capacitance, C_H, where both elements have been lumped into C_{bulk}. These two capacitances are dielectric in origin. In contrast to this, there is a third, chemical capacitance,[11,12] and is termed the surface state capacitance, C_{ss}.[5-8,13,14] This capacitance can be expressed by the equation:

$$C_{ss} = A_S q N_{ss} \frac{\partial f_{ss}}{\partial E_{Fn}} = A_S \frac{N_{ss} q^2}{k_B T} f_{ss}(1 - f_{ss}) \tag{5-3}$$

where N_{ss} is the surface density of the surface states, f_{ss} is the fractional occupancy of the state, and E_{Fn} is the electron Fermi level of the state. For the interpretation of the IS measurements of illuminated and dark hematite electrodes we adopt a classical model which is depicted in Figure 5-1a.[15] From this physical model, and the capacitances discussed above, we suggest the EC shown in Figure 5-1b. A formal derivation of the interfacial impedance is

given in Ref. [16] This EC can also be traced back to a large body of literature on IS of photoelectrochemical systems.[6-8,17]

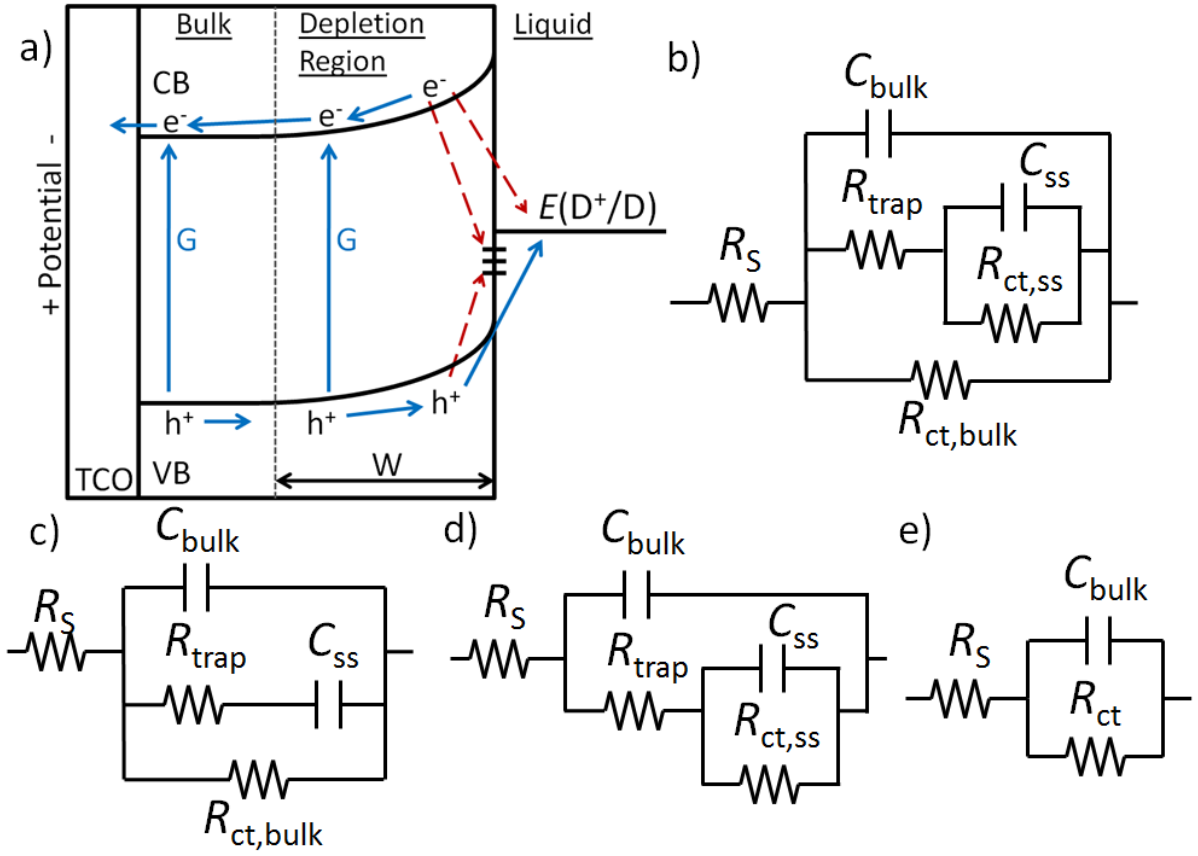

Figure 5-1. (a) Proposed physical model for the charge carrier dynamics in hematite electrodes, showing their generation, G, by light absorption, surface state trapping, and interfacial charge-transfer reactions. (b) Equivalent circuit corresponding to physical model in (a). (c) Simplified model used for IS interpretation created by removing $R_{ct,ss}$ (d) Simplified model used for IS interpretation created by removing $R_{ct,bulk}$. (e) Randles circuit

According to Equation (5-3) the surface state capacitance traces a peak with respect to Fermi level variation at the point $E_{Fn} = E_{ss}$, where E_{ss} is the energy level of the surface state. Therefore, a voltage scan of the capacitance should allow for a direct spectroscopic

measurement of the surface states of a semiconductor in the energy axis. This method has been applied over many years, especially using an inert electrolyte that totally blocks the current flow.[5,14] However, in general one must be careful when establishing the relationship between the applied voltage and the energy of the surface state. In a system containing an n-type semiconductor in contact with a well-defined redox couple, the voltage in a dark measurement relates to the difference of the Fermi level of electrons in the semiconductor, E_{Fn}, and the redox potential of the redox couple, as indicated in Figure 5-2a. When irradiated with suprabandgap illumination from the electrolyte side, electron–hole pairs are generated in the region where the light is absorbed, plus one diffusion length of the minority carriers,[15,18] which are the holes in this case. Excess minority carriers are therefore created close to the interface, with the concomitant lowering of their own Fermi level, as indicated in Figure 5-2b. The split of the Fermi levels produces a photovoltage, and for infinitely fast exchange of holes with the redox species across the interface, equilibrium would be achieved, where $E_{Fp}^{surface} = E_{redox}$. This means that the voltage will be given by $-qV = E_{Fn} - E_{redox}$, just as in Figure 5-2a. The usual case, however, is that $E_{Fp}^{surface} < E_{redox}$, due to sluggish exchange, particularly when intermediate steps for the reaction or surface states are involved.[19] Therefore, the Fermi level of holes at the surface becomes effectively disconnected from the applied voltage. The concepts discussed above will be used to interpret the following experimental results.

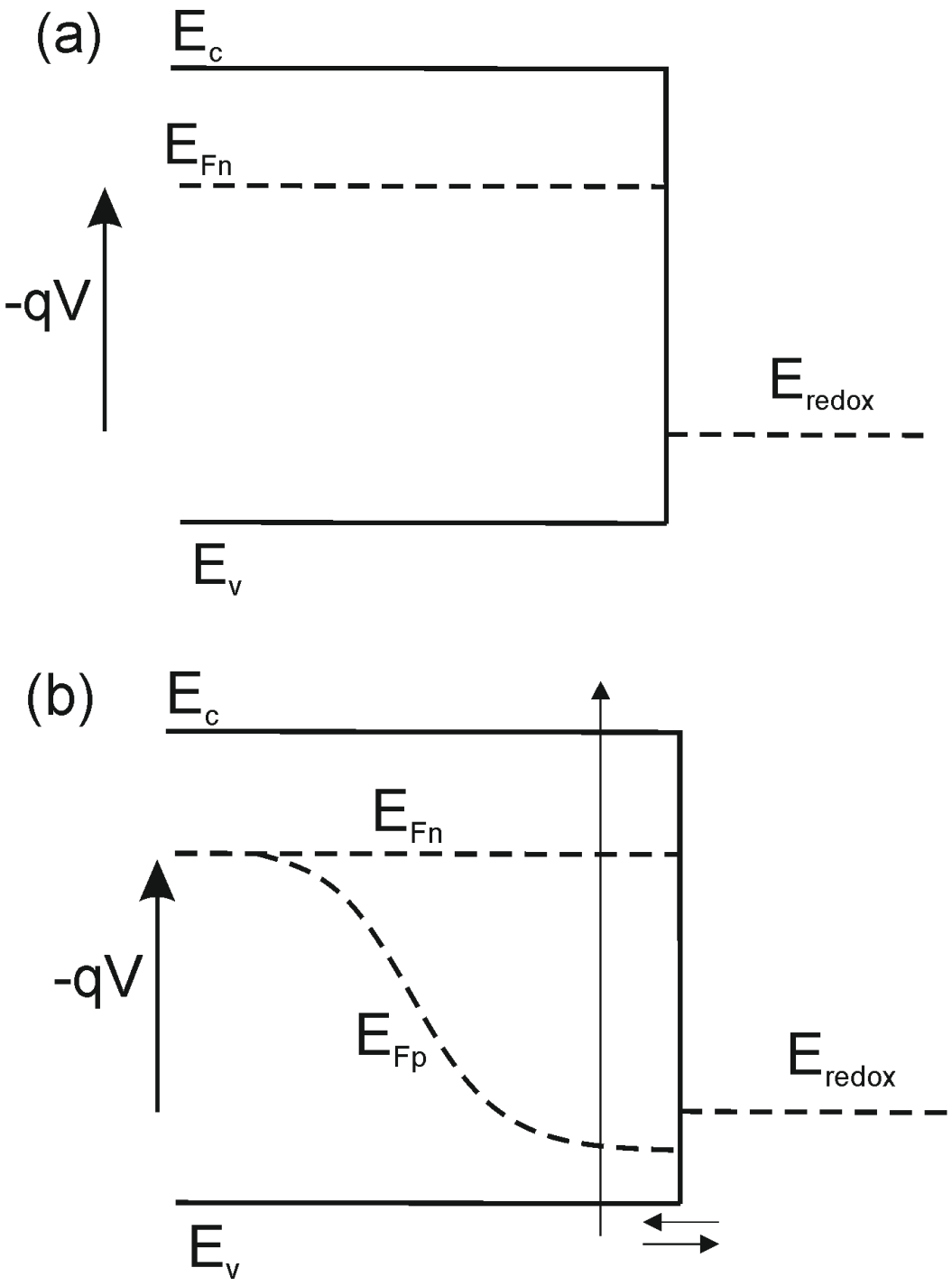

Figure 5-2. Scheme of a semiconductor with conduction band and valence band edges E_c and E_v, and the quasi-Fermi levels of the respective states. (a) Applied voltage V in the dark. (b) Photogeneration of electron hole pairs and charge transfer of hole to redox couple in solution.

5.3 Experimental

Thin films of hematite were deposited on fluorine-doped tin oxide (FTO) coated glass substrates (Hartford Glass, 12 Ω cm^{-2}) by atomic layer deposition (Savannah 100, Cambridge Nanotech Inc.) using a modified procedure to that described previously.[20] The modification consisted of using both ozone and water as the oxidation source instead of just ozone, which results in increased growth rate and uniformity of the hematite films compared to those made using only ozone as the oxygen source.[21] A single precursor-oxidation cycle consisted of a 20 second ferrocene pulse followed by an oxidation sub-cycle which included 10 cycles of a 0.015 s H_2O pulse followed by a 6 s ozone pulse, where each sub-cycle was separated by a 5 s purge. This oxidation cycle is thus essentially a 60 s "wet" ozone pulse. All films in this experiment were prepared by 1,200 ALD cycles and measured to be ~60 nm by absorption measurements (Perkin Elmer, Lambda 35 with a Labsphere integrating sphere) corrected for reflection as described previously, as well as ellipsometric measurements (Horiba Jobin Yvon, Smart-SE).[20]

Electrolytes were prepared at pH 6.9 (employing a 0.1 M phosphate buffer) and pH 13.3 (0.1 M KOH). The pH was determined with Fisher Scientific Accumet pH meter. All aqueous solutions contained 200 mM KCl as a supporting electrolyte. Hematite electrodes were masked with a 60 μm Surlyn film (Solaronix) with a 0.25 cm^2 hole to define the active area and to prevent scratching of the thin films which were clamped to a custom made glass electrochemical cell. Surlyn films were adhered to the electrodes by heating to 120° C. A homemade saturated Ag/AgCl electrode was used as a reference electrode and high surface area platinum mesh was used as the counter electrode. Impedance spectroscopic and photoelectrochemical measurements were made with an Eco Chemie Autolab potentiostat

coupled with Nova electrochemical software. IS data were gathered using a 10 mV amplitude perturbation of between 10,000 and 0.01 Hz. The IS data over this six order of magnitude variation of frequencies were simultaneously fit to the equivalent circuits described in the text using Zview software (Scribner Associates). The light source was a 450 W Xe arc lamp. An AM 1.5 solar filter and neutral density filters were used to simulate sunlight at 100 mW cm^{-2}; neutral density filters were also employed to reduce the light intensity to 33 and 10 mW cm^{-2}. All photoelectrochemical measurements were performed by shining light from the substrate-electrode (SE) interface. While all experiments shown in this work were performed multiple times, the data shown herein are from a single hematite electrode.

5.4 Results and Discussion

5.4.1 Photoelectrochemical Results

Plots of steady state photocurrent density, *J*, vs. applied voltage, *V*, curves in response to varying light intensities – 10, 33 and 100 mW cm^{-2} – are shown in Figure 5-3a for pH 6.9 and Figure 5-3b for pH 13.3. Since the water oxidation potential and the hematite bands both shift at the Nernstian rate of 59 mV / pH, the potentials were normalized to the reversible hydrogen electrode reference (RHE).[22-24] The *J-V* curves under 100 mW cm^{-2} illumination (1 sun) are plotted vs. RHE in Figure 5-3c. The curves show remarkable overlap, however the performance of the electrodes at pH 13.3 does show a somewhat improved current onset potential of about 100mV.

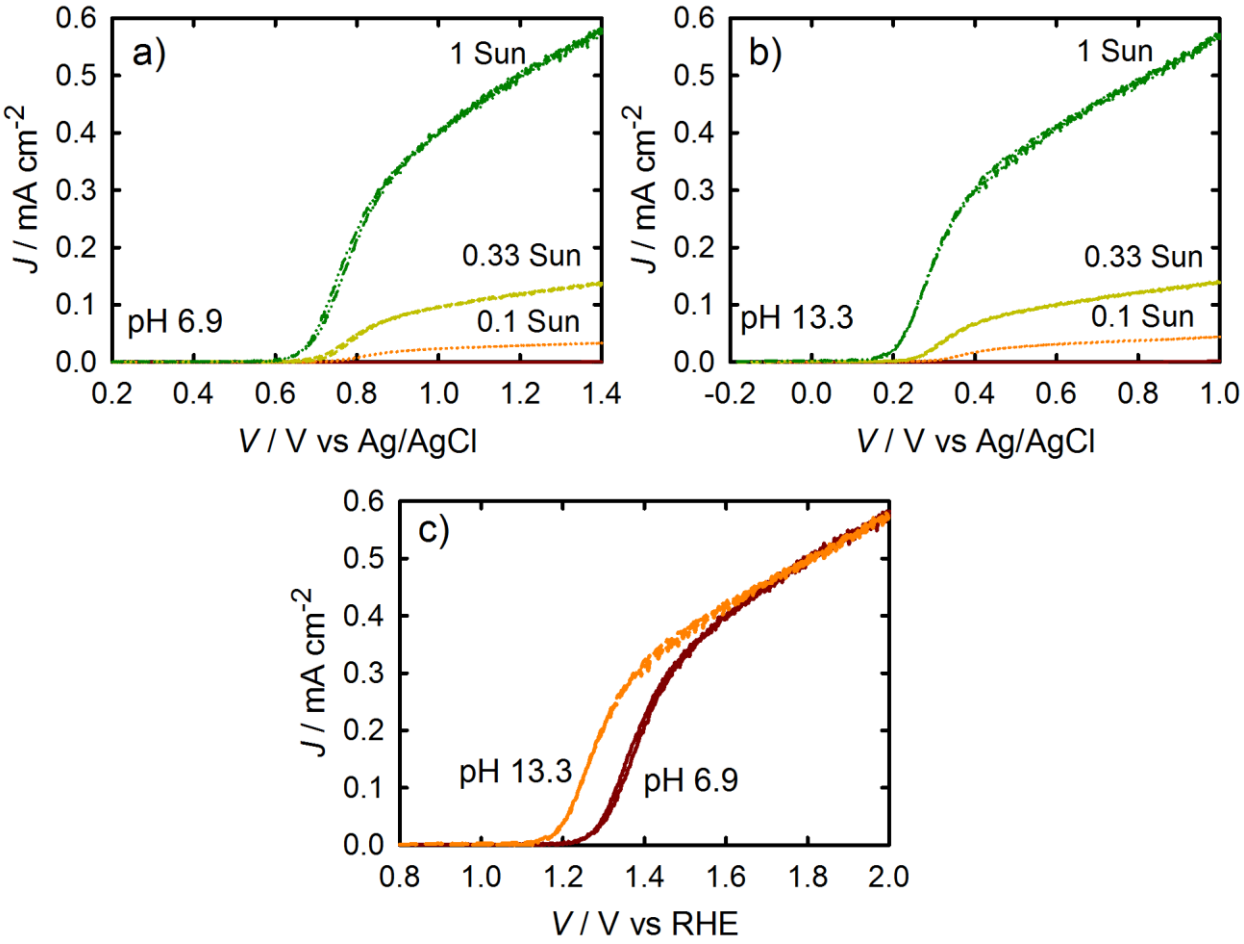

Figure 5-3. *J-V* curves for a 60 nm thick Fe_2O_3 electrode at pH 6.9 (a) and 13.3 (b) under different illumination intensities; dark *J-V* curves are indistinguishable from the x axis on this scale. (c) *J-V* curves measured under 1 sun illumination for electrodes measured at pH 6.9 and pH 13.3 plotted on the RHE scale.

IS measurements were performed over the same potential range as the *J-V* curves, under each light intensity and in the dark, at pH 6.9 and pH 13.3. Representative Nyquist plots under illumination are shown in Figure 5-4. Clearly there are two semicircles apparent in the impedance spectrum. Similar looking impedance spectra have recently been reported for hematite electrodes, and a variety of equivalent circuits put forth interpret these spectra.[3,25] In these analyses, the low frequency semicircle is generally attributed to the

series arrangement of the depletion capacitance of the semiconductor and the Helmholtz capacitance at the electrode surface, and the role of surface states has largely been ignored. The general EC proposed in Figure 5-1b, cannot unambiguously fit the impedance spectra since it cannot discriminate between $R_{ct,bulk}$ and $R_{ct,ss}$. Consequently, two simplifications of this general equivalent circuit have been employed, as shown in Figure 5-1c and 5-1d, which are labeled as 'model 1' and 'model 2' respectively for discussion purposes. In these simplifications, either $R_{ct,ss}$ or $R_{ct,bulk}$ is eliminated. The simplified equivalent circuits are excellent approximations if charge transfer (water oxidation) is dominated by one route, either from the valence band (Figure 5-1c, model 1) or surface states (Figure 5-1d, model 2).

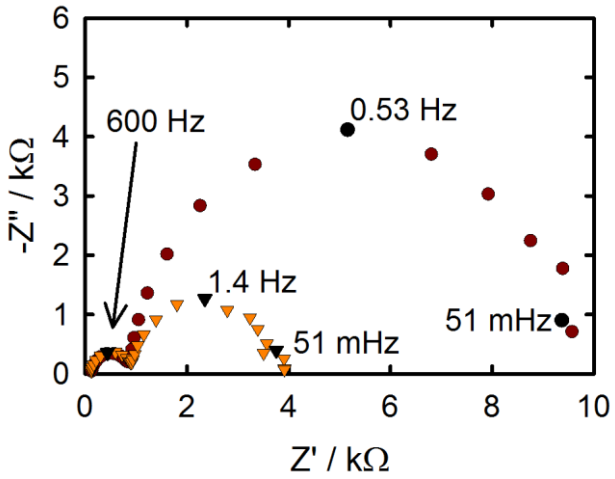

Figure 5-4. Nyquist plots measured at pH 6.9 at 0.65 V (red circles) and 0.70 V (orange triangles) vs. Ag/AgCl under 1 sun conditions. Select frequencies (black symbols) labeled.

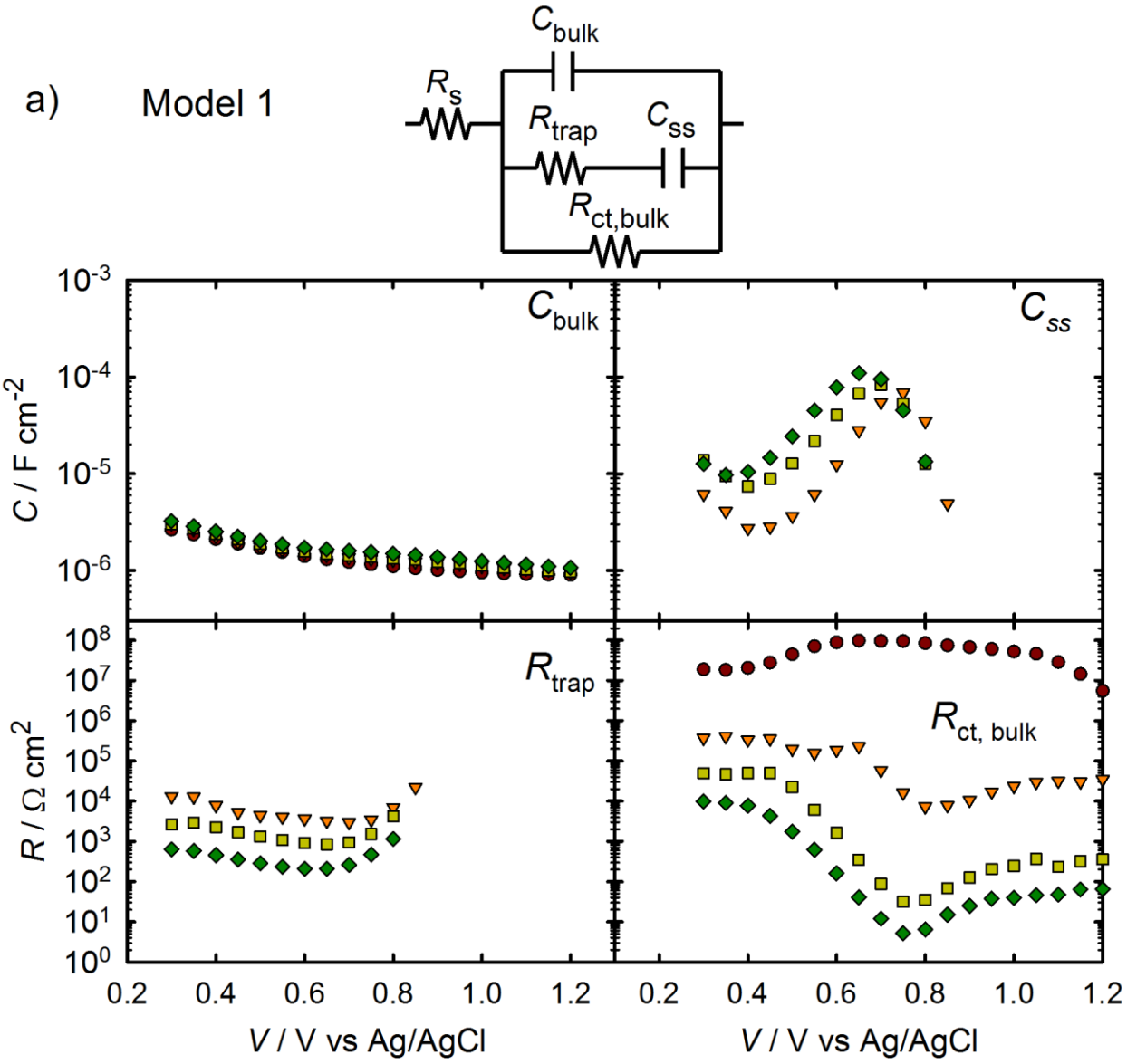

Figure 5-5a. Equivalent circuit parameters obtained from fitting IS data measured at pH 6.9 in the dark (red circles), at 0.1 sun (orange triangles), 0.33 sun (yellow squares), and 1 sun (green diamonds) light intensities measured to model shown in figure 5-1c.

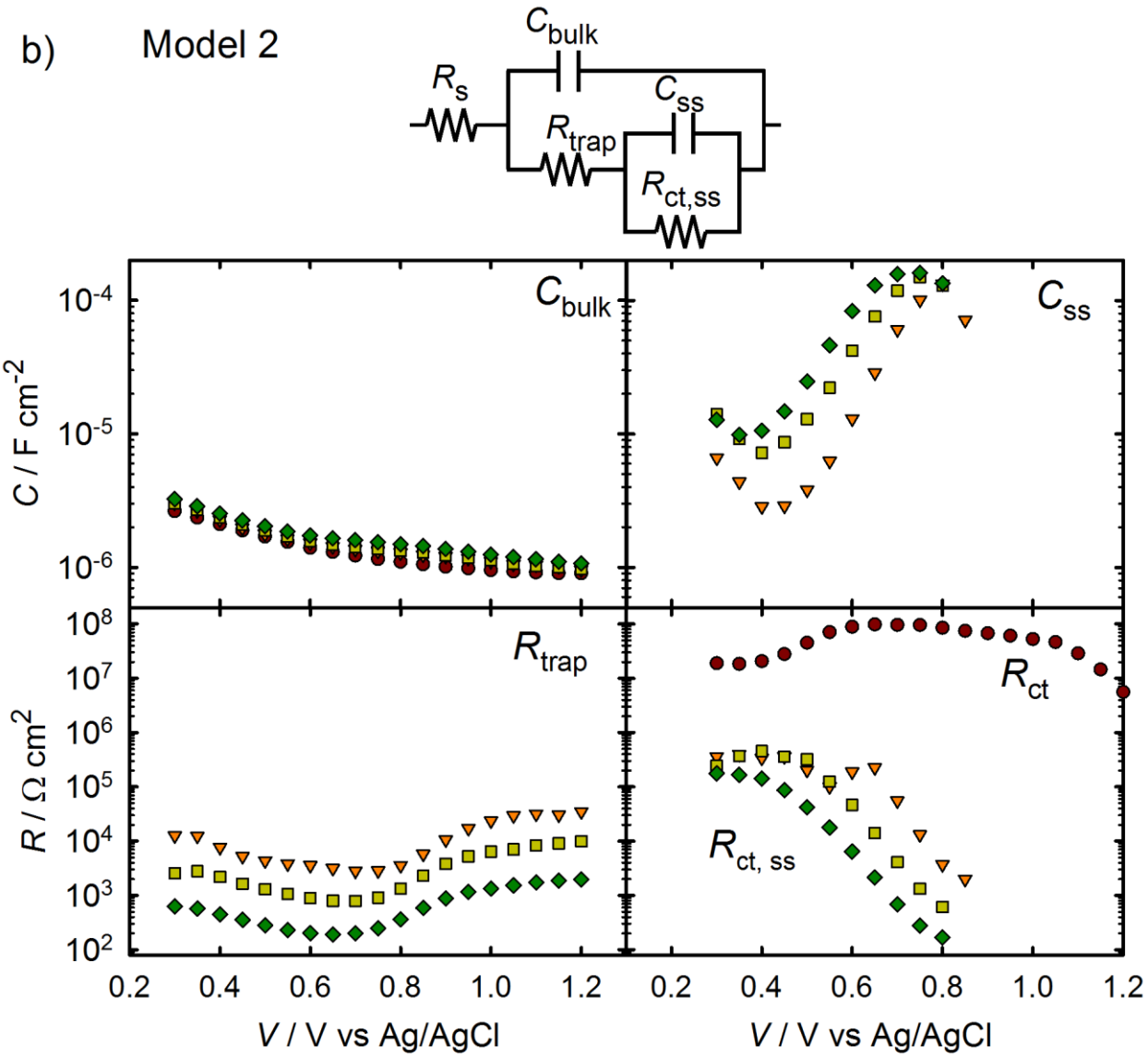

Figure 5-5b. Equivalent circuit parameters obtained from fitting IS data measured at pH 6.9 in the dark (red circles), at 0.1 sun (orange triangles), 0.33 sun (yellow squares), and 1 sun (green diamonds) light intensities measured to model shown in figure 5-1c.

5.4.2 Equivalent Circuit Justification

Both models 1 and 2 were used to fit the EIS data for which the fits can be viewed in figures 5-5a and 5-5b respectively. The fit results using both models produce very similar values for C_{bulk}, and C_{ss}. The evidence for a particular model can be found when comparing

the C_{ss} and charge transfer resistances for both models. Model 1 contains a peak in C_{ss} with a corresponding decrease in $R_{ct,bulk}$. This implies that as more charge is stored in the surface states, charge transfer from the bulk becomes more facile. This is counterintuitive and is in contrast to conclusions made by those who propose direct hole transfer from the valence band as general mechanism since an increased level of trapping in the surface states would be expected to decrease charge transfer from the bulk (increase $R_{ct,bulk}$).[26] A more reasonable mechanism then, is the one described by model 2. As charge is stored in the surface states, as indicated by a peak in C_{ss}, charge transfer from those surface states becomes more facile and the charge transfer resistance from those surface states, $R_{ct,ss}$, is reduced. The physical correlation of surface states and a charge transfer resistance from those surface states agree with the mathematical correlation of C_{ss} and $R_{ct,ss}$ suggesting that model 2 better fits the physical processes. The simplified model, model 2, is therefore the only model employed and discussed in interpreting the IS measurements below. Fits for data measured in pH 13.3 using model 2 can be found in the Appendix which show a similar trend as for pH 6.9.

5.4.3 Fitting Analysis

Figure 5-6 shows a plot of the total resistance, R_{tot} ($R_{tot} = R_S + R_{trap} + R_{ct,trap}$), directly measured by IS compared to that obtained by the derivation of R_{tot} from the *J-V* curves as shown in Equation (5-1). It is observed that both quantities are coincident, within experimental error. The excellent agreement between the R_{tot} calculated from the *J-V* curve and the IS parameters constitutes strong evidence that the factors determining the *J-V* are represented in the IS measurements.

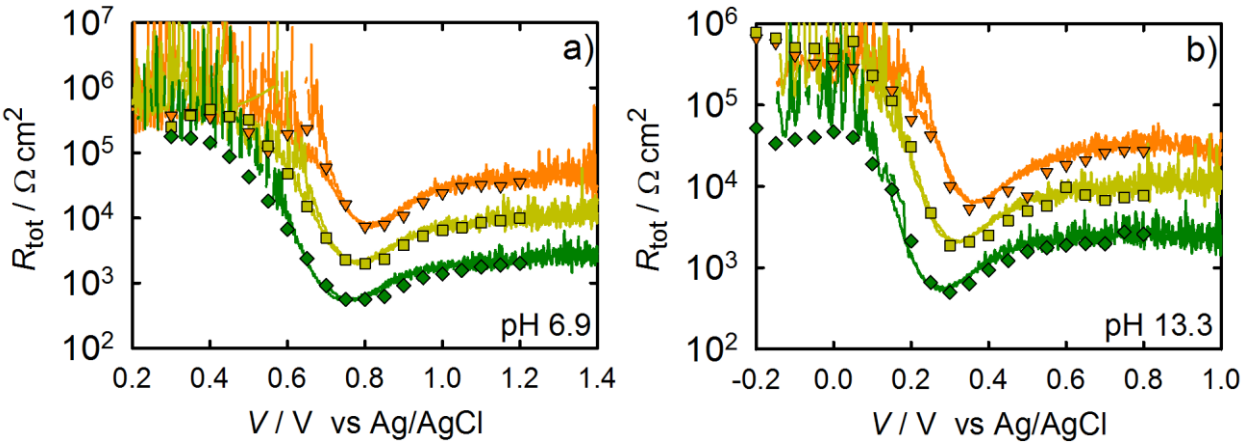

Figure 5-6. R_{tot} values determined by calculating dV/dJ from the J-V curves in Figure 5-4 (lines) as well as the calculated R_{tot} values by adding the resistances associated with charge transfer from IS (symbols) in pH 6.9 (a) and pH 13.3 (b) electrolytes. The colors correspond to different light intensities: 0.1 sun (orange triangles), 0.33 sun (yellow squares), and 1 sun (green diamonds).

The series resistance, R_S, was essentially constant and small, which is consistent with ohmic behavior at the FTO/hematite interface.[27-29] As mentioned above, C_{ss} is correlated to the decrease of $R_{ct,ss}$, where both C_{ss} and $R_{ct,ss}$ shift in concert for the different illumination conditions tested. This clearly indicates that hole transfer for the water splitting reaction takes place through the surface state. We note that similar behavior was obtained for multiple photoelectrodes, including those prepared with different thicknesses. Moreover, the photocurrent onset is also coincident with the charging of this surface state and the decrease of $R_{ct,ss}$, further confirming that charge transfer takes place from this surface state (Figure 5-7).

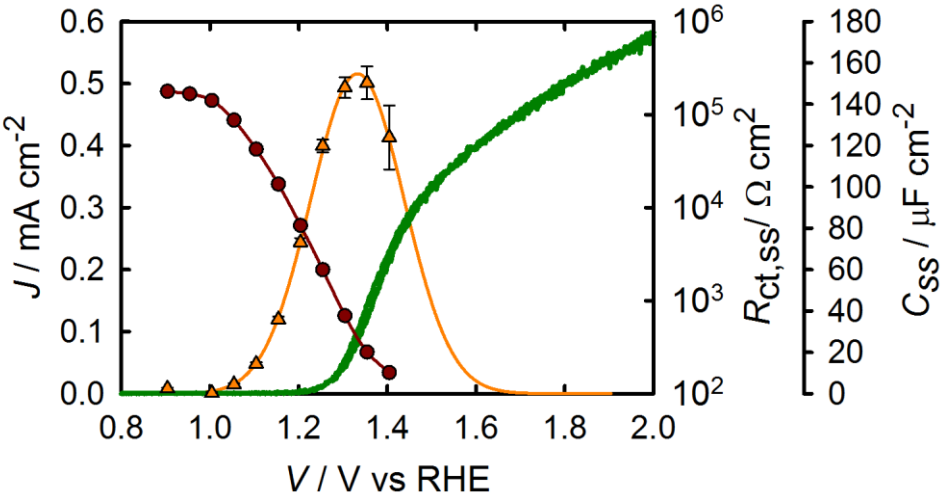

Figure 5-7. *J-V* curve (green solid line), C_{ss} (orange triangles) and $R_{ct,ss}$ (red circles) values obtained for a 60 nm hematite electrode under 1 sun illumination and pH 6.9.

The values for C_{ss} displayed in Figure 5-5 and 5-7 show Gaussian behavior when the sample is illuminated, in good agreement with the existence of a trap state described by equation 5-3. The peak of C_{ss} shifts to more negative potentials with increasing light intensity at pH 6.9. At pH 13.3, however, there is no clear trend in the C_{ss} peak with light intensity. The total magnitude of C_{ss} increases with light intensity at pH 6.9, however at pH 13.3 the magnitude is lower compared to pH 6.9 and essentially constant for the different illumination intensities. Comparing the position of the C_{ss} peaks at both pH values, there is a shift by approximately 59 mV/pH unit, demonstrating Nernstian behavior. The C_{ss} values can be used to calculate the energetic distribution of the density of states, $g(E_{Fn})$ or DOS, by [11,30]

$$C_{ss}(E) = q\, g(E_{Fn}) \tag{5-4}$$

The calculated DOS for hematite at pH 6.9 and 13.3 can be seen in Figure 5-8a plotted vs. Ag/AgCl under different light intensities. A plot of the DOS vs. RHE under 1 sun is also shown in Figure 5-8b. The formal potential for water oxidation (1.23 V vs. RHE) is also included. It is worth noting that the energetic distribution of the density of trap states peaks are very close to the formal potential of the oxygen evolution reaction, particularly at pH 13.3. This result suggests an equilibration of trap state energy and hole accepting species in the electrolyte. Since the water oxidation reaction involves the participation of four holes,[31] some complications in interpretation arise from the fact that holes have to be stored in intermediate states.[3]

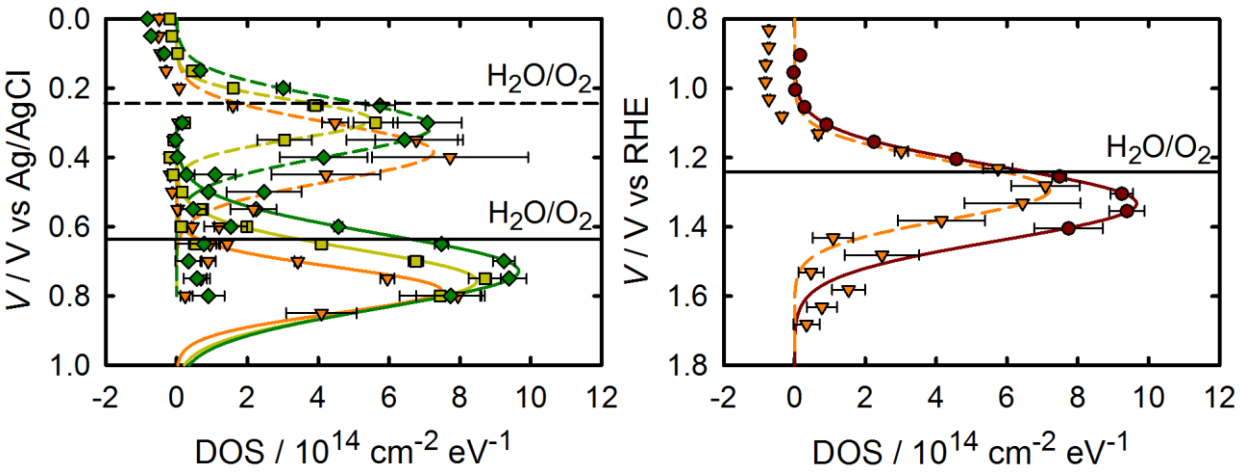

Figure 5-8. a) DOS as a function of potential for pH 6.9 (solid lines) and pH 13.3 (dashed lines) for 0.1 sun (orange triangles), 0.33 sun (yellow squares), and 1 sun (green diamonds) light intensities. b) DOS curves under 1 sun illumination vs. the RHE reference.

The values for C_{bulk} do not show a significant trend in the logarithmic representation of Figure 6. The values of C_{bulk} were fit using the Mott Schottky equation (eq. 5-2). The resultant Mott-Schottky plots are displayed in Figures 5-9a for pH 6.9 and 5-9b for pH 13.3.

The calculation of the flatband potential, E_{fb}, and the dopant density, N_D, for different light intensities, can be seen in Table 5-1. The dopant density, N_D is practically constant for all the tested conditions, in the range 3×10^{18} - 6×10^{18} cm^{-3} in good correspondence with previous values reported for this material.[20] The identity of these dopants has not been confirmed, due to the very small amount of impurity needed to produce these modest doping levels in the thin films studied. The typical assignment of oxygen vacancies for metal oxide electrodes, which can be related to the annealing and cooling of iron oxide independent of preparation method, may be applicable.[29,32] A recent report on the mechanism of the ALD of hematite suggests the dopants are due to a trace Nb impurity in the ALD reactor; thus the n-type doping may be due to Nb or other residual metal contamination in our ALD reactor.[33] In any case, we consistently obtain these doping levels, which is typical of hematite and other metal oxide electrodes.[28,29]

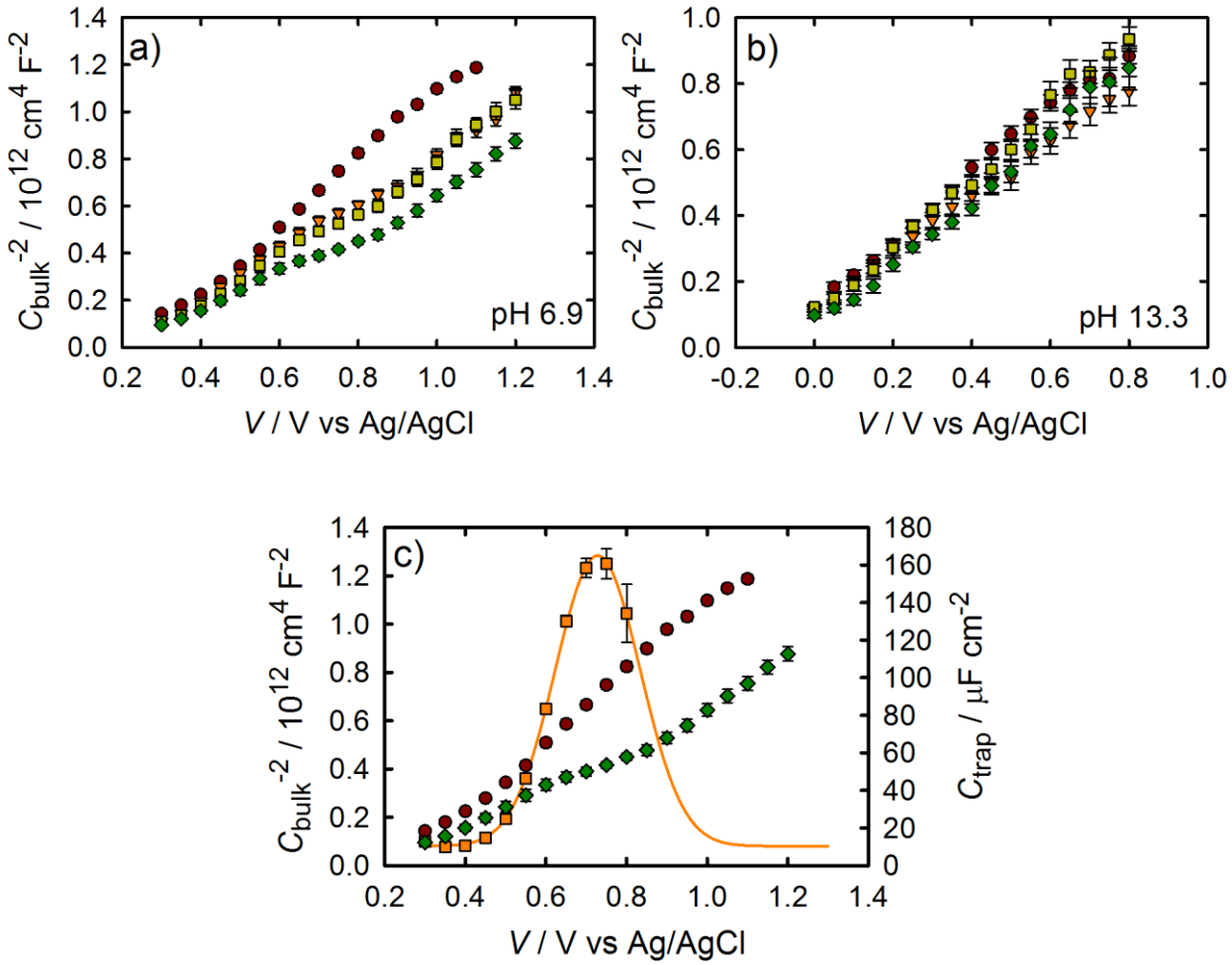

Figure 5-9. (a) MS plot at pH 6.9 under 0.1 (orange triangles), 0.33 (yellow squares), and 1 (green diamonds) sun illumination and in the dark (red circles). (b) Same as in (a) but for pH 13.3. (c) Mott Schottky plots at pH 6.9 in the dark (red circles) and under 1 sun (green diamonds). A plot of the trap state capacitance, C_{ss}, (orange squares) is superimposed to show the effect of Fermi level pinning.

At pH 6.9, there is an obvious positive shift in the Mott Schottky plot under illumination; the shift increases with light intensity. This behavior is consistent with surface state charging as described by Memming et. al.[8] This flat region in the Mott Schottky plot under illumination from approximately 0.6 V to 0.9 V vs. Ag/AgCl at pH 6.9 corresponds to

the peak of the C_{ss} measured under illumination. Figure 5-9c shows a plot of C_{ss} superimposed on the Mott Schottky plots at pH 6.9. This is a clear example of Fermi level pinning. At pH 13, the magnitude of the surface state capacitance is lower compared to pH 6.9 (Appendix). Consequently, a lower positive shift of the flat band potential can be anticipated by charging the surface state. This is indeed observed in Figure 5-9b. In quantitative terms, the shift of the flat band potential (ΔE_{fb}) can be related to that derived from the charging of the surface states, which is calculated from $\Delta V_{charging} = Q_{tot} / C_H$. The total charge Q_{tot} is obtained by integration of C_{ss} with voltage as:

$$Q_{tot} = \int C_{ss} dV \tag{5-5}$$

In Table 5-2, the values of Q_{tot} are listed for the different pH and illumination intensities tested. While there is good qualitative agreement between ΔE_{fb} and $\Delta V_{charging}$, good quantitative agreement is obtained only when the value of Helmholtz capacitance is $C_H = 2\times10^{-4}$ F cm^{-2} (Table 5-2). We note that this is an extremely high value for a Helmholtz capacitance.

Table 5-1. Parameters derived from the Mott Schottky plots under illumination. Calculations assume k=32.

	pH 7		pH 13.3	
Illumination / Sun	E_{fb} (V vs Ag/AgCl)	N_D (cm^{-3})	E_{fb} (V vs Ag/AgCl)	N_D (cm^{-3})
0 (Randle circuit)	0.25	3×10^{18}	-0.22	4.9×10^{18}
0.1	0.33	3.6×10^{18}	-0.20	5.8×10^{18}
0.33	0.38	3.4×10^{18}	-0.13	4.7×10^{18}
1	0.45	3.8×10^{18}	-0.07	4.8×10^{18}

Table 5-2. Correlation of the voltage shift in flat-band potential ΔV_{FB} and that calculated from the charging of the surface state $\Delta V_{charging}$ (with $C_H=2\times10^{-4}$ $F\cdot cm^{-2}$).

	pH 7			pH 13.3		
	Q_{tot} ($C\cdot cm^{-2}$)	ΔV_{FB} (mV)	$\Delta V_{charging}$ (mV)	Q_{tot} ($C\cdot cm^{-2}$)	ΔV_{FB} (mV)	$\Delta V_{charging}$ (mV)
0.1 sun	1.97×10^{-5}	76	98	2.42×10^{-5}	14	121
0.33 sun	3.05×10^{-5}	130	153	1.23×10^{-5}	82	61.4
1 sun	4.08×10^{-5}	197	204	2.42×10^{-5}	147	121

5.5 Conclusions

Impedance Spectroscopy was employed to investigate the photoelectrochemical behavior of hematite electrodes under water splitting conditions. The impedance spectra are characterized by the existence of a prominent surface state, which follows classical behavior in terms of capacitive features and the dependence on voltage and illumination intensity.[6] The strong correlation between the C_{ss} peak with the decrease in $R_{ct,ss}$, along with the photocurrent onset as illustrated in Figure 5-7 clearly indicates that the hole-transfer step

leading to water oxidation takes place from surface states, and not directly from valence band holes. This result represents an important step in understanding the mechanism of water oxidation at metal oxide electrodes. This conclusion is however in stark contrast to conclusions made by those who see an improvement in the water oxidation performance as a result of adding surface state passivating layers. According to our study, true surface state passivation would hinder water oxidation.[25] It is a goal of ongoing work in our lab to reconcile these different interpretations.

The details of the mechanism of water oxidation with metal oxide electrodes are still not clear, however it is generally believed to proceed from one or more surface hydroxyl (M-OH_X) intermediate states formed from hole transfer to a surface coordinated water and a concomitant deprotonation step.[34-37] We therefore suggest that the surface state capacitance that builds up during water photo-oxidation is due to a M-OH_X intermediate. It is well known that metal oxide electrodes in contact with aqueous solutions have hydroxy-terminated surfaces; it is the protonation/deprotonation equilibrium of these M-OH_X sites which gives rise to the pH-dependent variation of the band energies of metal oxide electrodes [28,38] in good agreement with the Nernstian behavior of the photoelectrodes observed in the present study. This could additionally account for the somewhat different IS behavior observed for water oxidation in pH 6.9 and 13.3 electrolytes since the surface termination chemistry would be different. More work is needed to clarify these points, however, which is the subject of ongoing research in our labs.

5.6 Acknowledgements

TWH acknowledges the Donors of the American Chemical Society Petroleum Research Fund (#51099-DNI10) for support of this research. JB acknowledges support by projects from

Ministerio de Ciencia e Innovación (MICINN) of Spain (Consolider HOPE CSD2007-00007), and Generalitat Valenciana (PROMETEO/2009/058). SG acknowledges support by MICINN of Spain under the Ramon y Cajal programme.

APPENDIX

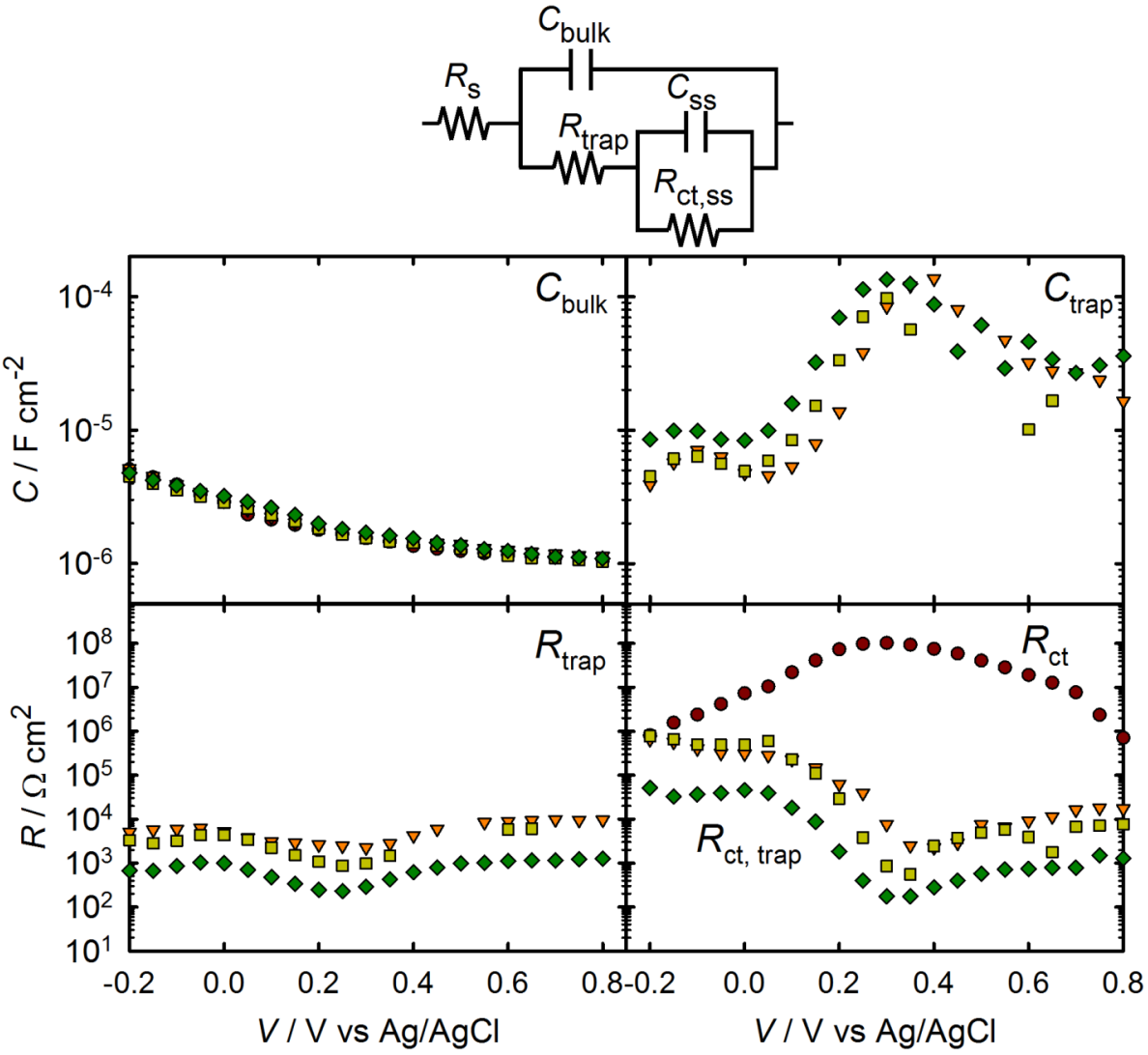

.

Figure A5-1. Equivalent circuit parameters obtained from fitting IS data measured at pH 13.3 in the dark (red circles), at 0.1 sun (orange triangles), 0.33 sun (yellow squares), and 1 sun (green diamonds) light intensities.

REFERENCES

REFERENCES

1. Barroso, M.; Cowan, A. J.; Pendlebury, S. R.; GraÌˆtzel, M.; Klug, D. R.; Durrant, J. R. *J. Am. Chem. Soc.* **2011**, *133*, 14868-14871.

2. Pendlebury, S. R.; Barroso, M.; Cowan, A. J.; Sivula, K.; Tang, J. W.; Gratzel, M.; Klug, D.; Durrant, J. R. *Chem. Commun.* **2011**, *47*, 716-718.

3. Wijayantha, K. G. U.; Saremi-Yarahmadi, S.; Peter, L. M. *Phys. Chem. Chem. Phys.* **2011**, *13*, 5264-5270.

4. Dotan, H.; Sivula, K.; Gratzel, M.; Rothschild, A.; Warren, S. C. *Energy Environ. Sci.* **2011**, *4*, 958-964.

5. Frese, K. W.; Morrison, S. R. *J. Electrochem. Soc.* **1979**, *126*, 1235-1241.

6. Allongue, P.; Cachet, H. *J. Electrochem. Soc.* **1985**, *132*, 45-52.

7. Lincot, D.; Vedel, J. *J. Electroanal. Chem.* **1987**, *220*, 179-200.

8. Kelly, J. J.; Memming, R. *J. Electrochem. Soc.* **1982**, *192*, 730-738.

9. Murphy, A. B.; Barnes, P. R. F.; Randeniya, L. K.; Plumb, I. C.; Grey, I. E.; Horne, M. D.; Glasscock, J. A. *Int. J. Hydrogen Energy*, **2006**, *31*, 1999-2017.

10. Glasscock, J. A.; Barnes, P. R. F.; Plumb, I. C.; Bendavid, A.; Martin, P. J. *Thin Solid Films*, **2008**, *516*, 1716-1724.

11. Bisquert, J. *Phys. Chem. Chem. Phys.* **2003**, *5*, 5360-5364.

12. Bisquert, J. *Phys. Chem. Chem. Phys.* **2008**, *10*, 49-72.

13. Hoffmann, P. M.; Oskam, G.; Searson, P. C. *J. Appl. Phys.* **1998**, *83*, 4309.

14. Scurtu, R.; Ionescu, N. I.; Lazarescu, M.; Lazarescu, V. *Phys. Chem. Chem. Phys.* **2009**, *11*, 1765-1770.

15. Reichman, J. *Appl. Phys. Lett.* **1980**, *36*, 574-577.

16. Bisquert, J. *J. Electroanal. Chem.* **2010**, *646*, 43–51.

17. Vanmaekelbergh, D.; Cardon, F. *J. Phys. D: Appl. Phys.* **1986**, *19*, 643-656.

18. Gartner, W. W. *Phys. Rev.* **1959**, *116*, 84-87.

19. Salvador, P. *J. Phys. Chem. B*, **2001**, *105*, 6128-6141.

20. Klahr, B. M.; Martinson, A. B. F.; Hamann, T. W. *Langmuir,* **2011**, *27*, 461-468.

21. Libera, J. A.; Hryn, J. N.; Elam, J. W. *Chem. Mater.* **2011**, *23*, 2150-2158.

22. Anderman, M.; Kennedy, J. H. *J. Electrochem. Soc.* **1984**, *131*, 1565-1570.

23. Klahr, B. M.; Hamann, T. W. *J. Phys. Chem. C,* **2011**, *115*, 8393-8399.

24. Launay, J. C.; Horowitz, G. *J. Cryst. Growth*, **1982**, *57*, 118-124.

25. Le Formal, F.; Tetreault, N.; Cornuz, M.; Moehl, T.; Gratzel, M.; Sivula, K. *Chem. Sci.* **2011**, *2*, 737-743.

26. Le Formal, F.; Sivula, K.; Grätzel, M. *J. Phys Chem. C,* **2012**, *116,* 26707-26720.

27. Glasscock, J. A.; Barnes, P. R. F.; Plumb, I. C.; Savvides, N. *J. Phys. Chem. C,* **2007**, *111*, 16477-16488.

28. Morrison, S. R. *Electrochemistry at Semiconductor and Oxidized Metal Electrodes*; Plenum: New York, 1980.

29. Finklea, H. O. *Semiconductor Electrodes*; Elsevier: Amsterdam, 1988.

30. Fabregat-Santiago, F.; Garcia-Belmonte, G.; Mora-Sero, I.; Bisquert, J. *Phys. Chem. Chem. Phys.* **2011**, *13*, 9083-9118.

31. Tang, J. W.; Durrant, J. R.; Klug, D. R. *J. Am. Chem. Soc.* **2008**, *130*, 13885-13891.

32. Gardner, R. F. G.; Sweett, F.; Tanner, D. W. *J. Phys. Chem. Solids* **1963**, *24*, 1183-1196.

33. Martinson, A. B. F.; DeVries, M. J.; Libera, J. A.; Christensen, S. T.; Hupp, J. T.; Pellin, M. J.; Elam, J. W. *J. Phys. Chem. C,* **2011**, *115*, 4333-4339.

34. Cook, T. R.; Dogutan, D. K.; Reece, S. Y.; Surendranath, Y.; Teets, T. S.; Nocera, D. G. *Chem. Rev.* **2010**, *110*, 6474-6502.

35. Conway, B. E.; Tilak, B. V. *Advances in Catalysis,* **1992**, *38*, 1-147.

36. Montoya, J. F.; Peral, J.; Salvador, P. *ChemPhysChem,* **2011**, *12*, 901-907.

37. Salvador, P. *J. Electrochem. Soc.* **1981**, *128*, 1895-1900.

38. Hamann, T. W.; Lewis, N. S. *J. Phys. Chem. B,* **2006**, *110*, 22291-22294.

Chapter 6:

The Nature of Surface States of Water Oxidation at Hematite Electrodes through the Comparison with a Fast Redox Shuttle

The results in this chapter were published in:

Electrochemical and photoelectrochemical investigation of water oxidation with hematite electrodes, Benjamin M. Klahr, Sixto Gimenez, Francisco Fabregat-Santiago, Juan Bisquert and Thomas W. Hamann. *Energy & Environmental Science*, **2012**, *5*, 7626-7636. Reproduced by permission of The Royal Society of Chemitry.

6.1 Abstract

Atomic layer deposition (ALD) was utilized to deposit uniform thin films of hematite (α-Fe_2O_3) on transparent conductive substrates for photocatalytic water oxidation studies. Comparison of the oxidation of water to the oxidation of a fast redox shuttle allowed for new insight in determining the rate limiting processes of water oxidation at hematite electrodes. It was found that an additional overpotential is needed to initiate water oxidation compared to the fast redox shuttle. A combination of electrochemical impedance spectroscopy, photoelectrochemical and electrochemical measurements were employed to investigate the cause of the additional overpotential. It was found that photogenerated holes initially oxidize the electrode surface under water oxidation conditions, which is attributed to the first step in water oxidation. A critical number of these surface intermediates need to be generated in order for the subsequent hole-transfer steps to proceed. At higher applied potentials, the behavior of the electrode is virtually identical while oxidizing either water or the fast redox shuttle; the slight discrepancy is attributed to a shift in potential associated with Fermi level pinning by the surface states in the absence of a redox shuttle. A water oxidation mechanism is proposed to interpret these results.

6.2 Introduction

There have been several recent studies, employing a variety of techniques, to understand the limited nature of the water splitting reaction with hematite photoelectrodes. For example, Durrant and co-workers used transient absorption (TA) spectroscopy to monitor the evolution of surface-trapped holes and acorrelated a long-lived trapped hole lifetime with the onset of photocurrent.[1-4] One limitation of TA, however, is the difficulty with assigning the energetics of the system, e.g. the position of the relevant surface states. Peter and co-workers recently used IS and intensity modulated photocurrent spectroscopy (IMPS) to study the kinetics of water oxidation at hematite electrodes which also pointed out the crucial role of surface-trapped holes.[5-7] We also recently employed IS at different conditions of voltage, light intensity and electrolyte pH to investigate the main steps involved in water oxidation.[8] Importantly, a general physical model, which includes the existence of a surface state at the semiconductor/liquid interface where holes accumulate, was established. These surface states were proposed to be intimately involved in the water oxidation mechanism, indicated by a build-up in charge which is concomitant with a decrease in charge transfer resistance as applied potentials become increasingly anodic. To investigate these surface states further, we compare the PEC behavior of hematite with ideally-behaving hole collector, $[Fe(CN)_6]^{3-/4-}$, with the behavior under water oxidation conditions. This comparison allows for isolation of the water oxidation steps from the behavior of the bulk hematite electrode. We employed IS and photoelectrochemical measurements to determine the main steps involved in water oxidation. From these combined results we propose a mechanism of water oxidation on hematite electrode surfaces.

6.3 Experimental

Thin films of iron oxide were deposited on fluorine-doped tin oxide (FTO) coated glass substrates (Hartford Glass, 12 Ω cm^{-2}) by atomic layer deposition (Savannah 100, Cambridge Nanotech Inc.) using a procedure described previously.[8] Films were prepared by 1,200 ALD cycles and measured to be ~60 nm by absorption measurements (Perkin Elmer, Lambda 35 with a Labsphere integrating sphere) corrected for reflection as described previously, as well as ellipsometry measurements (Horiba Jobin Yvon, Smart-SE). Films were determined to be hematite by Raman Spectroscopy and XRD measurements in a previous publication.[9]

Hematite electrodes were masked with a 60 μm Surlyn film (Solaronix) with a 0.25 cm^2 hole to define the active area and to prevent scratching of the thin films. Surlyn films were adhered to the electrodes by heating to 120° C. The hematite electrodes were examined in contact with aqueous solutions buffered to pH 6.9 using a 0.1 M phosophate buffer, with 200 mM KCl as a supporting electrolyte. The pH was determined with Fisher Scientific Accumet pH meter. Electrolytes containing the $[Fe(CN)_6]^{3-/4-}$ redox couple consisted of 200 mM $K_4Fe(CN)_6$ and 20 mM $K_3Fe(CN)_6$. The protected hematite electrodes were clamped to a custom made glass electrochemical cell. A homemade saturated Ag/AgCl electrode was used as a reference electrode and high surface area platinum mesh was used as the counter electrode. All potentials were converted to the reversible hydrogen electrode (RHE) scale by the equation $V_{RHE} = V_{Ag/AgCl} + 0.197 + pH(0.059)$. Impedance spectroscopy and photoelectrochemical measurements were made with an Eco Chemie Autolab potentiostat coupled with Nova electrochemical software. Impedance data were gathered using a 10 mV amplitude perturbation

of between 10,000 and 0.01 Hz. Data were fit using Zview software (Scribner Associates). The light source was a 450 W Xe arc lamp (Horiba Jobin Yvon). An AM 1.5 solar filter was used to simulate sunlight at 100 mW cm^{-2} (1 sun). Neutral density filters were used to adjust the intensity to 33 mW cm^{-2} (0.33 Sun) and 10 mW cm^{-2} (0.1 Sun). All photoelectrochemical measurements were performed by shining light on the hematite electrode through the FTO substrate such that there was no competitive light absorption from the adjacent electrolyte. Light chopped *J-V* curves were measured at a rate of 75 mV/s. The light was chopped using a computer controlled ThorLabs solenoid shutter which was set to activate every 266 ms such that the light was turned on or off every 20 mV. Steady state *J-V* curves were measured at a scan rate of 20 mV/s. Cyclic voltammogram surface state measurements were performed by applying a potential of 2.0 V vs RHE under 1 sun illumination for 60 seconds, and then scanning over a potential range in the dark.

6.4 Results

6.4.1 Steady State Behavior

Steady state *J-V* curves of a typical thin film hematite electrode immersed in an aqueous electrolyte (H_2O) and an aqueous electrolyte containing the $[Fe(CN)_6]^{3-/4-}$ redox couple can be seen in figure 6-1. We have recently shown that the *J-V* response of hematite thin film electrodes in contact with the $[Fe(CN)_6]^{3-/4-}$ redox couple is limited by the fraction of holes that reach the semiconductor/liquid interface which is determined by the potential drop across the electrode.[9-11] In other words, the surface-hole collection efficiency by $[Fe(CN)_6]^{4-}$ is essentially unity.[10] Since the same film is used in the *J-V* measurements shown in figure 6-1, in aqueous

electrolytes buffered to the same pH under the same illumination conditions, the discrepancy in photocurrent density and onset potential can be attributed to differences in the surface-hole collection efficiency under H_2O oxidation conditions (in the absence of a fast hole collector such as $[Fe(CN)_6]^{4-}$). The details underlying this discrepancy are discussed below.

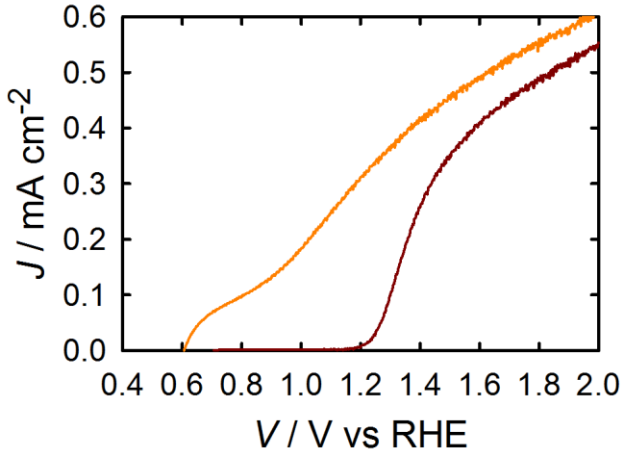

Figure 6-1. Steady state *J-V* curve of a hematite electrode in contact with a H_2O (red curve) and $[Fe(CN)_6]^{3-/4-}$ (orange curve) electrolyte.

6.4.2 Electrochemical Impedance Spectroscopy

IS measurements were also performed for nominally identical hematite electrodes under the same conditions as the *J-V* measurements with varying illumination intensities. Nyquist plots resulting from measurements in each electrolyte under 1 sun illumination at 1.3 V vs RHE and at 1.6 V vs RHE are displayed in figure 6-2a and 6-2b, respectively. At 1.3 V vs RHE, two clear semicircles are visible for the H_2O electrolyte. A full equivalent circuit representing the hematite/liquid junction is shown in figure 6-3a. The equivalent circuit elements include a space-charge capacitance of the bulk hematite, C_{bulk}, surface state capactitance, C_{ss}; the

resistances consist of a series resistance, R_S, a resistance which represents the trapping of charge in the surface states, R_{trap}, a charge transfer resistance from the surface states to solution, $R_{ct,ss}$, and a charge transfer resistance from the valence band to solution, $R_{ct,bulk}$. To allow unambiguous fitting of the impedance data to the equivalent circuit in figure 6-3a, $R_{ct,bulk}$ was removed for the case of water oxidation, which yielded the simplified equivalent circuit in figure 6-3b, for reasons that have been discussed in chapter 5.[8] At potentials positive of ~1.45 V, the impedance spectra for water oxidation loses the low frequency semicircle and becomes a single semicircle; in this case the simple Randle's circuit, shown in figure 6-3c, is used to fit these impedance spectra. Only one semicircle is visible at all potentials and light conditions measured with the $[Fe(CN)_6]^{3-/4-}$ electrolyte, therefore a simple Randle's circuit is also used to fit these impedance spectra.

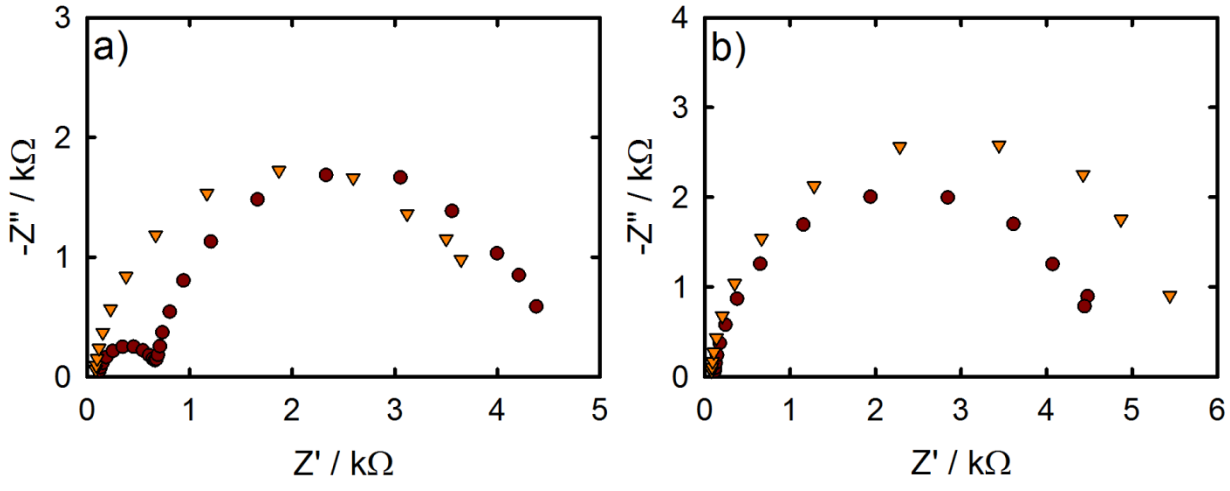

Figure 6-2. Nyquist plots for IS data measured under 1 sun illumination for H_2O (red circles) and $[Fe(CN)_6]^{3-/4-}$ (orange triangles) electrolytes at (a) 1.3 V vs. RHE and (b) 1.6 V vs. RHE.

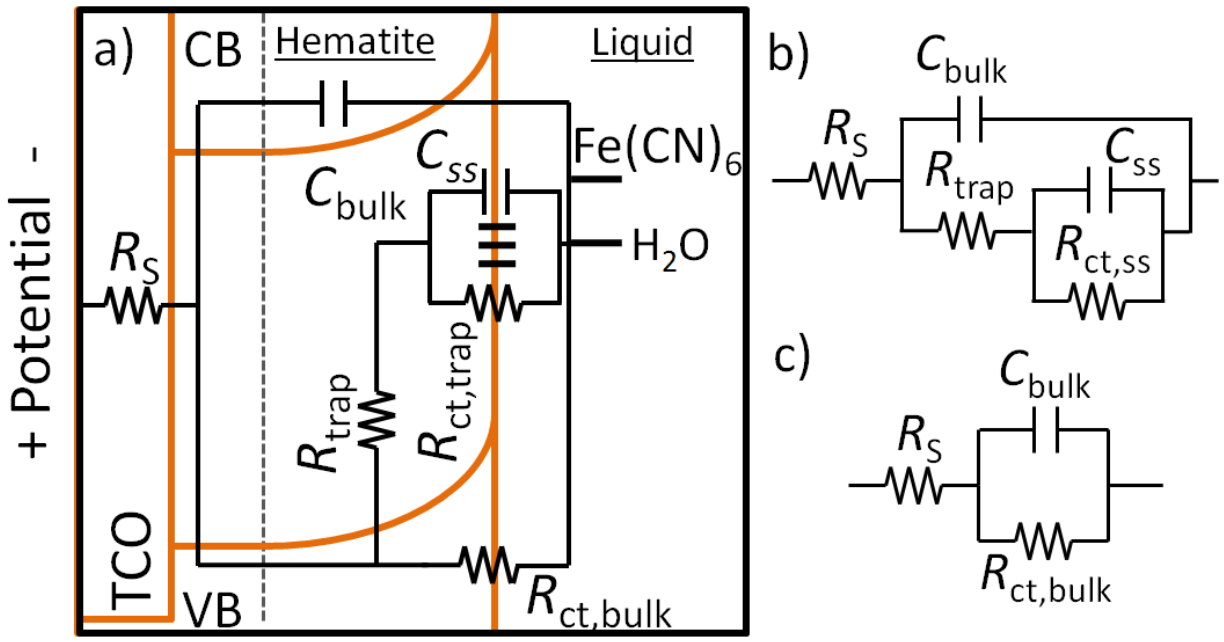

Figure 6-3. a) Full equivalent circuit used to conceptualize hematite-liquid junctions. b) Simplified model used to fit IS data for Nyquist plots that show 2 semicircles. c) Simplified model used to fit IS data for Nyquist plots that show 1 semicircle.

Results from fitting the impedance spectra to the appropriate equivalent circuits described above can be seen in figure 6-4 (additional fitting results not discussed are provided in the Appendix). Figure 6-4a shows a Gaussian distribution of C_{ss} in the H_2O electrolyte, which shifts to more negative potentials with increasing light intensity; this behavior was described previously.[8] The C_{ss} peak corresponds with a decrease in $R_{ct,ss}$ (Fig 6-4b), which indicates that interfacial charge transfer (water oxidation) occurs as a result of charging of these surface states.[8] With $[Fe(CN)_6]^{3-/4-}$ in solution, however, the charge transfer resistance is essentially constant over the measured potential range for a given light intensity as shown in figure 6-4c.

The absence of a measureable surface state capacitance and absence of a dip in the charge transfer resistance suggests that photooxidaiton of $[Fe(CN)_6]^{4-}$ does not involve surface states and can be described as a simple outersphere hole collection process from the valence band. In both electrolytes, there is an obvious decrease of the charge transfer resistance with increasing light intensity which is attributed to a concomitant increase in the number of photogenerated valence band holes with light intensity.

Mott Schottky plots were created from the derived C_{bulk} values from both H_2O and $[Fe(CN)_6]^{3-/4-}$ electrolytes in the dark and under 1 sun illumination conditions, which are shown in figure 6-4d. The Mott Schottky plots measured under illumination for water oxidation conditions show a significant horizontal shift compared to the dark, which is an example of Fermi level pinning.[8,12] The Mott Schottky plots with the $[Fe(CN)_6]^{3-/4-}$ electrolyte are identical in the dark and under illumination, however, further indicating that the surface states do not play a role in $[Fe(CN)_6]^{4-}$ oxidation. In addition, the impedance spectra and Mott Schottky plots are essentially identical for the H_2O and $[Fe(CN)_6]^{3-/4-}$ electrolytes in the dark, which indicates the surface states are only active under illumination. The details of the surface states are described further below.

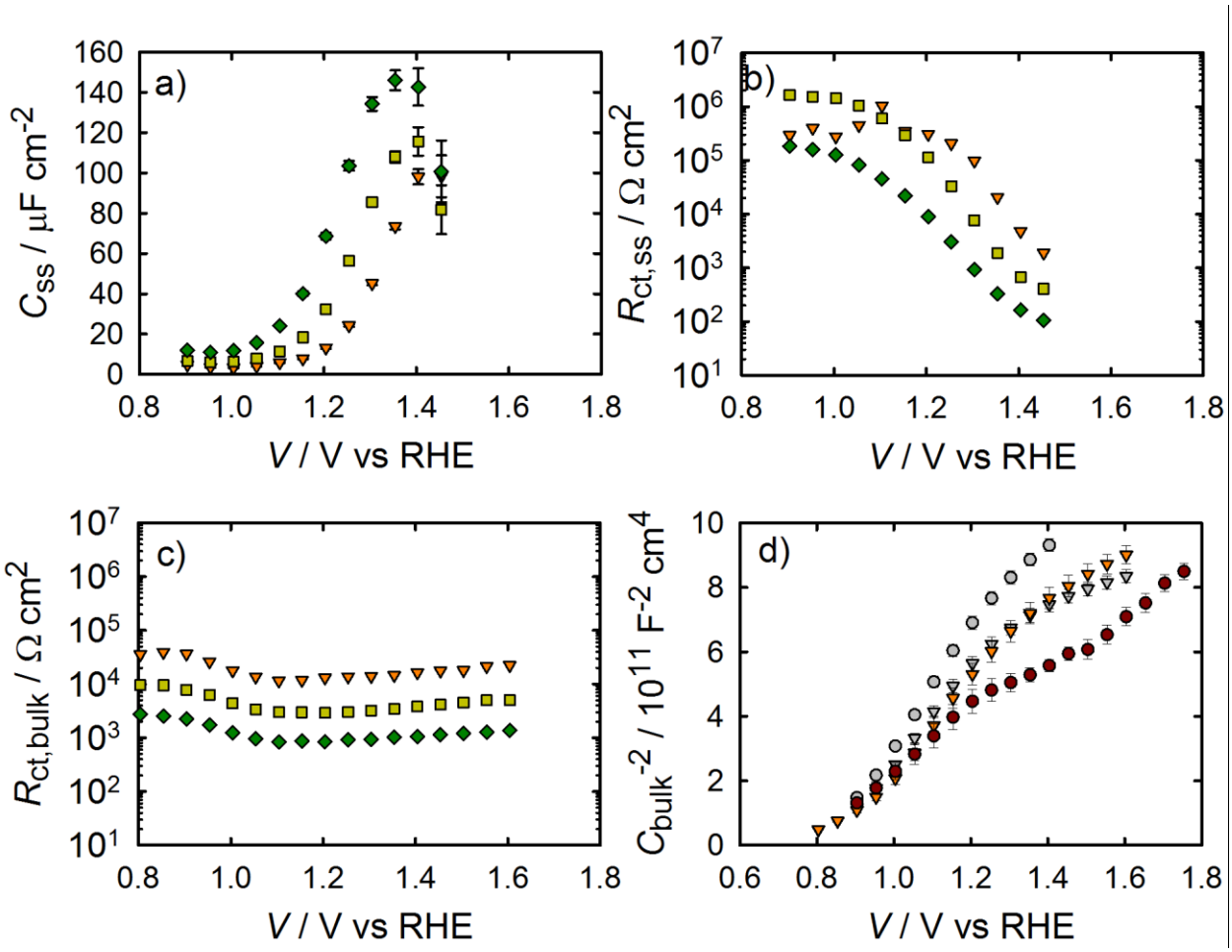

Figure 6-4. Equivalent circuit parameters obtained from fitting IS data for a hematite electrode in contact with H_2O (a and b) and $[Fe(CN)_6]^{3-/4-}$ (c) electrolytes under 0.1 sun (orange triangles), 0.33 sun (yellow squares) and 1 sun (green diamonds) illumination. d) Mott Schottky plots calculated from C_{bulk} values determined from fitting the impedance spectra for H_2O (circles) and $[Fe(CN)_6]^{3-/4-}$ (triangles) electrolytes in the dark (grey) and under 1 sun illumination (colored).

The total resistance, R_{tot} was calculated from the IS fittings ($R_{tot} = R_S + R_{trap} + R_{ct,ss}$ for H_2O oxidation and $R_{tot} = R_S + R_{ct,bulk}$ for $[Fe(CN)_6]^{4-}$ oxidation) and was compared to the resistance calculated from the *J-V* curves where $R_{tot}=dV/dJ$.[8] A plot of R_{tot} calculated from both methods for both H_2O and $[Fe(CN)_6]^{3-/4-}$ electrolytes can be seen in figure 6-5 under 1 sun illumination. The agreement between the calculated R_{tot} from the IS and *J-V* curves shows that all of the resistances which determin the *J-V* curve are represented in the impedance measurements. At potentials negative of the photocurrent onset potential for H_2O oxidation, R_{tot} is found to be approximately two orders of magnitude higher compared to R_{tot} for the oxidation of $[Fe(CN)_6]^{4-}$. This large resistance is consistent with the lack of photocurrent density at these potentials. At around 1.2 V, the R_{tot} due to water oxidation drops coincidently with the initiation of photocurrent. Interestingly, R_{tot} for both H_2O and $[Fe(CN)_6]^{3-/4-}$ electrolytes become equal at about 1.6 V vs RHE, suggesting that this hole transfer reaction is not the rate limiting step in water oxidation at positive potentials.

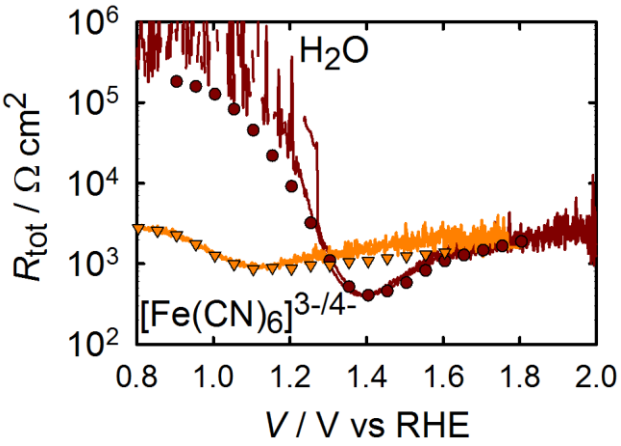

Figure 6-5. R_{tot} calculated from dV/dJ of the J-V curves (lines) and from IS data (symbols) for H_2O and $[Fe(CN)_6]^{3-/4-}$ electrolytes under 1 sun illumination.

6.4.3 Transient Behavior

In order to gain further insight into the differences in behavior of hematite electrodes in contact with H_2O and $[Fe(CN)_6]^{3-/4-}$ electrolytes, J-V curves were also measured under light chopping conditions and compared with J-V curves with constant illumination. Figure 6-6a shows the superimposed chopped and constant light J-V curves when $[Fe(CN)_6]^{3-/4-}$ is present in the solution. The instantaneous photocurrent density with chopped light reaches the constant light photocurrent density and remains constant until the light is turned off, where the current immediately decays to J_0.[11] This ideal behavior is consistent with the expectations of a fast hole collector efficiently scavenging valence band holes at the surface of a hematite photo-electrode.[10,13,14] In the case of water oxidation, however, the behavior is quite different: see figure 6-6b. At potentials from 0.8 – 1.2 V vs. RHE, there is a significant instantaneous photocurrent density when the chopped light is turned on, which quickly decays to the near zero

steady-state photocurrent density under constant illumination. Interestingly, the peak of the H_2O anodic transient photocurrent density closely matches the steady state photocurrent density measured with the $[Fe(CN)_6]^{3-/4-}$ electrolyte (also shown in 6-6b). This is attributed to the identical flux of photogenerated holes which initially reach the surface. When the holes that reach the surface are efficiently collected, as in the case of $[Fe(CN)_6]^{4-}$ oxidation, this flux determines the steady state photocurrent density. Under water oxidation conditions, however, the photocurrent density decay indicates that a faradaic current cannot be sustained and the hole transfer efficiency is therefore minimal. In this case, the flux of holes that reach the surface must either be trapped in surface states or recombine with conduction band electrons. When the light is switched off at potentials where transient anodic peaks are observed, transient cathodic peaks are also visible. The cathodic transients are thus attributed to reducing the surface-trapped holes. This behavior is consistent with previous reports where current transients were also attributed to the charging and discharging of surface states of α-Fe_2O_3,[14-16] CdTe,[17] and TiO_2.[18] Indeed, measuring transient peaks through light chopping has become a prevalent method of qualitatively probing the surface states of hematite.[13,19-23] All additional photogenerated holes, which are not stored in surface states, therefore undergo recombination.

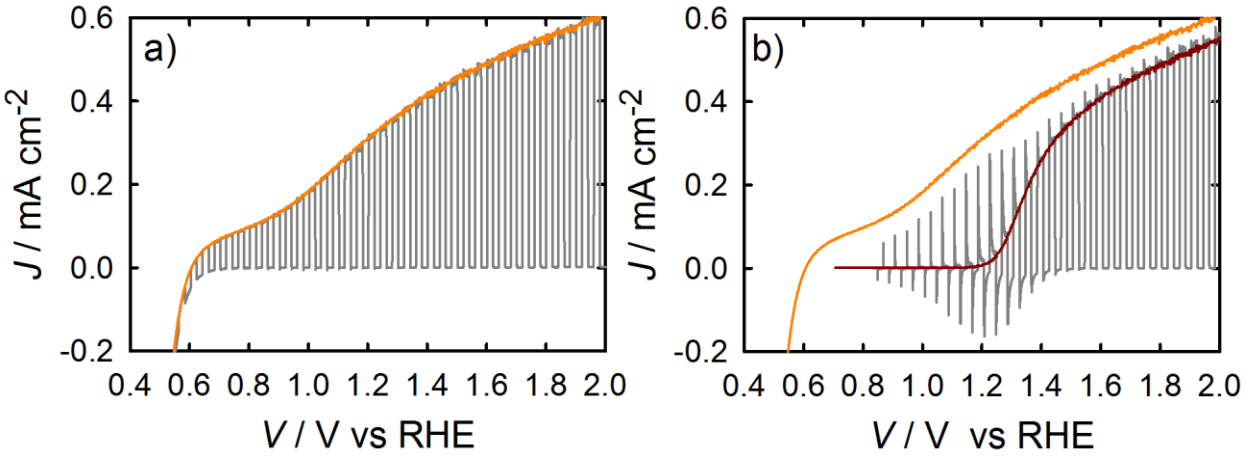

Figure 6-6. (a) Chopped light (grey line) and steady state (orange line) *J-V* measured under 1 sun illumination for a hematite electrode in contact with a $Fe(CN)_6^{3-/4-}$ electrolyte. (b) Chopped light (grey line) and steady state (red line) *J-V* measured under 1 sun illumination for a hematite electrode in contact with a H_2O electrolyte (the steady state *J-V* curve measured in a $Fe(CN)_6^{3-/4-}$ electrolyte (yellow line) is also shown for comparison).

In order to deconvolute the change in potential with change in current over time as in the data shown in figure 6-6b, current transients at a constant potential were also measured. These measurements were performed by measuring the current as a function of time at a fixed potential in response to turning on (anodic) and off (cathodic) 1 sun illumination. Plots of the anodic and cathodic current transients measured at various constant potentials can be seen in figures 6-7a and 6-7b, respectively. Clearly, there is a dependence in the magnitude of the current transient with potential as well as the rate of decay. In order to determine the amount of charge stored in the surface state at a given potential, the current vs. time plots in figure 6-7 were integrated. A plot of the anodic and cathodic charge stored as a function of potential is shown in figure 6-8a.

The anodic charge was not calculated for potentials above 1.2 V vs RHE because the faradaic and charging current cannot be separated accurately. The cathodic and anodic charge is approximately equal, at least for potentials up to 1.2 V vs RHE, suggesting that the charge measured is related to the amount of charge trapped in surface states on the hematite electrode. There is a clear peak in the stored charge at approximately 1.3 V vs RHE. Interestingly, this is near the potential which yields the peak C_{SS} from IS measurements. The same experiments were also performed in response to varying illumination intensities; the results are displayed in figure 6-8b which were calculated from cathodic current transients. The magnitude of the peak clearly increases with light intensity and the peak shifts to more negative potentials with increasing light intensity. This is the same trend found with the peak of C_{ss} as a function of light intensity measured by IS. The charge measured by the current transients can be related to C_{ss} by the equation $C_{SS} = \frac{\Delta Q}{\Delta V}$ where ΔV is the change in the quasi-Fermi level as a result of turning the light off at a constant potential. Assuming the surface states probed by IS and current transients are the same, ΔV can be calculated by plotting C_{SS} obtained from IS vs. ΔQ measured from current transients (see Figure 6-8d). From the slope of these plots, ΔV was found to be 0.08 , 0.13 and 0.17 V for 0.1, 0.33 and 1 sun respectively. This corresponds to an increase of 92 mV per 10 fold increase in light intensity, in good agreement with ideal behavior. The C_{ss} were calculated from the current transients and compared to the C_{ss} measured from IS and can be seen in figure 6-8c. Taken together, these results confirm that the C_{SS} measured with IS is the same entity probed by measuring the stored charge of the current transients.

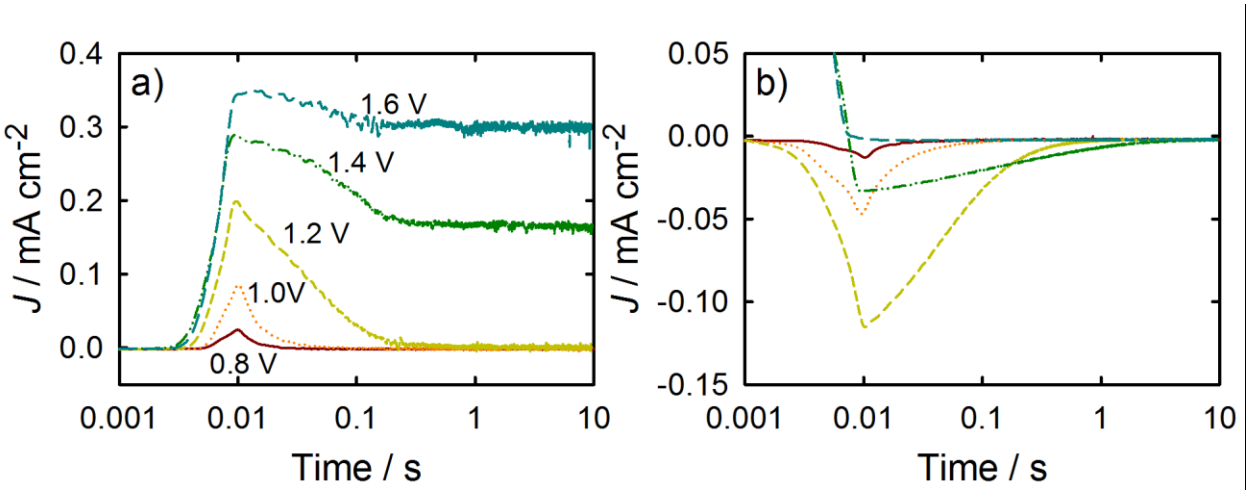

Figure 6-7. *J* measured for a constant *V* vs. RHE plotted vs. time for when 1 sun illumination is turned on (a) and off (b). Time is corrected so that the all of the peaks occur at 10 ms. Measurements are shown for 0.8 V (red solid line), 1.0 V (orange dotted line), 1.2 V (yellow small dashed line), 1.4 V (green dashed dotted line), and 1.6V (blue large dashed line) vs. RHE.

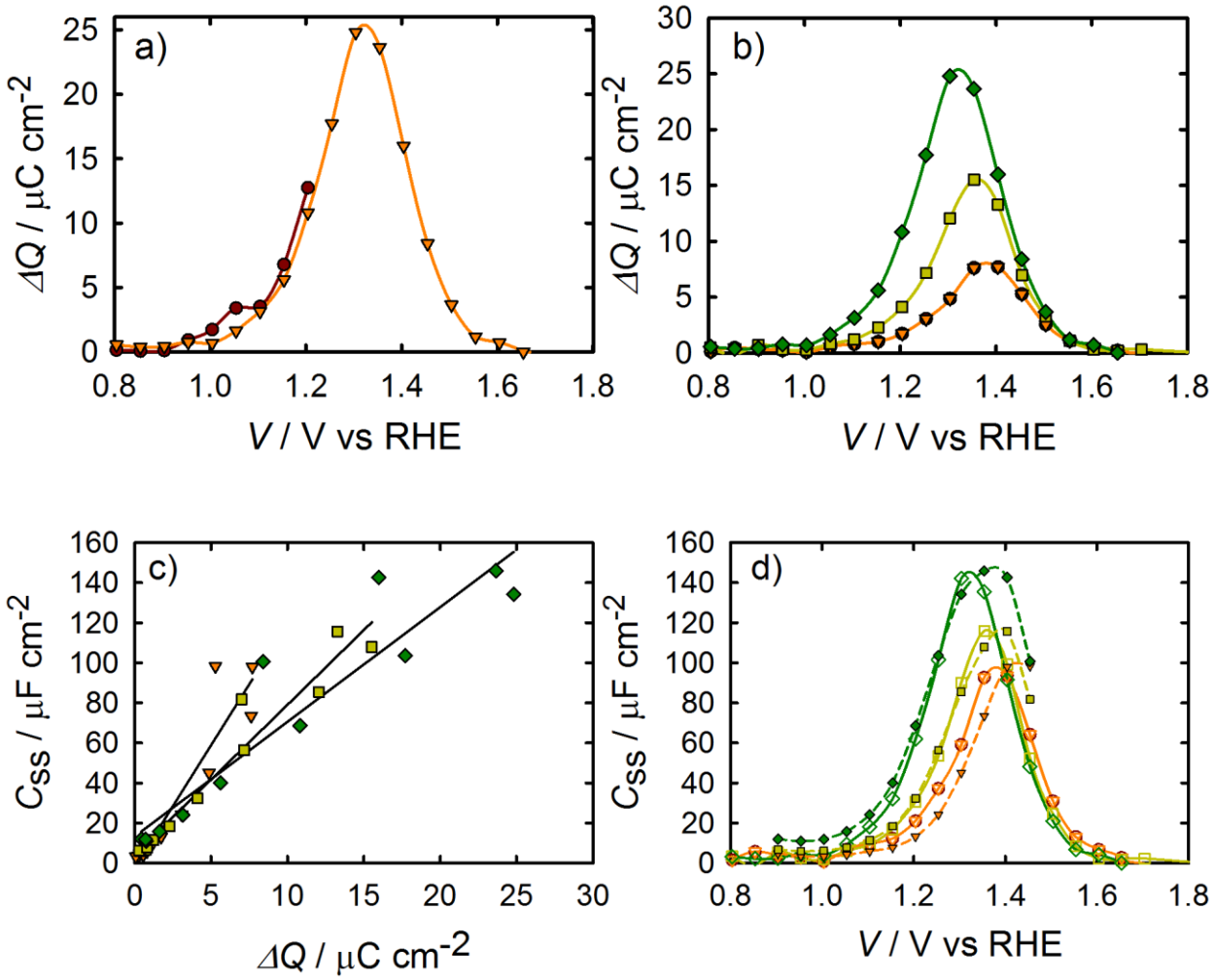

Figure 6-8. (a) Transient anodic (red circles) and cathodic (orange triangles) charge passed as a function of potential. (b) Transient cathodic charge vs. potential (c)) C_{ss} from EIS vs Q from transients for a given potential measured. d) C_{ss} determined from IS, (open shapes) and C_{SS} determined from current transients (filled in shapes). (b) (c) and (d) show data measured under 0.1 sun (orange triangles), 0.33 sun (yellow squares) and 1 sun (green diamonds) illumination.

The potential dependence of the transient photocurrent decay was also examined. Abrantes and Peter examined the decay of current transients of passive iron oxide electrodes in

an H_2O electrolyte and were able to gain kinetic insight on the back reaction of electrons reducing surface states (i.e. filling surface trapped holes) by fitting the decays to a single exponential function.[14] We found, however, that a double exponential decay is necessary to achieve good fits for the decays measured (See Appendix). Fitting the decays to a double exponential decay function ($J(t) = J(0)_1 e^{-t/\tau_1} + J(0)_2 e^{-t/\tau_2} + J(\infty)$ where $J(0)$ is the maximum current for the decay process at time = 0, τ is the lifetime of the process and $J(\infty)$ is the steady state current reached after both processes have fully decayed) produced two lifetimes that differ by approximately an order of magnitude, which are displayed in figure 9. Two lifetimes were also calculated from current transients for both doped and undoped hematite electrodes in water oxidation conditions by Glasscock et. al.[24] This result is also in reasonable agreement with a recent report by Pendlebury et. al. of transient absorption spectroscopic measurements on hematite electrodes under water oxidation conditions.[1] Both lifetimes are dependent on potential where the lifetimes increase by approximately an order of magnitude from when there is no faradaic current (1.0 V vs RHE) to when there is signification faradaic current (>1.4 V vs RHE). This also agrees with a recent paper correlating long lived holes and photocurrent on hematite electrodes.[1]

The origin of the two lifetimes found actually result from a single process: the discharging of the surface state. As mentioned above, under illumination, charge is accumulated in the surface state. At short times after switching off the light, the conditions of the trap state (amount of charge accumulated, trap transfer resistance) are similar as when under illumination. Therefore, the short lifetimes obtained from the transients in figure 7-7b are very close to the

relaxation times of the surface state at 1 sun: $\tau_1 \approx (R_S + R_{trap}) \times C_{SS}$. As the surface state discharges (is reduced), both R_{trap} and C_{SS} change. In fact, the amount of charge accumulated in the surface states sweeps the states produced at lower light intensities until reaching dark conditions. Thus, the discharging time rises providing the second, slower process, τ_2. Figure 9 shows the two lifetimes fit from the double exponential decay of the transients (figure 7-7b) as well as the relaxation time of the trapped electrons measured from IS data under 1 sun and 0.1 sun illumination. It is observed that there is a good match between the fast time constant of the transient discharge time and the relaxation time measured under 1 sun illumination. As the light intensity diminishes, conditions approach those in the dark thus the surface state discharging time obtained at 0.1 sun approaches the slow time constant found from the cathodic discharge. The increase in the time constant obtained is due to the increase in R_{trap} during the discharge of the surface state.

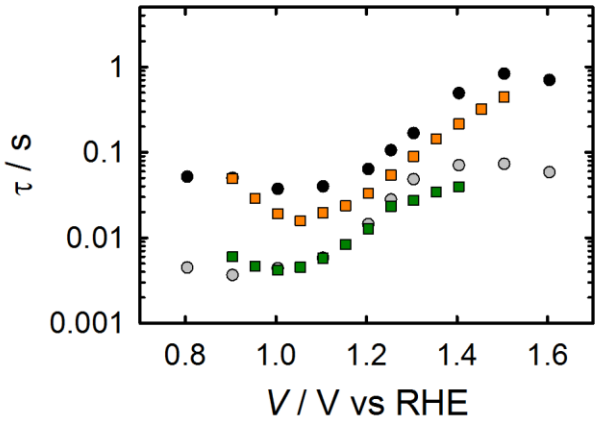

Figure 6-9. A plot of the 2 different lifetimes (black and grey circles) fit from a double exponential of the cathodic decays shown in figure 6-7b. The lifetime of the surface state charging-discharging process at 1 sun (green squares) and at 0.1 sun (orange squares) are also shown.

6.4.4 Cyclic Voltammetry

The anodic and cathodic current density transients measured above are attributed to the reversible oxidation and reduction, respectively, of surface species. In other words, surface trapping of holes means the photooxidation of a chemical species on the surface (discussed below), and surface recombination is the reduction of that oxidized surface species. We therefore reasoned that we should also be able to measure the light-generated surface trapped holes using cyclic voltammetry in the dark. In this experiment, holes accumulate on the surface by applying a positive potential under illumination,[25] followed by measuring the cathodic current in the dark as the potential is scanned negatively and the surface states are reduced.[26,27] A representative experiment measured at 200 mV s^{-1} is shown in figure 6-10a. On the first cycle, shown as a red solid line, a peak in current appears at around 1.3 V and 0.8 V vs RHE. On the second cycle, both of these peaks are gone. The fact that the peaks cannot be seen on the

second cycle is consistent with the idea that these peaks represent the reduction of surface trapped holes as the potential is scanned negative on the first cycle. These holes are not re-oxidized by the application of a positive potential (at least on the relatively fast timescale of the experiment) which indeed means that the holes are generated by photoexcitation of hematite and not by the potential. Thus there are no longer oxidized surface species to be reduced on the second cycle. The peak at 1.3 V is very close to the peak of C_{SS} fit by the IS data, shown in figures 6-4a, as well as the potential where the maximum transient charge is found, shown in figure 6-8. This suggests the peak at 1.3 V is due to filling the surface states which are associated with water oxidation. In order to probe the timescale of the transient peaks, a scan rate dependence of the CV measurements was performed. Capacitance plots were then calculated by dividing the current density by the scan rate, which can be seen in figure 6-10b for varying scan rates. It is apparent that the species probed at 1.3 V vs RHE decreases with scan rate which means the states occupancy decays over time. The time constant(s) of this decay process cannot be confirmed quantitatively because of the constantly changing potential, however the timescale is in general agreement with the transient lifetimes displayed in Fig 6-9. This further suggests that the state measured is the same measured in the current transients. The charge passed from the surface states corresponding to the peak at 1.3 V vs RHE was calculated to be 25 $\mu C\ cm^{-2}$ when measured at a fast scan rate of 1 $V\ s^{-1}$. The similar values between the charge measured through the CV peak, the C_{SS} peak from IS and the charge passed through current transients, as well as the lifetimes measured from the decay of the CV peak and current transients, all suggest that the species being measured around 1.3 V vs RHE is the same for all measurements. Similar CV measurements were also performed with $[Fe(CN)_6]^{3-/4-}$ in solution,

(see Appendix) however no cathodic current was measured until the reduction of the $[Fe(CN)_6]^{3-}$ began, again suggesting that the surface states are associated with water oxidation intermediates and not intrinsic to the hematite electrode.

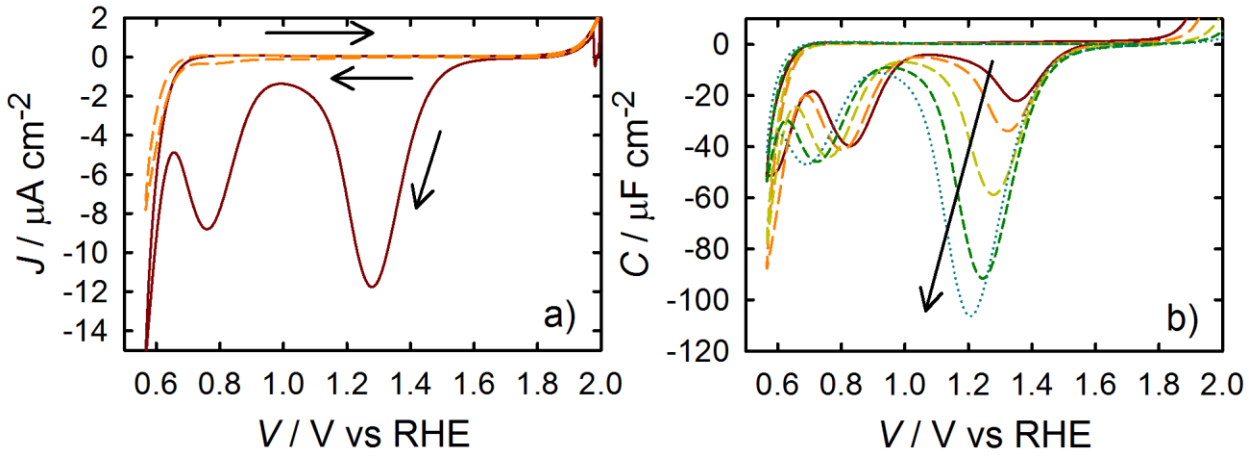

Figure 6-10. (a) Cyclic voltametry of hematite in H_2O scanned at 200 mV s^{-1} after holding the electrode at a potential of 2 V vs RHE for 60 seconds under 1 sun illumination. The first cycle is a solid red line and the second cycle is a dashed orange line. (b) CVs measured with the same conditions as (a) at different scan rates: 20 mV s^{-1} (red, solid), 50 mV s^{-1} (orange, long dash), 200 mV s^{-1} (yellow, medium dash), 500 mV s^{-1} (green, short dash) and 1,000 mV s^{-1} (blue, dots).

6.5 Discussion

The *J-V* curves of hematite electrodes immersed in an aqueous electrolyte containing $[Fe(CN)_6]^{3-/4-}$ can be described by the potential dependent fraction of photogenerated holes that reach the electrode surface.[11] These valence band holes at the surface are efficiently collected

by $[Fe(CN)_6]^{4-}$, and this faradaic charge transfer results in a steady-state photocurrent density.[10] Under H_2O oxidation conditions the flux of holes to reach the surface (which is just a property of the same bulk semiconductor) is the same, however a steady-state photocurrent is not produced at low applied potentials. Instead of the surface holes undergoing interfacial charge transfer to solution, a fraction of the holes are initially (at low potentials) trapped in surface states; the remainder recombine. This charging of surface states was observed through IS, transient photocurrent and cyclic voltammetric measurements. These results provoke questions regarding the identity of these surface states and their role in the water oxidation process. Instead of being what is generically termed a surface state, we believe the surface states presented herein actually consist of intermediates in the overall water oxidation reaction. One piece of (albeit indirect) evidence of this is that the surface state is only, and always, observed under water oxidation conditions – not in the dark or in the presence of a competitive hole scavenger. In addition, the pH-dependant surface state is at the same energy as the water oxidation potential,[3] which we believe is not just a coincidence.

We therefore propose that the charging of the surface state is actually the first oxidative step in the overall water oxidation reaction. The fully hydroxylated species, $(OH)_3–Fe–H_3O_3–R$ where R represents the bulk hematite crystal, is the thermodynamically most stable surface configuration of the (0001) surface.[28] Hellman and Pala recently suggested that the first step of water oxidation on hematite electrodes is the proton coupled oxidation of such surface hydroxide species.[29] This is also in agreement with one of the general mechanisms of water oxidation at metal oxide electrodes previously reviewed by others.[30-32] The initial step is thus given by:

$$Fe(III)-OH \underset{e^-}{\overset{h^+}{\rightleftarrows}} Fe(IV)=O+H^+ \quad (1)$$

We believe this reaction is what is referred to as "hole trapping" or "surface state charging." Hellman and Pala further calculated that the most stable configuration during water oxidation (at higher applied potentials) is the oxidized $(OH)_3$-Fe-O_3-R surface, also consistent with this assignment.[29] Since the oxidized species on the surface, Fe=O, can be reduced, as demonstrated by the cathodic current transients (figure 6-7) and the CV measurements (figure 10), the reaction is written as reversible.

While it is very challenging to directly determine the identity of surface states on a bulk electrode, there are molecular iron catalysts which can serve as analogs. There are several examples of Fe(IV)=O complex intermediates which are known to be involved in catalytic cycles.[33,34] For example, a Fe-TAML complex was recently shown to catalyze the oxidation of water to dioxygen.[35] Further, Collins and co-workers have shown that the Fe(IV)-oxo species has a reduction potential of 0.9 V vs NHE in basic conditions, according to the reaction

$$\left[\mathrm{Fe(IV)L(=O)(OH_2)}\right]^{2-} + \mathrm{e^-} + \mathrm{H_2O} \rightarrow \left[\mathrm{Fe(III)L(OH)(OH_2)}\right]^{2-} + \mathrm{OH^-} \quad (2)$$

which is essentially the recombination reaction (reduction of the surface intermediate species) proposed herein.[34] This behavior of the Fe(III)-OH / Fe(IV)=O molecular complexes is therefore in good agreement with the proposed first water oxidation step on hematite electrodes. In addition, it was shown that an intermediate Fe(IV)=O complex has a broad absorption spectrum centered at 820 nm.[33] This absorbance is also consistent with the broad near IR absorption observed during water oxidation with hematite electrodes.[1,7]

There are two important features of the surface state behavior that provide further insight into the water oxidation mechanism. The first is that at potentials where the surface oxidation begins, the formation of the proposed intermediate Fe=O doesn't result in subsequent water oxidation steps as indicated by the lack of steady-state photocurrent; i.e. the transient photocurrent at these potentials decays to zero. Attack of the surface Fe=O by water molecules, leading to a surface bound peroxide followed by decomposition to O_2, should be thermodynamically downhill.[29] In this case, it is expected that the steady-state concentration of surface Fe=O should lead to photocurrent production. Since no photocurrent is observed under these conditions, this is not the predominant mechanism. The other feature is the fact that steady-state concentration of surface Fe=O reaches a peak that is coincident with a sharp drop in the charge transfer resistance and an increase of photocurrent. This indicates that a critical concentration of the surface intermediate species is necessary before the further water oxidation steps can proceed. The necessary number of surface intermediates can be estimated by integrating the capacitance as a function of potential. The C_{SS} peaks determined from IS data were fit to a Gaussian curve and integrated to calculate the total charge of the surface states to be 24.3, 31.6 and 38.8μC cm^{-2} for 0.1, 0.33, and 1 sun illumination respectively. Using the value for 1 sun illumination as an example, this corresponds with a surface coverage of 2.4×10^{14} cm^{-2}. The surface coverage is then calculated to be ~53%, by using the unit cell parameters for the 0001 surface of hematite, and estimating 1 active site per unit cell.[29,36-39] This behavior is consistent with the surface intermediate decomposing bimolecularly, such as:

$$2Fe(IV) = O \longrightarrow 2Fe(III) + O_2 \quad (3)$$

We note that such an oxygen formation mechanism has been proposed extensively before, although not applied to hematite photoelectrodes.[30-32] A water molecule, or hydroxide, could then quickly coordinate to the open iron site to complete the photocatalytic cycle.

At positive potentials (≥1.45 V vs. RHE) the current transients become negligible, the low frequency semicircle disappears from the IS spectra and high steady state photocurrent densities are achieved. This behavior is essentially indistinguishable from when the fast hole collector $[Fe(CN)_6]^{4-}$ is present in solution (figure 6-6b). Further, these two systems have the same charge transfer resistance at positive potentials. Therefore, the surface hole collection efficiency must also be essentially unity under water oxidation conditions at such positive potentials. Thus, once a sufficient concentration of intermediate is built up, allowing the subsequent steps of water oxidation to proceed, water oxidation is not the rate limiting step in the photoelectrochemical behavior of hematite electrodes; the flux of holes to the electrode surface limits the photocurrent density at these potentials.

We note that the *J-V* curves of the H_2O and $[Fe(CN)_6]^{3-/4-}$ electrolytes, as seen in figure 6-1, do not overlap exactly, even at positive potentials; the H_2O electrolyte always produces somewhat lower photocurrents at a given positive potential compared to $[Fe(CN)_6]^{3-/4-}$. Since we have demonstrated the surface hole collection efficiency is essentially unity for both of these systems, and the surface hole concentration is determined by the potential drop of the electrode, the discrepancy can be attributed to the extra potential needed to compensate for Fermi level pinning in the H_2O electrolyte. According to the Mott-Schottky plots, the bands under water oxidation are shifted positive compared to $[Fe(CN)_6]^{3-/4-}$, or compared to the MS at low applied

potentials. The shift in the band is calculated to be ~140 mV, as shown in figure 6-11a. Shifting the *J-V* curve in the H_2O electrolyte by 200 mV produces excellent agreement with the $[Fe(CN)_6]^{3-/4-}$ *J-V* curve at positive potentials (Figure 6-11b). These plots show that the lower current measured at high applied potential in water oxidation compared to $[Fe(CN)_6]^{3-/4-}$ can be almost entirely attributed to Fermi-level pinning, and not decreased hole transfer kinetics.

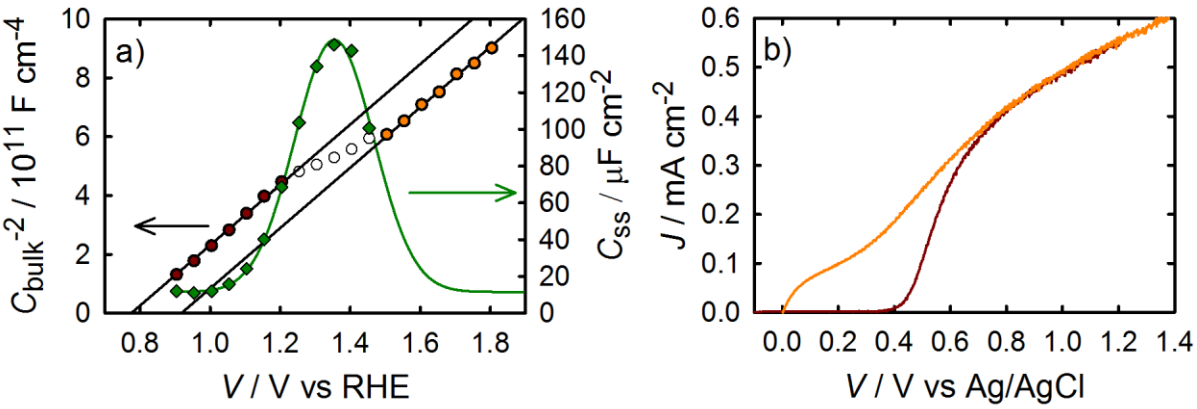

Figure 6-11. a) Mott Schotty plot made from C_{bulk} values measured under 1 sun illumination. The lines represent lines of best fit of the points measured at potentials negative (red circles) and positive (green circles) of the shift in the flat band. The white circles were not used in either fit. Both sets of data were made to share the same slope in the fit. Using this method, the shift in flat band potential is calculated to be 140 mV. Also included is the C_{ss} measured under one sun illumination (green diamonds) and the Gaussian fit (green line). b) *J-V* curve measured for a hematite electrode in a $[Fe(CN)_6]^{3-/4-}$ electrolyte (orange curve) and in a H_2O electrolyte (red curve). The H_2O curve has been shifted by 200 mV to overlap with the $[Fe(CN)_6]^{3-/4-}$ curve.

Finally, the above discussion of the intrinsic role of the surface state seen at 1.3 V does not include the other state that we observed around 0.8 V in the CV measurements. Since this state's energy is significantly higher than the water oxidation potential, and it is not observed in the impedance spectra at photocurrent onset, we do not think it plays an active role in water oxidation. There are surface terminations of hematite, in addition to the $(OH)_3$–Fe–H_3O_3–R termination discussed above, that are stable. According to Trainor et. al., the other most relevant surface is the $(OH)_3$–R termination.[28] This surface can also be oxidized, i.e. trap a hole, but it is thermodynamically uphill for subsequent water oxidation. Importantly, this termination's oxidation potential is approximately 0.5 V more negative than the $(OH)_3$–Fe–H_3O_3–R termination, which is in excellent agreement with the differences in potential of the two surface states we observed.

6.6 Conclusions

The photoelectrochemical behavior of hematite electrodes in contact with H_2O and $[Fe(CN)_6]^{3-/4-}$ electrolytes were compared. The steady state photocurrent onset potential was approximately 0.6 V higher in H_2O compared to $[Fe(CN)_6]^{3-/4-}$, which is in accord with literature reports.[10,13,40] The much more positive onset potential represents a loss of energy which must be minimized for any practical use of hematite in water splitting applications. A combination of impedance spectroscopy, photocurrent transient and cyclic voltammetry measurements were therefore employed to determine the cause of the large overpotential for water splitting. We found that at moderate potentials, prior to the photocurrent onset potential, photogenerated holes became trapped in surface states. We deduce that the physical meaning of

photogenerated holes being trapped at the surface is that this is the first step in the water oxidation process, specifically the reversible oxidation of surface hydroxide species. It is only after a buildup of these oxidized intermediates that water oxidation proceeds. This calls into question the strategy of passivating surface states on hematite electrodes which has been pursued recently since they might be an inherent feature of oxidizing water, and not necessarily deleterious.[21,23] It is well known that water oxidation proceeds by an innersphere mechanism, thus a proposed mechanisms should account for this;[32] describing this reaction as a charge transfer from a valence band hole is misleading. In addition, the negligible faradaic, steady state photocurrent densities at these potentials is often attributed to slow hole transfer kinetics of water oxidation.[2,3,5,6,15] We suggest that this may be an intrinsic part of the bimolecular mechanism of water oxidation on the hematite surface. At high applied potentials, however, the photocurrent density is essentially the same for the H_2O and $[Fe(CN)_6]^{3-/4-}$ systems; the minor difference is attributed to Fermi level pinning in the H_2O electrolyte. This ideal behavior at high potentials is consistent with the idea that water oxidation is not the rate limiting step, once a critical concentration of surface intermediates is formed. While the addition of catalysts have been shown to improve performance, the cause of the improvement has not been established.[4,19,41-44] Insight into the mechanism of water oxidation on hematite, and other surfaces, is critical for the design of better catalysts or other systems aimed at improving the efficiency of water splitting. Work is ongoing in our lab to clarify these points.

6.7 Acknowledgements

TWH thanks the National Science Foundation (CHE-1150378) and the Donors of the American Chemical Society Petroleum Research Fund (51099-DNI10) for support of this research. TWH and BK also thank Jesse Ondersma for helpful conversations. JB & FFS acknowledge support by projects from Minis- terio de Economia y Competitividad of Spain (MINECO) (Consolider HOPE CSD2007-00007), and Generalitat Valenciana (PROMETEO/2009/058). SG acknowledges support by MINECO of Spain under the Ramon y Cajal programme.

APPENDIX

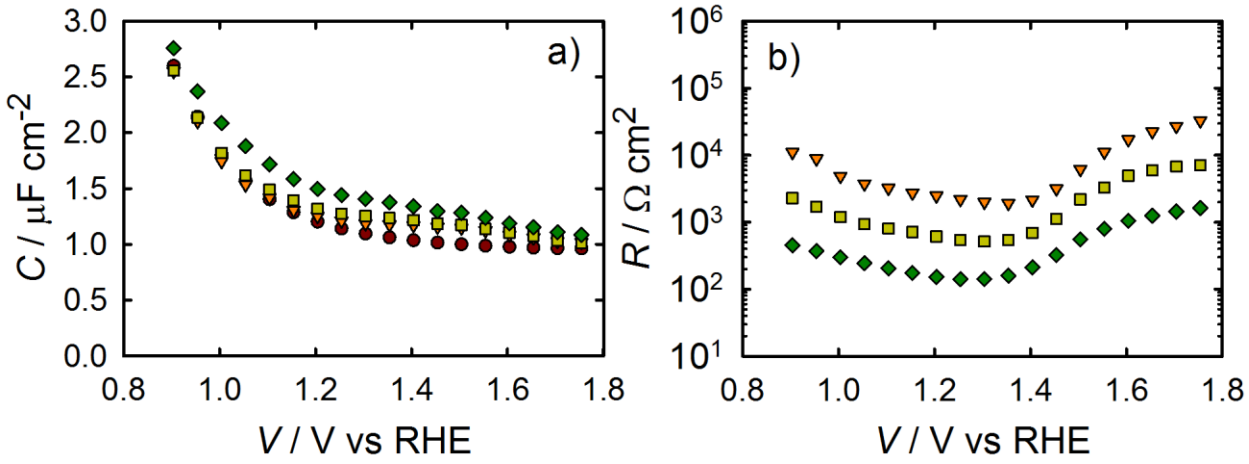

Figure A6-1. a) C_{bulk} and b) R_{trap} values fit from IS data of a hematite electrode in contact with a H_2O electrolyte in the dark (red circles), under 0.1 sun (orange triangles), 0.33 sun (yellow squares) and 1 sun (green diamonds) illumination.

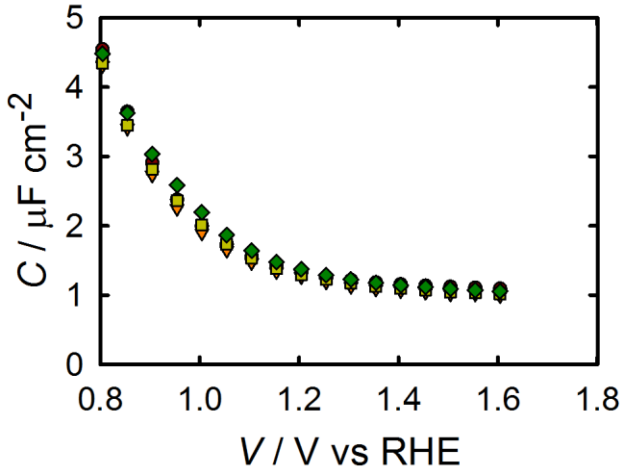

Figure A6-2. C_{bulk} values fit from IS data of a hematite electrode in contact with a $[Fe(CN)_6]^{3-/4-}$ electrolytes in the dark (red circles), under 0.1 sun (orange triangles), 0.33 sun (yellow squares) and 1 sun (green diamonds) illumination.

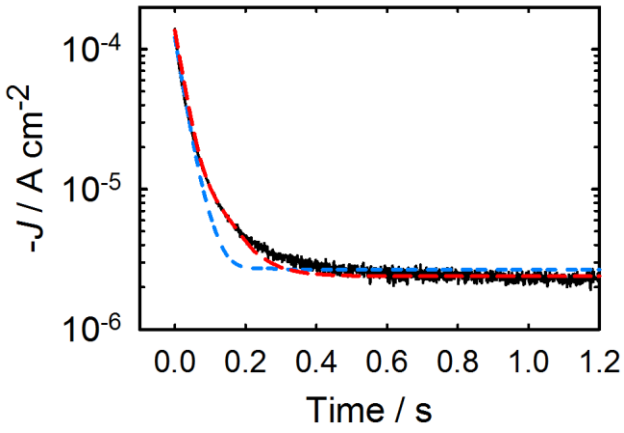

Figure A6-3. Experimentally measured decay measured at 1.2 V vs RHE (black line) and fits for a single exponential decay (blue small dashed line) and double exponential decay (red long dashed line)

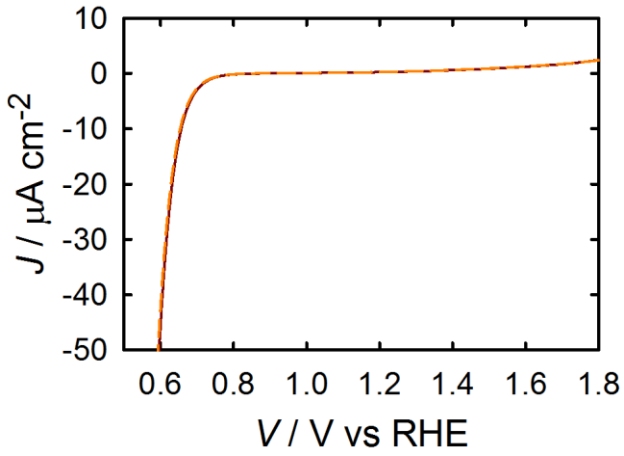

Figure A6-4. Cyclic voltammetry of hematite in $[Fe(CN)_6]^{3-/4-}$ electrolyte scanned at 200 mV s^{-1} after holding the electrode at a potential of 2 V vs RHE for 60 seconds under 1 sun illumination. The first cycle (solid red line) and the second cycle (dashed orange line) are overlapping.

REFERENCES

REFERENCES

1. Pendlebury, S. R.; Cowan, A. J.; Barroso, M.; Sivula, K.; Ye, J.; Gratzel, M.; Klug, D. R.; Tang, J.; Durrant, J. R. *Energy Environ. Sci.* **2012**, *5*, 6304-6312.

2. Pendlebury, S. R.; Barroso, M.; Cowan, A. J.; Sivula, K.; Tang, J. W.; Gratzel, M.; Klug, D.; Durrant, J. R. *Chem. Commun.* **2011**, *47*, 716-718.

3. Cowan, A. J.; Barnett, C. J.; Pendlebury, S. R.; Barroso, M.; Sivula, K.; Grätzel, M.; Durrant, J. R.; Klug, D. R. *J. Am. Chem. Soc.* **2011**, *133*, 10134-10140.

4. Barroso, M.; Cowan, A. J.; Pendlebury, S. R.; Grätzel, M.; Klug, D. R.; Durrant, J. R. *J. Am. Chem. Soc.* **2011**, *133*, 14868-14871.

5. Upul Wijayantha, K. G.; Saremi-Yarahmadi, S.; Peter, L. M. *Phys. Chem. Chem. Phys.* **2011**, *13*, 5264-5270.

6. Peter, L. M.; Wijayantha, K. G. U.; Tahir, A. A. *Faraday Discuss.* **2011**, *155*, 309-322.

7. Cummings, C. Y.; Marken, F.; Peter, L. M.; Upul Wijayantha, K. G.; Tahir, A. A. *J. Am. Chem. Soc.* **2012**, *134*, 1228-1234.

8. Klahr, B.; Gimenez, S.; Fabregat-Santiago, F.; Bisquert, J.; Hamann, T. W. *J. Am. Chem. Soc.* **2012**, *134*, 4294-4302.

9. Klahr, B. M.; Martinson, A. B. F.; Hamann, T. W. *Langmuir*, **2011**, *27*, 461-468.

10. Klahr, B. M.; Hamann, T. W. *J. Phys. Chem. C*, **2011**, *115*, 8393-8399.

11. Klahr, B. M.; Hamann, T. W. *Appl. Phys. Lett.* **2011**, *99*, 063508.

12. Morrison, S. R. *Electrochemistry at Semiconductor and Oxidized Metal Electrodes*; Plenum: New York, 1980.

13. Dotan, H.; Sivula, K.; Gratzel, M.; Rothschild, A.; Warren, S. C. *Energy Environ. Sci.* **2011**, *4*, 958-964.

14. Abrantes, L. M.; Peter, L. M. *J. Electroanal. Chem.* **1983**, *150*, 593-601.

15. Dareedwards, M. P.; Goodenough, J. B.; Hamnett, A.; Trevellick, P. R. *J. Chem. Soc., Faraday Trans. 1 F*, **1983**, *79*, 2027-2041.

16. Hardee, K. L.; Bard, A. J. *J. Electrochem. Soc.* **1977**, *124*, 215-224.

17. Lincot, D.; Vedel, J. *J. Electroanal. Chem.* **1987**, *220*, 179-200.

18. Salvador, P. *J. Phys. Chem.* **1985**, *89*, 3863-3869.

19. McDonald, K. J.; Choi, K. S. *Chem. Mater.* **2011**, *23*, 1686-1693.

20. Le Formal, F.; Graetzel, M.; Sivula, K. *Adv. Funct. Mater.* **2010**, *20*, 1099-1107.

21. Le Formal, F.; Tetreault, N.; Cornuz, M.; Moehl, T.; Gratzel, M.; Sivula, K. *Chem. Sci.* **2011**, *2*, 737-743.

22. Sivula, K.; Zboril, R.; Le Formal, F.; Robert, R.; Weidenkaff, A.; Tucek, J.; Frydrych, J.; Grätzel, M. *J. Am. Chem. Soc.* **2010**, *132*, 7436-7444.

23. Hisatomi, T.; Le Formal, F.; Cornuz, M.; Brillet, J.; Tetreault, N.; Sivula, K.; Gratzel, M. *Energy Environ. Sci.* **2011**.

24. Glasscock, J. A.; Barnes, P. R. F.; Plumb, I. C.; Savvides, N. *J. Phys. Chem. C* ,**2007**, *111*, 16477-16488.

25. ****, We found the addition of light was necessary to obtain reproducible results by fully oxidizing the surface species.

26. Bisquert, J.; Fabregat-Santiago, F.; Mora-Sero, I.; Garcia-Belmonte, G.; Barea, E. M.; Palomares, E. *Inorg. Chim. Acta,* **2008**, *361*, 684-698.

27. Boschloo, G.; Fitzmaurice, D. *J. Phys. Chem. B.* **1999**, *103*, 2228-2231.

28. Trainor, T. P.; Chaka, A. M.; Eng, P. J.; Newville, M.; Waychunas, G. A.; Catalano, J. G.; Brown Jr, G. E. *Surf. Sci.* **2004**, *573*, 204-224.

29. Hellman, A.; Pala, R. G. S. *J. Phys. Chem. C*, **2011**, *115*, 12901-12907.

30. Dau, H.; Limberg, C.; Reier, T.; Risch, M.; Roggan, S.; Strasser, P. *ChemCatChem*, **2010**, *2*, 724-761.

31. Cook, T. R.; Dogutan, D. K.; Reece, S. Y.; Surendranath, Y.; Teets, T. S.; Nocera, D. G. *Chem. Rev.* **2010**, *110*, 6474-6502.

32. Conway, B. E.; Tilak, B. V. *Advances in Catalysis*, **1992**, *38*, 1-147.

33. Rohde, J.-U.; In, J.-H.; Lim, M. H.; Brennessel, W. W.; Bukowski, M. R.; Stubna, A.; Münck, E.; Nam, W.; Que, L. *Science*, **2003**, *299*, 1037-1039.

34. Popescu, D.-L.; Vrabel, M.; Brausam, A.; Madsen, P.; Lente, G.; Fabian, I.; Ryabov, A. D.; van Eldik, R.; Collins, T. J. *Inorg. Chem.* **2010**, *49*, 11439-11448.

35. Ellis, W. C.; McDaniel, N. D.; Bernhard, S.; Collins, T. J. *J. Am. Chem. Soc.* **2010**, *132*, 10990-10991.

36. Blake, R. L.; Hessevick, R. E. *Am. Mineralogist*, **1966**, *51*, 123-129.

37. Eggleston, C. M.; Hochella, M. F. *Am. Mineralogist,* **1992**, *77,* 911-922.

38. Eggleston, C. M.; Stack, A. G.; Rosso, K. M.; Higgins, S. R.; Bice, A. M.; Boese, S. W.; Pribyl, R. D.; Nichols, J. J. *Geochim. Cosmochim. Acta,* **2003**, *67*, 985-1000.

39. ****, The number of active sites per unit cell is estimated by assuming one Fe atom in a given plane per unit cell. Each atom is estimated to have only 1 active site because the formation of 2 oxo groups on a single Fe atom is energetically unfavorable.

40. Sanchez, H. L.; Steinfink, H.; White, H. S. *J. Solid State Chem.* **1982**, *41*, 90-96.

41. Zhong, D. K.; Cornuz, M.; Sivula, K.; Graetzel, M.; Gamelin, D. R. *Energy Environ. Sci.* **2011**, *4*, 1759-1764.

42. Cummings, C. Y.; Marken, F.; Peter, L. M.; Tahir, A. A.; Wijayantha, K. G. U. *Chem. Commun.* **2012**, *48*, 2027-2029.

43. Zhong, D. K.; Gamelin, D. R. *J. Am. Chem. Soc.* **2010**, *132*, 4202-4207.

44. Zhong, D. K.; Sun, J. W.; Inumaru, H.; Gamelin, D. R. *J. Am. Chem. Soc.* **2009**, *131*, 6086-6087.

Chapter 7:

Methanol Photo-Oxidation at Hematite Electrodes and the Implications for Water Oxidation

7.1 Abstract

Fe_2O_3 photoanodes synthesized by Atomic Layer Deposition (ALD) were photoelectrochemically characterized in the presence of CH_3OH in H_2O. Systematic photoelectrochemical characterization along with O_2 evolution measurements, were carried out in order to better understand the mechanisms of both H_2O and methanol oxidation at hematite electrodes. It was found that while methanol oxidation is preferred in methanol-water mixtures, hole transfer to methanol is not unity and therefore, cannot be used to probe the properties of the bulk hematite electrode. Photoelectrochemical and impedance spectroscopic measurements show two different reaction pathways for methanol oxidation at hematite electrodes. In addition, the oxidation of water and methanol mixtures show that increasing the methanol concentration decreases the surface state capacitance and oxygen evolution proportionally, further confirming that the surface states are an integral part of the water oxidation mechanism.

7.2 Introduction

Methanol (CH_3OH) oxidation in the presence of H_2O is a well-studied process, particularly for its relevance for the development of methanol based fuel cells.[1] Methanol has also attracted considerable attention for fundamental studies oriented to the photocatalytic elimination of organic compounds in polluted water and air.[2] The oxidation of CH_3OH results in several different intermediates and products, including formate and formaldehye under varied conditions which are then able to be qualitatively analyzed.[3-6] The identity of methanol oxidation intermediates and products thus provide deep insight into the mechanism of oxidiation at a metal oxide electrode. The oxidation of this small molecule is also expected to contain analogies with the mechanism of water oxidation due to the similar chemical structure and bond angles of the molecules. The present study aims to further understand the mechanisms of hole transfer for water and methanol photo-oxidation with hematite electrodes.

7.3 Experimental

Hematite electrodes (~60 nm thick) were measured in contact with aqueous electrolytes containing a 0.1 M phosphate buffer (pH 6.9) with 0.2 M KCl as supporting electrolyte. This aqueous electrolyte contained varying amounts CH_3OH. Electrolytes containing only CH_3OH as the solvent also contained 0.2 M tetrabutylammonia chloride as supporting electrolyte. The pure CH_3OH solution was prepared and sealed in an electrochemical cell under nitrogen in a glove box to minimize the H_2O content. Experiments were also performed with pH 13.6 (1M KOH) solutions and with different electrodes which all showed the same trends.

Photoelectrochemical and impedance measurements made in aqueous electrolytes were made using a homemade saturated Ag/AgCl reference electrode. Those made in the pure CH_3OH electrolyte were made using a commercial Ag/AgCl electrode (ESA 66-EE009 "no leak"). Both electrodes were calibrated to a saturated calomel electrode (Koslow Scientic) and tested regularly in a $Fe(CN)_6^{3-/4-}$ solution and to ensure consistency. A platinum mesh electrode was used as the counter electrode. All measurements were made under 1 sun illumination (AM 1.5 , 100 mW cm^{-2}). Cyclic voltammetry (CV) measurements were carried out immediately after the electrode was held at a positive potential (of 1.6 V vs Ag/AgCl for aqueous electrolytes and 1.8 V vs Ag/AgCl for the CH_3OH electrolyte) and 1 sun illumination for 60 seconds. This is expected to fully oxidize the surface intermediates. Immediately before scanning the CV, the light is turned off and the CV measurement is made in the dark. Steady state current vs. voltage ,*J-V,* curves were measured at 20 mV/s. Chopped light *J-V* curves were measured at a scan rate of 75 mV/s and the light was chopped every 266 ms. The current was sampled at a rate of 500 Hz. In order to deconvolute the chopped light *J-V* curve from potential, constant potential transients were measured after turning the light on (where the anodic current is measured) and turning the light off (where the cathodic current is measured). These transients are labeled the anodic and cathodic transients respectively. The current was sampled at a rate of 1000 Hz. Impedance measurements were measured at different applied biases using a perturbation amplitude of 10 mV. The frequency range was 10 kHz-10 mHz. Data were fit using Zview software (Scribner Associates). The light source was a 450 W Xe arc lamp (Horiba Jobin Yvon). An AM 1.5 solar filter (Sciencetech Inc.) was used to simulate sunlight at 100 mW cm-2 (1 sun). The pH was determined with an Accumet pH meter.

Oxygen measurements were made with an Ocean Optics spectrophotometer using a FOSPOR fluorescent patch. The electrode was illuminated at 2 suns to produce more oxygen and to reduce noise. The theoretical amount of oxygen produced was calculated by assuming that 4 holes are required to produce 1 molecule of oxygen.

7.4 Results

7.4.1 Steady State Oxygen Evolution

Figure 7-1a shows the current density, *J*, vs. applied voltage, *V*, curves of Fe_2O_3 in contact with electrolytes with varying concentrations of CH_3OH. When CH_3OH is added to H_2O, a slight cathodic shift of the photocurrent onset takes place (see Figure 7-1b), in good agreement with observations made by other researchers.[7] For pure methanol, there is a slow photocurrent onset observed at a similar potential (0.7 V vs Ag/AgCl), followed by a steeper current onset which mimics the shape measured with water oxidation at hematite electrodes. Surprisingly, there was an anodic shift of approximately 300 mV which was needed to sustain a given photocurrent density of 200μA cm^{-2} compared to water based electrolytes. This result is in contrast to literature results of hematite photoelectrodes in contact with good hole scavengers, such as $[Fe(CN)_6]^{3-,4-}$ and H_2O_2.[8,9]

A fluorescence probe was used to measure the amount of O_2 produced, which can be used to evaluate the faradaic efficiency of H_2O oxidation. O_2 concentration was measured at an applied potential of 1.4 V vs Ag/AgCl for H_2O and CH_3OH-H_2O mixture electrolytes and 1.6 V vs Ag/AgCl for the CH_3OH electrolyte such that the currents were approximately equal. This

also accounts for the difference in the E_{FB} potentials between aqueous and methanol based electrolytes, *vide infra*. In the case of the aqueous electrolyte, the faradaic efficiency due to O_2 production is approximately unity as shown in Figure 7-1c and Table 7-1. As increasing amounts of CH_3OH added to H_2O, the faradaic efficiency due to O_2 generation decreased where no O_2 generation could be detected in pure CH_3OH. This is expected since the oxidation of CH_3OH should produce formaldehyde, not O_2.[10-12] Interestingly, however, a significant amount of O_2 was generated even with large concentrations of CH_3OH. A summary of the amount of O_2 measured for different CH_3OH concentrations at applied potentials of 0.75 and 1.4 V vs Ag/Agl can be seen in Table 1. Relative rates, v_R, for CH_3OH oxidation compared to water oxidation was calculated by the equation $v_R = \left(\frac{1-FE}{[CH_3OH]}\right)\left(\frac{FE}{[H_2O]}\right)^{-1}$, where FE is the faradaic efficiency for O_2 generation, and can also be found in Table 7-1. This equation describes the ratio of the FE of methanol oxidation over the FE of water oxidation, both of which are normalized for their concentration. Despite an obvious preference for CH_3OH oxidation compared to H_2O oxidation based on the relative rates shown in Table 7-1, the total hole transfer rate (current) is not significantly altered by adding CH_3OH to H_2O as shown in figure 7-1a. Poor current onset potentials still exist with CH_3OH in solution, showing that it is not acting as a fast and model hole collector.

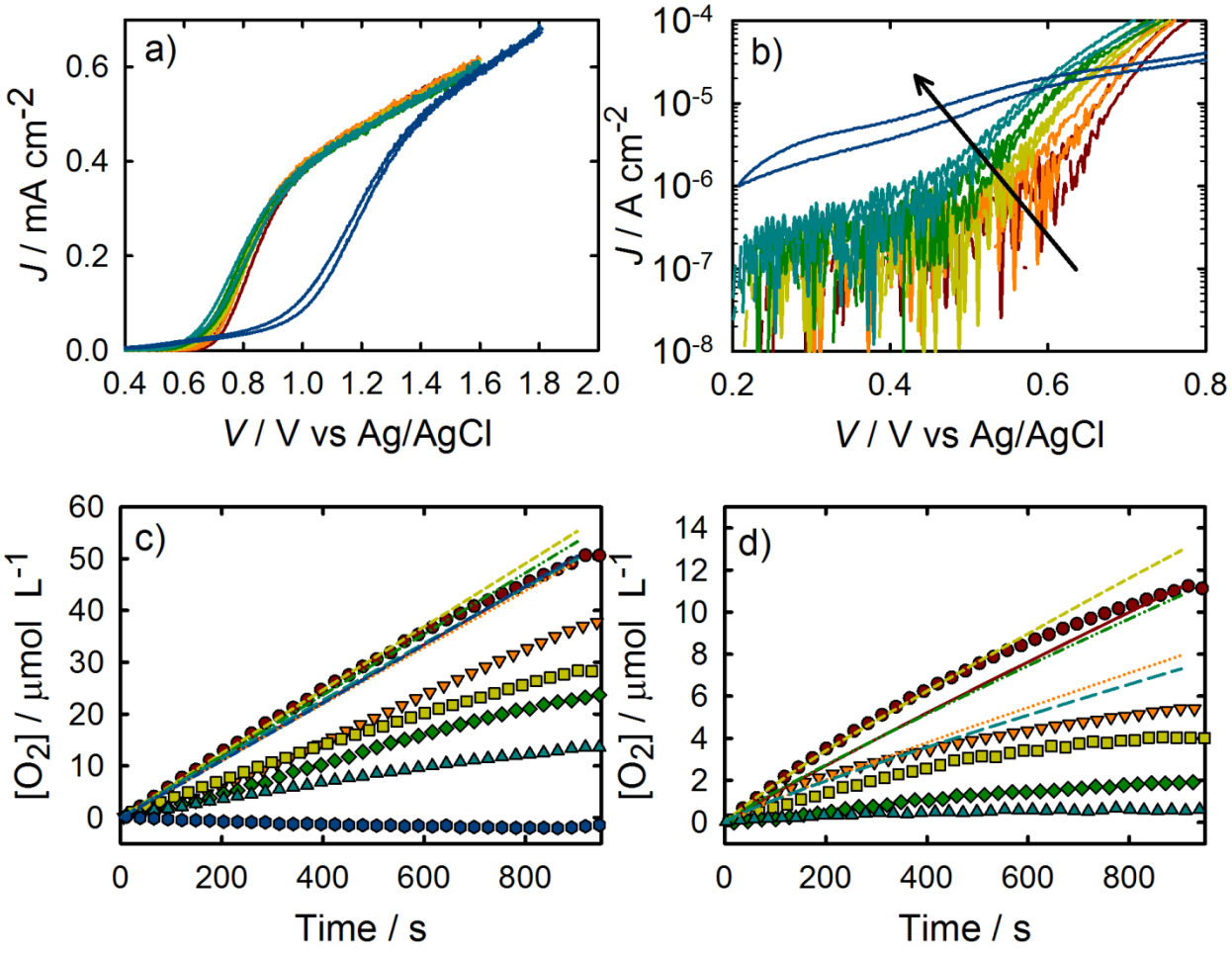

Figure 7-1. (a) *J-V* curves of a hematite electrode under 1 sun illumination in contact with H_2O (red), 0.2M MeOH (orange), 2M (yellow), 5M (green), 10M (teal), and pure MeOH (blue) vs Ag/AgCl. (b) Same data as (a), on a semi-logarithmic plot. (c) Theoretical $[O_2]$ produced under 2 suns (lines) and measured $[O_2]$ (shapes) for a hematite electrode in contact with H_2O (solid line and circles), 0.2M MeOH (dotted line and downward triangles), 2M (short dashed line and squares), 5M (green double dotted dashed line and diamonds), 10M (long dashed line and upward triangles), and pure MeOH (single dotted line and hexagons). Measured at 1.4 and 1.6 V vs Ag/AgCl for aqueous and the MeOH electrolyte respectively. (d) Same as (c) but for 0.75 V vs Ag/AgCl (CH_3OH not shown).

Table 7-1. Summary of faradaic efficiency due to O_2 generation for varying concentrations of CH_3OH in H_2O

0.75 V vs Ag/AgCl					
		[O_2] / μmoles L^{-1}			
[CH_3OH]/ M	**[H_2O] / M**	**Theoretical**	**Measured**	**O_2 Faradaic Efficiency**	**Relative Rate***
0.0	55.0	11.17	11.11	**99.42%**	
0.2	58.0	7.90	5.41	**68.48%**	133.48
2.0	51.0	12.90	4.01	**31.09%**	56.52
5.0	44.0	10.77	1.89	**17.55%**	41.35
10.0	33.0	7.29	0.59	**8.06%**	37.65
1.4 V vs Ag/AgCl					
		[O_2] / μmoles L^{-1}			
[CH_3OH]/ M	**[H_2O] / M**	**Theoretical**	**Measured**	**O_2 Faradaic Efficiency**	**Relative Rate***
0.0	55.0	50.13	49.81	**99.36%**	
0.2	58.0	49.20	36.00	**73.17%**	106.33
2.0	51.0	55.15	28.35	**51.40%**	24.11
5.0	44.0	53.15	22.80	**42.90%**	11.71
10.0	33.0	49.86	15.94	**31.97%**	7.02

*Ratio of CH_3OH to H_2O oxidation

Mott Schottky plots were generated for pure H_2O, CH_3OH and 5M CH_3OH electrolytes by fitting impedance spectra measured under dark conditions to a Randle's circuit. Since the electrode, and therefore dopant density, is the same for all electrolytes, the slope of the Mott Schottky is expected to be independent of the electrolyte. This is indeed the case, apparent from inspection of figure 7-2a. Therefore, to fit the Mott Schottky plots, the slopes of all 3 electrolytes were fit globally. The extracted dopant density, N_D, was calculated to be 5.3×10^{18} cm^{-3}, in good correspondence with previous results.[13,14] The flat band potential was also calculated from the Mott Schottky plots to be 0.137, 0.143 and 0.330 V vs. Ag/AgCl for H2O, 5M CH_3OH and pure CH_3OH respectively. The measured E_{FB} for the aqueous electrolytes are nearly equal. In pure CH_3OH however, the E_{FB} is moved ~200 mV positive. Part of the difference in *J-V* curves can therefore be attributed to a shift in the band energies. In order to carry out an adequate comparison between the different electrolytes, potentials were normalized to their respective E_{FB}'s. Normalized *J-V* curves are shown in Figure 7-2b. At high positive applied potentials, the current achieved in all electrolytes is approximately equal. We have suggested previously that in these thin films, at high applied potential, all of the holes that reach the surface oxidize water. Thus, adding a fast hole collector (e.g. H_2O_2, CH_3OH, $Fe(CN)_6^{3-/4-}$) should not increase the current at a given positive Fermi level. Even when correcting for the change in the E_{FB}, the steep current onset of pure CH_3OH oxidation occurs at more positive potentials compared to H_2O oxidation suggesting that photoelectrochemical differences cannot be solely attributed to differences in the position of the bands of Fe_2O_3 in different media.

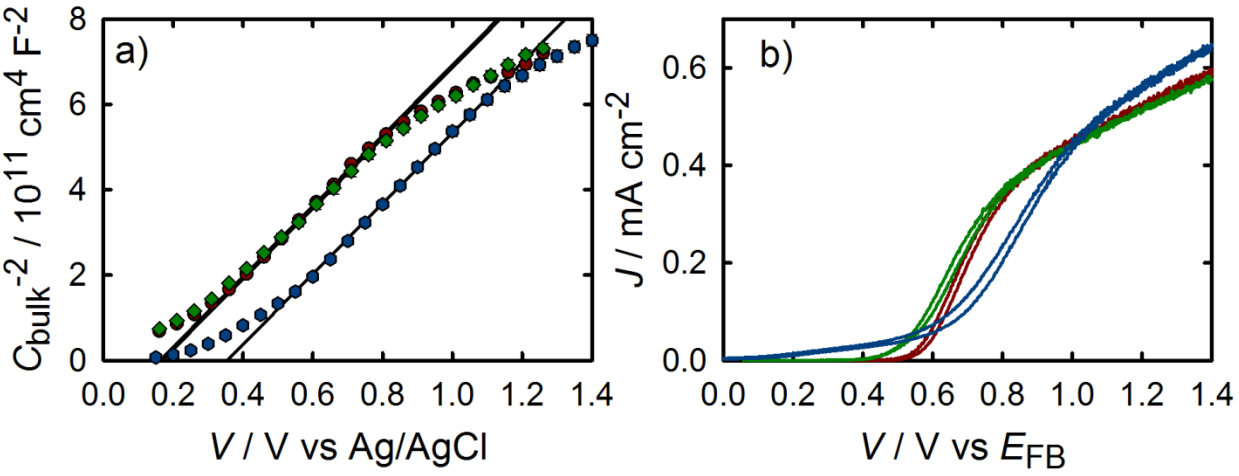

Figure 7-2. (a) Mott Schottky plot of C_{bulk} measured in the dark for H_2O (red circles), 5M CH_3OH (green diamonds) and CH_3OH electrolytes (blue hexagons). (b) *J-V* curves of a hematite electrode under 1 sun illumination in contact with H_2O (red), 5M CH_3OH (green) and CH_3OH (blue) plotted vs E_{FB}.

7.3.2 Electrochemical Impedance Spectroscopy

In order to get more detailed mechanistic information of water and methanol oxidation, impedance spectroscopy (IS) was employed under illuminated conditions. Aqueous electrolytes produced Nyquist plots with two clearly distinguishable semicircles near the current onset potential which are shown in Figure 7-3a. A physical model which has been previously developed for the interpretation of charge transfer from hematite electrodes to water can be seen in the form of an equivalent circuit, EC, shown in Figure 7-4a.[13,14] This general model includes the presence of a surface state able to capture conduction band electrons and valence band holes; the trapping-detrapping kinetics are related to R_{trap}, and the occupancy of the surface state

produces a capacitance, C_{ss}. Charge transfer takes place through this surface state with a charge transfer resistance, $R_{ct,ss}$. Additionally, a bulk capacitance, C_{bulk}, accounts for the space charge capacitance. This EC was used to fit IS data gathered in H_2O and 5M CH_3OH electrolytes. For the pure H_2O electrolyte, a clear peak in C_{ss} develops with voltage which is coincident with the current onset potential (Figure 7-5a). This peak highlights the requirement for charge accumulation at the surface for water oxidation to occur, and has been pointed out by other researchers.[15] When CH_3OH is added to the aqueous solution, a C_{ss} peak is also observed, at the same potential vs E_{FB} as shown in Figure 7-5a. The magnitude of this peak is lower, however, reflecting that fewer holes are accumulated at the surface. This result is in good agreement with the O_2 evolution measurements displayed in Figures 7-1c and 7-1d, which indicated that both oxidation of water and methanol lead to the obtained photocurrent. A corresponding decrease in C_{ss} and O_2 generation with the addition of CH_3OH further shows that water oxidation occurs through a surface state intermediate. Despite methanol reducing the measured capacitance of surface states due to water oxidation, two capacitive features are still observed in impedance spectra measured in the pure methanol electrolyte (Figure 7-3b). Since it appears that charge transfer to methanol occurs through a different pathway than that of water, we invoke another possible EC to describe pure methanol oxidation at hematite electrodes shown in figure 7-4b. This model was chosen due to its corroboration with photoelectrochemical experiments discussed below. As in the EC used to describe H_2O oxidation, this EC still contains a surface state capacitance, C_{ss} and a resistance of transfer to those surface states, R_{trap},

based on the observation of 2 clear capacitances in the Nyquist plot. However, instead of charge transfer through those surface sates, this EC contains a separate charge transfer resistance which is not directly associated with those surface states, R_{ct}. This model could imply direct charge transfer from the valence band of the hematite to methanol through an outersphere electron transfer mechanism. However, a more likely possibility is that a surface state or surface intermediate is generated, such as a surface adsorbed methoxy species (Fe-O-CH_3) which is the analogous adsorbed species responsible for charge transfer for photogenerated holes on TiO_2.[10] This mechanism could be interpreted as a single charge transfer resistance if the steady state concentration is very low, resulting in a very low or immeasurable capacitance. By using this model, the obtained surface state capacitance shows a double peak feature, with a significantly lower intensity compared to water based electrolytes (Figure 7-5a).

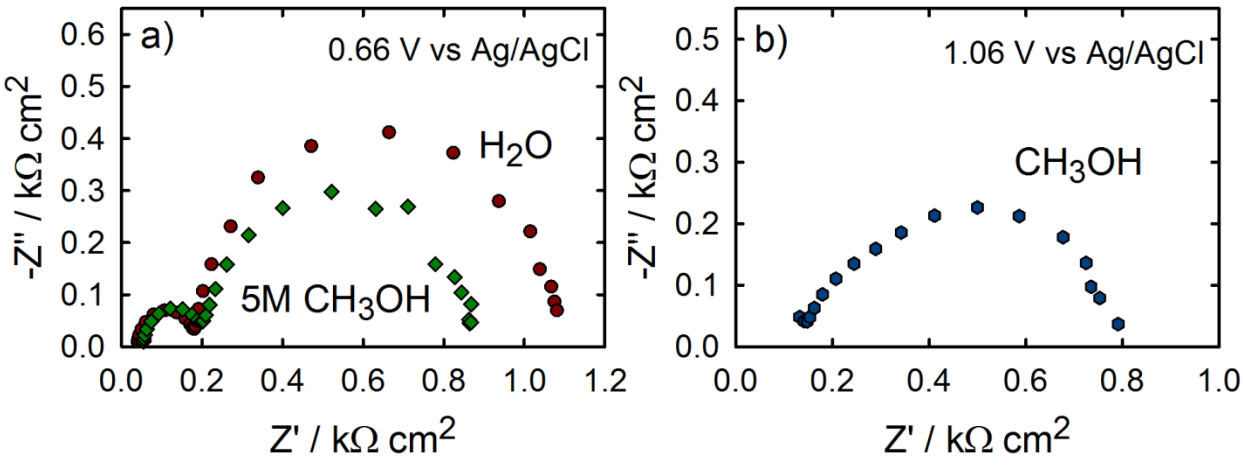

Figure 7-3. (a) Nyquist plots of impedance data gathered under 1 sun illumination for a H_2O (red circles) and 5M CH_3OH in H_2O (green diamonds) electrolytes at 0.66 V vs Ag/AgCl. (b) Nyquist plot in CH_3OH measured at 1.06 V vs Ag/AgCl.

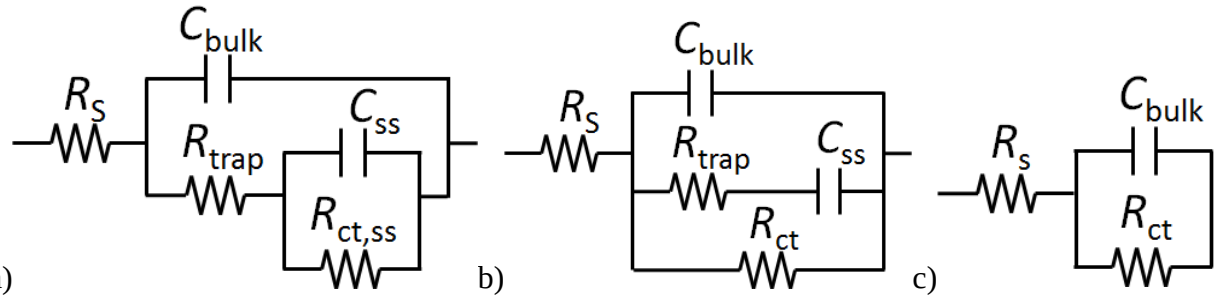

Figure 7-4. (a) Equivalent circuit used to analyze impedance data measured for hematite electrodes in contact with electrolytes containing H_2O (b) Equivalent circuit used to analyze impedance data measured for hematite electrodes in contact with pure CH3OH electrolytes. (c) Randles circuit.

The values of charge transfer resistance, R_{ct}, are shown in Figure 7-5b for the different electrolytes. At low bias (0 - 0.4V vs E_{FB}), the addition of CH_3OH to H_2O reduces the charge transfer resistance. This is because we are measuring the charge transfer resistance from the surface states (due to water oxidation) which is reduced with the addition of CH_3OH, as shown by O_2 evolution measurements and C_{ss}. In other words, for a constant potential, the resistance of charge transfer to water through water oxidation intermediates is reduced because the current due to water oxidation is reduced. Compared to aqueous electrolytes, R_{ct} for methanol oxidation is higher positive of 0.4 V vs E_{FB}, consistent with the lower photocurrents measured at more anodic bias. The values of R_{trap} are compiled in Figure 7-5c, and are identical for both water based electrolytes and higher for pure methanol between 0 V vs E_{FB} and 0.7 V vs E_{FB}.

Confirmation of the fits can be gained by plotting the total resistance from impedance ($R_{tot}=R_s+R_{trap}+R_{ct,ss}$ for aqueous electrolytes and $R_{tot}=R_s+R_{ct,bulk}$ for the CH_3OH electrolyte) and comparing that to the resistance calculated from the *J-V* curves ($R_{tot}=dV/dJ$). This plot can be seen in figure 7-5d. All electrolytes show R_{tot} from *J-V* curves and R_{tot} from IS are in good general agreement indicating that the main resistances which control the *J-V* are represented in the impedance spectra. It is interesting to note that pure methanol oxidation involves two different R_{tot} dips, around 0.4 V vs E_{FB} and 0.8 V vs E_{FB}, related to the two small trap C_{ss} peaks shown in Figure 7-5a. This suggests that two different oxidation mechanisms exist; one between 0.2-0.6 V vs E_{FB} where the slope of the *J-V* curve is low, and one above 0.6 V vs E_{FB}, where the *J-V* curve takes a similar slope as that of aqueous solutions (see Figure 7-2b).

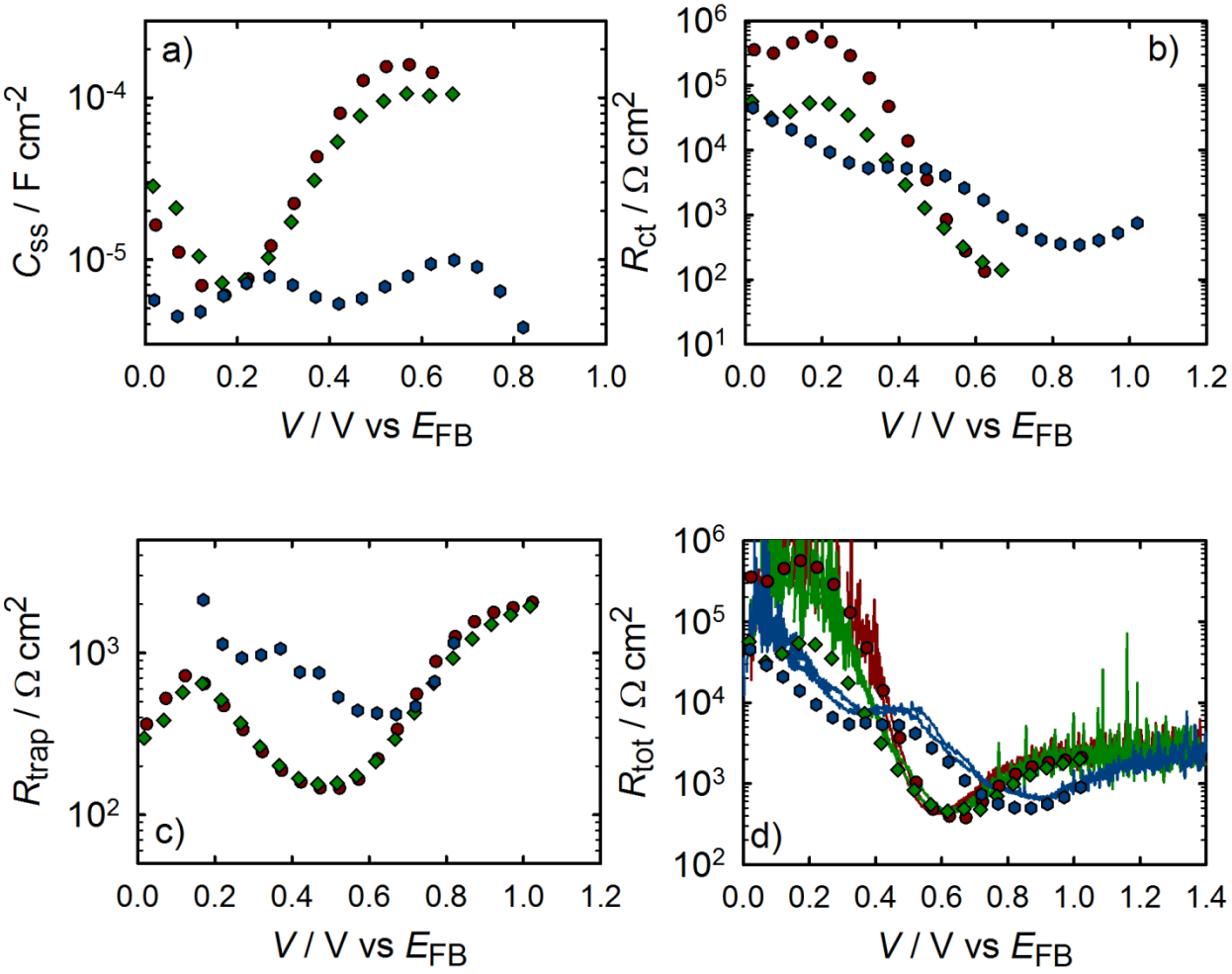

Figure 7-5. (a) C_{ss} (b)R_{ct}, (c)R_{trap} and (d) R_{tot} vs E_{FB} extracted from IS analysis under illumination (100 mW·cm^2) for a hematite electrode in contact with H_2O (red circles) 5M CH_3OH in H_2O (green diamonds) and CH_3OH (blue hexagons).

7.4.3 Cyclic Voltammetry

Cyclic voltammetry experiments were carried out on Fe_2O_3 films to measure surface states as previously reported.[13] First, high positive bias (1.6 V vs Ag/AgCl for aqueous electrolytes and 1.8 V vs Ag/AgCl for methanol electrolyte) was applied under illumination to

fill the surface states with holes. The light was then turned off and a CV was immediately scanned several times (Appendix Figure A7-1). Cathodic peaks were observed for all electrolytes on the first scan at potentials similar to the potentials where a C_{ss} is observed from IS measurements (Figure 7-6). These peaks are observed at the same energy and with similar relative intensity to those observed in the peaks of C_{ss} in Figure 7-5a. Additional figures including data measured in all CH_3OH electrolytes can be seen in figure 7-6b which confirms the trend of decreasing cathodic peak currents with the addition of CH_3OH. On the second scan, these peaks disappear because the surface states are not reoxidized on the timescale of this experiment (Appendix, Figure A7-1). The evolution of this peak with scan rate (Appendix, Figure A7-2) also confirms its capacitive nature. Upon zooming in on the cyclic voltammetry curve for methanol (Figure 7-6b), two small peaks are evident, which is consistent with the C_{ss} measured by IS using the model in figure 7-4b. It should be noted that these two peaks were not observed in the IS interpretation using the model in figure 7-4a. Thus these two peaks corroborate the selection of the equivalent circuit for interpreting CH_3OH oxidation at the hematite surface.

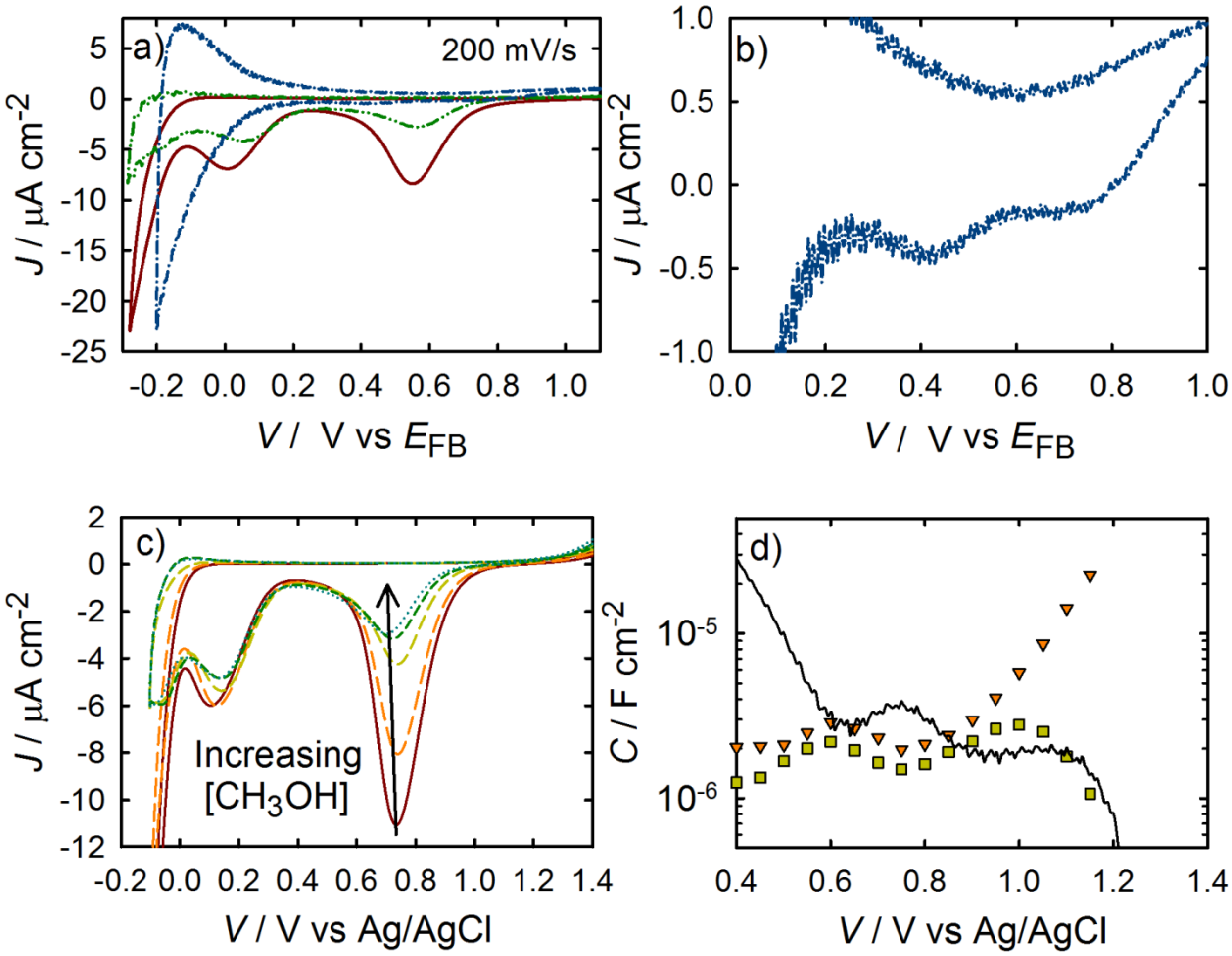

Figure 7-6. (a) Comparison of the first scan of the CV measured at 200 mV/s in H_2O (red solid line), 5M MeOH in H_2O (green double dot dashed line) and MeOH (blue single dot dashed line). (b) A magnified image of the MeOH curve which shows 2 small peaks. (c) First scan of the CVs measured in the dark for a hematite electrode in contact with H_2O (red), 0.2 M (orange), 2 M (yellow), 5M (green), and 10 M MeOH (teal) measured at 200 mV/s). (d) C_{ss} values fit from model shown in figure 7-3a (orange triangles) and C_{ss} values fit from model shown in figure 7-3b (yellow squares) as well as capacitance calculated of the first scan of CV experiments in MeOH solution measured at 1000 mV/s . C=J/scan rate.

The capacitive nature of the surface states of both H_2O and CH_3OH surface states was examined by transient light experiments. Chopped light *J-V* curves were obtained and compared to those with constant illumination (Appendix, Figure A7-3). In all tested electrolytes, the presence of anodic and cathodic transients indicated the presence of surface states.[8,16,17] These spikes were analyzed quantitatively by switching the light on (anodic) and off (cathodic) at a constant potential while measuring the current as a function of time. Examples of current transients can be seen in Figure 7-7a and in Appendix Figures A7-4 through A7-7. Integration of the cathodic current provides a quantitative measurement of the charge stored in the surface states, which is Figure 7-7b. The charge measured in the current transients was compared to the C_{ss} measured by impedance and a good agreement in the trend was observed, confirming that the current transients are primarily a result of charging and discharging of surface states.

Single exponential lifetimes of the cathodic transients were calculated and can be seen in Figure 7-7c. The lifetimes are approximately equal for H_2O and 5M CH_3OH electrolytes throughout the potential range with the exception of potentials greater than ~0.6 V vs E_{FB} where the mixture has lower lifetimes. These decays are attributed to electrons from the conduction band reducing the oxidized surface states. Since the dominant surface state is related to water oxidation, it is not surprising that these measured lifetimes are constant for the two aqueous electrolytes. We note that this result disagrees with Cowan *et. al.* who showed a decrease in lifetime for a 10% CH_3OH in H_2O solution compared to a H_2O solution under no applied bias.[18] It is possible, however, the techniques of transient electrochemistry employed herein and transient absorption spectroscopy employed by Cowan *et. al.* are measuring different species. In

the CH_3OH electrolyte, the lifetimes of these transients are approximately an order of magnitude lower than those measured in aqueous electrolytes at potentials where photocurrent is measured. This is attributed to an increased rate of recombination to surface CH_3OH oxidation intermediates compared to surface H_2O oxidation intermediates.[11]

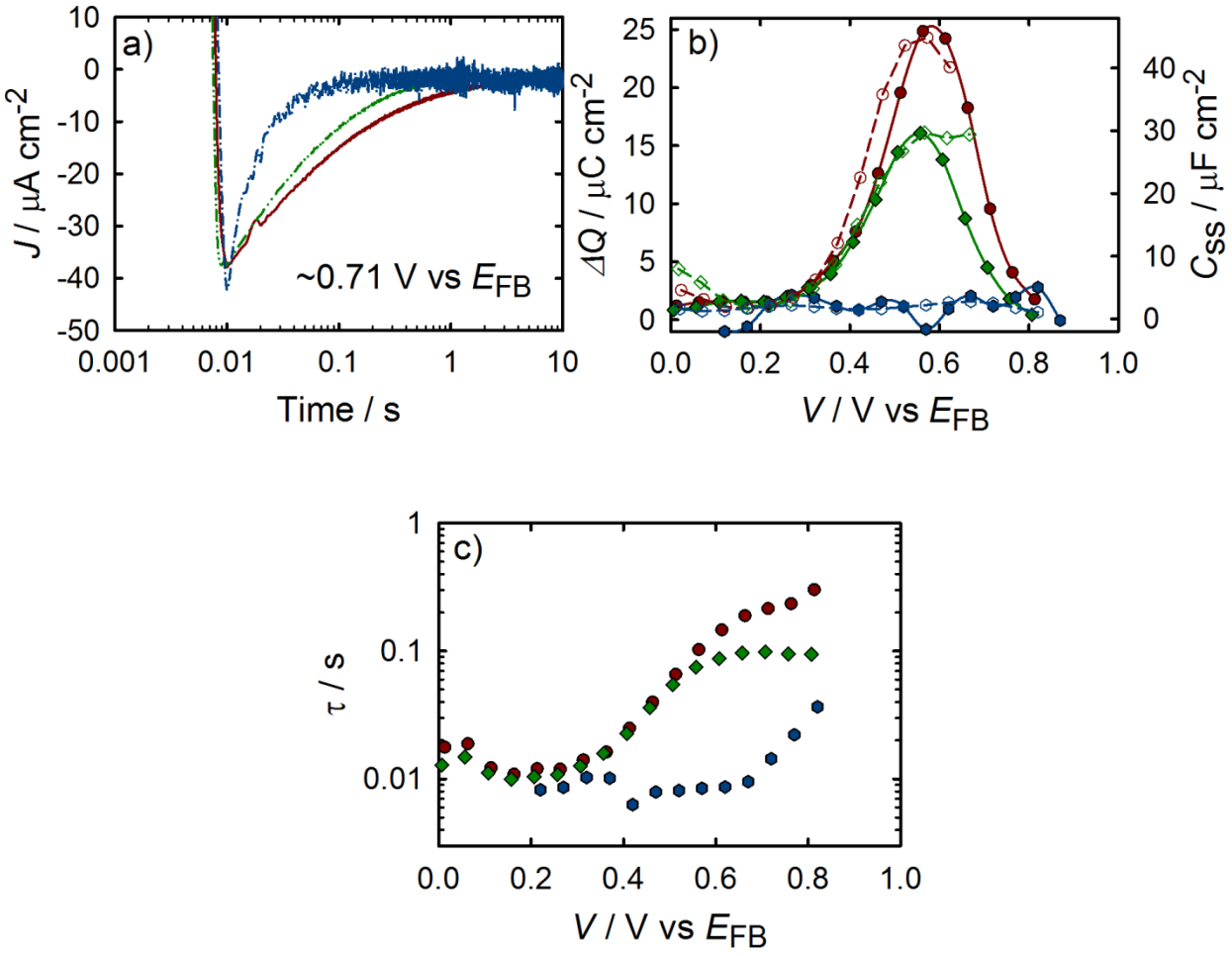

Figure 7-7. (a) Cathodic transients in H_2O (red solid line), 5M CH_3OH in H_2O (green double dot dashed line) and CH_3OH (blue single dot dashed line) measured within 5 mV of 0.71 V vs E_{FB}. (b) The calculated charge passed measured by integrating cathodic transients (filled symbols, solid lines) along with C_{trap} measured by IS (hollow symbols, dashed lines) for a hematite electrode in contact with H_2O (red circles) 5M CH_3OH in H_2O (green diamonds) and CH_3OH (blue hexagons). (c) Lifetimes of transients fit by a single exponential decay for H_2O (red circles), 5M CH_3OH (green diamonds), and CH_3OH (blue hexagons).

7.5 Discussion

From the double peak feature observed for C_{ss} from EIS analysis of pure methanol oxidation, correlated to respective dips in the charge transfer resistance (R_{ct}) and total resistance (R_{tot}), it appears that methanol oxidation takes place by two distinct processes, as previously mentioned. While there is limited information studying the photooxidation of methanol on hematite electrodes, there is a wealth of information of the photooxidation of methanol on TiO_2 which is often considered as a model system for metal oxide surfaces.[3,19] There are two general mechanisms typically discussed for methanol oxidation at TiO_2 photoelectrodes: (1) a direct charge transfer mechanism where an adsorbed methanol or methoxy species is directly oxidized, or (2) an indirect charge transfer mechanism where a surface hydroxyl is oxidized which subsequently oxidizes methanol. The existence of these two mechanisms are said to be responsible for both formate and formaldehyde intermediates identified during methanol oxidation. There is, however, discrepancy when assigning the mechanism responsible for a particular intermediate where several researchers discuss formate and formaldehyde as a result of direct and indirect mechanism respectively,[4,20] whereas others propose the opposite relationship.[6] When considering a direct mechanism, there has also been significant debate over whether the relevant photogenerated hole transfer occurs through a surface adsorbed molecular methanol or through a dissociatively adsorbed methoxy group.[3,19] Both molecular and dissociatively absorbed methoxy groups are commonly observed on TiO_2 which agrees with DFT calculations which show molecular and dissociated states on a Ti^{4+} site are nearly

isoenergetic.[21-23] More recently, studies employing temperature programmed desorption on (110) rutile TiO_2[10] and FTIR on anatase nanoparticle TiO_2[12] have found that the most relevant hole transfer is through a dissociatively adsorbed methoxy species. The observation of different possible reactants (adsorbed methanol, methoxy, hydroxyl species) combined with possible mechanisms (direct, indirect) and intermediates (formate, formaldehyde), show that methanol oxidation may occur via different reaction pathways on TiO_2. It is not surprising then that the *J-V* curve, surface state capacitance and charge transfer resistance measured for water oxidation at hematite photoelectrodes shows two oxidation features at different potentials. The molecular details of this mechanism are currently being investigated in our lab.

7.6 Conclusions

Fe_2O_3 photoanodes synthesized by atomic layer deposition were electrochemically characterized with H_2O, CH_3OH and H_2O- CH_3OH mixture electrolytes. Compared to aqueous electrolytes, the photo-oxidation of methanol required a more anodic bias to sustain similar photocurrent values. The corresponding decrease in the O_2 generation and C_{ss} with the addition of CH_3OH further confirms that the surface states are actively participating in the hole transfer mechanism to H_2O, as suggested in previous studies.[13,14] This reduction in surface states has been measured by IS, CV and transient measurements. IS analysis suggests that methanol oxidation occurs through a single resistor which does not involve the build up of a capacitance through a surface state. It should be noted, however, that a simple outersphere hole transfer to CH_3OH cannot be assigned with certainty. An innersphere mechanism is possible if the

intermediate had a very low and capacitance, resulting in an equivalent circuit parameter appearing as a simple charge transfer resistance. More work is necessary to determine the nature of this charge transfer. A significantly lower surface state capacitance with two distinct peaks associated with corresponding charge transfer dips was also identified for methanol oxidation, suggesting two different reaction mechanisms depending on the applied bias.

7.7 Acknowledgements

I would like to thank Sixto Gimenez, Francisco Fabregat-Santiago, Juan Bisquert and Thomas Hamann for contributing to this work.

APPENDIX

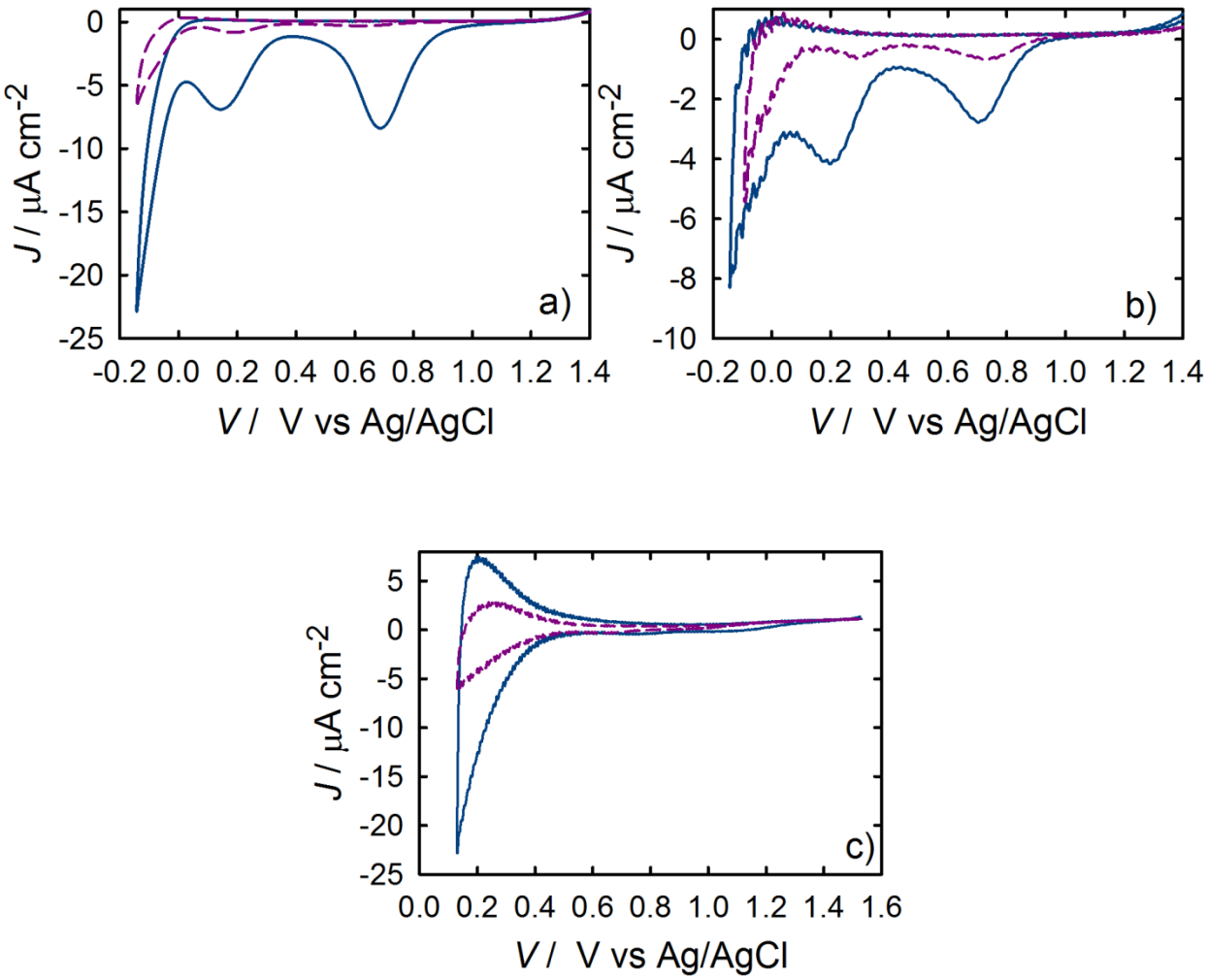

Figure A7-1. The first (solid blue line) and second (dashed purple line) scan of a CV measured in the dark of a hematite electrode in contact with (a) H_2O (b) 5M CH_3OH in H_2O (c) and CH_3OH

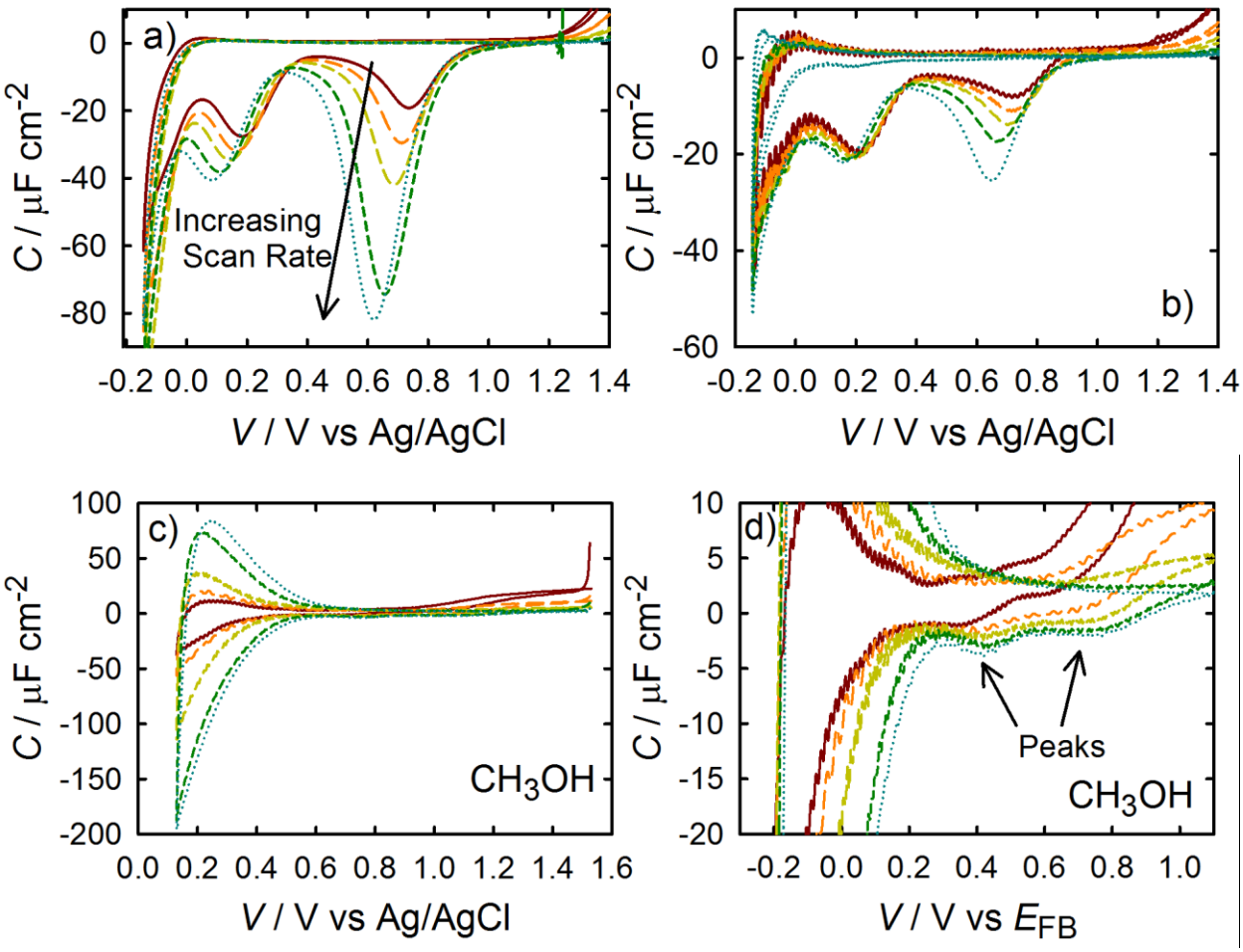

Figure A7-2. Calculated capacitance of the first scan of the CVs measured in the dark for a hematite electrode in contact with (a) H_2O (b) 5M CH_3OH in H2O (c) and CH_3OH. (d) Magnified image of (c). The capacitance was calculated by C=J/scan rate. Scan rates were 50 mV/s (red solid line), 100 mV/s (orange long line), 200 mV/s (yellow short line), 500 mV s (green shorter line) and 1000 mV/s (blue dotted line)

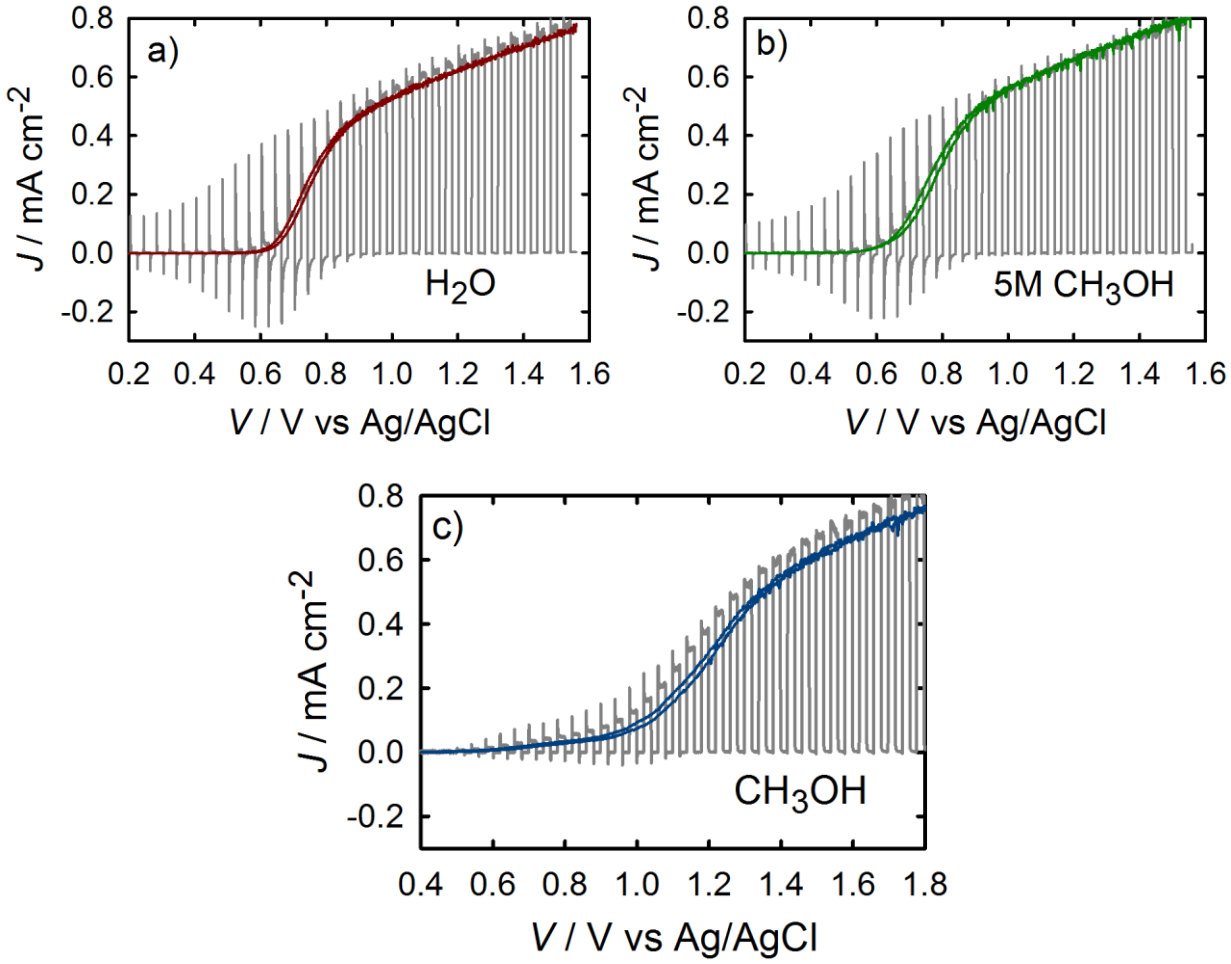

Figure A7-3. Chopped light (grey line) and steady state (colored line) *J-V* measured for a hematite electrode in contact with (a) H_2O (b) 5M CH_3OH in H_2O and (c) CH_3OH.

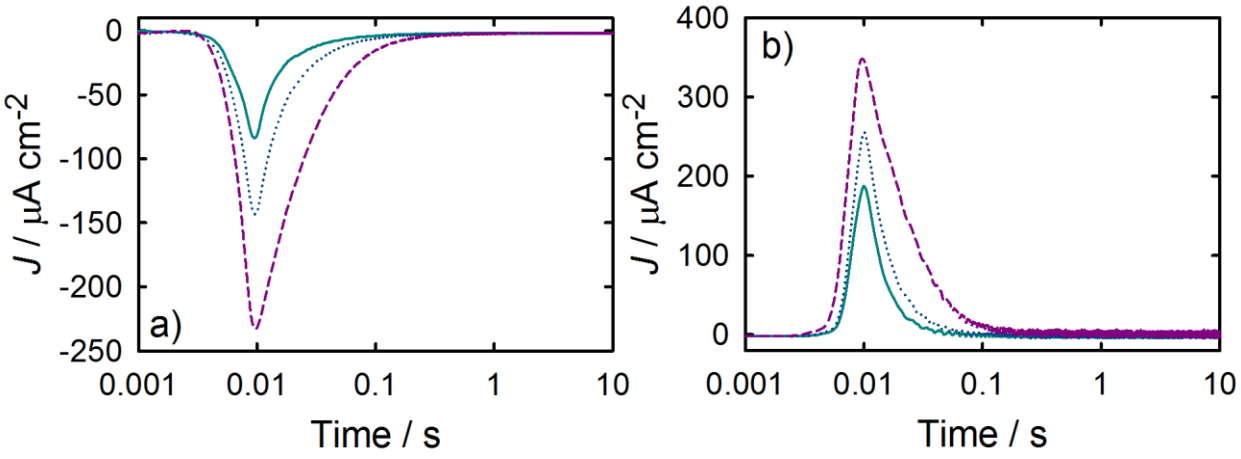

Figure A7-4. (a) cathodic and (b) anodic transients measured for a hematite electrode in contact with H_2O at applied potentials of 0.35 (solid teal line), 0.45 (dotted blue line) and 0.55 (dashed purple line) V vs Ag/AgCl.

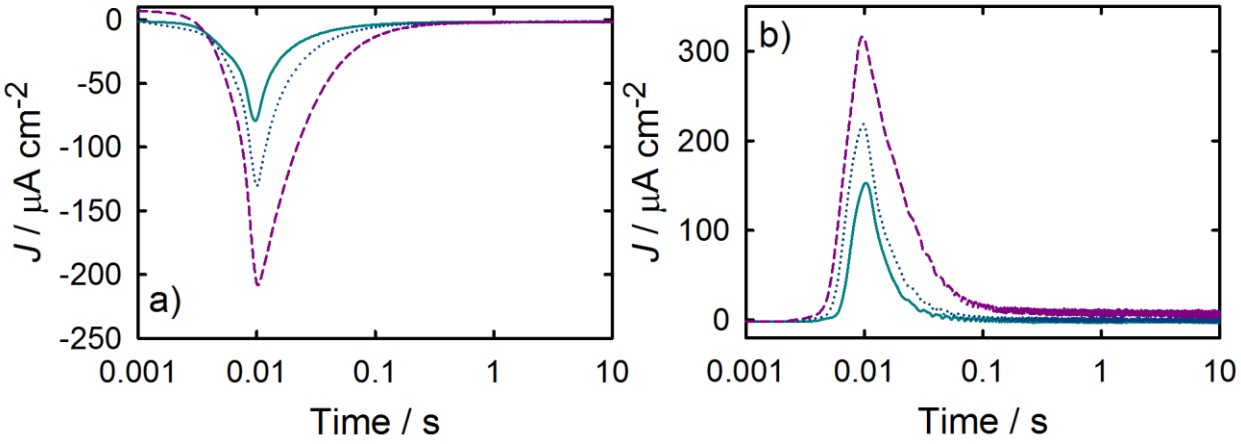

Figure A7-5. (a) cathodic and (b) anodic transients measured for a hematite electrode in contact with 5M CH_3OH in H_2O at applied potentials of 0.35 (solid teal line), 0.45 (dotted blue line) and 0.55 (dashed purple line) V vs Ag/AgCl.

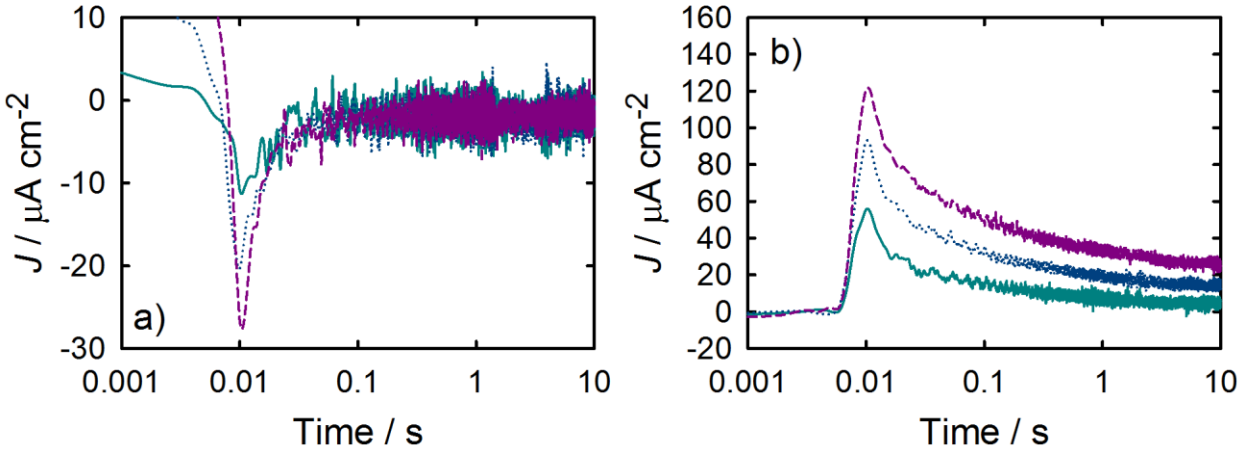

Figure A7-6. (a) cathodic and (b) anodic transients measured for a hematite electrode in contact CH_3OH at applied potentials of 0.55 (solid teal line), 0.65 (dotted blue line) and 0.75 (dashed purple line) V vs Ag/AgCl.

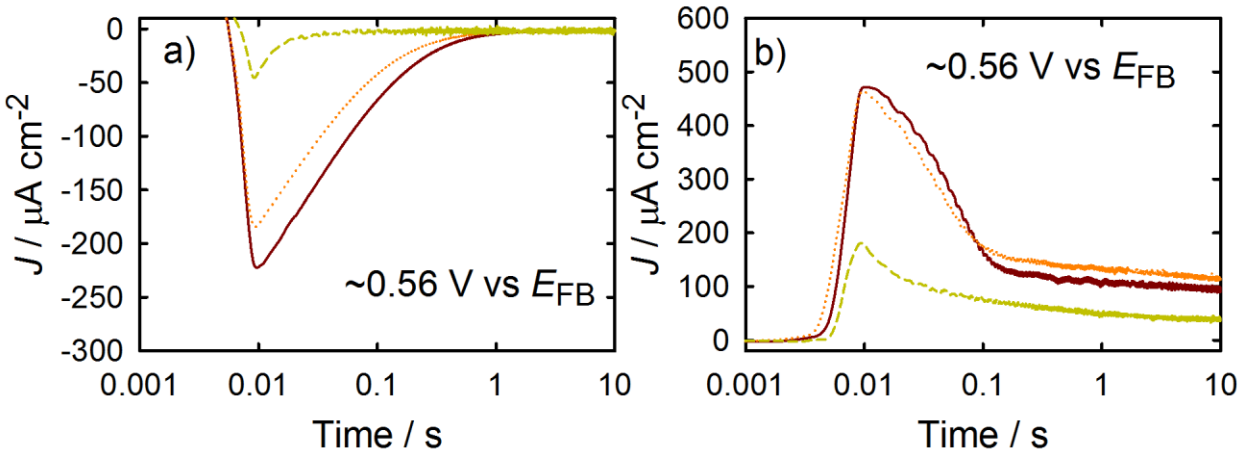

Figure A7-7. (a) anodic and (b) cathodic transients in H_2O (red solid line), CH_3OH in H_2O (orange dotted) and MeOH (yellow dashed line) measured within 5 mV of 0.56 V vs E_{FB}.

REFERENCES

REFERENCES

1. Iwasita, T. *Electrochim. Acta,* **2002**, *47*, 3663-3674.

2. Hoffmann, M. R.; Martin, S. T.; Choi, W.; Bahnemann, D. W. *Chem. Rev.* **1995**, *95*, 69-96.
3. Henderson, M. A. *Surf. Sci. Rep.* **2011**, *66*, 185-297.

4. Wang, C.-y.; Rabani, J.; Bahnemann, D. W.; Dohrmann, J. K. *J. Photochem. Photobiol., A* **2002**, *148*, 169-176.

5. Zhou, C.; Ren, Z.; Tan, S.; Ma, Z.; Mao, X.; Dai, D.; Fan, H.; Yang, X.; LaRue, J.; Cooper, R.; Wodtke, A. M.; Wang, Z.; Li, Z.; Wang, B.; Yang, J.; Hou, J. *Chem. Sci.* **2010**, *1*, 575-580.

6. Wu, W.-C.; Chuang, C.-C.; Lin, J.-L. *J. Phys. Chem. B,* **2000**, *104*, 8719-8724.

7. Pendlebury, S. R.; Barroso, M.; Cowan, A. J.; Sivula, K.; Tang, J. W.; Gratzel, M.; Klug, D.; Durrant, J. R. *Chem. Commun.* **2011**, *47*, 716-718.

8. Dotan, H.; Sivula, K.; Gratzel, M.; Rothschild, A.; Warren, S. C. *Energy Environ. Sci.* **2011**, *4*, 958-964.

9. Klahr, B. M.; Hamann, T. W. *J. Phys. Chem. C,* **2011**, *115*, 8393-8399.

10. Shen, M.; Henderson, M. A. *J. Phys. Chem. Lett.* **2011**, *2*, 2707-2710.

11. Villarreal, T. L.; Gomez, R.; Neumann-Spallart, M.; Alonso-Vante, N.; Salvador, P. *J. Phys. Chem. B,* **2004**, *108*, 15172-15181.

12. Panayotov, D. A.; Burrows, S. P.; Morris, J. R. *J. Phys. Chem. C,* **2012**, *116*, 6623-6635.

13. Klahr, B.; Gimenez, S.; Fabregat-Santiago, F.; Bisquert, J.; Hamann, T. *Energy Environ. Sci.* **2012**, *5*, 7626-7636.

14. Klahr, B.; Gimenez, S.; Fabregat-Santiago, F.; Hamann, T.; Bisquert, J. *J. Am. Chem. Soc.* **2012**, *134*, 4294-4302.

15. Cummings, C. Y.; Marken, F.; Peter, L. M.; Tahir, A. A.; Wijayantha, K. G. U. *Chem. Commun.* **2012**, *48*, 2027-2029.

16. McDonald, K. J.; Choi, K. S. *Chem. Mater.* **2011**, *23*, 1686-1693.

17. Le Formal, F.; Tetreault, N.; Cornuz, M.; Moehl, T.; Gratzel, M.; Sivula, K. *Chem. Sci.* **2011**, *2*, 737-743.

18. Cowan, A. J.; Barnett, C. J.; Pendlebury, S. R.; Barroso, M.; Sivula, K.; Grätzel, M.; Durrant, J. R.; Klug, D. R. *J. Am. Chem. Soc.* **2011**, *133*, 10134-10140.

19. Diebold, U. *Surf. Sci. Rep.* **2003**, *48*, 53-229.

20. Araña, J.; Doña-Rodríguez, J. M.; Cabo, C. G. i.; González-Díaz, O.; Herrera-Melián, J. A.; Pérez-Peña, J. *Appl. Catal., B* **2004**, *53*, 221-232.

21. Guo, Q.; Xu, C.; Ren, Z.; Yang, W.; Ma, Z.; Dai, D.; Fan, H.; Minton, T. K.; Yang, X. *J. Am. Chem. Soc.* **2012**, *134*, 13366-13373.

22. de Armas, R. S.; Oviedo, J.; San Miguel, M. A.; Sanz, J. F. *J. Phys. Chem. C,* **2007**, *111*, 10023-10028.

23. Oviedo, J.; Sánchez-de-Armas, R. o.; San Miguel, M. A. n.; Sanz, J. F. *J. Phys. Chem. C* **2008**, *112*, 17737-17740.

Chapter 8:

Photoelectrochemical and Impedance Spectroscopic Investigation of Water Oxidation with "Co-Pi" coated Hematite Electrodes

Adapted with permission from:

Photoelectrochemical and Impedance Spectroscopic Investigation of Water Oxidation with "Co-Pi"-Coated Hematite Electrodes, Benjamin M. Klahr, Sixto Gimenez, Francisco Fabregat-Santiago, Juan Bisquert and Thomas W. Hamann. *Journal of the American Chemical Society*, **2012**, *134*, 16693-16700.

8.1 Abstract

Uniform thin films of hematite (α-Fe_2O_3) deposited by atomic layer deposition (ALD) coated with varying amounts of the cobalt phosphate catalyst, "Co-Pi," were investigated with steady state and transient photoelectrochemical measurements as well as impedance spectroscopy. Systematic studies as a function of Co-Pi thickness were performed in order to clarify the mechanism by which Co-Pi enhances the water splitting performance of hematite electrodes. It was found that under illumination, the Co-Pi catalyst can efficiently collect and store photogenerated holes from the hematite electrode. This improved charge separation reduces surface state recombination which results in increased water oxidation efficiency. It was also found that thicker Co-Pi films produced increased water oxidation efficiencies which are attributed to a combination of superior charge separation and increased surface area of the porous film. These combined results provide important new understanding of the enhancement and limitations of the Co-Pi catalyst coupled with semiconductor electrodes for water splitting applications.

8.2 Introduction

The previous three chapters discussed how a large applied potential is required to achieve efficient photoelectrochemical (PEC) water oxidation at hematite electrodes. This large photocurrent onset potential is generally attributed to slow water oxidation kinetics at the hematite surface which competes with surface state recombination.[1-5] In order to reduce the required applied potential, various catalysts have been added to the hematite surface including IrO_2, cobalt ions and the cobalt phosphate catalyst, "Co-Pi".[6-12] Co-Pi has specifically gained a lot of recent attention because it uses earth-abundant elements, shows effective water oxidation characteristics and is stable over time due to its "self-healing" mechanism.[13-15] Consequently, it has also been applied to many potential photoanodes including ZnO, $BiVO_4$, Si and Fe_2O_3, and has shown improvements in both current onset potential and photocurrent density.[7-11,16-22] The reasons for this improvement, however, are not yet fully understood. Thus far, the increased performance has been attributed to accelerating the oxygen evolution kinetics,[7] increasing band bending,[11,23] facilitating charge separation[7,8] and reducing surface state recombination.[10] Despite the cathodic shift frequently measured for Co-Pi coated electrodes, Zhong and Gamelin described evidence of a kinetic bottleneck on Co-Pi coated hematite electrodes.[9] Thorough knowledge of the physical origin of both the improvement and limitation of water oxidation with Co-Pi coated hematite electrodes is essential to guide further advances in catalyst and semiconductor design and integration into PEC water splitting systems.

In this work, we employ photoelectrochemical measurements and impedance spectroscopy to investigate the effect of the Co-Pi catalyst on thin film hematite electrodes. The

thin film hematite electrodes were prepared by atomic layer deposition (ALD),[24-26] and were subsequently coated with Co-Pi films by photoelectrodeposition.[9,10,21] These thin hematite films have been shown to be a good model system for studying the limitations of water oxidation at the hematite surface, thus allowing us to separate the effect of the catalyst from the bare electrode.[27,28] Also, the planar geometry of these films allowed us to perform a controlled thickness dependence study where increasing the amount of Co-Pi deposited uniformly increases the Co-Pi thickness in one dimension. The Co-Pi coated hematite films were also analyzed by impedance spectroscopy and PEC experiments as a function of Co-Pi thickness to elucidate the factors controlling the enhanced performance of the Co-Pi coated hematite electrode. These combined results provide new insight and allow for further development of a thorough mechanistic picture of this important system.

8.3 Experimental

Thin films of hematite were deposited on fluorine-doped tin oxide (FTO) coated glass substrates (Hartford Glass, 12 Ω cm^{-2}) by ALD (Savannah 100, Cambridge Nanotech Inc.) using ferrocene as the metal precursor and ozone as the oxidation source. ALD is a process which employs alternating metal precursor and oxidation pulses, each separated by a nitrogen purge such that chemistry only occurs in a self-limiting fashion where the previous precursor has adsorbed. The metal precursor was heated to 70°C and pulsed for 20 seconds. After purging the oxidation pulse was performed. The oxidation pulse consisted of a 0.015 second pulse of H_2O, immediately followed by a 1 second pulse of ozone (~4.5% by weight O_3 in ultra-high purity O_2 produced by Yanco Industries ozone generator), followed by a 5 second purge time. This cycle

was performed 10 times to create 1 oxidation macrocycle. Integrating water with O_3 has been found to be necessary for uniform deposition of hematite in our system. Films were prepared by 1000 ALD cycles and measured to be ~60 nm by absorption measurements (Perkin Elmer, Lambda 35 with a Labsphere integrating sphere) corrected for reflection as described previously, as well as ellipsometric measurements (Horiba Jobin Yvon, Smart-SE).[26] Films were characterized by Raman Spectroscopy and XRD of these films previously.[26] Hematite electrodes were masked with a 60 μm Surlyn film (Solaronix) with a 0.28 cm^2 hole to define the active area and to prevent scratching of the thin films. Surlyn films were adhered to the electrodes by heating to 120 °C. The protected hematite films were clamped to a custom made glass electrochemical cell. A homemade saturated Ag/AgCl electrode was used as a reference and was frequently calibrated to a commercial saturated calomel reference electrode (Koslow Scientific). Potentials vs Ag/AgCl were converted to the reversible hydrogen electrode (RHE) scale by the equation $E_{RHE} = E_{Ag/AgCl} + 0.197V + (0.059V)\,pH$. A high surface area platinum mesh was used as the counter electrode.

Co-Pi catalyst films were deposited onto hematite by photo-assisted electrodeposition.[10] Hematite electrodes were immersed in a solution containing 0.5 mM $Co(NO_3)_2 \cdot 6H_2O$ in a 0.1 M phosphate buffer (pH 6.9). A bias of 0.9 V vs RHE was applied under illumination. The thickness of the Co-Pi layer was controlled by varying the amount of charge allowed to pass during the deposition. For the electrodes reported herein, 5 thicknesses were prepared by allowing 1, 2, 15, 45 and 90 mC cm^{-2} to pass. After the catalyst was deposited, the electrodes were lightly rinsed with DI water to remove any excess cobalt ions. Co-Pi coated hematite

electrodes were prepared separately for SEM examination. After Co-Pi was photoelectrodeposited, electrodes were allowed to air dry. SEM images were taken on an Auriga CrossBeam FIB-SEM (Carl Zeiss Microscopy).

The water oxidation properties of the catalyst coated hematite films were then examined in contact with an aqueous solution buffered at pH 6.9 using a 0.1 M phosophate buffer containing 200 mM KCl as a supporting electrolyte. The pH was determined with Fisher Scientific Accumet pH meter. Impedance spectroscopic and photoelectrochemical measurements were made with an Eco Chemie Autolab potentiostat coupled with Nova electrochemical software. Impedance data were gathered using a 10 mV amplitude perturbation of between 10,000 and 0.01 Hz. Data were fit using Zview software (Scribner Associates). The light source was a 450 W Xe arc lamp. An AM 1.5 solar filter (Sciencetech Inc.) was used to simulate sunlight at 100 mW cm^{-2}. All photoelectrochemical measurements were performed by shining light from the substrate-electrode (SE) interface which avoids competitive light absorption of the Co-Pi. Light chopping *J-V* curves were measured at a rate of 75 mV/s. The light was chopped using a computer controlled ThorLabs solenoid shutter which was set to activate every 266 ms such that the light was turned on or off every 20 mV. Steady state *J-V* curves were measured at a scan rate of 5 mV/s.

Oxygen was detected by using an Ocean Optics spectrometer which probed the fluorescent decay of the FOSPOR patch. The FOSPOR patch was placed in solution which filled an airtight cell. The cell was filled so that very little headspace existed. The solution was stirred vigorously so that the O_2 measurement would be as close to real time as possible. Measurements were made under 4 sun illumination at 1.25 V vs RHE to increase oxygen production and reduce noise. In the calculation of the faradaic efficiency, the assumption was made that no oxygen

diffused into the very small headspace during the timescale of these experiments.

While these experiments were performed multiple times with many electrodes, only 3 different, but nominally identical electrodes were used to collect the photoelectrochemical data shown here: one for current transient and *J-V* curves, one for EIS measurements and one for O_2 measurements. The use of one electrode for each experiment allowed us to control for any small differences between bare electrodes. For experiments with varying amounts of Co-Pi, the Co-Pi was removed by applying a potential of 0.55 V vs RHE under dark conditions which slowly removed the Co-Pi film. After the Co-Pi was removed, the electrodes were examined to ensure that the performance was consistent with a bare electrode before applying Co-Pi for the next experiment.

8.4 Results

Thin film hematite electrodes were coated with varying thickness of the Co-Pi catalyst via photoelectrodeposition.[9,10,21] At the potential applied during the deposition (0.9 V vs RHE) steady state water oxidation does not occur with or without the Co-Pi catalyst (*vide infra*), thus any charge passed is assumed to be due to deposition of the catalyst. Film thicknesses can then be estimated by assuming that a single electron passed deposits one cobalt atom with surrounding ligands which occupies a volume of approximately 125 $Å^3$.[13] The thicknesses of the Co-Pi layers deposited by 1, 2, 15, 45 and 90 mC cm^{-2} was calculated to be 8, 15, 113, 337 and 675 nm, respectively. Co-Pi coated hematite films were analyzed by SEM to measure thickness and morphology; all of the films were found to be flat and uniform. Figure 8-1 shows a hematite film coated with Co-Pi by allowing 90 mC cm^{-2} to pass. This film was allowed to air dry immediately after the deposition. Assuming a 90 degree plane of the edge of the Co-Pi with

respect to the underlying hematite, and a viewing angle of 45 degrees, the thickness of this film is estimated to be ~425 nm. This thickness is largely the same throughout the film and on other films prepared by depositing 90 mC cm^{-2} Co-Pi, which is considerably less than the calculated thickness of 675 nm. Therefore, either the size of the cobalt cluster represents an overestimation or not all the charge passed is productive at depositing the film. In order to avoid ambiguity in the discussion of the Co-Pi films, the thicknesses will be referred to by the amount of charge passed (mC cm^{-2}) in the deposition, which was found to be roughly proportional to the film thickness. The morphology of the Co-Pi shown in the SEM image is consistent throughout the film.

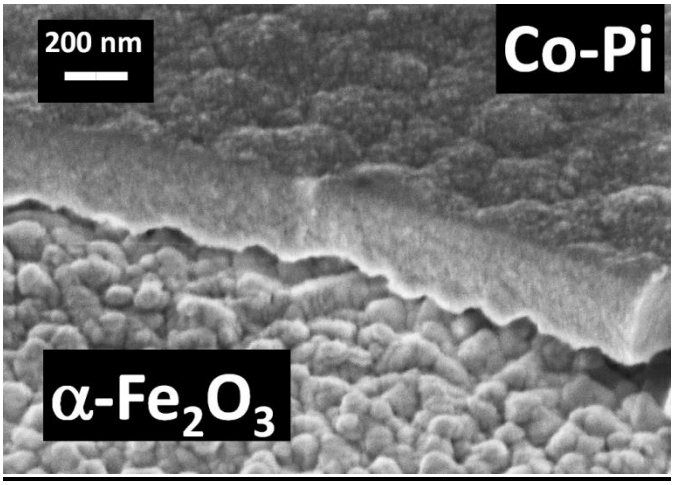

Figure 8-1. SEM image of a Co-Pi film deposited by passing 90 mC cm^{-2}. Sample was air dried immediately after deposition. The viewing angle is 45 degrees.

8.4.1 Steady State Behavior

Current density, *J*, vs. applied voltage, *V*, curves measured under 1 sun (100 mW cm^{-2}) illumination for a bare hematite electrode and the same hematite electrode coated with the

varying thicknesses of the Co-Pi catalyst can be seen in figure 8-2a. Steady state current measurements were also performed where the photocurrent was sampled after stabilizing over several minutes for individual potentials (Figure 8-2b). It was found that the steady state current densities are equal to the current densities of the cathodic scan of the *J-V* curves, thus confirming that the *J-V* measurements presented herein represent steady-state behavior (Figure 8-2c). The faradaic efficiency of the *J-V* curves was also measured by a fluorescent O_2 sensor. The O_2 concentration was measured at 1.25 V vs RHE which showed an increase in detected O_2 with increasing Co-Pi thickness for Co-Pi amounts up to 15 mC cm^{-2}; the O_2 detected was consistent with ~100% faradaic efficiency when considering the number of coulombs that have passed (Figure 8-3). Clearly, the addition of Co-Pi to the hematite improves the water oxidation efficiency. Figure 8-2b shows a semi-logarithmic plot of the cathodic shift of the of the *J-V* curves in figure 8-2a by sampling the potential needed to sustain a 200 μA cm^{-2} current density. The shift in photocurrent onset potential increases with Co-Pi thickness, quickly reaching a saturated shift of ~0.23 V for Co-Pi thicknesses greater than 15 mC cm^{-2}. This behavior is consistent with experiments examining Co-Pi on planar FTO coated glass, which was attributed to an increase in the number of active catalytic sites.[13] This trend, however, was not observed in a recent study examining Co-Pi deposited on high surface area hematite.[10] Thus, the simple explanation of increasing the number of active catalytic sites does not adequately describe the enhanced performance of the Co-Pi–hematite system. An alternative explanation is discussed below. In addition to the shift of the *J-V* curve, a slight increase in the photocurrent density at potentials positive of 1.4 V vs RHE is observed. This enhancement, however, is independent of

Co-Pi thickness. The improved PEC performance is generally consistent with previous reports of Co-Pi coated hematite electrodes.[7,10,11]

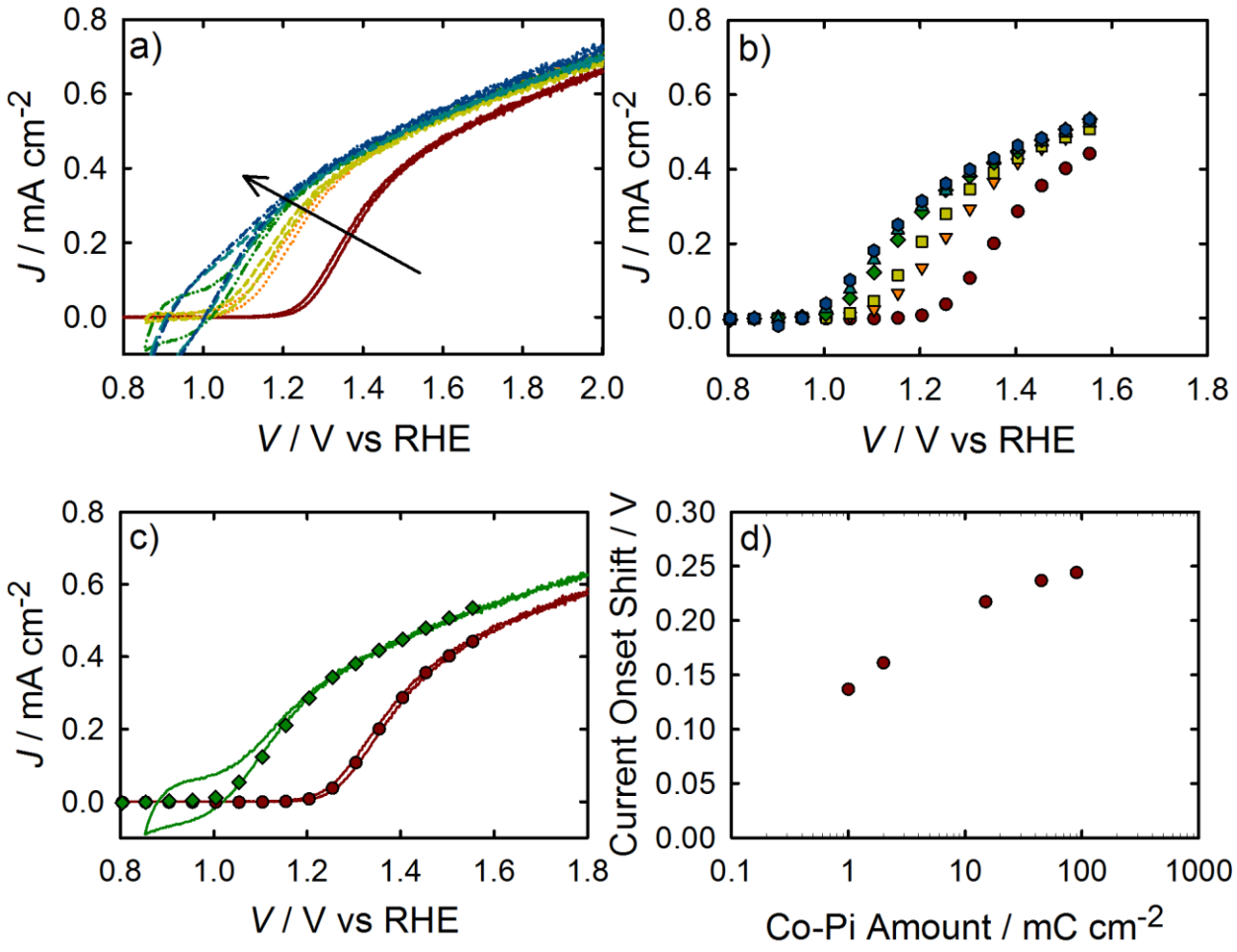

Figure 8-2. (a) *J-V* curves measured under 1 sun illumination of a bare electrode (red solid line) and the same electrode with 1 (orange dotted) 2 (yellow short dashed) 15 (green dashed double dotted) 45 (teal long dashed) and 90 (blue dashed single dotted) mC cm^{-2} Co-Pi. (b) Steady state photocurrent. (c) Steady state photocurrents (shapes), plotted with *J-V* curves (lines) to show that they overlap for a bare electrode (red circles) and one with 15 mC cm^{-2} Co-Pi (green diamonds). (d) Potential shift of the current onset relative to the bare electrode measured at 200 mA cm^{-2}.

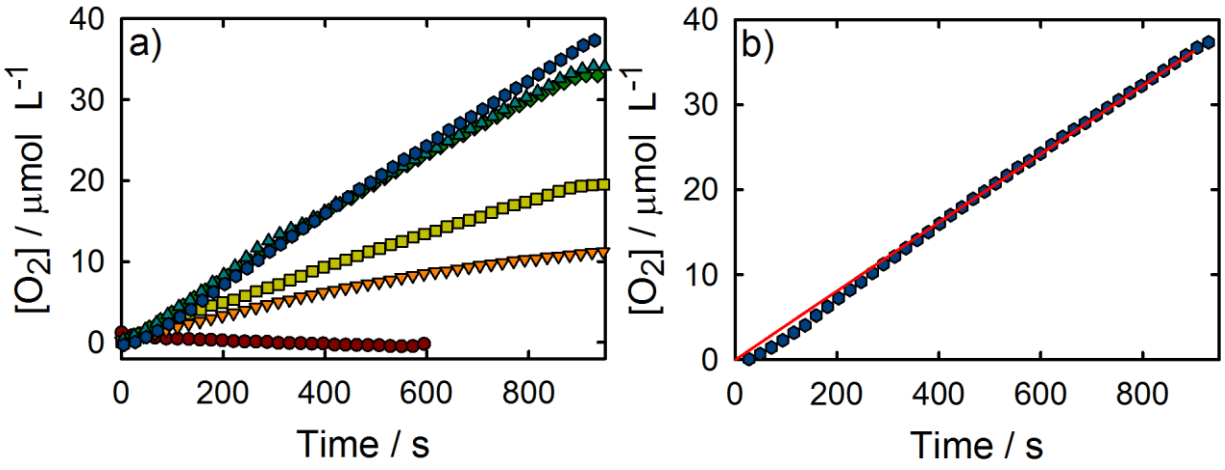

Figure 8-3. (a) Oxygen detected over time at 1.25 V vs RHE under 4 sun illumination for a bare hematite electrode (red circles) and the same electrode with 1 (orange pointing down triangles), 2 (yellow squares), 15 (green diamonds), 45 (teal pointing up triangles) and 90 (blue hexagons) mC cm^{-2} Co-Pi. (b) The calculated amount of O_2 that should be produced based on the number of coulombs passed (red line) compared to the O_2 that was detected (blue hexagons) for a hematite electrode coated with 90 mC cm^{-2} Co-Pi.

8.4.1 Transient Behavior

While performing steady state measurements, it became apparent that increasing the Co-Pi thickness required an increasing amount of time to reach steady state. Current transients were therefore measured in response to turning on (anodic) and off (cathodic) 1 sun illumination at a constant potential. Examples of anodic and cathodic current transients for different thicknesses of Co-Pi on hematite electrodes can be seen in figures 8-4a and 8-4b, respectively, at an applied bias of 1.05 V vs RHE. As shown previously for bare hematite electrodes,[27] at potentials negative of the current onset potential (such as 1.05 V vs RHE), an anodic spike in current is

visible when the light is turned on which quickly decays to the steady state current density. When the light is turned off a cathodic spike in current is observed which quickly decays to J_0. These spikes have been attributed to the charging (trapping of holes) and discharging of surface states, or oxidizing and reducing surface species.[27] Analogous behavior is observed when Co-Pi is added to the surface of hematite, however the amount of charge passed in the transients obviously increases with Co-Pi thickness. This suggests that the processes governing the transients are controlled by the Co-Pi. The anodic transients are attributed to the oxidation of Co(III) in the Co-Pi catalyst layer to Co(IV) by photogenerated holes in the valence band. This assignment is based on the recent observation of Co(IV) by EPR from Co-Pi which was electrodeposited during water oxidation.[29] Since such a large amount of charge is passed, and the quantity scales with thickness of the Co-Pi layer, the catalyst film must have the Co(IV) species distributed throughout. This indicates efficient diffusion of holes through the catalyst film via charge transfer from/to the cobalt centers, consistent with recent self-exchange measurements of Co-Pi using a model cubane molecule.[30] The cathodic transient measured after turning the light off is attributed to the reduction of Co(IV) to Co(III) by electrons from the conduction band of the hematite (i.e. recombination). The recombination time scale indicated by the cathodic transients generally scales with Co-Pi thickness, with thicker films requiring a longer time to reduce all the stored Co(IV), however in a less straightforward manner than the anodic transients. The initial current peak is the same for the 1 and 2 mC cm^{-2} Co-Pi films, then decreases monotonically with increasing Co-Pi thickness. The peak current should be proportional to the concentration of electrons in the conduction band and electron acceptors, [Co(IV)], at the interface, and the total charge passed proportional to the total number of Co(IV)

centers stored. At a given applied bias it is not expected that changing the Co-Pi thickness would change the concentration of electrons in the conduction band immediately after turning off the light, assuming a constant conduction band position (*vide infra*). Therefore, the decreasing cathodic peak heights can be attributed to decreasing concentrations of Co(IV) for Co-Pi thicknesses larger than 2 mC cm^{-2} at an applied bias of 1.05 V vs RHE. This corresponds to the same Co-Pi thickness that water oxidation occurs at 1.05 V vs RHE. Since water oxidation represents a parallel pathway that would deplete the Co-Pi film of Co(IV), it makes sense that increasing water oxidation kinetics would lead to a decreased concentration of Co(IV) in the film. In order to test this hypothesis, we also measured cathodic current transients at 0.95 V vs RHE where water oxidation does not occur for 1, 2 or 15 mC cm^{-2} films (see figure 8-5a). At this potential, the initial anodic peak current was the same for all films and the total charge passed is clearly proportional to film thickness, as expected. In addition, cathodic current transients were measured as a function of applied potential (see figure 8-5b). The initial peak current drops rapidly with increasing applied bias as expected since increasing the applied bias should decrease the conduction band concentration at the electrode surface as well decrease Co(IV) due to increasing water oxidation.

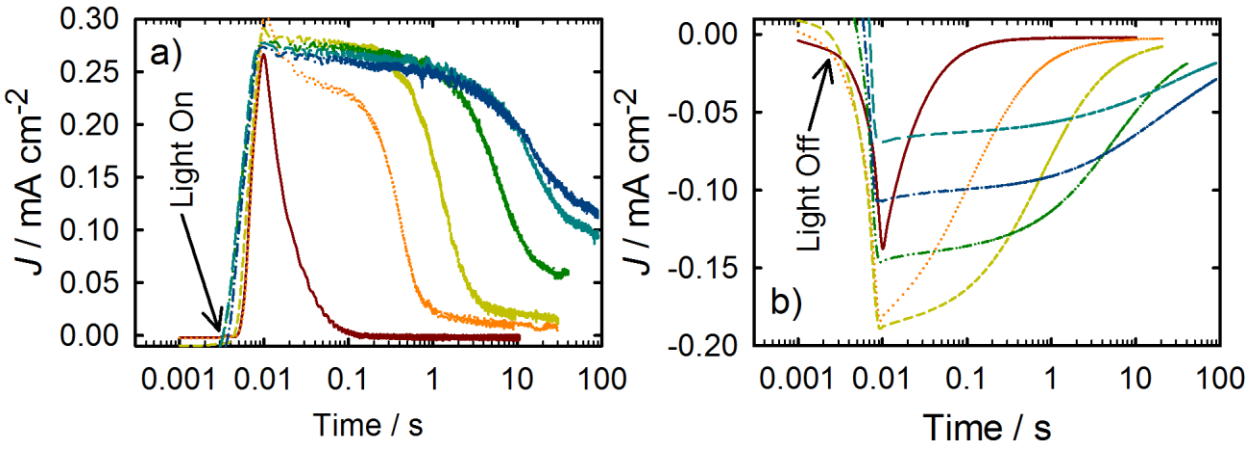

Figure 8-4. (a) anodic and (b) cathodic transients measured for a bare hematite electrode (red solid line) and the same electrode with 1 (orange dotted line) 2 (yellow short dashed line) 15 (green dashed double dotted line) 45 (teal long dashed line) and 90 (blue dashed single dotted line) mC cm^{-2} Co-Pi catalyst at an applied bias of 1.05 V vs RHE.

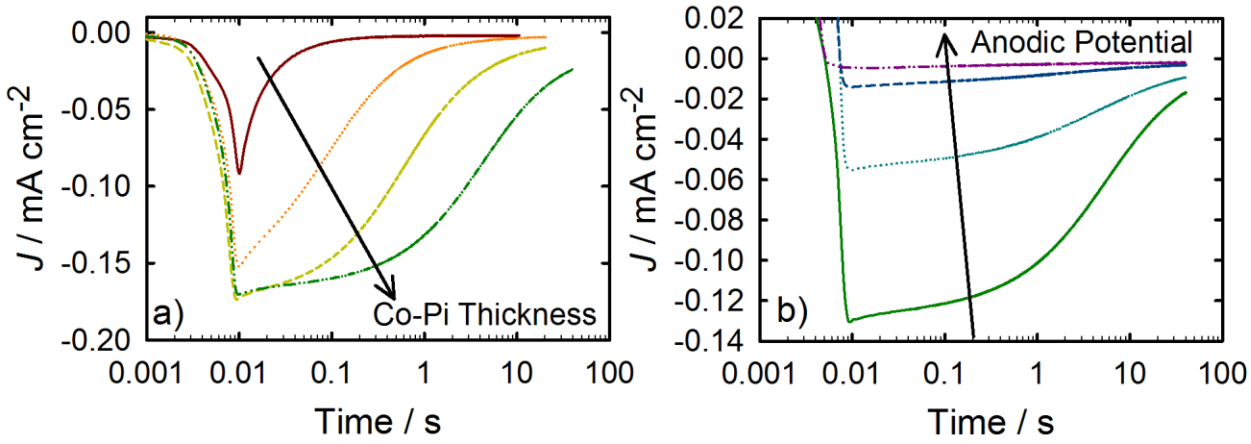

Figure 8-5. (a) Cathodic transients measured after turning the light off at an applied potential of 0.95 V vs RHE for a bare hematite electrode (red solid line), one with 1 (orange dotted line), 2 (yellow dashed line), and 15 mC cm^{-2} (green dashed, dotted line) of Co-Pi. (b) Cathodic transients after turning the light off for a hematite with 15 mC cm^{-2} Co-Pi measured at 1.05 (green solid line), 1.15 (teal dotted line), 1.25 (blue dashed line), and 1.35 V vs RHE (purple dashed, dotted line).

Light chopping experiments were also performed for electrodes with varying thicknesses of Co-Pi. Figure 8-6 shows a *J-V* curve measured under chopped and constant 1 sun illumination for a 15 mC cm^{-2} Co-Pi coated hematite electrode. The maximum current of the chopped light *J-V* is approximately linear which is reached instantaneously upon turning the light on. This behavior is similar to previous reports of hematite electrodes measured in contact with an electrolyte containing a fast redox shuttle.[27,31,32] Two different regions are observed when comparing the chopped light *J-V* curve to the steady state *J-V* curve. One is at potentials positive of ~1.4 V vs RHE where the instantaneous photocurrent measured by chopped light is equal to

the steady state *J-V* curve. The other region is between 0.85 and 1.4 V vs RHE where the instantaneous photocurrent measured by light chopping is much higher than the steady state photocurrent. In other words, at these potentials, charge is being transferred to and stored in the Co-Pi film without steady state water oxidation occurring. This "trapping" in the Co-Pi film presents an opportunity for recombination of electrons in the conduction band and Co(IV) to produce Co(III). This balance of charge separation and recombination may account for the different behavior observed for high aspect ratio electrodes.[10] Chopped light *J-V* curves measured for different Co-Pi thicknesses can be seen in the Appendix.

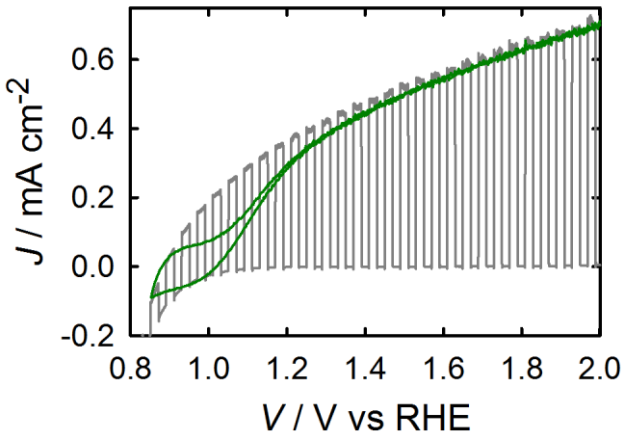

Figure 8-6. *J-V* curve for a hematite electrode coated with 15 mC cm^{-2} Co-Pi measured under constant 1 sun illumination (green line) and under chopped 1 sun illumination (grey line).

8.4.3 Electrochemical Impedance Spectroscopy

IS measurements were also performed for electrodes with varying thicknesses of Co-Pi. An example of a Nyquist plot measured under illumination for a bare hematite electrode and a hematite electrode coated with 15 mC cm^{-2} of Co-Pi at 1.25 V vs RHE can be seen in figure 8-7.

Around the photocurrent onset, two semicircles are clearly visible for both bare and Co-Pi coated hematite electrodes. The low frequency (high impedance) semicircle is clearly much smaller for Co-Pi coated electrodes compared to the bare electrodes. At more positive potentials (> 1.25 V vs RHE), the low frequency semicircle disappears for Co-Pi coated hematite electrodes.

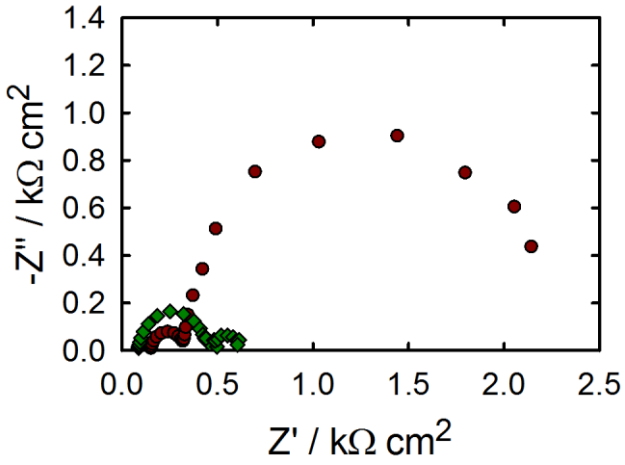

Figure 8-7. Nyquist plots measured under illumination of a bare hematite electrode (red circles) and with 15 mC cm^{-2} Co-Pi catalyst (green triangles) measured at 1.25 V vs RHE.

The complete equivalent circuit, EC, used to interpret the IS data is shown in figure 8-8a. The proposed circuit includes the circuit established previously for a bare hematite electrode under illumination which has also recently been modeled in detail.[28,33] This EC consists of the capacitance of the bulk hematite, C_{bulk}, charge transfer resistance from the valence band of the hematite, $R_{ct,bulk}$, a resistance which is related to the rate of trapping holes in surface states, R_{trap}, a capacitance of the surface states, C_{ss}, and a charge transfer resistance from the surface

states, $R_{ct,ss}$.[28] Additional electrical components were added to account for the Co-Pi layer including the capacitance of the Co-Pi layer, $C_{Co\text{-}Pi}$, and charge transfer resistance from the Co-Pi layer, $R_{ct,Co\text{-}Pi}$. Clearly, the full EC shown in figure 8-8a cannot be used to unambiguously fit the IS data for Co-Pi coated hematite electrodes. One thing that allowed us to simplify the equivalent circuit was independent examination of the low frequency semicircle; the capacitance of this feature increases approximately linearly with increasing Co-Pi thickness (shown and discussed below). This allowed assignment of this capacitance to $C_{Co\text{-}Pi}$. In addition, as shown in Figure 8-9b, charge transfer resistance from Co-Pi ($R_{ct,Co\text{-}Pi}$), which were also found to be proportional to the Co-Pi film thickness, showed much lower values compared to those found for bare hematite ($R_{ct,ss}$). Thus the complete EC could be simplified to that shown in figure 8-8b.

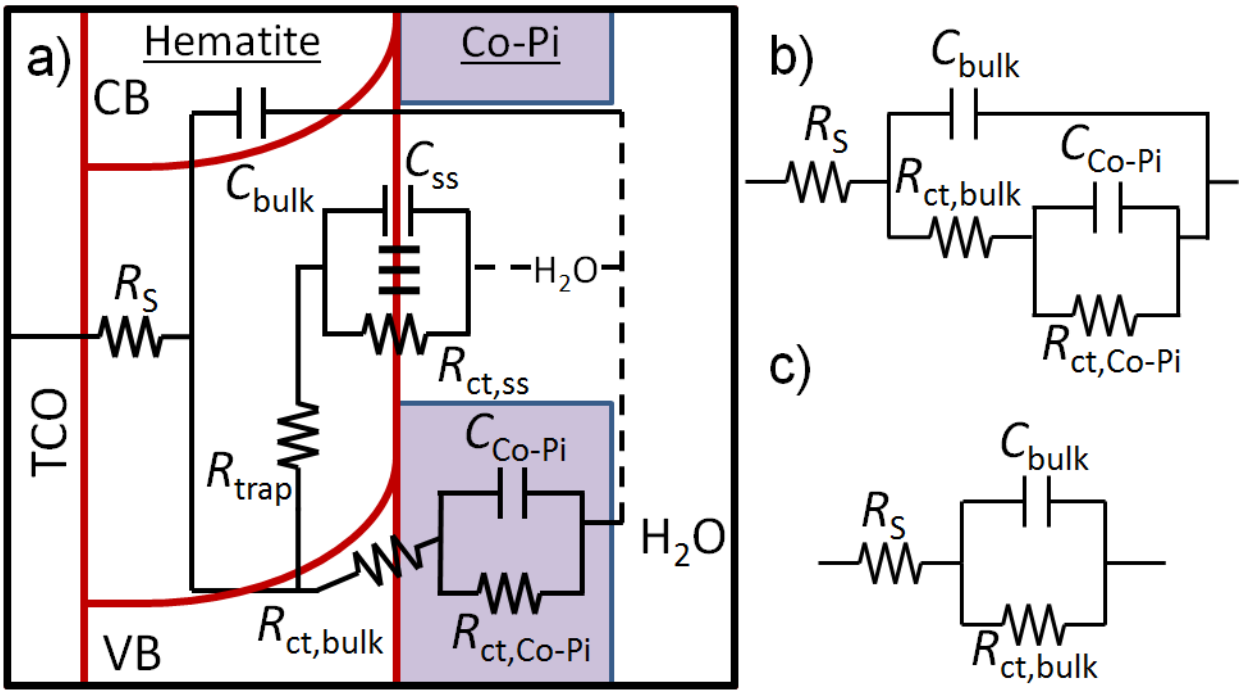

Figure 8-8. a) Proposed full equivalent circuit used for interpretation of hematite electrodes coated with Co-Pi catalyst. b) Simplified equivalent circuit used for interpretation of or Co-Pi coated Fe_2O_3. c) Randles' circuit used when only one semicircle is visible.

The impedance spectra of hematite electrodes with varying amounts of Co-Pi deposited, measured under 1 sun illumination, were fit to the EC shown in figure 8-8b. Figure 8-9a shows plots of $C_{Co\text{-}Pi}$ vs. applied potential for the different thicknesses of Co-Pi deposited on the hematite film. The $C_{Co\text{-}Pi}$ increases with thickness which is consistent with the assignment of this capacitance to the chemical capacitance of Co-Pi. This is also consistent with the trend of increasing charge passed before reaching a steady state current in the current transient measurements displayed in figure 8-4. Evidence of a capacitance due to the Co-Pi is also observed by performing *J-V* measurements at various scan rates of Co-Pi coated hematite

electrodes in a recent study by Zhong et. al.[9] The values for $R_{ct,Co\text{-}Pi}$, shown in figure 8-9b, are also related to the Co-Pi layer thickness; the resistance decreases with increasing Co-Pi thickness. When deposited on FTO, Co-Pi is known to be a porous material which shows a decrease in the required applied potential with an increasing amount of the catalyst.[13] The dependence of the decreasing $R_{ct,Co\text{-}Pi}$ with Co-Pi thickness is also consistent with the Co-Pi being a porous material. For all Co-Pi thicknesses, $R_{ct,Co\text{-}Pi}$ decreases exponentially with increasing potential. Similar to the current transients discussed above, there are two clear regions that are observed in the Nyquist plots. One is at potentials less than 1.4 V vs RHE which shows two clear semicircles where the contribution of the Co-Pi can be observed. However at potentials greater than 1.4 V vs RHE the low frequency capacitive feature disappears, and meaningful values for $C_{Co\text{-}Pi}$ and $R_{ct,Co\text{-}Pi}$ cannot be calculated. For these data, a simple Randles' circuit (figure 8-8c) is used to fit the impedance spectra and calculate values for $R_{ct,bulk}$ and C_{bulk}. The low frequency semicircle also disappears for bare hematite electrodes at more positive potentials (> 1.5 V vs RHE), which has recently been attributed to a hole transfer from the surface states of iron oxide to solution which is not the rate limiting step of water oxidation.[28] Similarly, we propose that at potentials where this low frequency capacitive feature measured on Co-Pi coated electrodes disappears, charge transfer from the Co-Pi to solution is not the rate limiting step. This is the cause of the independence of photocurrent measured at potentials positive of ~1.4 V vs RHE for increasing Co-Pi thickness. At these positive potentials, the photocurrent is controlled by the number of holes that reach the hematite surface for both bare and Co-Pi coated hematite electrodes.[32]

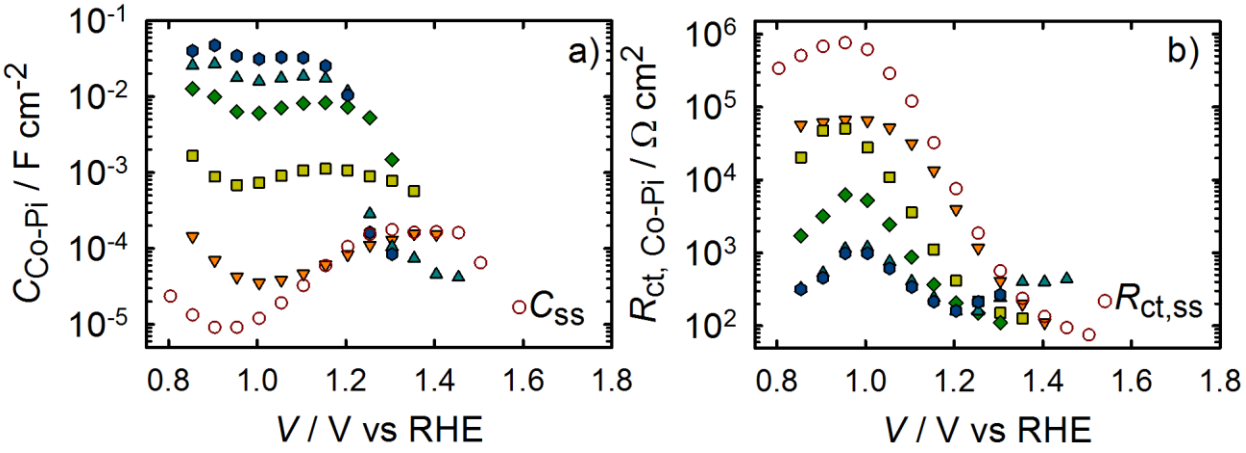

Figure 8-9. (a) $C_{Co\text{-}Pi}$ and (b) $R_{ct,Co\text{-}Pi}$ values fit from impedance response of hematite electrodes with 1 (orange triangles pointing down), 2 (yellow squares), 15 (green diamonds) 45 (teal triangles pointing up) and 90 mC cm^{-2} (blue hexagons) Co-Pi deposited. Bare hematite fitting parameters of a) C_{ss}, b) $R_{ct,ss}$ are shown for comparison (red open circles)

Values of $R_{ct,bulk}$, which represent the charge transfer from the hematite to the Co-Pi catalyst, can be found in figure 8. $R_{ct,bulk}$ is on the order of 10^2-10^3 Ω cm^2. These resistances are comparable to when a fast redox shuttle such as $[Fe(CN)_6]^{3-/4-}$ is used as a hole scavenger as reported previously.[27] This is consistent with having fast charge transfer of holes from the valence band of hematite to the Co-Pi. At potentials negative of the current onset potential, $R_{ct,Co\text{-}Pi}$ is much higher than $R_{ct,bulk}$. This is consistent with light chopping experiments where at these low applied potentials, charge transfer to Co-Pi is facile, yet water oxidation from the Co-Pi does not occur according to the steady state *J-V* curves and O_2 measurements. $R_{ct,Co\text{-}Pi}$ is

also included in the same graph as $R_{ct,bulk}$ emphasizing which resistance is the limiting resistance for a given potential. The total resistance, R_{tot} was calculated (R_s+ $R_{ct,Co\text{-}Pi}$ +$R_{ct,bulk}$) and compared to the resistance derived from the *J-V* curve ($R_{tot} = A_s(dV/dJ)$). A plot of R_{tot} derived from both impedance and *J-V* results can be seen in Figure 8-10b. The overlap of the R_{tot} determined from IS and the *J-V* curve shows how $R_{ct,bulk}$ and $R_{ct,Co\text{-}Pi}$ determine the shape of the *J-V* curve.

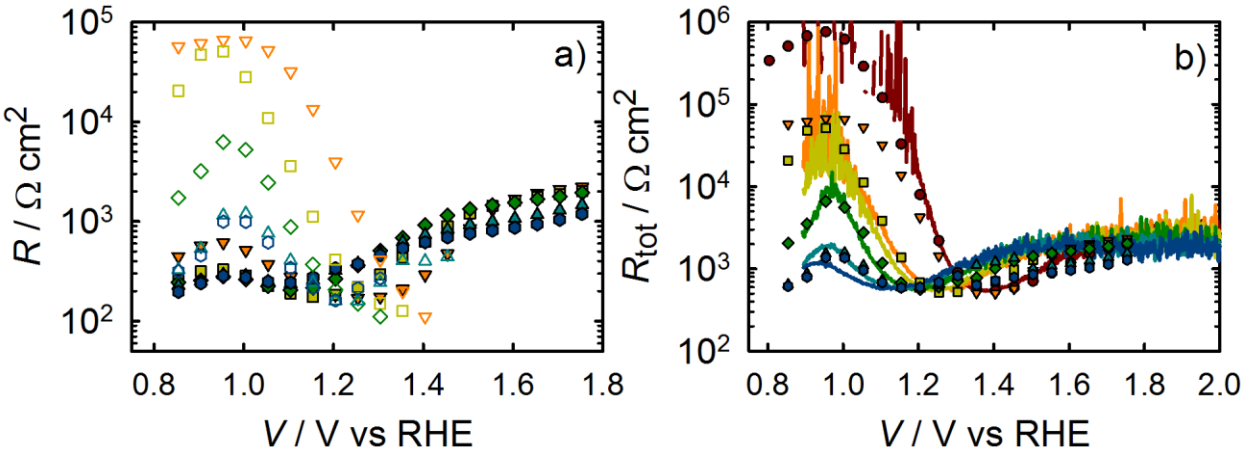

Figure 8-10. (a)$R_{ct,bulk}$ (solid shapes) and $R_{ct,Co\text{-}Pi}$ (open shapes) measured for a hematite electrode coated with 1 (orange pointing down triangles), 2 (yellow squares), 15 (green diamonds), 45 (teal pointing up triangles) and 90 mC cm^{-2} (blue hexagons) Co-Pi. (b) R_{tot} calculated from IS (shapes) and *J-V* curves (lines) for a bare hematite electrode (red circles) and the same electrode with Co-Pi.

Plots of C_{bulk} values can be seen in figure 8-11a. These values are essentially constant for all thicknesses of Co-Pi and the bare hematite electrode. Mott Schottky (MS) plots were

prepared from these C_{bulk} values and are displayed in figure 8-11b. As shown previously for bare hematite electrodes, MS plots show a horizontal shift which we attribute to Fermi level pinning by surface trapped holes.[27,28] This pinning is not observed in dark conditions (see Figure A8-3 in the Appendix). The MS plots measured with the Co-Pi coated hematite electrode shows a much more linear behavior compared to the bare electrode suggesting that Fermi level pinning is reduced. This is consistent with photogenerated holes being transferred to the Co-Pi layer instead of being trapped in surface states. Also, the flat band potential extrapolated from both bare and Co-Pi coated hematite electrodes is very similar, within the error of this measurement, suggesting that Co-Pi does not shift of the band positions. This is in contrast with a recent report that has suggested the primary role of Co-Pi on Co-Pi coated hematite electrodes is increased band bending.[11] The flat band potential and dopant density extracted from the MS plots are in good agreement with previously reports of thin film hematite electrodes.[26-28]

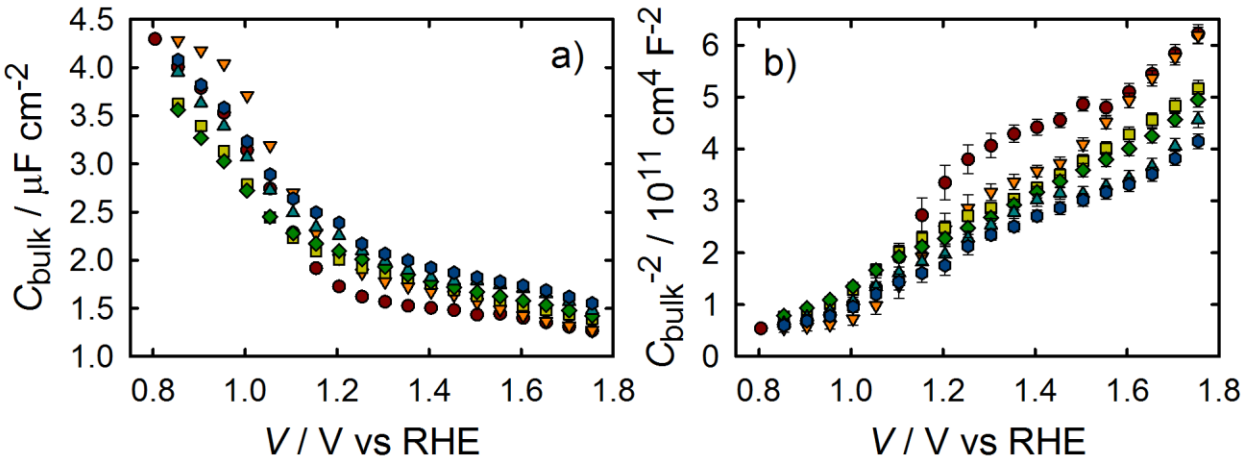

Figure 8-11. (a) C_{bulk} values fit from IS data of a bare hematite electrode (red circles) and the same electrode with 1 (orange pointing down triangles), 2 (yellow squares), 15 (green diamonds), 45 (teal pointing up triangles) and 90 (blue hexagons) mC cm^{-2} Co-Pi deposited. (b) Mott Schottky plot of C_{bulk} values shown in (a)

8.5 Discussion

To summarize the results presented above, deposition of the Co-Pi catalyst to planar hematite electrodes produces a favorable shift in the photocurrent onset potential. This shift increases with increasing Co-Pi thickness up to a saturated value of ~240 mV. Transient photocurrent and chopped light measurements showed that valence band holes in hematite efficiently oxidize Co(III) in the Co-Pi film to Co(IV). The transient anodic and cathodic photocurrent measurements, as well as the $C_{Co\text{-}Pi}$ measured by IS, as a function of Co-Pi thickness clearly show that photogenerated holes from hematite can be stored as Co(IV) throughout the Co-Pi layer. Also, the decreasing $R_{ct,Co\text{-}Pi}$ with increasing Co-Pi thickness showed that the Co-Pi is porous and has active sites throughout. The resistances extracted from

the IS measurements accurately account for the steady-state *J-V* behavior of Co-Pi coated hematite electrodes which we further showed corresponds to unity faradaic efficiency of oxygen generation. Therefore these results clearly demonstrate that water oxidation occurs predominately from the Co-Pi film, not the hematite surface. Cathodic current transients show that recombination of electrons from the hematite conduction band to Co(IV) is also a fast process, which decreases with increasing Co-Pi thickness. The improved photocurrent onset potential with increasing thickness of Co-Pi can therefore be accounted for by improved charge separation since an increasing fraction of Co(IV) is distributed throughout the Co-Pi film away from the hematite surface. It was also found that at potentials >~1.4 V vs RHE, the photocurrent does not increase with increasing Co-Pi thickness. We propose that at these potentials, there are enough adjacent Co(IV) active sites that when a hole reaches the hematite-Co-Pi interface, it can be immediately turned into faradaic photocurrent (oxygen). This is consistent with current transients which instantaneously reach the maximum current upon illumination, as well as IS which shows the disappearance of the low frequency semicircle attributed to trapping of holes, be it in surface states for a bare electrode or in the Co-Pi for a Co-Pi coated electrode.[27,28]

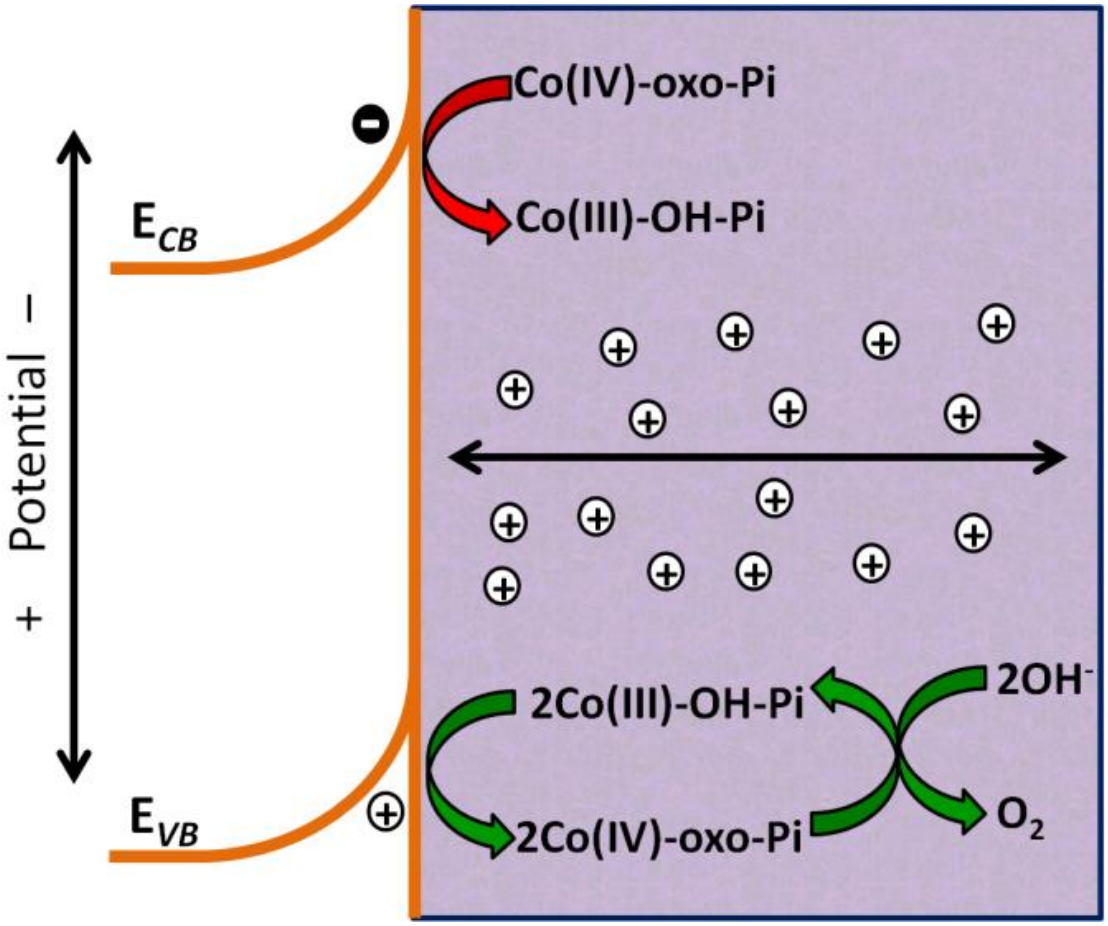

Figure 8-12. Diagram of a Co-Pi coated hematite electrode at under illumination and applied bias; the mechanism of Co-Pi is adopted from reference [34].

We now are in a position to compare our findings with the literature. The cathodic shifts in photocurrent onset potential measured in this study are higher than the ~180 mV shifts observed when Co-Pi is deposited on hematite electrodes with higher surface area.[9-11] Also, for high surface area hematite, the shift did not increase with Co-Pi thickness, and required the optimization of thin Co-Pi layers.[9,10] Based on our results, a higher surface area hematite electrode would provide a larger source of electrons to recombine with the Co(IV) since thicker layers of Co-Pi may bridge two regions of hematite and thus not produce better charge

separation. In addition, it is worth pointing out that measurements on structured hematite films are performed by shining light from the front (electrode) side, whereas we shine light from the back (FTO substrate) side. Since Co-Pi films broadly absorb visible light,[11] the measurements of thick Co-Pi films on structured electrodes are difficult to interpret since the decreasing light absorption by the hematite with thicker Co-Pi films is convoluted with the effect of the Co-Pi film. Although the thin films used herein are not practical for achieving the highest photocurrents, the use of such films allowed us to perform a controlled thickness dependence which showed an increasing performance with increasing Co-Pi thickness; a trend consistent with Co-Pi on FTO.[13] Transient absorption measurements have also recently been employed to determine the role of Co-Pi in enhancing the performance of a variety of hematite electrodes.[11,23] These authors suggested that Co-Pi acts as an electron acceptor which causes increased band bending and enhancement of charge separation within the hematite, and not hole transfer to the Co-Pi. This interpretation implies that water oxidation occurs at the hematite surface and not through the Co-Pi. Our measurements of C_{bulk} however, including their representation in Mott-Schottky plots, indicate that the band bending is essentially constant upon the addition of Co-Pi. Further, as described above, our measurements clearly show efficient hole transfer from hematite to Co-Pi and that water oxidation is occurring from the Co-Pi catalyst, not the hematite surface. Thus, the results presented herein are in stark contrast to several recent reports. We note that the hematite films being compared were prepared in different fashion and geometry, and very different techniques were employed to interrogate them, which may account for these differences in interpretation.

8.5 Conclusions

Uniform thin films of hematite were coated with varying amounts of the Co-Pi and investigated with a variety of steady-state and transient photoelectrochemical measurements and impedance spectroscopy. These systematic studies allowed for the identification of the mechanism by which Co-Pi enhances the water splitting performance of hematite electrodes. The Co-Pi catalyst efficiently collects and stores photogenerated holes from the hematite electrode. This charge separation reduces recombination which results in lower photocurrent onset potentials and hence water oxidation efficiency. One way of rationalizing the better water oxidation efficiency with increasing charge separation is through a bimolecular water oxidation mechanism which requires the oxidation of two adjacent cobalt atoms before oxidizing water. This mechanism has been previously proposed for Co-Pi on FTO electrodes.[13] In this case, long lived Co(IV) species are necessary in order to move to an adjacent Co(IV). This framework allows several analogies to be drawn between the bare hematite electrode and the Co-Pi coated electrode. Both require the oxidation of a water oxidation active site to an intermediate species before facile water oxidation occurs.[27] The accumulation of intermediates at illuminated bare hematite surface in contact with water has been measured in several recent papers by photoelectrochemical impedance spectroscopy,[2,27,28] intensity modulated photocurrent spectroscopy,[12] transient absorption spectroscopy,[5,23,35] and near edge X-ray absorption fine structure measurements.[36] In the case of a bare electrode this is possibly the oxidation of an Fe(III)-hydroxide to an Fe(IV)-oxo intermediate, although the identity of this Fe(IV)-oxo intermediate has not yet been confirmed.[27,37,38] In the case of Co-Pi, this is likely the oxidation

of a Co(III)-hydroxyl to a Co(IV)-oxo intermediate (figure 8-12).[13,29] The water oxidation intermediates of both bare and Co-Pi coated hematite electrodes are both, however, subject to recombination or reduction by electrons in the conduction band. For both bare and Co-Pi coated electrodes, this recombination is turned off with an applied potential and high band bending. Co-Pi coated hematite electrodes differ from bare hematite electrodes by efficiently separating charge and thereby reducing recombination and allowing longer lived holes as Co(IV) species. Despite this improved charge separation, Co-Pi is not immune to recombination from electrons in the conduction band. For Co-Pi to improve photoanodes further, recombination of electrons from the conduction band must be reduced.

8.6 Acknowledgements

TWH thanks the National Science Foundation (CHE-1150378) for support of this research. JB & FFS acknowledge support by projects from Ministerio de Industria y Competitividad (MINECO) of Spain (Consolider HOPE CSD2007-00007), and Generalitat Valenciana (PROMETEO/2009/058 and the "Institute of Nanotechnologies for Clean Energies", under project ISIC/2012/008). FFS thanks the funding of University Jaume I- Bancaixa (Grant P1·1B2011-50). SG acknowledges support by MINECO of Spain under the Ramon y Cajal programme.

APPENDIX

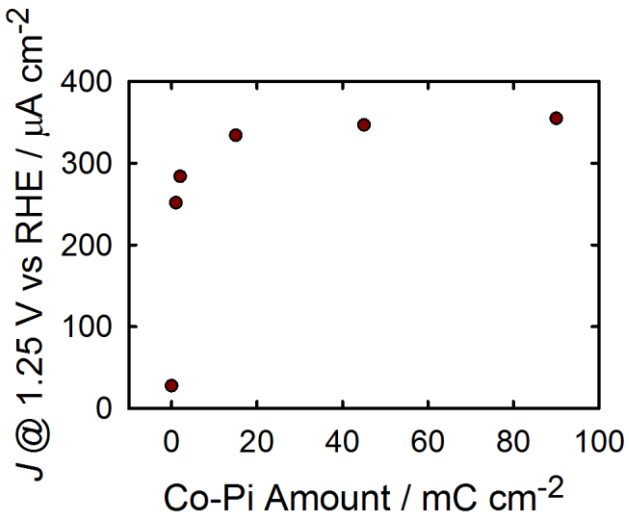

Figure A8-1. The current measured at 1.25 V vs RHE under 1 sun illumination. The trend agrees with O_2 production in figure 8-3a.

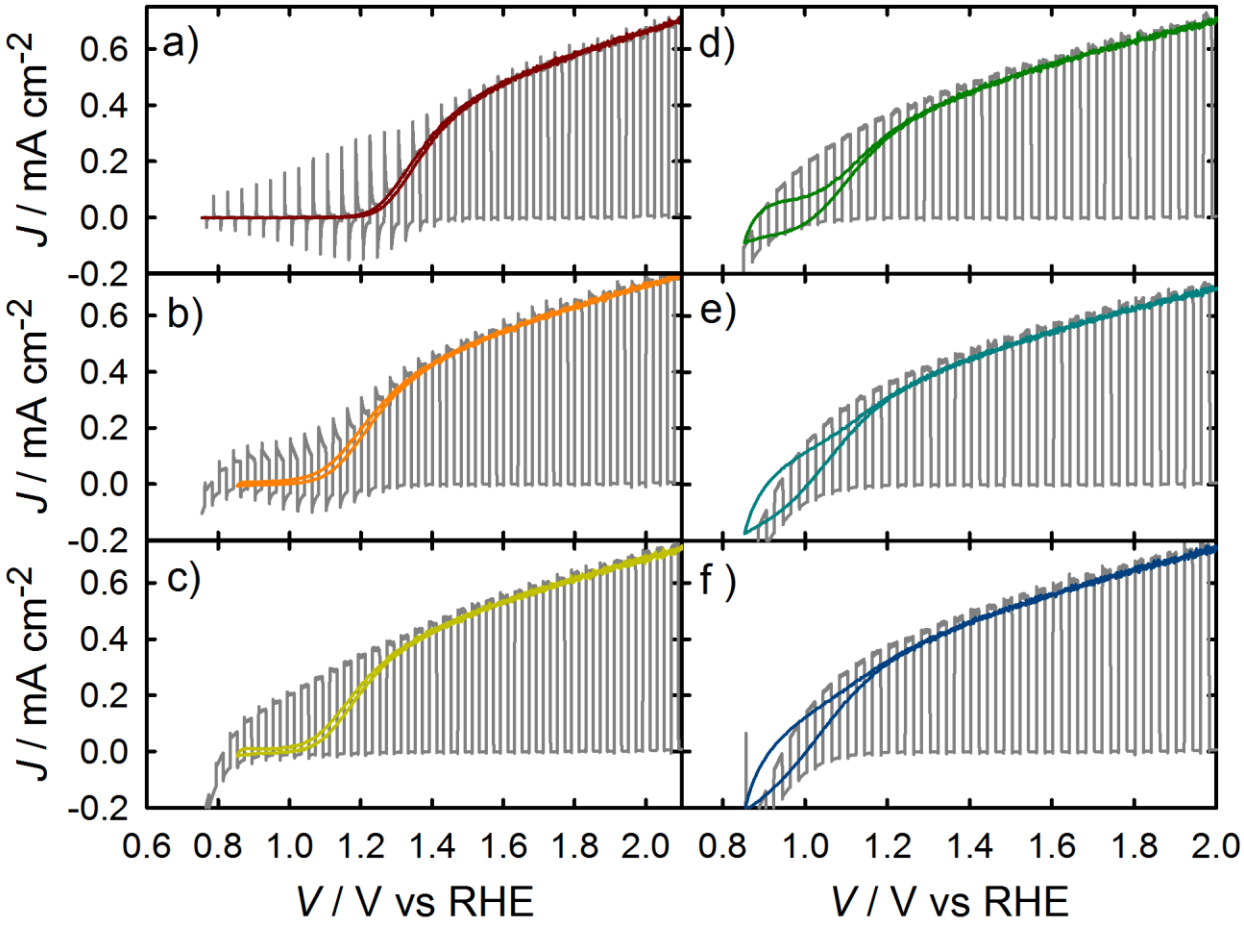

Figure A8-2. *J-V* curve measured under 1 sun illumination (colored line) and chopped light (grey line) for a) bare hematite electrode and the same electrode coated with b) 1, c) 2, d) 15, e) 45 and f) 90 mC cm^{-2} of Co-Pi.

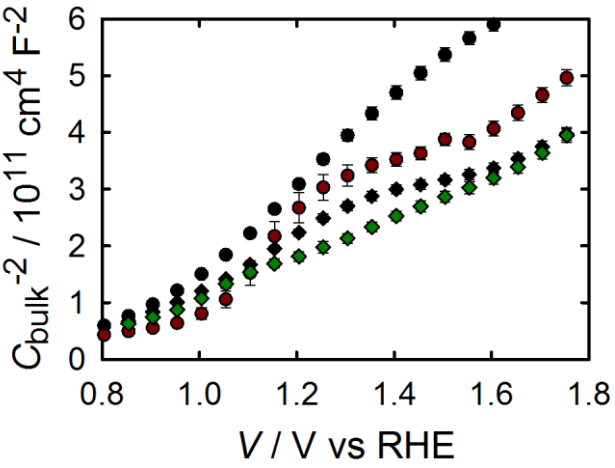

Figure A8-3. Mott Schottky plot for a bare hematite electrode (circles) in the dark (black circles) and under 1 sun illumination (red circles) as well as the same hematite electrode coated with 15 mC cm^{-2} Co-Pi (diamonds) measured in the dark (black diamonds) and under 1 sun illumination (green diamonds).

REFERENCES

REFERENCES

1. Dareedwards, M. P.; Goodenough, J. B.; Hamnett, A.; Trevellick, P. R. *J. Chem. Soc., Faraday Trans. 1 F*, **1983**, *79*, 2027-2041.

2. Upul Wijayantha, K. G.; Saremi-Yarahmadi, S.; Peter, L. M. *Phys. Chem. Chem. Phys.* **2011**, *13*, 5264-5270.

3. Peter, L. M.; Wijayantha, K. G. U.; Tahir, A. A. *Faraday Discuss.* **2012**, *155*, 309-322.

4. Cowan, A. J.; Barnett, C. J.; Pendlebury, S. R.; Barroso, M.; Sivula, K.; Grätzel, M.; Durrant, J. R.; Klug, D. R. *J. Am. Chem. Soc.* **2011**, *133*, 10134-10140.

5. Pendlebury, S. R.; Barroso, M.; Cowan, A. J.; Sivula, K.; Tang, J. W.; Gratzel, M.; Klug, D.; Durrant, J. R. *Chem. Commun.* **2011**, *47*, 716-718.

6. Tilley, S. D.; Cornuz, M.; Sivula, K.; Grätzel, M. *Angew. Chem. Int. Ed.* **2010**, *49*, 6405-6408.

7. McDonald, K. J.; Choi, K. S. *Chem. Mater.* **2011**, *23*, 1686-1693.

8. Zhong, D. K.; Sun, J. W.; Inumaru, H.; Gamelin, D. R. *J. Am. Chem. Soc.* **2009**, *131*, 6086-6087.

9. Zhong, D. K.; Gamelin, D. R. *J. Am. Chem. Soc.* **2010**, *132*, 4202-4207.

10. Zhong, D. K.; Cornuz, M.; Sivula, K.; Graetzel, M.; Gamelin, D. R. *Energy Environ. Sci.* **2011**, *4*, 1759-1764.

11. Barroso, M.; Cowan, A. J.; Pendlebury, S. R.; Grätzel, M.; Klug, D. R.; Durrant, J. R. *J. Am. Chem. Soc.* **2011**, *133*, 14868-14871.

12. Cummings, C. Y.; Marken, F.; Peter, L. M.; Tahir, A. A.; Wijayantha, K. G. U. *Chem. Commun.* **2012**, *48*, 2027-2029.

13. Surendranath, Y.; Kanan, M. W.; Nocera, D. G. *J. Am. Chem. Soc.* **2010**, *132*, 16501-16509.
14. Kanan, M. W.; Nocera, D. G. *Science*, **2008**, *321*, 1072-1075.

15. Lutterman, D. A.; Surendranath, Y.; Nocera, D. G. *J. Am. Chem. Soc.* **2009**, *131*, 3838-3839.

16. Hong, Y.-R.; Liu, Z.; Al-Bukhari, S. F. B. S. A.; Lee, C. J. J.; Yung, D. L.; Chi, D.; Hor, T. S. A. *Chem. Commun.* **2011**, *47*.

17. Pilli, S. K.; Deutsch, T. G.; Furtak, T. E.; Turner, J. A.; Brown, L. D.; Herring, A. M. *Phys. Chem. Chem. Phys.* **2012**, *14*, 7032-7039.

18. Abdi, F. F.; van de Krol, R. *J. Phys. Chem. C,* **2012**, *116*, 9398-9404.

19. Zhong, D. K.; Choi, S.; Gamelin, D. R. *J. Am. Chem. Soc.* **2011**, *133*, 18370-18377.

20. Seabold, J. A.; Choi, K.-S. *Chem. Mater.* **2011**, *23*, 1105-1112.

21. Steinmiller, E. M. P.; Choi, K.-S. *PNAS,* **2009**, *106*, 20633-20636.

22. Pijpers, J. J. H.; Winkler, M. T.; Surendranath, Y.; Buonassisi, T.; Nocera, D. G. *PNAS,* **2011**.

23. Barroso, M.; Mesa, C. A.; Pendlebury, S. R.; Cowan, A. J.; Hisatomi, T.; Sivula, K.; Grätzel, M.; Klug, D. R.; Durrant, J. R. *PNAS,* **2012**.

24. Martinson, A. B. F.; DeVries, M. J.; Libera, J. A.; Christensen, S. T.; Hupp, J. T.; Pellin, M. J.; Elam, J. W. *J. Phys. Chem. C,* **2011**, *115*, 4333-4339.

25. George, S. M. *Chem. Rev.* **2010**, *110*, 111-131.

26. Klahr, B. M.; Martinson, A. B. F.; Hamann, T. W. *Langmuir,* **2011**, *27*, 461-468.

27. Klahr, B.; Giménez, S.; Fabregat-Santiago, F.; Bisquert, J.; Hamann, T. *Energy Environ. Sci.* **2012**, *5*, 7626-7636.

28. Klahr, B.; Gimenez, S.; Fabregat-Santiago, F.; Hamann, T.; Bisquert, J. *J. Am. Chem. Soc.* **2012**, *134*, 4294-4302.

29. McAlpin, J. G.; Surendranath, Y.; Dincă, M.; Stich, T. A.; Stoian, S. A.; Casey, W. H.; Nocera, D. G.; Britt, R. D. *J. Am. Chem. Soc.* **2010**, *132*, 6882-6883.

30. Symes, M. D.; Surendranath, Y.; Lutterman, D. A.; Nocera, D. G. *J. Am. Chem. Soc.* **2011**, *133*, 5174-5177.

31. Sanchez, H. L.; Steinfink, H.; White, H. S. *J. Solid State Chem.* **1982**, *41*, 90-96.

32. Klahr, B. M.; Hamann, T. W. *Appl. Phys. Lett.* **2011**, *99*, 3.

33. Bertoluzzi, L.; Bisquert, J. *J. Phys. Chem. Lett.* **2012**, *3*, 2517-2522.

34. Kanan, M. W.; Surendranath, Y.; Nocera, D. G. *Chem. Soc. Rev.* **2009**, *38*, 109-114.

35. Pendlebury, S. R.; Cowan, A. J.; Barroso, M.; Sivula, K.; Ye, J.; Gratzel, M.; Klug, D. R.; Tang, J.; Durrant, J. R. *Energy Environ. Sci.* **2012**, *5*, 6304-6312.

36. Braun, A.; Sivula, K.; Bora, D. K.; Zhu, J.; Zhang, L.; Grätzel, M.; Guo, J.; Constable, E. C. *J. Phys. Chem. C,* **2012**, *116*, 16870-16875.

37. Hellman, A.; Pala, R. G. S. *J. Phys. Chem. C*, **2011**, *115*, 12901-12907.

38. Trainor, T. P.; Chaka, A. M.; Eng, P. J.; Newville, M.; Waychunas, G. A.; Catalano, J. G.; Brown Jr, G. E. *Surf. Sci.* **2004**, *573*, 204-224.

Chapter 9:

Water Oxidation at Co-Pi coated Hematite Electrodes: Reducing Recombination to Co-Pi with an Al_2O_3 Blocking Layer

9.1 Abstract

Uniform thin films of hematite (α-Fe_2O_3) deposited by atomic layer deposition (ALD) were coated with Al_2O_3 (alumina) before depositing the cobalt phosphate catalyst, "Co-Pi." Compared to a hematite electrode coated only with Co-Pi, the alumina blocking layer was found to effectively push move the water oxidation current onset potential by an additional 200 mV cathodically. Steady state and transient photoelectrochemical studies were paired with impedance spectroscopic analysis in order to clarify the role of the Al_2O_3 layer. It was found that adding Al_2O_3 prevents recombination of electrons in the conduction band of the hematite to the Co-Pi, resulting in a near quantitative hole collection.

9.2 Introduction

In the previous chapter, we performed systematic studies of water oxidation at Co-Pi coated hematite electrodes. Through photoelectrochemical and impedance spectroscopic measurements, the Co-Pi was found to shift water oxidation to more cathodic potentials as a result of storing holes capable of oxidizing water as oxidized intermediates and reducing recombination of electrons in the conduction band to those oxidized states in the Co-Pi. A thickness dependence showed that the water oxidation continued to shift cathodically as the thickness of Co-Pi was increased as a result of separating electrons in the conduction band from oxidized intermediates in the Co-Pi layer even further. These intermediates are hypothesized to be Co(IV)-oxo species.[1,2] However, it was observed that even thick layers (~400 nm) of Co-Pi were still susceptible to electron recombination which prevent steady state water oxidation at the most cathodic potentials.[1] In addition, the very thick films of Co-Pi required to obtain a large shift in the current onset potential are not useful on practical, high aspect ratio substrates because of the large non-productive optical absorption. While thin film hematite offers advantages for studying catalysts on semiconductor electrodes, it is likely that only high aspect ratio hematite electrodes will be practical. Thus, efficient catalysts will also need to be optically transparent.

In order to reduce recombination an alumina blocking layer was deposited onto the hematite by atomic layer deposition before the photoelectrodeposition of Co-Pi. A similar strategy has been used to reduce recombination of electrons in the conduction band of TiO_2 to cobalt based redox shuttles of dye-sensitized solar cells.[3-6] In this work, we employ photoelectrochemical measurements and impedance spectroscopy to investigate the effect of the alumina blocking layer on the water oxidation Co-Pi coated hematite.

9.3 Experimental

Thin films of hematite were deposited on fluorine-doped tin oxide (FTO) coated glass substrates (Hartford Glass, 12 Ω cm^{-2}) by ALD (Savannah 100, Cambridge Nanotech Inc.) using ferrocene as the metal precursor and ozone as the oxidation source. Deposition conditions have been described in detail elsewhere.[7,8] The hematite films were annealed by heating to 500° C over 30 minutes and soaking at 500° C for 30 minutes. Films were prepared by 800 ALD cycles and measured to be ~48 nm by absorption measurements (Perkin Elmer, Lambda 35 with a Labsphere integrating sphere) corrected for reflection as described previously, as well as ellipsometric measurements (Horiba Jobin Yvon, Smart-SE).[9] Films were characterized by Raman Spectroscopy and XRD as described previously.[9]

Al_2O_3 was deposited on the hematite films by ALD using trimethylaluminum and water as the precursors. Pulses of both precursors were each 0.015 seconds separated by a 6 second nitrogen purge time. Precursors were used at room temperature and the substrate was heated to 200° C. The growth rate of the deposition was measured to be 1.1 angstroms per cycle by ellipsometry analysis on witness silicon wafer chips. The growth rate is assumed to be the same on the hematite electrodes. Samples were annealed after Al_2O_3 deposition by heating to 500°C over 30 minutes and soaking at 500° C for 30 minutes.

Electrodes were masked with a 60 μm Surlyn film (Solaronix) with a 0.28 cm^2 hole to define the active area and to prevent scratching of the thin films. Surlyn films were adhered to the electrodes by heating to 120° C. The protected hematite films were clamped to a custom

made glass electrochemical cell. A homemade saturated Ag/AgCl electrode was used as a reference where potentials were converted the reversible hydrogen electrode (RHE) scale by the equation $E_{RHE} = E_{Ag/AgCl} + 0.197 + 0.059\,pH$. A high surface area platinum mesh was used as the counter electrode.

Co-Pi catalyst films were deposited by photoelectrodeposion which was originally described on ZnO electrode by Steinmiller and Choi and later adapted to hematite by Zhong and Gamelin.[10,11] Photoelectrodeposition has been shown to provide a superior deposition at the photoactive anode which is in contrast to electrodeposition which favors deposition at the underlying conductive substrate.[10-12] Hematite electrodes were immersed in a solution containing 0.5 mM $Co(NO_3)_2 \cdot 6H_2O$ in a 0.1 M phosphate buffer (pH 6.9). A bias of 0.8 V vs. RHE was applied under illumination. At this potential, steady state water oxidation does not occur with or without the Co-Pi catalyst, thus any charge passed is assumed to be due to deposition of the catalyst. In this study the amount of Co-Pi deposited was controlled by allowing 15 mC cm^{-2} of charge to pass. Thicknesses were estimated by assuming that a single electron passed deposits one cobalt atom with surrounding ligands which occupies 125$Å^3$.[2] Using this calculation, the deposition of 15 mC cm^{-2} corresponds with a thickness of 113 nm. However, due to the dynamic nature of the catalyst, which is continuously removed and re-deposited during water oxidation, catalyst thicknesses will be identified in terms of mC cm^{-2} to avoid ambiguity.[1,2]

After the catalyst was deposited, the electrodes were lightly rinsed with DI water to remove any excess cobalt ions. The water oxidation properties of the catalyst coated hematite

films were then examined in contact with an aqueous solution buffered at pH 6.9 using a 0.1 M phosophate buffer containing 200 mM KCl as a supporting electrolyte. The pH was determined with Fisher Scientific Accumet pH meter. Impedance spectroscopic and photoelectrochemical measurements were made with an Eco Chemie Autolab potentiostat coupled with Nova electrochemical software. Impedance data were gathered using a 10 mV amplitude perturbation of between 10,000 and 0.01 Hz. Data were fit using Zview software (Scribner Associates). The light source was a 450 W Xe arc lamp. An AM 1.5 solar filter was used to simulate sunlight at 100 mW cm^{-2}. All photoelectrochemical measurements were performed by shining light from the substrate-electrode (SE) interface which avoids competitive light absorption of the Co-Pi.

Light chopping *J-V* curves were measured at a rate of 75 mV/s. The light was chopped using a computer controlled ThorLabs solenoid shutter which was set to activate every 266 ms such that the light was turned on or off every 20 mV. Steady state *J-V* curves were measured at a scan rate of 5 mV/s.

Oxygen was detected by using an Ocean Optics spectrometer which probed the fluorescent decay of the FOSPOR patch. The FOSPOR patch was placed in solution which filled an airtight cell. The cell was filled so that very little headspace existed. The solution was stirred vigorously so that the O_2 would quickly diffuse through solution. Measurements were made under 4 sun illumination at 1.3 V vs RHE to increase oxygen production and reduce noise. In the calculation of the faradaic efficiency, the assumption was made that no oxygen diffused into the very small headspace during the timescale of these experiments.

9.4 Results and Discussion

Alumina was deposited on to hematite electrodes by ALD. As a control, the effect of an alumina layer on hematite films was examined without the addition of Co-Pi in a pH 6.8 aqueous

solution. It was observed that 1 cycle of alumina had little to no effect on the characteristics of the *J-V* where 5 cycles caused anodic shifts in the current onset potential and lower current density at positive potentials (Figure 9-1a). Figure 9-1b shows *J-V* curves of a hematite electrode with 5 cycles of alumina which shifts cathodically with increasing the number of scans. This shows the instability of the alumina layer under water oxidation conditions which is expected since alumina is well known to be unstable in the basic conditions associated with water oxidation. The lack of at least a temporary cathodic shift in the current onset potential for alumina coated hematite electrodes with respect to bare electrodes is in contrast to a recent study which has measured a cathodic shift in the water oxidation of hematite films with the addition of Al_2O_3 at pH 13.6.[13]

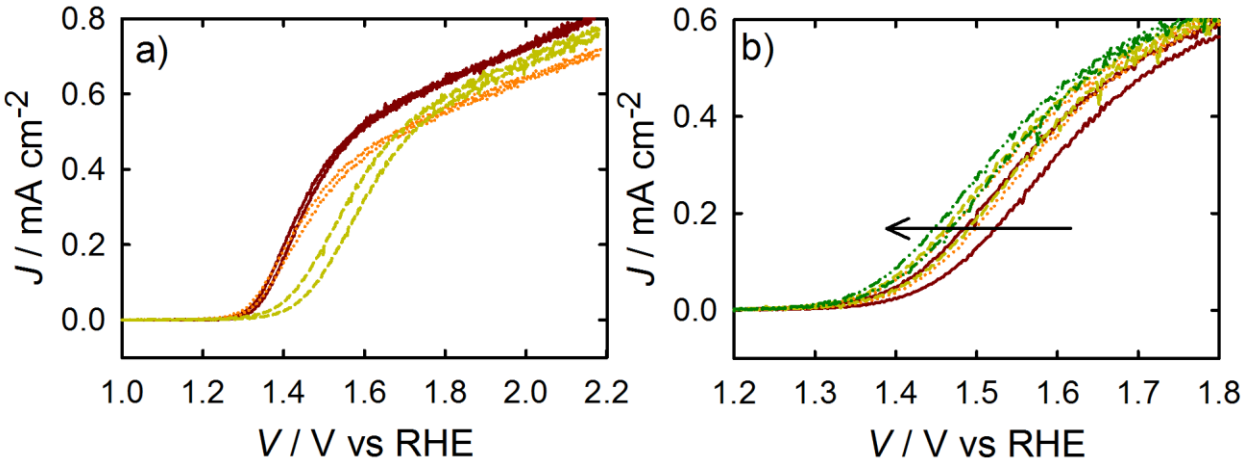

Figure 9-1. (a) *J-V* curves of a ~48 nm thick bare hematite electrode (red solid line), one coated with 1 cycle Al_2O_3 (orange dotted line) and one coated with 5 cycles of Al_2O_3 (yellow dashed line) in a phosphate buffered aqueous solution (pH 6.8). (b) *J-V* curves of a hematite electrode with 5 cycles of Al_2O_3. The arrow shows *J-V* curves taken sequentially.

A series of hematite electrodes were prepared with varying cycles of alumina deposited before the photoelectrodeposition of Co-Pi. To each alumina coated hematite electrode, 15 mC cm^{-2} of Co-Pi was added by photoelectrodepositon by applying a potential of 0.8 V vs RHE under illumination in a $Co(NO_3)_2$ solution. The effect of the thickness of the alumina layer can be seen in Figure 9-2a. With increasing layers of alumina, the current onset shifts cathodically. However, the current measured throughout most of the potential range is reduced with increasing alumina thickness. While thicker layers of alumina shift the current onset marginally, the decrease in photocurrent detracts from the total power that can be gained from this system. Therefore, to study this system further, an electrode containing only 1 cycle of alumina separating the Co-Pi and the hematite was used. Figure 9-2b shows the *J-V* curves of the only electrodes used for the remainder of the study: a bare hematite electrode, one coated with 15 mC cm^{-2} of Co-Pi and one with a single alumina layer separating the hematite and the Co-Pi. This shows that current can be measured with the Al_2O_3 blocking layer at potentials ~200 mV cathodic compared to Co-Pi electrodes without the blocking layer.

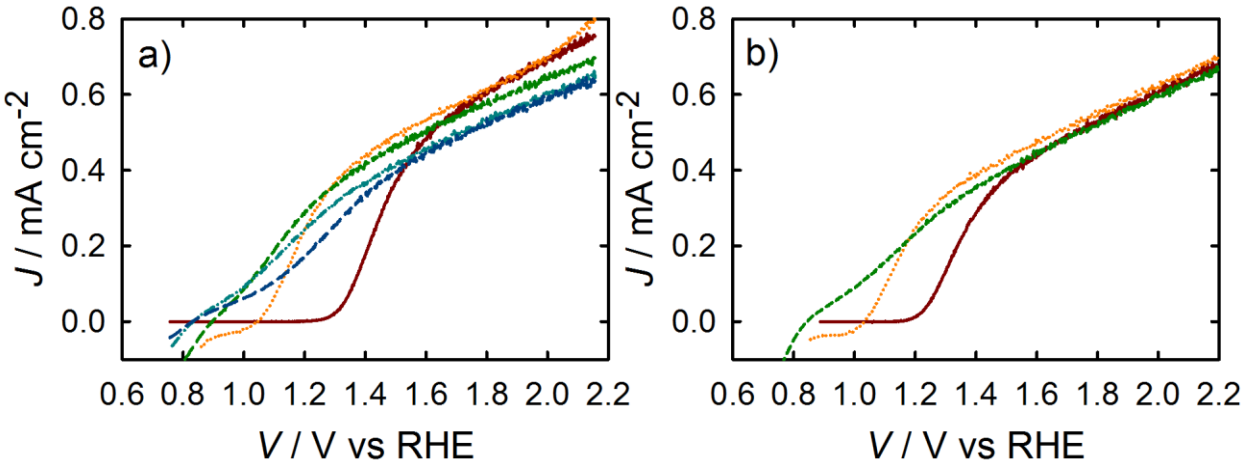

Figure 9-2. (a) *J-V* curves for a bare hematite electrode (red solid line) an electrode coated with 15 mC cm^{-2} Co-Pi (orange dotted line), and hematite films with 15 mC cm^{-2} Co-Pi separated by 1 (green short dashed line) 3 (teal double dotted dashed line) and 5 (blue long dashed line) cycles of alumina. (b) *J-V* curves for a bare hematite electrode (red solid line) an electrode coated with 15 mC cm^{-2} Co-Pi (orange dotted line), and hematite films with 15 mC cm^{-2} Co-Pi separated by 1 cycle of alumina (green dashed line). Figures only show cathodic scan for clarity. *J-V* curves of both cathode and anodic scan can be seen in the Appendix.

To ensure that the current measured by the *J-V* curves was stable and non-transient, steady state current measurements were performed where the photocurrent was sampled after the current was allowed to stabilize for 1 minute for individual potentials. It was found that the steady state current densities are equal to the current densities of the cathodic scan of the *J-V* curves, confirming that the *J-V* measurements presented herein represent steady-state behavior (Figure 9-3a). The faradaic efficiency of the *J-V* curves was also measured by a fluorescent O_2 sensor. The O_2 concentration was measured at 1.0 V vs. RHE to see if the current at such

cathodic potentials could be attributed to water oxidation. Due to the low currents at this potential, oxygen measurement were carried out under simulated solar illumination equivalent to 4 suns. The amount of O_2 detected is closely consistent with ~100% faradaic efficiency when considering the number of coulombs that have passed (figure 2b). The deviation measured after 400 seconds is expected to be an experimental deviation where O_2 is diffusing in to the small volume of headspace. This deviation appears to be large because of the low currents and low O_2 concentrations being generated at these very cathodic potentials. Despite this, it is clear that the addition of the Al_2O_3 blocking layer in between Co-Pi and hematite makes it possible to oxidize water at the very cathodic potentials of 1.0 V vs. RHE.

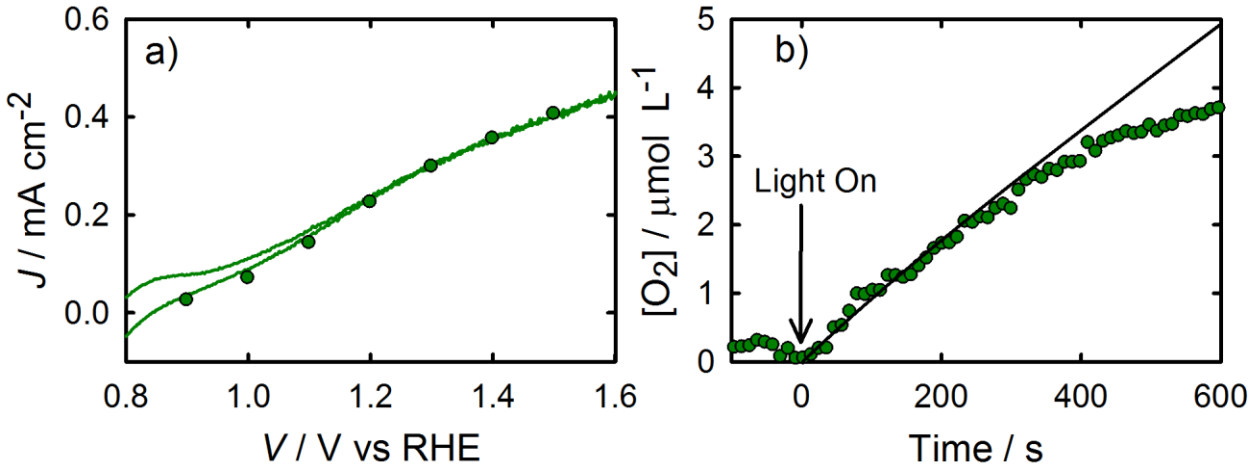

Figure 9-3. (a) Photocurrent measured after one minute at the applied potential to reach steady state (circles) and *J-V* measured at 5 mV/s for an Al_2O_3 modified Co-Pi coated hematite electrode. (b) Oxygen detected over time at 1.0 V vs RHE under 4 sun illumination for the same electrodes. The black line shows the theoretical amount of oxygen produced based on 100% faradaic efficiency

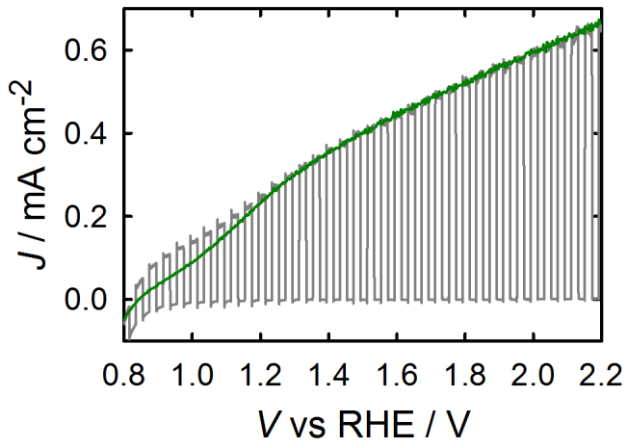

Figure 9-4. *J-V* curve for a hematite electrode coated with 15 mC cm^{-2} Co-Pi measured under constant 1 sun illumiation scanned at 5 mV/ s (green line) and under chopped 1 sun illumination.

In chapters 6 and 8, we used chopped *J-V* curves to emphasize the difference between steady state and transient behavior. For hematite electrodes in contact with a fast redox shuttle, $[Fe(CN)_6]^{3-/4-}$, the chopped *J-V* curves matched closely with the steady state *J-V* curves showing that the redox couple is collecting all of the holes that reach the surface without significant recombination (Figure 6-6a). On the other hand, for hematite electrodes in contact with just an aqueous electrolyte which excludes a fast redox shuttle, current spikes are measured which represent the significant recombination at surface states (Figure 6-6b). Thus the difference between the number of holes that reach the surface can be compared to the number of holes that perform steady state oxidation can be examined by analyzing the chopped and steady state *J-V* respectively. The chopped illumination *J-V* curve shown in Figure 9-4 (grey line) shows a transient behavior which is almost consistent with the steady state behavior. This suggests that almost all of the holes that are being transferred to the Co-Pi are participating in water oxidation.

This is in contrast to Co-Pi coated hematite electrodes which show transient behavior significantly different from steady state measurements, especially at anodic potentials (Figure 8-6). For Co-Pi coated electrodes without the alumina modification, this difference was attributed to the large amount of recombination that still occurs in the Co-Pi. The fact that the Al_2O_3 reduces this difference in the transient behavior suggests that the alumina is reducing recombination to the Co-Pi and that the Co-Pi is oxidizing water nearly quantitatively with the holes that it is exposed to.

Electrochemical impedance spectroscopy was employed to further understand the role of the alumina layer in the composite electrodes. Nyquist plots measured under 1 sun illumination and at a potential of 1.15 V vs RHE are shown in Figure 9-5. Nyquist plots of all three electrodes show similar characteristics which include two semicircles. For both Co-Pi coated electrodes, an equivalent circuit was used which contains the series resistance R_s, the capacitance of the bulk hematite, C_{bulk}, the resistance of charge transfer to the Co-Pi, $R_{ct,bulk}$, a capacitance of the Co-Pi, $C_{Co\text{-}Pi}$, and a charge transfer resistance from the Co-Pi to solution, $R_{ct,Co\text{-}Pi}$. This equivalent circuit has been discussed and justified for Co-Pi coated hematite electrodes previously.[1] An in depth discussion on the impedance interpretation of bare electrodes,[7,8] and the comparison of bare to Co-Pi coated electrodes can be found elsewhere.[1] For clarity, only the impedance results of Co-Pi coated hematite electrodes and alumina modified Co-Pi coated hematite electrodes will be discussed.

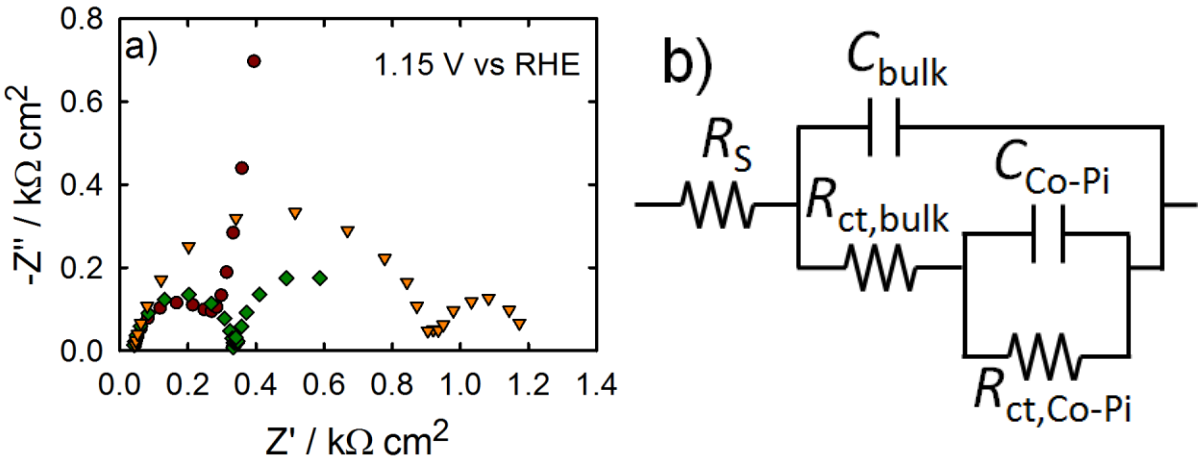

Figure 9-5. (a) Nyquist plots measured at 1.15 V vs RHE under 1 sun illumination for a bare hematite electrode (red circles), one coated with 15 mC cm^{-2} Co-Pi (green diamonds) and one with a Al_2O_3 layer separating the hematite and the Co-Pi (orange triangles). (b) Equivalent circuit used to fit impedance data.

The capacitance measured of the Co-Pi, $C_{Co\text{-}Pi}$ as a function of potential under 1 sun illumination can be found in figure 9-6a. For the Co-Pi coated hematite electrode there is a large capacitance peak which is consistent with results in the previous chapter for Co-Pi films of similar thickness.[1] The capacitance disappears at a potential of 1.3 V vs RHE which corresponds to when the *J-V* curve becomes linear and is limited by charge reaching the surface.[7,14] The capacitance of Co-Pi measured for the alumina modified electrode is approximately 5 times lower. One possibility for the lower capacitance could be that the Co-Pi layer is thinner on the alumina modified film. For example, since the number of coulombs were used to determine the thickness, it is possible that fewer of the coulombs passed when depositing the Co-Pi film on the alumina modified could actually be contributed to building the Co-Pi film. However, if the

thickness of the Co-Pi is lower for alumina modified Co-Pi coated hematite electrodes, the charge transfer from the Co-Pi, $R_{ct,Co\text{-}Pi}$, would be expected to be higher. We have recently shown, as result of increasing the thickness of Co-Pi on bare hematite electrodes, the $C_{Co\text{-}pi}$ increases as more charge can be stored in the Co-Pi, and the $R_{ct,Co\text{-}Pi}$ decreases as the porous Co-Pi increases the surface area able to participate in water oxidation. In light of this, the $R_{ct,Co\text{-}Pi}$ of the alumina modified electrode actually is decreased compared to the Co-Pi hematite electrode. This suggests that the decreased $C_{Co\text{-}Pi}$ and the decreased $R_{ct,Co\text{-}Pi}$ are a result of the alumina layer, and not related to a difference (if any) of the Co-Pi on each electrode. The decreased $C_{Co\text{-}Pi}$ with the addition of an alumina blocking layer suggests that a lower amount of charge is stored in the Co-Pi film. A decreased $R_{ct,Co\text{-}Pi}$, for an assumed identical (if not smaller) amount of Co-Pi suggests that there are more sites (oxidized cobalt species) which are capable of oxidizing water. This is consistent with a reduction in electron recombination from the conduction band of the hematite to those oxidized cobalt species in the Co-Pi film.

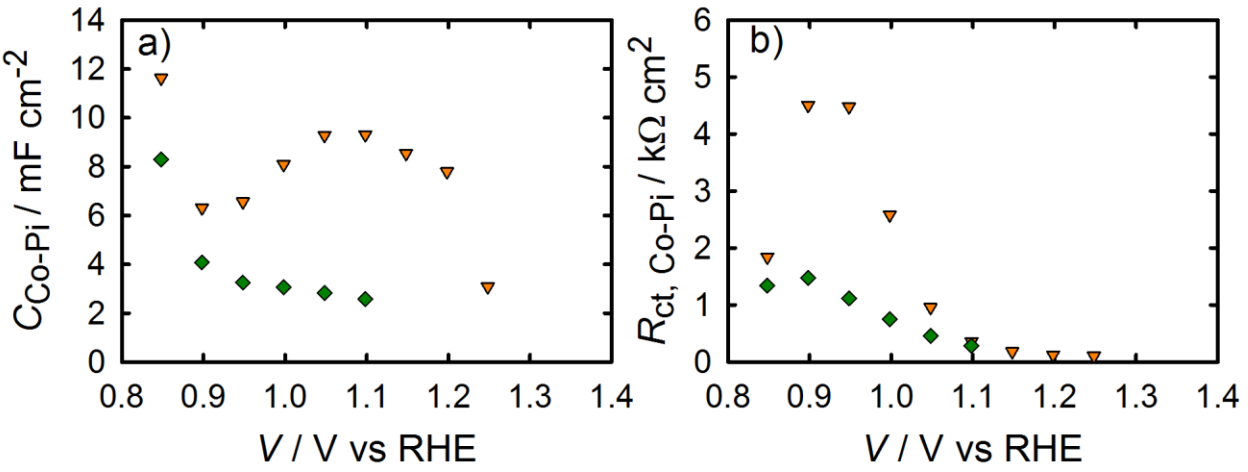

Figure 9-6. (a) $C_{Co\text{-}Pi}$ and (b) $R_{ct,Co\text{-}Pi}$ values fit from impedance response of a hematite electrode coated with 15 mC cm^{-2} Co-Pi (orange triangles), and hematite films with 15 mC cm^{-2} Co-Pi separated by 1 cycle of alumina (green diamonds).

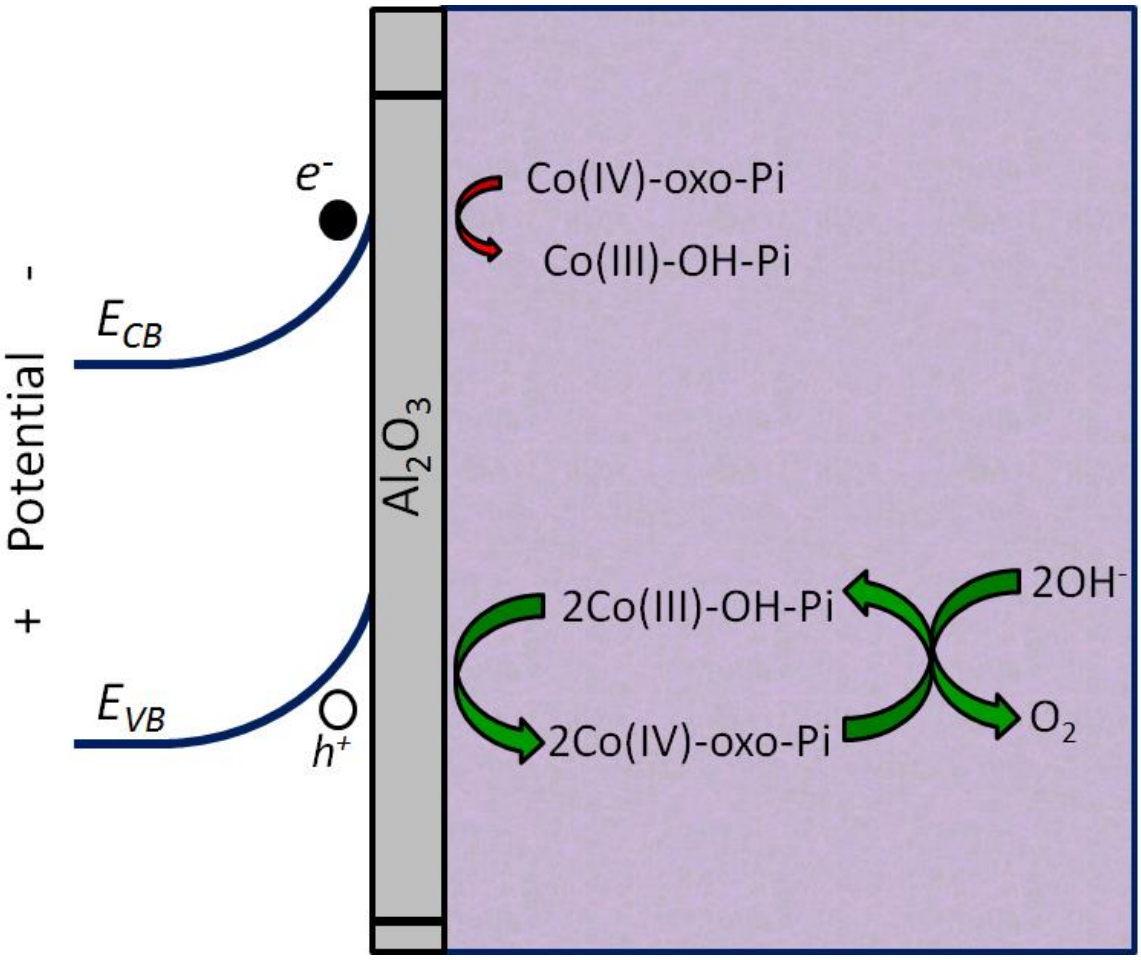

Figure 9-7. Scheme of the effect of an alumina blocking layer in Co-Pi coated hematite electrodes. Figure adapted from figure 8-12 and reference [15].

9.5 Conclusion

The addition of a Co-Pi layer to planar hematite electrodes was shown to shift the current onset potential cathodically due to a separation of electrons in the conduction band of the hematite from holes capable of oxidizing water. However, despite a reduced recombination, stored holes in the Co-Pi were still found to be vulnerable to recombination from electrons in the conduction band.[1] In this chapter, this recombination was successfully reduced further by

separating the hematite and the Co-Pi with a single layer of alumina which was deposited by ALD. This allowed for water to be oxidized at potentials ~200 mV cathodic of a Co-Pi coated hematite electrode without the alumina blocking layer. The comparison of chopped light and steady state behavior showed that nearly all holes that reach the surface can be used to oxidize water. The assignment of reduced electron recombination from the conduction band of hematite to stored holes in the Co-Pi agrees with the impedance spectroscopy analysis. A scheme of the effect of the alumina blocking layer in Co-Pi coated hematite electrodes can be found in figure 9-7. This figure shows how the alumina reduces the deleterious recombination of electrons in the conduction band to the oxidized Co-Pi (likely a Co(IV)-oxo), while allowing the favorable oxidation of the Co-Pi. It is observed, however, that thicker alumina layers also hinders hole transfer from the hematite to the Co-Pi. A possible reason for this effect is the fact that alumina is a wide band gap semiconductor in which the conduction band is at a higher energy than the conduction band of hematite and the valence band of alumina is at a lower energy than the valence band of hematite. This would prevent the transfer of both holes and electrons from the hematite to the Co-Pi by an energetic barrier. However, the description of a conduction band is not likely relevant for a layer of alumina of only ~1.1 angstroms thick. A more detailed description of the cause of the reduced recombination by the addition of alumina layer is currently being developed in our lab.

APPENDIX

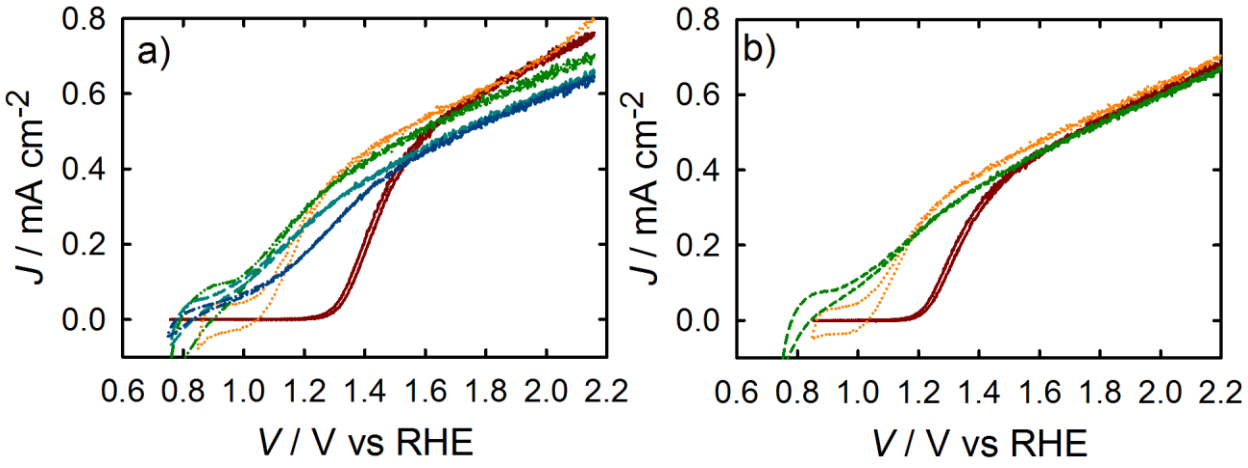

Figure A9-1. *J-V* curves for a bare hematite electrode (red solid line) an electrode coated with 15 mC cm^{-2} Co-Pi (orange dotted line), and hematite films with 15 mC cm^{-2} Co-Pi separated by 1 (green short dashed line) 3 (teal double dotted dashed line) and 5 (blue long dashed line) cycles of alumina. b) *J-V* curves for a bare hematite electrode (red solid line) an electrode coated with 15 mC cm^{-2} Co-Pi (orange dotted line), and hematite films with 15 mC cm^{-2} Co-Pi separated by 1 cycle of alumina (green dashed line).

REFERENCES

REFERENCES

1. Klahr, B.; Gimenez, S.; Fabregat-Santiago, F.; Bisquert, J.; Hamann, T. W. *J. Am. Chem. Soc.* **2012**, *134*, 16693-16700.

2. Surendranath, Y.; Kanan, M. W.; Nocera, D. G. *J. Am. Chem. Soc.* **2010**, *132*, 16501-16509.

3. Hamann, T. W.; Farha, O. K.; Hupp, J. T. *J. Phys. Chem. C*, **2008**, *112*, 19756-19764.

4. Klahr, B. M.; Hamann, T. W. *J. Phys. Chem. C*, **2009**, *113*, 14040-14045.

5. Ondersma, J. W.; Hamann, T. W. *J. Phys. Chem. C*, **2010**, *114*, 638-645.

6. DeVries, M. J.; Pellin, M. J.; Hupp, J. T. *Langmuir*, **2010**, *26*, 9082-9087.

7. Klahr, B.; Giménez, S.; Fabregat-Santiago, F.; Bisquert, J.; Hamann, T. *Energy Environ. Sci.* **2012**, *5*, 7626-7636.

8. Klahr, B.; Gimenez, S.; Fabregat-Santiago, F.; Hamann, T.; Bisquert, J. *J. Am. Chem. Soc.* **2012**, *134*, 4294-4302.

9. Klahr, B. M.; Martinson, A. B. F.; Hamann, T. W. *Langmuir*, **2011**, *27*, 461-468.

10. Steinmiller, E. M. P.; Choi, K.-S. *PNAS* **2009**, *106*, 20633-20636.

11. Zhong, D. K.; Cornuz, M.; Sivula, K.; Graetzel, M.; Gamelin, D. R. *Energy Environ. Sci.* **2011**, *4*, 1759-1764.

12. Zhong, D. K.; Gamelin, D. R. *J. Am. Chem. Soc.* **2010**, *132*, 4202-4207.

13. Le Formal, F.; Tetreault, N.; Cornuz, M.; Moehl, T.; Gratzel, M.; Sivula, K. *Chem. Sci.* **2011**, *2*, 737-743.

14. Klahr, B. M.; Hamann, T. W. *Appl. Phys. Lett.* **2011**, *99*, 3.

15. Kanan, M. W.; Surendranath, Y.; Nocera, D. G. *Chem. Soc. Rev.* **2009**, *38*, 109-114.

Chapter 10:

Conclusions and Future Directions

10.1 Conclusions

Atomic layer deposition was used to deposit thin films of hematite onto planar substrates. This process was studied and optimized so that thin, pinhole free, crystalline films could be prepared in a reproducible fashion. These thin films were used in systematic studies to evaluate the limitations of hematite for use in the water oxidation half of photoelectrochemical water splitting. The following conclusions were made from this work:

1. Hematite films were evaluated in contact with a fast redox shuttle, $[Fe(CN)_6]^{3-/\mathbf{4}-}$. It was shown that this redox shuttle can collect all of the holes that reach the surface. This redox shuttle was used to probe the properties of the bulk hematite by removing the limitations at the surface associated with water oxidation (chapters 3 and 6).[1,2]

2. A controlled thickness dependence, made possible by the controlled deposition by ALD, was performed in contact with $[Fe(CN)_6]^{3-/4-}$. It was found that the optimum thickness of hematite electrodes was approximately the thickness of the depletion region according to Mott Schottky analysis. This suggests that the diffusion length is approximately zero and charge can only be collected in the presence of an electric field (chapter 2).[3] This is confirmed by modifying the electric field through the modification of redox shuttles and pH in the contacting electrolyte (chapter 3).[1] This conclusion allowed us to model the linear current-voltage characteristics under illumination for hematite electrodes in contact with $[Fe(CN)_6]^{3-/4-}$ (chapter 4).[4]

3. Water oxidation was then studied at hematite electrodes under illumination using electrochemical impedance spectroscopy. An equivalent circuit was developed and

justified in order to interpret the experimental impedance data. This model included a surface state capacitance and an associated charge transfer resistance. The coincident observation of a peak in the surface state capacitance, a valley in the charge transfer resistance from those surface states, and the photocurrent onset for an applied potential suggests that water oxidation occurs from these surface states (chapter 5).[5] The charge of these surface states were also detected by current transient and cyclic voltammetry measurements. The requirement of the buildup of charge in the surface states was found to be responsible for Fermi level pinning which accounted for an additional ~140 mV applied potential to obtain a similar Fermi potential in the electrode compared when it is in contact with a fast redox shuttle. The remaining difference of photocurrent between the oxidation of a fast redox shuttle and water is attributed to recombination from electrons in the conduction band to oxidized intermediates at the surface (chapter 6).[2]

4. The photooxidation of water and methanol was examined independently and in competition with each other at hematite electrodes. Oxygen evolution experiments allowed the measurement of a faradaic efficiency for water oxidation with different amounts of methanol added to solution. A decreasing faradaic efficiency and measured surface state capacitance as a result of an increasing concentration of methanol further confirms that water oxidation occurs from the electrochemically measured surface states (chapter 7).
5. In order to avoid recombination at the surface, the Co-Pi catalyst was deposited onto the hematite electrode. Co-Pi was found to efficiently collect photogenerated holes from the hematite which helped separate them from electrons in the conduction band. This was confirmed by a systematic Co-Pi thickness dependence which showed the current onset

potential shift cathodically with an increasing amount of Co-Pi. Despite this advantage, Co-Pi was still susceptible to electron recombination as indicated by a comparison of the steady state and chopped illumination *J-V* measurements (chapter 8).[6] This recombination was reduced by adding an alumina blocking layer in between the hematite and the Co-Pi layer. This allowed for a near quantitative charge collection efficiency where nearly all of the holes that reach the surface were able to participate in water oxidation.

10.2 Future Directions

While surface states have been identified as a crucial component in the mechanism for water oxidation at hematite electrodes, the identity of those surface states has only been speculated on. For example, in chapter 6, we have hypothesized that a surface Fe(III)-OH is oxidized Fe(IV)=O where Fe(IV)=O is the charge which is observed in the impedance, cyclic voltammetry and current transient measurements. Water oxidation may require the accumulation of two adjacent Fe(IV)=O which would result in the requirement of a buildup of charge or a measured capacitance. The determination of the chemical identity of these intermediates would provide insight into the detailed mechanism of water oxidation at hematite electrodes, as well as guide the discovery/synthesis of more efficient water oxidation photocatalysts. In attempts to identify these intermediates, in-situ Raman, UV-Vis and IR spectroscopies should be performed. Depending on the sensitivity of the technique, high surface area electrodes may be required to increase the signals attributed to the surface.

The Co-Pi catalyst was added to hematite electrodes and nearly quantitative charge collection was achieved by adding an alumina blocking layer which prevented electron recombination to the Co-Pi. However, this was only accomplished on planar films which

employed a relatively thick layer of Co-Pi (>50 nm). This Co-Pi modification would not be as effective on nanostructured films due to the competitive light absorption of the Co-Pi film. Thus, optically transparent catalysts must be developed. To this end, thin layers (less than one monolayer) of $Co(OH)_2/Co_3O_4$ were deposited onto planar and high aspect ratio hematite.[7] Although these electrodes were not able to achieve quantitative hole collection, this modification shifted the current onset potential by ~200 mV while being optically transparent, even on high aspect ratio substrates. This enhancement was confirmed to be catalytic in nature by electrochemical impedance spectroscopy. More work is necessary to achieve quantitative hole collection at the surface of hematite with optically transparent overlayers.

Assuming a perfect overlayer/catalyst can be deposited onto hematite, the problem still remains of getting holes, generated deep within the bulk, to the surface so that they may oxidize water. Aside from the obvious benefits of nanostructuring electrodes in order to maximize light absorption with minimizing the length charge must travel before being collected, other strategies which increase the distance charge travels before recombining should be examined. For example, adding titanium impurities to hematite has been observed to increase the photocurrent density for water oxidation. This has been attributed to wide range of explanations including Ti acting as an electrical dopant,[8] an increased crystallinity,[9] and the passivation of surface states.[10] More recently, the systematic control of morphology, light absorption and Ti concentration in hematite films prepared by ALD has ruled out the effect of Ti as an electrical dopant, catalyst, or a surface passivation layer. Rather, the enhancement of Ti impurities in thin films was attributed to fixing the "dead layer" which is hypothesized to result from a lattice mismatch of the substrate

and the hematite.[11] Further fundamental studies are required to understand the role of other impurities so that the discovery of beneficial additives can be systematically pursued.

Chapters 2 through 4 have pointed out that charge can only be collected in the presence of an electric field in the hematite electrodes studied herein. For a given applied potential, the electric field within the hematite can be increased by creating a p-n junction. One possible example of this is coating hematite with a nickel oxide layer, a p-type semiconductor with band positions that should facilitate charge separation. Finding a surface modification which can increase the electric field within the hematite electrode and combining that with a surface catalyst capable of quantitative charge collection offers the possibility of an efficient water oxidation electrode made of inexpensive and stable materials.

REFERENCES

REFERENCES

1. Klahr, B. M.; Hamann, T. W. *J. Phys. Chem. C*, **2011**, *115*, 8393-8399.

2. Klahr, B.; Giménez, S.; Fabregat-Santiago, F.; Bisquert, J.; Hamann, T. *Energy Environ. Sci.* **2012**, *5*, 7626-7636.

3. Klahr, B. M.; Martinson, A. B. F.; Hamann, T. W. *Langmuir* **2011**, *27*, 461-468.

4. Klahr, B. M.; Hamann, T. W. *Appl. Phys. Lett.* **2011**, *99*, 3.

5. Klahr, B.; Gimenez, S.; Fabregat-Santiago, F.; Hamann, T.; Bisquert, J. *J. Am. Chem. Soc.* **2012**, *134*, 4294-4302.

6. Klahr, B.; Gimenez, S.; Fabregat-Santiago, F.; Bisquert, J.; Hamann, T. W. *J. Am. Chem. Soc.* **2012**, *134*, 16693-16700.

7. Riha, S. C.; Klahr, B. M.; Tyo, E. C.; Seifert, S.; Vajda, S.; Pellin, M. J.; Hamann, T. W.; Martinson, A. B. F. *ACS Nano*, **2013**, *7*, 2396-2405.

8. Wang, G.; Ling, Y.; Wheeler, D. A.; George, K. E. N.; Horsley, K.; Heske, C.; Zhang, J. Z.; Li, Y. *Nano Lett.* **2011**, *11*, 3503-3509.

9. Tang, H.; Matin, M. A.; Wang, H.; Deutsch, T.; Al-Jassim, M.; Turner, J.; Yan, Y. *J. Appl. Phys.* **2011**, *110*, 123511-123517.

10. Chemelewski, W. D.; Hahn, N. T.; Mullins, C. B. *J. Phys. Chem. C*, **2012**, *116*, 5255-5261.

11. Zandi, O.; Klahr, B. M.; Hamann, T. W. *Energy Environ. Sci.* **2013**, *6*, 634-642.